Dissertation zur Erlangung des Doktorgrades
der Fakultät für Chemie und Pharmazie
der Ludwig–Maximilians–Universität München

Light-induced molecular processes in organic-based energy conversion and biomimetic synthesis of natural products

Patrick Marco Kölle

aus

Frankfurt am Main, Deutschland

2016

Erklärung:

Diese Dissertation wurde im Sinne von §7 der Promotionsordnung vom 28. November 2011 von Frau Prof. Dr. Regina de Vivie-Riedle betreut.

Eidesstattliche Versicherung:

Diese Dissertation wurde eigenständig und ohne unerlaubte Hilfe erarbeitet.

München, den 24.06.2016

Dissertation eingereicht am:	24.06.2016
1. Gutachterin:	Prof. Dr. Regina de Vivie-Riedle
2. Gutachter:	Prof. Dr. Christian Ochsenfeld
Tag der mündlichen Prüfung:	09.08.2016

Contents

Abstract

Processes initiated by sunlight are fundamental steps in photovoltaic devices as well as in biosyntheses. The present work investigates the photoinduced processes in organic-based energy conversion materials and biomimetic synthesis of natural products by quantum chemical calculations. The work is performed in close collaboration with experimental groups and enables a deeper understanding of the observations. The detailed knowledge allows to predict the optimal conditions to initiate the photochemical syntheses and the chemical substitution to achieve the desired properties. In the first and second part of the thesis, two classes of molecules commonly used in organic-based optoelectronic devices are considered and potential factors influencing the performance of the optical devices are revealed. In the third part, the photochemical and biomimetic syntheses of two natural products and the details of the complex reaction mechanisms are elucidated.

In the first part of the present work the deactivation pathways from the first excited singlet state S_1 of thiophene and of small oligothiophenes containing up to four rings are investigated by state-of-the-art quantum chemical methods. For thiophene a low-lying S_1/S_0 conical intersection seam is easily accessible and drives the fast internal conversion. In the oligothiophenes barriers in combination with fast intersystem crossing channels inhibit this passage. The calculated spin-orbit coupling strength together with the singlet-triplet energy gaps can explain the decreasing triplet and increasing fluorescence quantum yields for growing chain length. The present theoretical results allow a deeper understanding of the deactivation pathways of thiophene and small oligothiophenes and are of potential interest for the photophysics of longer oligothiophenes and polythiophenes used in optoelectronic devices.

In the second part the photoinduced dynamics of perylene diimide dyads based on a donor-spacer-acceptor motif are considered. The dyads based on pyridine spacer undergo energy transfer from the donor to the acceptor with near-unity quantum efficiency. In contrast in the dyads with phenyl spacers the energy transfer decreases below 50%, suggesting the presence of a competing electron transfer from the spacer to the donor. However, the measurements indicate that the spacer itself mediates the energy transfer dynamics. *Ab initio* calculations reveal the existence of bright charge transfer states which enable the energy transfer. This new energy transfer represents a first example that show how electron transfer can be connected to energy transfer for the use in novel photovoltaic devices. Additional experiments and calculations of subsystems demonstrate that the solvation time and not the polarity of the solvent is surprisingly the crucial property of the solvent for the charge and energy transfer dynamics.

In the last part the photochemical syntheses of the two natural products intricarene and aplydactone are studied. Intricarene was isolated from a Carribbean coral and according to its proposed biosynthesis it arises from an oxidopyrylium intermediate *via* an intramolecular 1,3-dipolar cycloaddition. By a combination of experiments and theory it is shown that oxidopyrylium indeed forms under biomimetic and photochemical conditions and that it represents the key intermediate in the complex reaction cascade leading to intricarene. Triplet states as well as conical intersections enable the formation of intricarene and of an intriguing by-product which may constitute a new natural product. In the second part of the last chapter a quantum chemical study of the [2+2] photocycloaddition of dactylone to aplydactone is performed. Both compounds were isolated from a Madagascan sea hare and especially aplydactone exhibits an unprecedented molecular structure. However, for both compounds no total syntheses have been reported yet. According to the proposed biosynthesis, aplydactone is formed by a photochemical

[2+2] cycloaddition out of dactylone but attempts to synthesize aplydactone through irradiation of dactylone failed. In the present work quantum chemical calculations elucidate the optimal biomimetic conditions to initiate the photochemical reaction and the different reaction pathways on the excited state potential energy surface are revealed. Overall, the last chapter highlights the importance of weak absorption bands and long-lived triplet states for the photochemical synthesis of natural products.

List of publications

The thesis is based on the following four publications listed in chronological order. They are reprinted in the chapters 2 (**3**), 3 (**2, 4**) and 4 (**1**).

1 D. Stichnoth, P. Kölle, T. J. Kimbrough, E. Riedle, R. de Vivie-Riedle and D. Trauner.
Photochemical formation of intricarene.
Nat. Commun. **5**, 5597 (2014).

2 P. Kölle, I. Pugliesi, H. Langhals, R. Wilcken, A. J. Esterbauer, R. de Vivie-Riedle and E. Riedle.
Hole-transfer induced energy transfer in perylene diimide dyads with a donor-spacer-acceptor motif.
Phys. Chem. Chem. Phys **17**, 25061-25072. (2015).

3 P. Kölle, T. Schnappinger and R. de Vivie-Riedle.
Deactivation pathways of thiophene and oligothiophenes: internal conversion versus intersystem crossing.
Phys. Chem. Chem. Phys **18**, 7903-7915. (2016).

4 P. Kölle, A. Nenov, U. Megerle, P. Krok, H. Langhals, R. de Vivie-Riedle and E. Riedle.
Ultrafast emission quenching in a perylene diimide by structure rearrangement induced electron transfer from its substituent.
Manuscript, (unpublished).

Additional publications listed in chronological order:

5 A. Nenov, P. Kölle, M. A. Robb and R. de Vivie-Riedle.
Beyond the van der Lugt / Oosterhoff model: When the Conical Intersection Seam and the S1 Minimum Energy Path do not Cross.
J. Org. Chem. **75**, 123-129. (2010).

6 M. Vrabel, P. Kölle, K. M. Brunner, M. J. Gattner, V. López-Carrillo, R. de Vivie-Riedle and T. Carell.
Norbornenes in inverse electron-demand Diels-Alder reactions.
Chem. Eur. J. **19**, 13309-13312. (2013).

7 S. Thallmair, R. Siemering, P. Kölle, M. Kling, M. Wollenhaupt, T. Baumert and R. de Vivie-Riedle.
The Interplay of Nuclear and Electronic Motion in the Control of Molecular Processes: A Theoretical Perspective.
in: Molecular Quantum Dynamics – From Theory to Applications, F. Gatti (Ed.), Springer, 213-248, (2014).

8 P. Kölle, D. Stichnoth, E. Riedle, D. Trauner and R. de Vivie-Riedle.
Photochemische Synthese von Intricaren.
GIT Labor-Fachzeitschrift, **59**, 45-47, (2015).

Introduction

The large and fast growing global energy demand is one of the major challenges for the humanity and will have tremendous impact on the lives of future generations. The current energy regimen relies mainly on nonrenewable and polluting energy sources and has unsustainable consequences for the environment and the society [1]. The renewable source having the theoretically highest capability to meet the global energy demand is solar energy [1, 2].

One of the most promising technology to harvest this energy are solar cells. The present photovoltaic (PV) technology is dominated by solar cells based on inorganic materials which can achieve relatively high energy conversion efficiencies. However, high material and manufacturing costs and related environmental issues limit their widespread application [3]. Therefore, extensive research is conducted towards the development of low-cost PV technologies. Among these, organic solar cells (OSCs) are one of the most potential ones due to their unique properties of easy fabrication, large scale, light weight, flexibility and abundant raw materials [4]. They also exhibit the smallest ecological footprint and the shortest energy payback time [1, 4] and are associated with a broad range of possible applications [3]. Two remaining challenges for OSCs are the power conversion efficiencies and the operational lifetimes. Both are still behind those of inorganic solar cells, especially of the currently available commercial modules [1]. The concept of bulk-heterojunction (BHJ) based OSCs is considered as the most effective strategy to obtain higher performances [4]. In a BHJ structure, a donor and acceptor material are mixed together to form a bicontinuous interpenetrating network to allow large interfacial areas for efficient exciton dissociation and charge carrier transport [2, 4–6]. The used donor and acceptor materials can be divided into two different categories depending on whether their main constituent are small molecules or large polymers. The two classes of materials differ mainly in their synthesis, purification and device fabrication processes [1, 3]. Polythiophenes, especially poly(3-hexylthiophene) (P3HT), are one of the most used donor materials in polymer based solar cells (PSCs) [7,8]. They also represent widely used benchmark systems, which allow to unravel structure-property relationships and device engineering method for other high-performance polymers [2].

In the first part of the present work the deactivation processes of thiophenes are investigated by quantum chemical calculations. The theoretical methods and basis concepts used therefor and for the remaining part of this thesis are outlined in the first chapter. In the second chapter the deactivation pathways of photoexcited thiophene and of small oligothiophenes up to four rings are addressed. Despite several theoretical studies have already been performed [9–17], this work provides for the first time a balanced description of all systems by state-of-the-art quantum chemical methods taking into account singlet as well as triplet states and the spin-orbit coupling between them.

In the third chapter the energy transfer in perylene diimide dyads is considered. Several special designed compounds have been studied by time resolved spectroscopy. In this thesis quantum chemical calculations are performed to interpret and unravel the surprising experimental results. Perylene diimides are one promising class of acceptor materials used in organic solar cells due to their high electronic affinity and significant charge transport behavior [18]. Their properties can be readily modified by chemical modification and they therefore also serve as model systems to investigate energy and charge transfer processes. Charge as well as energy transfer play a crucial role for the novel concept of ternary OSCs. These OSCs consist of two donor materials of different absorption features to maximize the light harvesting [19, 20]. In the present work

the photoinduced dynamics and energy transfer mechanism of perylene diimide dyads based on a donor-spacer-acceptor motif are investigated. Since charge transfer (CT) states are the key actors of the observed dynamics, strong solvent effects are expected and their influence on the electron and energy transfer are elucidated in the second part of third chapter.

Alternative to photovoltaic cells the solar light can be collected by converting it into chemical energy through photochemical reactions. The most prominent example is the photosynthesis which converts the light energy via a whole series of steps to harness it for the production of simple organic nutrients from carbon dioxide and water. Photochemical reactions are also frequently the key steps in the synthesis of natural products [21], compounds which often exhibit attractive molecular architectures and interesting pharmacological properties [22, 23]. In photochemical reactions the high energy obtained by the absorption of light enables to overcome large activation barriers [24]. As a result, many photochemical reactions are unique as their reaction pathways cannot be accessed by other methods. The large energy available in photochemical reactions allow for astonishing transformations and the formation of remarkable molecular structures [21].

In the fourth chapter of the present work the photochemical syntheses of two novel natural products are investigated. The first natural product is intricarene which was isolated from a Caribbean coral and exhibits potential pharmacological properties [25]. Intricarene has attracted much interest of the synthetic community and its total synthesis was achieved by a thermal conversion from bipinnatin J [22, 26, 27]. Bipinnatin J was likewise discovered in the Caribbean coral and is proposed to be also the biosynthetic precursor [26–28]. The biosynthesis should involve a 1,3-dipolar cycloaddition from an intermediate oxidopyrylium species, a type of reaction observed very rarely in biosyntheses of natural products. However, the reaction conditions used in the reported syntheses of intricarene certainly cannot be deemed 'biomimetic' as high temperatures and refluxing in the solvent DMSO or DBU are required [26, 27]. In the present thesis the mechanism of the first realized biomimetic synthesis of intricarene is presented. The photochemical synthesis of intricarene was achieved in the group of Dirk Trauner. The optimal conditions to initiate the photochemical reaction and the mechanism underlying the light-induced reaction cascade are addressed by *ab initio* calculations.

In the second part of the fourth chapter the photocycloaddition of dactylone to aplydactone is considered. Dactylone and aplydactone are further natural products of marine origin and were isolated from a Madagascan sea hare [29, 30]. Especially aplydactone exhibits a novel molecular structure with an extremely strained and unprecedented tetracyclic framework. However, for both compounds no total syntheses have been reported yet. According to the proposed biosynthesis, aplydactone is formed by a photochemical [2+2] cycloaddition out of dactylone [30]. In the last part of the present work this photochemical cycloaddition is studied by quantum chemical calculations. Based on the knowledge of the study of intricarene, the conditions necessary for the photochemical synthesis of aplydactone and the details of the reaction mechanism are investigated.

1. Theoretical background

In the present work photoinduced processes are investigated by quantum chemical calculations. This chapter gives an overview of the main concepts used. Section 1.1 briefly introduces the quantum chemical methods and in section 1.2 the concept of conical and singlet-triplet intersections is described.

1.1. Quantum chemical methods

The singlet ground state structures of all studied systems in this work were optimized with the density functional theory (DFT) using the B3LYP functional [31–34]. The popular hybrid DFT functional B3LYP is still able to compete in accuracy with more sophisticated methods and density functionals regarding the determination of ground state geometries and thermochemical quantities and often requires only a fraction of the CPU time [35].

For the proper description of excited states and especially of regions where two electronic states get close to each other, multi-reference methods are required. Conical intersections are the most prominent examples of such regions and play a crucial role in all investigated molecules of this thesis. In the present work the complete active space self consistent field (CASSCF) approach [36–39] was used as multi-reference method. The CASSCF method is a modification of the multi configuration self consistent field (MCSCF) ansatz and its underlying concept is the simultaneous optimization of the configuration interaction (CI) and molecular orbital (MO) coefficients for a chosen subset of orbitals. The restriction to a subspace of orbitals, referred to as the active space, often prevents the CASSCF method of providing quantitative results. The complete active space second-order perturbation theory (CASPT2) method takes into account higher order excitations as perturbation to the CASSCF wave function and therewith often leads to almost quantitative results and was used throughout this work. However, the results of the CASPT2 method still crucially depend on the chosen active space. Therefore the active spaces were benchmarked against the results of the robust coupled cluster methods CC2 [40] and CCSD [41]. For the investigation of the basis set dependence, calculations with the efficient time-dependent density functional theory (TDDFT) method using the CAM-B3LYP functional [42] have been carried out.

In chapter 2 and 4 triplet states and diradicals are considered. To treat such open-shell systems it is convenient to use unrestricted methods like the unrestricted Hartree-Fock theory (UHF) [43] and allow each spin orbital to have a different spatial orbital. However, in the UHF formalism the resulting wave function is not an eigenfunction of the spin operator $\hat{S}^2$ and can be contaminated by higher spin states which can have a major impact on the quality of the results [44]. Within the unrestricted Kohn-Sham (UKS) formulation of the density functional theory, also the Kohn-Sham (KS) wave function can be spin contaminated. But it has been pointed out that a KS single determinant may properly exhibit spin contamination for open-shell systems, since it is only the density which has a meaning [45]. The KS determinant is only the wave function of the non-interacting reference system and not of the correct system and is used to construct the densities, from which the energies are evaluated. Furthermore the spin contamination is often very small for the unrestricted DFT method [44, 46]. Generally, there are several approaches to remove or minimize the spin contamination via spin projection and annihilation operators [47–49]. However, spin projection can yield poor results for potential energy surfaces while the

unrestricted DFT method using the UB3LYP functional leads to qualitatively correct values [46]. Therefore additional to the reliable CASSCF method, the efficient UBL3YP functional has been used to describe the triplet states and diradicals in this thesis. In particular, the UB3LYP optimized structures served as starting geometries for the optimizations at the CASSCF level of theory.

In chapter 3 charge transfer states will play an important role for the studied systems. Due to the high dipole moments of the charge transfer states, strong solvent effects are expected and are investigated by quantum chemical calculations and compared to experimental results. In general, two main types of approaches exist in quantum chemistry to describe solvent effects. The first one is the discrete molecular description of the medium. In the second type, the solvent is treated as a continuous medium (implicit description) characterized by a specific solvent dependent dielectric constants ϵ. At the quantum mechanical level the discrete description of the solvent is associated with a high computational cost and hence the solvent molecules are usually described classically by a force field. Therefore continuum models are regarded until now as an ideal conceptual framework to describe solvent effects within the quantum mechanical approach [50]. Among the available approaches the polarizable continuum model (PCM) has become the preferential one to account for solvent effects [51]. It has been shown that the PCM approach provides a reliable description of solvent effects on both, ground and excited state properties [50]. The so-called state specific model within the framework of the PCM is based on the explicit evaluation of the ground and excited wave function of the solute and describes the solute-solvent interaction properly through an iterative procedure [52–54]. For phenomena in which the solute undergoes a sudden change in its charge distribution, in addition the dynamic response of the solvent has to be taken into account. Examples for such phenomena are vertical electronic excitations, electron and energy transfer and nuclear vibrations [50]. Within the PCM framework these fast processes are considered by partitioning the solvent response into a slow and fast component and allow for non-equilibrium solvation situations [52]. The fast component can be related to the response of the solvent electrons, whereas the slow component can be ascribed to the response of the solvent nuclei. The mentioned capabilities of the PCM approach are implemented in the Gaussian 09 software package [55] and make it an appropriate tool to study the solvent effects on the electron and energy transfer processes in chapter 3.

The program package MOLPRO [56,57] was used for the CASSCF and CASPT2 calculations, while the DFT, TDDFT and CCSD calculations were carried out using the Gaussian 09 software package [55]. For the second-order approximate coupled cluster (CC2) calculations the TURBOMOLE program package [58] was used.

1.2. Conical and singlet-triplet intersections

The excess energy of an optically excited molecule can be dissipated through unimolecular processes either as radiation or by radiationless transitions [59]. The nonradiative processes are usually divided into internal conversion (IC) and intersystem crossing (ISC) and are of fundamental importance in photochemistry and photobiology. Internal conversion - the transition between states of equal spin multiplicity - is typically very fast and mediated by crossing points of different potential energy surfaces (PES). These intersections are referred to as conical intersections and are not isolated points but are rather part of an extended seam (intersection seam or space) [60,61]. At conical intersections the energetic degeneracy is lifted along a two-dimensional subspace which is termed as the branching space. This space is spanned by two vectors, the gradient difference vector and the non-adiabatic coupling vector. In a system with n coordinates, orthogonal to the branching space the n-2 dimensional intersection space exist where the crossing states remain degenerate. Conical intersections provide very efficient funnels for non-adiabatic transitions and have been shown to be ubiquitous in polyatomic molecules [59, 62–65].

In contrast thereto intersystem crossing - the transition between states of different spin multiplicity - was for a long time believed to play a minor role and to be much slower than IC. However, in the last years the number of studies on ISC has proliferated and it was shown by experiment and theory that ISC can occur on a (sub)picosecond timescale competing directly with IC [66–83]. Regions prone to favor ISC and being the equivalents to CoIns, are singlet-triplet crossing (STC) points [64, 84]. At these points the potential energy surfaces of a singlet and triplet state cross and the corresponding branching space is characterized by only one degeneracy-lifting coordinate, the gradient difference vector. For STC points, the non-adiabatic coupling vector is zero as the off-diagonal matrix elements of the Hamiltonian between a singlet and triplet state vanish [85]. Therefore the intersection space, which preserves the degeneracy and lies perpendicular to the branching space, is n-1 dimensional as opposed to the n-2 dimensional intersection space in the case of CoIns.

Intersystem crossing is made possible by the interaction of states of different multiplicity by spin-orbit coupling (SOC). Within the framework of the time-dependent perturbation theory the rate constant k_{ISC} for ISC is given by the Fermi golden rule expression [86–88] which depends quadratically on the spin-orbit coupling term $\hat{H}_{\mathrm{SO}}$ between the wave functions of the initial and final state Ψ_{i} and Ψ_{f}:

$$k_{\mathrm{ISC}} = \frac{2\pi}{\hbar} |\langle \Psi_{\mathrm{f}} | \hat{H}_{\mathrm{SO}} | \Psi_{\mathrm{i}} \rangle|^2 \rho_E \tag{1.1}$$

with ρ_E being the density of states, given by the number of energy levels per energy unit in the final state at the energy of the initial state [89]. Ψ_{i} and Ψ_{f} are here wave functions of different multiplicity (e.g. singlet and triplet wave functions). As the SOC scales approximately with the fourth power of the nuclear charge [90], the spin-orbit interaction is typically small for molecules lacking heavy atoms and hence ISC has been regarded as negligible. However, in the weak coupling limit the rate constant k_{rt} for radiationless transition depends, based on the energy gap law [91], exponentially on the adiabatic energy differences ΔE. In its simplest form, the energy gap law can be written as:

$$k_{\mathrm{rt}} \sim \exp\left(\frac{-\gamma \Delta \mathrm{E}}{\hbar \omega_{\mathrm{M}}}\right) \tag{1.2}$$

where γ is a term that can be expressed in terms of molecular parameters, and ω_{M} is the maximum vibrational frequency available in the system [92]. Therewith in cases where two electronic states of different multiplicity are close in energy, small coupling elements can be sufficient to induce a transition between them. Examples for such a scenario that the degeneracy of singlet and triplet states can compensate for small spin-orbit coupling, have been recently provided by Richter *et al.* [77, 82].

The importance of conical and of singlet-triplet intersections will also be demonstrated in the present thesis. In chapter 2 it will be shown that fast ISC can compete with IC and that both processes are responsible for the radiationless deactivation of the optical excited molecules. Furthermore, in chapter 4 it will be revealed that ISC and IC can also initiate and enable photochemical reactions leading to the formation of natural products.

2. Deactivation pathways of thiophenes

Oligothiophenes and polythiophenes have been shown to be some of the most promising candidates of organic materials for technological applications [93, 94]. In particular, owing to their efficient light harvesting, structural versatility and intrinsic charge transport behavior, thiophene based π-conjugated systems have attracted much attention as donor materials in organic solar cells [7]. As poly(3-hexylthiophene) (P3HT) they form in combination with phenyl-C61-butyric acid methyl ester (PCBM) the famous P3HT/PCBM solar cell. This material combination is still one of the most general and popular one for fundamental and conceptual studies [8]. Especially for the investigation of the initial processes after photoexcitation thiophenes serve as model systems. Furthermore, oligothiophenes exhibit additional interesting intrinsic properties like extremely high triplet quantum yields [95]. The large ISC rates deviate from the common behavior found in most molecules where the ratio of ISC to IC and fluorescence is rather small. In contrast to the oligothiophenes the monomer thiophene decays ultrafast exclusively *via* its singlet states to the ground state without the involvement of triplet states [11, 13, 15, 96]. In addition the high triplet quantum yields of the oligothiophenes decrease while the fluorescence quantum yields increase with the chain length of the oligomer [95].

The understanding of these experimental observations and trends and of the underlying radiative and nonradiative processes could allow to improve the performance of oligothiophene-based devices. For this purpose, the deactivation processes from the first excited state S_1 of thiophene and of small oligothiophenes up to four rings are investigated by quantum chemical calculations in the article "Deactivation pathways of thiophene and oligothiophenes: internal conversion *versus* intersystem crossing" published in *Physical Chemistry Chemical Physics* [97]. The focus in this work is on the bright S_1 state and its relaxation paths after optical excitation as this state is discussed to be crucial for the use of oligothiophenes in optical devices. By calculations of the low-lying excited states and of the spin-orbit coupling of the S_1 state and the triplet states the details of the deactivation pathways of thiophene (1T), bithiophene (2T), terthiophene (3T) and quaterthiophene (4T) are elucidated. The key statements of the article are:

- For the monomer 1T a low-lying conical intersection (CoIn) intersection seam is associated with a very small barrier and an ring-opening and is responsible for the fast internal conversion. ISC and triplet states are not present in the deactivation process due to small spin-orbit coupling (SOC) and large singlet-triplet energy gaps.

- In the oligothiophenes 2T-4T barriers inhibit the passage towards the CoIns and the relaxation paths are dominated by ISC. The triplet formation is made possible by two ISC channels whereby the first one is responsible for the high triplet quantum yields. It takes place along the initial relaxation which is correlated with a planarization of the molecules. During the planarization to the first excited state minimum (S_1-Min-a) the S_1 state intersects with a triplet state and opens the first ISC path. This degeneracy can compensate the moderate spin-orbit interaction of the involved states and allow a fast and efficient ISC consistent with the energy gap law [91]. The second, less effective ISC channel occurs around S_1-Min-a and is induced by thermal torsional fluctuations. The two ISC channels are in agreement with the experimental observation which reveal that the S_1 decay and the triplet formation of the oligothiophenes is described by a fast and a slow time constant [98–102].

- The diminishing SOC from 2T to 4T and increasing S_1-triplet energy gaps at S_1-Min-a can explain the decreasing triplet and increasing fluorescence quantum yields.
- From the triplets the relaxation back to the ground state occurs *via* two different kinds of triplet cascades which are enabled by inter-ring torsions. For the even-numbered oligothiophenes a $T_3 \rightarrow T_2 \rightarrow T_1$ cascade allows the fast relaxation, while for the odd oligothiophene an additional direct $T_3 \rightarrow T_1$ path exists. Finally, T_1/S_0 crossings which are characterized by open-ring structures, complete the deactivation pathways of the oligothiophenes.
- Preliminary calculations for the longer oligothiophenes 5T-10T show, with the exception of 6T, also an intersection of the S_1 state with a triplet state along the initial planarization coordinate. The special behavior of 6T is consistent with its highest fluorescence quantum yield in the row from 2T to 7T [95]. The exceptional property of 6T could also be one reason why it is one of the most frequently used molecule in organic devices [14, 103].

The quantum chemical calculations clearly reveal the importance of the initial photoinduced processes in thiophene and in small oligothiophenes. In thiophene a CoIn seam associated with a ring-opening is easily accessible while in the oligothiophenes the initial relaxation leads to the planarization of the systems and the formation of long-lived triplet states. In the oligothiophenes the low-lying triplet states, induced by the extension of the π-system, prevent the fast energy loss *via* internal conversion (IC) as present in the monomer. The absence of efficient IC of the absorbed energy is vital for the use of the thiophenes in optical devices as well as the avoidance of geometrical rearrangements such as ring-opening as in 1T. Even if, upon irradiation, only a small fraction of the molecules would undergo rearrangements like bond breaking, on a long timescale this would be quite detrimental for the thiophene-based devices.

The preliminary calculations demonstrate that triplet states could be significant for the photophysics of the longer oligothiophenes as well. For polythiophenes in solution and in films it was shown that the fluorescence quantum yield decreases due to more efficient nonradiative decay channels when the non-planarity of the thiophene backbone is increased by substitution [104]. The higher degree of non-planarity could, as shown for the oligothiophenes, enhance the SOC and prolong the interaction time for the ISC. Also in polythiophene-based solar cells triplet states are observed [105, 106] and they are discussed to be beneficial for advanced solar cells due to their relatively long lifetimes and transport distances [107–110]. Therefore further investigation of triplet states and their relaxation processes as well as the factors influencing the efficiency of these processes could be of potential interest for the improvement of the performance of thiophene-based devices.

In the following, the article "Deactivation pathways of thiophene and oligothiophenes: internal conversion *versus* intersystem crossing" published in *Physical Chemistry Chemical Physics* is reprinted with permission from *Phys. Chem. Chem. Phys* **18**, 7903-7915. (2016). The supporting information of this article is available under http://dx.doi.org/10.1039/C5CP07634J.

PCCP

PAPER

Cite this: *Phys. Chem. Chem. Phys.*, 2016, **18**, 7903

Deactivation pathways of thiophene and oligothiophenes: internal conversion *versus* intersystem crossing†

Patrick Kölle, Thomas Schnappinger and Regina de Vivie-Riedle*

Received 10th December 2015,
Accepted 2nd February 2016

DOI: 10.1039/c5cp07634j

www.rsc.org/pccp

Oligothiophenes and polythiophenes are building blocks of organic-based energy conversion materials. Therefore the lifetime of the excited states plays a central role. As a first step to understand the factors influencing the performance, we investigated the deactivation processes from the first excited state S_1 of thiophene and small oligothiophenes containing up to four rings using quantum chemical calculations. For thiophene a low-lying S_1/S_0 conical intersection seam is easily accessible and drives the fast internal conversion. In oligothiophenes barriers inhibit this passage while deactivation pathways *via* intersystem crossing channels open. The first one is responsible for the high triplet quantum yields and takes place shortly after the Franck–Condon region. The second one occurs in the vicinity of a local S_1 minimum. The calculated spin–orbit coupling strength together with the singlet–triplet energy gaps can explain the decreasing triplet and increasing fluorescence quantum yields for growing chain length. From the triplets the ground state is reachable by inter-ring torsions and T_1/S_0 intersections. The present results allow a deeper understanding of the deactivation pathways of thiophene and small oligothiophenes and are of potential interest for the photophysics of longer oligothiophenes and polythiophenes used in optical devices.

1 Introduction

In the last few decades polythiophenes and oligothiophenes have been shown to be some of the most promising candidates of organic materials for technological applications.[1,2] In particular, they have been used in solar cells,[3,4] light emitting diodes,[5,6] photoswitches[7] and as biological labels.[8–10] Gaining detailed knowledge of the radiative and nonradiative mechanisms and the factors tuning these processes in the isolated oligomers should be the first step in improving the performance of oligothiophene-based devices.

Static absorption measurements and time-resolved spectroscopic studies have been reported for thiophene (1T) and oligothiophenes containing up to seven thiophene rings.[11–40] In our nomenclature *n*T is an oligothiophene with *n* thiophene units. The monomer 1T was shown to be non-fluorescent and non-phosphorescent.[37] With the aid of static quantum chemical[41–43] and nonadiabatic molecular dynamics calculations[44–46] it was revealed that 1T decays ultrafast primarily *via* its singlet states and conical intersections to the ground state without the involvement of triplet states. In contrast the rates of internal conversion (IC) of the oligothiophenes are very small and the relaxation processes are dominated by triplet formation and fluorescence.[13,21,22,25] It was shown that the fluorescence quantum yields increase while the triplet quantum yields decrease when extending the chain length of the oligomer. These trends are mainly attributed to changes in the nonradiative decay processes, which are dominated by effective intersystem crossing (ISC) from the singlet to the triplet manifold. Photodetachment photoelectron spectroscopy (PD-PES) measurements[32,47] explained this dependence of the triplet quantum yield as a function of the oligomer size mainly by the growing energy differences between the singlet S_1 state and the triplet T_2 state. It is important to note that the triplet energies determined by PD-PES are based on radical anions. The anion equilibrium structure of the oligothiophenes is mostly planar and thus closer to the minimum structure of the S_1 states than to the non-planar minimum of the neutral ground states.[47] Therefore the triplet energies and the state order deduced from PD-PES are also not related to the Franck–Condon (FC) region but to the structure of the S_1 minimum. For bithiophene (2T) it was shown by quantum chemical calculations that the triplet T_4 and T_3 states are below the S_1 state in the non-planar S_0 minimum geometry but above the S_1 state in its planar equilibrium geometry.[48] Furthermore femtosecond time-resolved spectroscopy measurements suggested that for 2T and 3T ultrafast ISC takes place from a twisted S_1 state responsible for the highly

Department of Chemistry, Ludwig-Maximilians-Universität München, Butenandtstraße 5-13, 81377 München, Germany.
E-mail: Regina.de_Vivie-Riedle@cup.uni-muenchen.de

† Electronic supplementary information (ESI) available: Complete computational results and optimized geometries: Tables S1–S20 and Fig. S1–S23. See DOI: 10.1039/c5cp07634j

effective triplet generation.[28,33,34] In addition oligothiophenes are considered to be quite flexible molecules with respect to the rotation around the inter-ring bonds. Nevertheless the T_4 and T_3 states were regarded until now to play only a minor role in the efficient ISC pathways of the oligothiophenes.

In this work, we will demonstrate the crucial role of the T_3 state for the effective triplet formation and elucidate the details of the ISC processes and relaxation pathways of bithiophene (2T), terthiophene (3T) and quaterthiophene (4T). By quantum chemical calculations of the low-lying excited states and the spin–orbit coupling between the S_1 and the triplet states we will show that efficient and ultrafast ISC occurs along the geometry relaxation of the S_1 state leading to the high triplet quantum yields of the oligothiophenes. In addition we will reveal why the relaxation pathway of thiophene is dominated by its singlet states and conical intersections (CoIns) and why these CoIns are not active anymore in the oligothiophenes. The current results in conjunction with previous work offer quite a complete picture of the photophysical properties of the molecules and may be linked to the application of the oligothiophenes in optical devices.

2 Computational details

The ground state optimizations of 1T–4T have been carried out using the B3LYP functional[49–52] and the 6-311G** basis set.[53] In a theoretical study of 2T it was demonstrated that the optimized geometries at the B3LYP/6-311G** level of theory exhibit the best agreement with the experiments and that the torsional angle between the adjacent thiophene rings is very sensitive to both the basis set and the method used.[54]

The electronic states of 1T, 2T and 3T were computed with the complete active space second-order perturbation theory method (CASPT2),[55] the equation of motion coupled cluster singles and doubles method (CCSD)[56] and the time-dependent density functional theory method (TDDFT) using the CAM-B3LYP functional.[57] The electronic states of the larger system 4T were calculated using the CCSD and the TDDFT methods. For the CCSD calculations the 6-311+G** (1T–3T) and 6-31G* (4T) basis sets[58] were used. The TDDFT calculations were carried out using the 6-311+G** basis set, while for the more demanding CASPT2 method the 6-31G* basis set was used throughout.

The reference wave function and the molecular orbitals for the CASPT2 calculation were determined using the state-averaged complete active space self-consistent field method (SA-CASSCF). For 1T and 3T five singlet and four triplet states were included in the state-averaging procedure while for 2T six singlet and four triplet states were incorporated. The CASPT2 calculations were performed using a shift of 0.3 a.u. For 1T the active space was composed of eight electrons and seven orbitals (CAS(8/7)). In addition to the π-orbitals one pair of σ-orbitals (σ/σ*) was included in the active space. The geometry optimizations of the excited states of 1T have been carried out at the CASPT2 level of theory. The Hessian matrix for the optimization of the transition state of the S_1 state was calculated numerically.

The active space of 2T contained one σ*-orbital in addition to the π-space (12 electrons/10 orbitals) in all calculations to describe the πσ* singlet state (CAS(12/11)). For the calculation of the S_1/S_0 conical intersections, the T_1/S_0 intersection and the $S_1(\pi\sigma^*)$ minima either one (CAS(14/12)) or two pairs (CAS(16/14)) of σ-orbitals were included in the active space depending on whether one or two C–S bond cleavages should be described. For the calculation of the spin–orbit coupling matrix elements (SOMEs) along the relaxation path from the FC point to the local $S_1(\pi\pi^*)$ minimum the CAS(12/11) active space was used. The SOME computations along the ring-opening path leading to one broken C–S bond were performed with the CAS(14/12) active space. The optimizations of the excited states, conical intersections and the T_1/S_0 intersection of 2T have been carried out using the CASSCF method.

For the energy calculations of 3T the complete π-valence active space was used (CAS(18/15)). Like in a previous study of 3T[59] the CASSCF optimizations of the excited states were performed with a smaller active space, 12 electrons/12 orbitals, where the three deepest π-orbitals were kept inactive. For the optimization of the S_1/S_0 conical intersection and the T_1/S_0 intersection of 3T this active space was extended by one pair of σ-orbitals (σ/σ*). For the SOME calculations along the relaxation path from the FC point to the local $S_1(\pi\pi^*)$ minimum the smaller π-active space (CAS(12/12)) was extended by three σ*-orbitals (CAS(12/15)) to keep the active space stable. For 4T the optimizations of the excited states have been carried at the TDDFT/6-31G* level.

The spin–orbit coupling (SOC) strength between selected singlet (S_l) and triplet (T_k) states was computed as

$$\mathrm{SOC}_{lk} = \sqrt{\sum_u \left|\langle T_{l,u}|\hat{H}_{SO}|S_k\rangle\right|^2} \quad u = x,\ y,\ z$$

which can be considered as the length of the spin–orbit coupling vector SOC_{lk}.[60] Its component $\langle T_{l,u}|\hat{H}_{SO}|S_k\rangle$ corresponds to the calculated SOME. The SOMEs were calculated by an efficient method using the Breit–Pauli spin–orbit operator[61] implemented in the Molpro software package.[62,63]

The CASSCF method has been employed to compute the transition dipole moments. Energy differences corrected by the CASPT2 method were used in the oscillator strength formula. The program package MOLPRO[62,63] was used for the CASSCF and CASPT2 calculations, while the DFT, TDDFT and CCSD calculations were carried out using the Gaussian 09 software package.[64]

3 Results and discussion

3.1 Vertical excited states of thiophene (1T) and oligothiophenes (2T–4T)

The optimized structures for the ground state minima of 1T–4T are shown in Fig. 1. The 1T geometry is planar and has C_{2v} symmetry, while all others are non-planar. The *trans* conformation of 2T exhibits C_2 symmetry and is characterized by a torsional angle α of 150.4° between the rings. This conformation has been shown to be the global minimum of the internal rotational

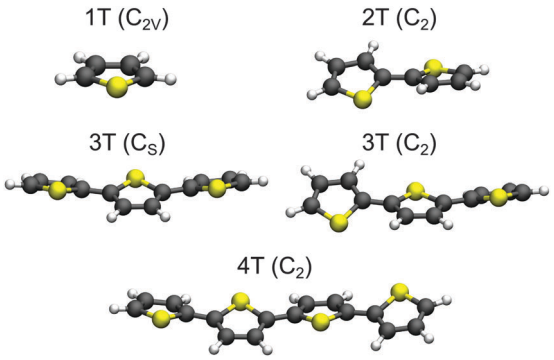

Fig. 1 Optimized B3LYP/6-311G** ground state geometries of 1T–4T. For 3T both nearly isoenergetic minima are shown. The point groups of the structures are given in parentheses.

potential surface.[54] For 3T two nearly isoenergetic minima exist among the total number of ten already reported in previous theoretical studies.[59,65–67] The global minimum is the twisted *trans–trans–syn* conformation with C_s symmetry (α = 153.8°) and the *trans–trans–anti* conformation with C_2 symmetry (α = 154.6°) is only 0.02 eV (ΔG) above. Also the transition state between both conformers lies only 0.05 eV (ΔG) above the global minimum (Fig. S13 and Table S10 in the ESI†). The flatness of the torsional potential is in agreement with the experimental observation that more than one twisted conformation is present in solution.[68] The all-*trans* conformation found as a minimum structure with C_2 symmetry for 4T is characterized by an α value of 157.1° between the central rings. Like a previous study[47] our calculations show that the degree of planarity increases from 2T (α = 150°) to 4T (α = 157°).

At these geometries the low-lying ππ* and the πσ* singlet states plus the first four triplet states of 1T–4T were computed. The excitation energies, the electronic characters and oscillator strengths are listed in Table 1 together with the corresponding experimental data. To facilitate the comparison of the electronic states of the different systems, the HOMO of all molecules is denoted π_1 and the LUMO π_1* orbital (for details, see ESI†). When possible the calculations were performed on the CASPT2, CCSD and TDDFT levels of theory for comparison and we found a good agreement for all molecules studied. A complete list with the results of all methods used is given in Tables S1–S5 in the ESI.† Our focus is on the bright S_1 state and its relaxation paths after optical excitation as this state is discussed to be crucial for the use of oligothiophenes in organic devices. The πσ* singlet state is responsible for a nonradiative relaxation *via* a ring opening path and the triplet states induce the ISC. The results in Table 1 are discussed from these aspects. In the FC region the S_1 state has ππ* character and is completely delocalized for all investigated systems. The excitation energy of the S_1 state decreases from 1T to 4T and its corresponding oscillator strength increases. The calculated vertical excitation energy of the S_1 state agrees very well for 1T and 2T with the experimental values while for 3T and 4T larger deviations are observed. The use of larger basis sets reduces these deviations (see Tables S12, S13 and S16, ESI†). But the combination with the large active spaces required for 3T and 4T (see Section 3.2.4) cannot be handled within a reasonable computation time. The state order of the πσ* singlet state increases systematically from the S_3 state in 1T to the S_7 state in 4T as more and more ππ* states intrude (see Tables S1–S5 in the ESI†). The πσ* state is due to the σ* character more localized and does not profit as much as the ππ* states from the elongation of the π-system.

In 1T the T_3 and T_4 states have πσ* character and lie substantially above the S_1 state. The energy gap to the T_2 state with ππ* character is also large (0.83 eV). In 2T more ππ* states exist due to the extension of the system. T_2 and T_3 are such additional ππ* states and lie below the S_1 state with a small S_1–T_3 energy gap of only 0.10 eV (see Table 1). The T_4 state has comparable character to the T_2 state of 1T and is nearly isoenergetic with the S_1 state in agreement with a previous study.[48] Also in the larger oligothiophenes the four lowest triplet states are characterized

Table 1 Calculated vertical singlet and triplet excitation energies (eV) for the low-lying valence excited states plus the πσ* singlet state of 1T–4T at their ground-state minima compared with experimental data. For 3T the excitation energies are shown for both isoenergetic conformers (C_s and C_2 symmetry). Oscillator strengths are given in parentheses. The HOMO of all molecules is denoted π_1 and the LUMO π_1* orbital (for details, see ESI)

1T (C_{2v})				2T (C_2)				3T (C_s)				3T (C_2)				4T (C_2)			
State	Char.	CASPT2	Exp.	State	Char.	CASPT2	Exp.	State	Char.	CASPT2	CCSD	State	CASPT2	CCSD	Exp.	State	Char.	CCSD	Exp.
$S_1(A_1)$	$\pi_2\pi_1$*	5.58 (0.06)	5.26[a]	$S_1(B)$	$\pi_1\pi_1$*	4.51 (0.45)	4.29[c]	$S_1(A'')$	$\pi_1\pi_1$*	4.03 (0.55)	4.15 (0.79)	$S_1(B)$	4.08 (0.52)	4.14 (0.77)	3.5[f]	$S_1(B)$	$\pi_1\pi_1$*	4.00 (1.30)	3.2[g]
$S_2(B_2)$	$\pi_1\pi_1$*	5.92 (0.11)	5.64[a]	$S_2(B)$	$\pi_4\pi_1$*	4.85 (0.14)	5.08[c]	$S_2(A'')$[e]	$\pi_2\pi_1$*	4.42 (0.06)	4.97 (0.00)	$S_2(B)$	4.39 (0.08)	4.98 (0.00)	—	$S_2(A)$	$\pi_1\pi_2$*	4.89 (0.00)	
$S_3(B_1)$	$\pi_1\sigma_1$*	6.37 (0.00)	—	$S_5(A)$	$\pi_1\sigma_1$*	5.40 (0.00)	—	$S_6(A')$	$\pi_1\sigma_1$*	—	5.46 (0.00)	$S_6(B)$	—	5.49 (0.00)	—	$S_7(B)$	$\pi_1\sigma_1$*	5.62 (0.00)	
$T_1(B_2)$	$\pi_1\pi_1$*	3.76	3.74[b]	$T_1(B)$	$\pi_1\pi_1$*	2.86	2.32[d]	$T_1(A'')$	$\pi_1\pi_1$*	2.40	2.56	$T_1(B)$	2.42	2.56	1.90[d]	$T_1(B)$	$\pi_1\pi_1$*	2.36	1.75[d]
$T_2(A_1)$	$\pi_2\pi_1$*	4.75	4.50[b]	$T_2(A)$	$\pi_1\pi_2$*	3.82	—	$T_2(A')$	$\pi_1\pi_2$*	3.19	3.38	$T_2(A)$	3.17	3.36	2.99[d]	$T_2(A)$	$\pi_1\pi_2$*	3.00	2.56[d]
$T_3(B_1)$	$\pi_1\sigma_1$*	6.11	—	$T_3(A)$	$\pi_3\pi_1$*	4.41	—	$T_3(A'')$	$\pi_1\pi_3$*	3.85	4.07	$T_3(B)$	3.87	4.08	—	$T_3(B)$	$\pi_1\pi_3$*	3.64	
$T_4(A_2)$	$\pi_2\sigma_1$*	6.13	—	$T_4(B)$	$\pi_4\pi_1$*	4.48	—	$T_4(A')$	$\pi_3\pi_1$*	4.30	4.41	$T_4(A)$	4.29	4.39	—	$T_4(A)$	$\pi_2\pi_1$*	4.16	

[a] Magnetic circular dichroism.[11] [b] Electron energy loss spectroscopy.[36] [c] Gas-phase absorption spectrum at room temperature.[19] [d] Photodetachment photoelectron spectrum in the gas phase.[47] [e] At the CASPT2 level of theory the S_2 state of both the 3T conformers is described by an $\pi_2\pi_1$* excitation, while with the CCSD method the S_2 state has $\pi_1\pi_2$* character and A' and A symmetry, respectively, (see Tables S3 and S4 in the ESI). [f] Absorption spectrum in solution at room temperature.[22,25,30] [g] Absorption spectrum in solution at room temperature.[13,22,25]

by ππ* excitations, whereby the T_4 state becomes more localized for 3T and 4T and therewith shifts slightly above the S_1 state. In 3T the S_1 state is energetically close to the T_3 state. At the CASPT2 level of theory only the inclusion of all π-orbitals in the active space results in the correct electronic state order consistent with the CCSD results. The use of a smaller active space leads to artificial stabilization of the S_1 state with respect to the triplet states shifting it below the T_3 state[59] (see Table S11 in the ESI†). Also in 4T the S_1 state is only slightly above the T_3 state at the CCSD level of theory.

Of the studied molecules only 1T exhibits large singlet–triplet energy gaps at the FC point. In combination with the low-lying πσ* singlet state S_3 this gives a first hint why photoexcited 1T decays primarily *via* singlet states and no intersystem crossing occurs.[37,41–43] In contrast thereto, the oligothiophenes 2T–4T show small singlet–triplet energy gaps, which however increase with the chain length (0.03 eV for 2T, 0.18 eV (C_s) and 0.21 eV (C_2) for 3T and 0.36 eV for 4T). This is consistent with the experimental observation of extremely high triplet quantum yields for the oligothiophenes, which however decrease again with size (0.99 for 2T, 0.95 for 3T and 0.73 for 4T).[25] The details of the relaxation pathways of the different systems will be discussed in the next sections.

3.2 Deactivation pathways

For 1T–3T all results are at the CASPT2 level of theory and when possible confirmed by CCSD calculations. For the larger 4T system the CCSD and TDDFT methods were used.

3.2.1 Thiophene (1T). For thiophene it was demonstrated by theory[41–44] and experiment[37] that after excitation to the $S_1(\pi\pi^*)$ state, it quickly relaxes to the local S_1 minimum (S_1-Min-a, Fig. 2). This process is described by a time constant of 80 fs.[37] Thereafter the main part of the population overcomes a barrier to reach the global minimum of the S_1 state (S_1-Min-b). This relaxation is characterized by a ring-opening *via* the dissociative πσ* character and a time constant of 25 fs leading to C–S bond cleavage. In the vicinity of S_1-Min-b, a conical intersection (CoIn) with the ground state, associated with a small barrier of 0.06 eV,[43] completes the ultrafast internal conversion.

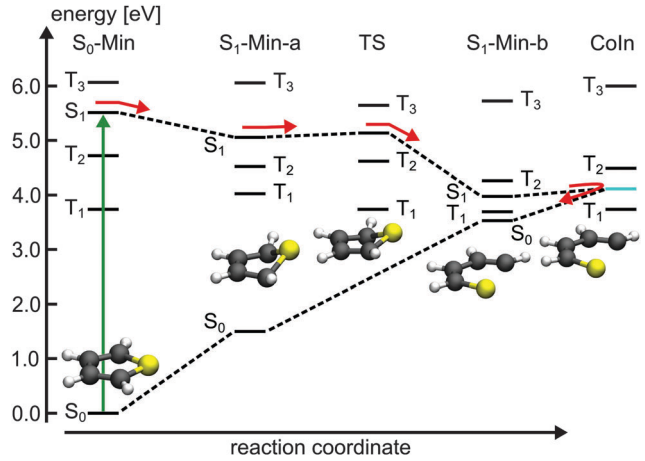

Fig. 2 Schematic illustration of the proposed deactivation mechanism of 1T after excitation to the S_1 state. The deactivation pathway is represented by red arrows. The S_1/S_0 CoIn is indicated by cyan line. The relevant optimized geometries are shown as well.

So far the barrier height for the ring-opening from S_1-Min-a to S_1-Min-b was estimated by linear interpolation at the CCSD level of theory to be 0.26 eV and understood as a consequence of an avoided crossing.[43] We were able to locate the transition state (TS) separating the two S_1 minima at the CASPT2 level of theory (Fig. 2, for details, see Fig. S2 and Table S6 in the ESI†). Therewith the barrier height is reduced to 0.07 eV. We also found that the CoIn is part of a low lying and thus very efficient seam along the d_{SCCC} dihedral angle (see Fig. S3 and S4 in the ESI†).

Salzmann *et al.*[41] argued that due to vanishing spin–orbit coupling (SOC) and large S_1–triplet energy gaps at the FC point and at S_1-Min-a (see Fig. 2) a notable probability for ISC may only exist along the ring-opening path. However the ISC has to compete with the highly effective irreversible ring-opening path through the CoIn seam. Thus our additional results further support the interpretation that thiophene after excitation to the S_1 state decays mainly *via* its singlet electronic states, which is consistent with the observed dynamics and the absence of fluorescence and phosphorescence.[37]

3.2.2 Bithiophene (2T)

Triplet states and intersystem crossing. In 2T the triplet states T_4 and T_3 are below and close to the S_1 state at the FC point. Optimization of the S_1 state leads to the conversion of the non-planar structure to a planar minimum with C_{2h} symmetry (S_1-Min-a) and lowers its energy below the T_4 and T_3 states (see Table 2). We constructed a simplified reaction path RC_S by linear interpolation between the optimized S_0-Min and S_1-Min-a geometries. The calculated energies along the RC_S reveal the intersection of the S_1 state with the T_4 and T_3 states (Fig. 3a).

For an effective ISC between singlet and triplet states, the spin–orbit coupling (SOC) should be reasonably strong and the states involved should be close in energy. First semiempirical calculations using the INDO/SCI approach showed for 2T, 3T and 6T that the SOC values decay with decreasing torsion angle α.[69]

Table 2 Calculated CASPT2 vertical singlet and triplet excitation energies (eV) for the low-lying valence excited states of 2T at the ground-state (S_0-Min) and S_1 state (S_1-Min-a) minima. In addition the lowest excited singlet state with πσ* character is given (S_5). Oscillator strengths are shown in parentheses

		S_0-Min (C_2)		S_1-Min-a (C_{2h})		
State	Character	Sym.	CASPT2	Sym.	CASPT2	Exp.
S_1	$\pi_1 \rightarrow \pi_1^*$	*B*	4.51 (0.45)	B_u	3.71 (0.43)	3.43[a]
S_2	$\pi_4 \rightarrow \pi_1^*$	*B*	4.85 (0.14)	A_g	4.22 (0.00)	—
S_5	$\pi_1 \rightarrow \sigma_1^*$	*A*	5.40 (0.00)	A_u	4.74 (0.00)	—
T_1	$\pi_1 \rightarrow \pi_1^*$	*B*	2.86	B_u	1.99	2.32[b]
T_2	$\pi_1 \rightarrow \pi_2^*$	*A*	3.82	A_g	3.57	—
T_3	$\pi_3 \rightarrow \pi_1^*$	*A*	4.41	A_g	4.11	—
T_4	$\pi_4 \rightarrow \pi_1^*$	*B*	4.48	B_u	4.26	—

[a] Maximum of the fluorescence spectrum in dioxane at room temperature.[25] [b] Photodetachment photoelectron spectrum in the gas phase.[47]

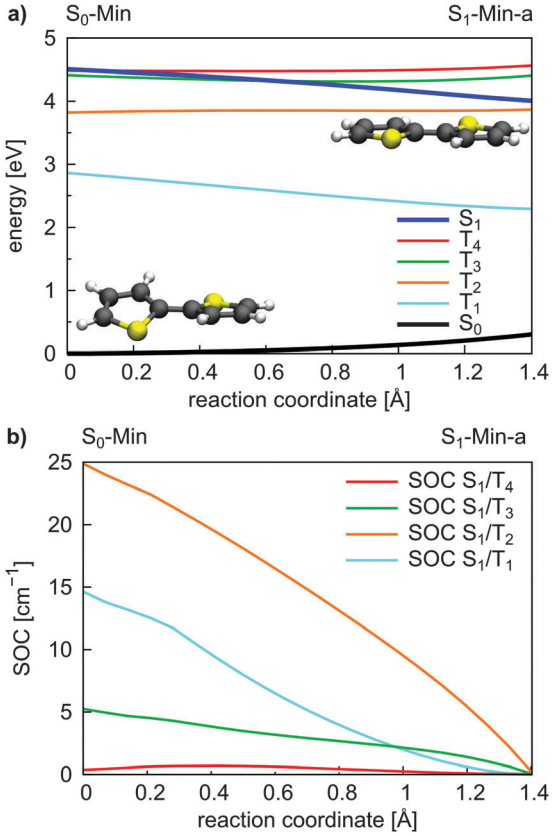

Fig. 3 Energy profile of the S_0, the S_1 and the four lowest lying triplet states (a) and the SOC between the S_1 and triplet states (b) along the S_1 relaxation coordinate of 2T. The energy calculations were performed at the CASPT2/6-31G* level of theory and confirmed at the CCSD level (Fig. S9 in the ESI†). The SOCs were calculated using the CASSCF method. The reaction coordinate was generated by linear interpolation between the optimized S_0-Min and S_1-Min-a geometries.

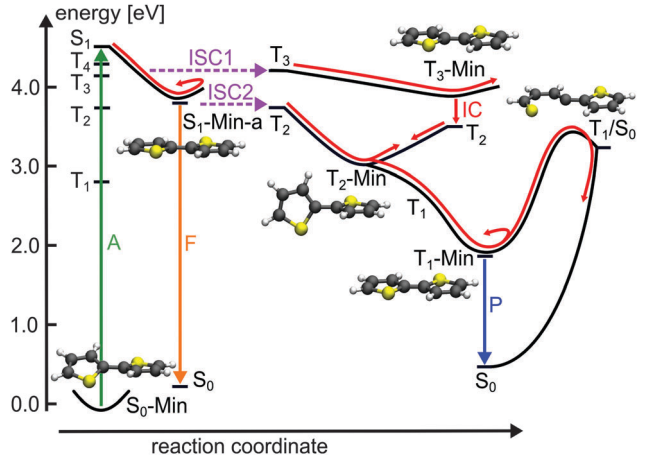

Fig. 4 Schematic illustration of the proposed deactivation mechanism of 2T after excitation to the S_1 state (A: absorption; F: fluorescence; ISC: intersystem crossing; IC: internal conversion; P: phosphorescence). The deactivation pathway is represented by red arrows. The relevant optimized geometries are shown as well.

Since we are interested in the relaxation pathways from the S_1 state, we calculated the SOC between the S_1 and the four lowest lying triplet states along the reaction coordinate RC_S at the CASSCF level (Fig. 3b).

All SOC values also decrease along this coordinate and vanish at S_1-Min-a. Between S_1 and T_2/T_3 the SOC is zero for symmetry reasons, between S_1 and T_1/T_4 it vanishes, although the coupling is symmetry allowed. In general, for strong SOC, contributions from orbitals of heavy atoms have to be involved in the electronic configuration of the mixing states. The σ* orbital is localized on the S-atom and occurs *via* small πσ* contributions in the S_1 state of 2T. This πσ* contribution systematically decays along the RC_S as the planarization reduces the σ/π mixing. Correspondingly, all SOCs, also the symmetry allowed ones, decrease and vanish along this coordinate.

In view of the calculated SOC and the S_1–triplet energy gaps, the highest ISC probability along the relaxation coordinate RC_S exists with the T_3 state. The intermediate degeneracy of the S_1 and the T_3 states should compensate for their moderate spin–orbit interaction and allow a fast ISC. An example for such a scenario has been shown recently for uracil by Richter *et al.*[70] and has been discussed for benzene by Worth and co-workers.[71,72]

For the population that reaches S_1-Min-a a second ISC path opens between the S_1 and the T_2 states (ISC2, see Fig. 4). Here both states are close in energy and although the SOC vanishes at the minimum geometry, the torsional out-of-plane motion can induce moderate coupling. Such motions have been shown to be highly active during the S_1 dynamics of 2T–4T.[45,46]

The possibility of two ISC channels is consistent with the experimental observations of Paa *et al.*[34] using femtosecond time-resolved spectroscopy. They obtained a biexponential decay for the transient $S_1 \rightarrow S_n$ absorption (ESA) bands, with a fast (τ = 1.4 ps) and slow (τ = 29.6 ps) component. In addition the rise of the triplet–triplet absorption (TTA) is characterized by a fast time constant of 1.4 ps and a slower one of 58 ps. Therefore the authors proposed an ISC mechanism with two channels: the fast one starting from a twisted S_1 state geometry and taking place during the initial geometry relaxation. The second slower ISC channel starts from the relaxed S_1 state and competes with fluorescence from S_1-Min-a. Although the oscillator strength is reasonable at S_1-Min-a (see Table 2), the fluorescence quantum yield is reported to be small (ϕ_F = 0.014).[25] Thus we suggest that the major part of the S_1 population decays *via* the two ISC paths. The quantum yield ϕ_F of 2T is increased when the temperature is lowered from 298 to 77 K.[25] Under these conditions the first ISC path is less populated as the lower temperature enhances the planarity of the ground state.[25]

Next we discuss the relaxation from T_3 and T_2 back to the ground state. The T_3 relaxation leads to the planar T_3 state minimum where the T_3 and T_2 states are close in energy (ΔE = 0.28 eV, see Table S8 in the ESI†). Therewith the T_2 state can also be populated by a fast internal conversion from T_3 (Fig. 4). T_2 is the only state considered which is described by an excitation to the π_2^* orbital (see Table 2). This orbital is characterized by an antibonding π-interaction between the thiophene rings (see Fig. S5 in the ESI†), therefore the T_2 minimum is a twisted structure with orthogonal thiophene rings (T_2-Min, Fig. 4).

At this minimum the T_2 state is degenerate with the T_1 state[47] (see Table S8 in the ESI†) suggesting the existence of a T_2/T_1 CoIn from where relaxation into the global excited state minimum T_1-Min (Fig. 4) can take place. The calculated vertical emission energy at this planar minimum is 1.77 eV and corresponds to the maximum of the phosphorescence spectrum (2.06 eV).[32] Since the phosphorescence is weak ($\phi_P = 10^{-5}$),[32] we conclude that by far most of the population return back to the ground state by a nonradiative process.[25] This process will be discussed in combination with a possible decay *via* CoIns in the next section.

Conical intersections. A remaining question is why for 2T the deactivation path is dominated by ISC not by the ring-opening path *via* the S_1/S_0 CoIns which is the major path for 1T. We therefore optimized the S_1/S_0 CoIns and the S_1-Min-b minima for 2T. For 1T only one open-chain structure with a broken C–S bond is distinguishable. For the *trans* conformation of 2T several open-chain structures are possible. First of all four singly and six doubly opened geometries can be discriminated. The singly opened structures can be planar or non-planar and the inner or the outer C–S bond can be broken. The four optimized CoIns are shown in Fig. 5 (CoIn1–4) and are as in 1T in the vicinity of the S_1-Min-b minima. In all these structures the S_1 state has $\pi\sigma^*$ character while the S_0 state is the closed shell electronic configuration. The geometries of the CoIns1–4 and the S_1-Min-b minima are quite similar to the corresponding ones of 1T, *e.g.* the distances of the broken C–S bonds are nearly identical (1T CoIn: 3.41 Å). Also the barrier from the S_1-Min-b minima to the CoIns is at most 0.1 eV (Table 3) and mainly associated with a small elongation of the C–S bond (see Fig. S10 in the ESI†). CoIn1 and CoIn3 lie below and CoIn2 and CoIn4 above S_1-Min-a (see Table 3). The cleavage of an outer C–S bond leads to steric repulsion between the sulfur atom and the adjacent thiophene ring (see Fig. 5) resulting in the destabilization of CoIn2 and CoIn4. The cleavage of the inner C–S bonds leads to a lower steric repulsion and explains the stabilization of CoIn1 (0.2 eV) and CoIn3 (0.4 eV), whereby CoIn3 is the lowest intersection due to the orthogonal position of the thiophene rings.

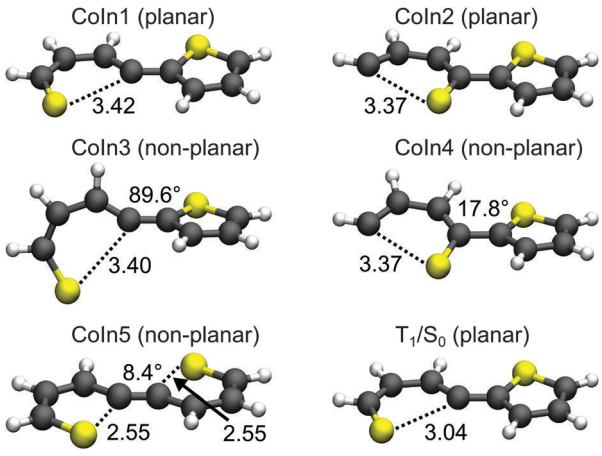

Fig. 5 Optimized geometries of the conical intersections (CoIns) and the T_1/S_0 intersection of 2T obtained at the CASSCF/6-31G* level of theory. The distance of the broken C–S bonds are given in Angstrom (Å). For the non-planar geometries the torsional angle between the thiophene rings is also shown (defined by the S–C–C–S dihedral angle).

Table 3 Adiabatic CASPT2 excitation energies (eV) to the S_1-Min-b minima and the optimized CoIns. The stabilization energies of the CoIns relative to the S_1-Min-a are given. Negative values indicate destabilization. The barriers between S_1-Min-a and S_1-Min-b were obtained by linear interpolation between the optimized geometries and calculated at the CCSD/6-31G* level of theory

	CoIn1	CoIn2	CoIn3	CoIn4	CoIn5
S_1-Min-b	3.75	4.13	3.58	4.12	—
Conical intersection	3.85	4.22	3.60	4.20	4.09
Stabilization energy	0.16	−0.21	0.41	−0.19	−0.08
Barrier	0.40	0.87	1.04	0.92	—

Based on these results we identified the most promising one of the six doubly opened geometries. The optimized non-planar structure CoIn5 (Fig. 5) shows that when two C–S bonds are broken the S_1/S_0 degeneracy is achieved already for smaller elongations of the C–S distance to 2.55 Å. Nevertheless CoIn5 lies above S_1-Min-a (Table 3) and is further neglected.

From the energetics at least CoIn1 and CoIn3 could be reached from S_1-Min-a. But the possible barriers in between have to be considered. This was investigated again by using simplified reaction paths RC_{S2} constructed by linear interpolation between S_1-Min-a, S_1-Min-b and the respective CoIn. Based on the good agreement between CASPT2 and CCSD results obtained for the energy profile along the RC_S (see Fig. 3a and Fig. S9 in the ESI†), we calculated the four continuing ring-opening paths RC_{S2} using the faster CCSD method. The single-reference method CCSD has previously been used to study the deactivation paths of thiophene[43] and furan[73] and was found to give energies of good quality even in the vicinity of CoIns. This is also found for the paths towards CoIn1/CoIn3 (Fig. 6) and CoIn2/CoIn4 (Fig. S11 in ESI†). The positions of the CoIns at the CCSD level are only slightly shifted with respect to the CASSCF results and thus the CCSD results are sufficiently accurate to estimate the barriers. The reported values for the barriers in Table 3 are an upper limit for the real ones. Optimization of the corresponding transition states would lower these barriers as shown for 1T (see Section 3.2.1). Nevertheless from the barrier heights one can see that CoIn1 is associated with the smallest barrier of 0.4 eV and the lowest CoIn (CoIn3) with a barrier of 1.0 eV. This can be understood as the geometrical distortion necessary to reach the non-planar CoIn3 from the planar S_1-Min-a is significantly larger than from the planar CoIn1. This is also reflected in the larger RC_{S2} values for CoIn3 (Fig. 6b).

In summary, CoIn1 is the most favorable intersection of 2T and should be reachable due to an accumulated relaxation energy of 0.5 eV from the FC point to S_1-Min-a. Thus some of the excited molecules should decay to the ground state through this passage. This is, however, in contrast to the measured near-unity triplet quantum yield of 2T. A possible explanation is that also along the ring-opening path to CoIn1 the S_1 state can couple to the triplet states. We calculated the four lowest lying triplet states along this path and, indeed found several intersections

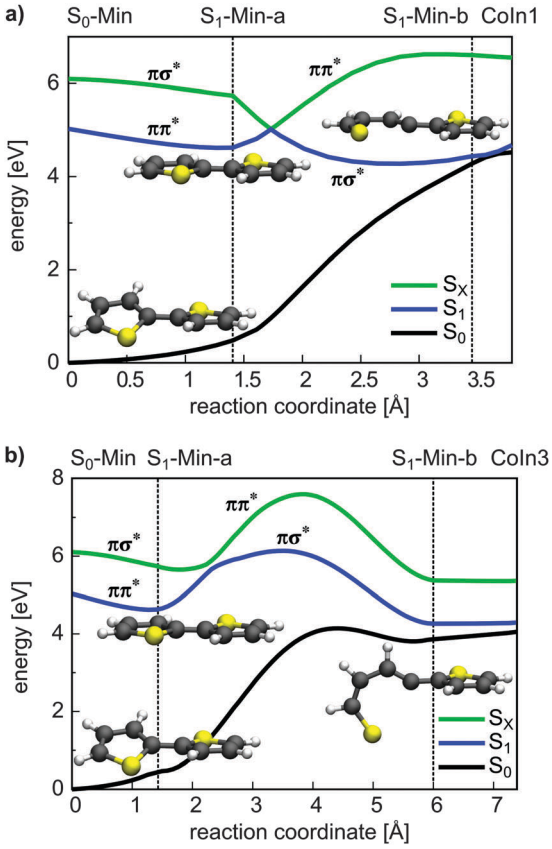

Fig. 6 Energetic course of the ground, ππ* and πσ* singlet states along the reaction path leading to CoIn1 (a) and CoIn3 (b). The energy calculations were performed at the CCSD/6-31G* level of theory. The reaction coordinates were generated by linear interpolation between the CASSCF optimized geometries. The positions of the minima and CoIns are indicated by vertical lines. The electronic character and the minimum structures are shown as well along each path.

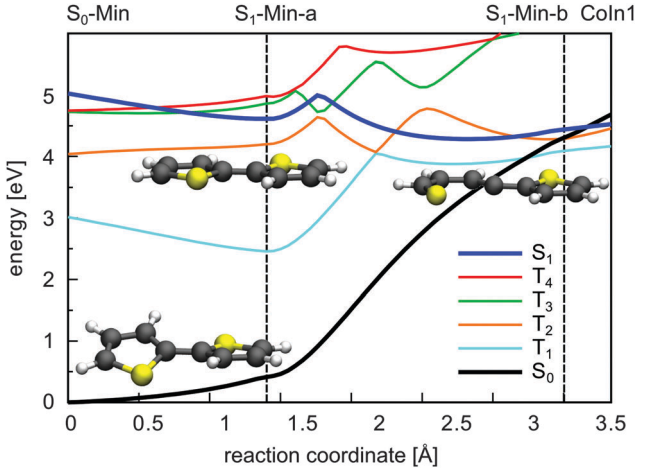

Fig. 7 Adiabatic course of the S_0, the S_1 and the four lowest lying triplet states along the reaction path leading to CoIn1. The energy calculations were performed at the CCSD/6-31G* level of theory. The reaction coordinate was generated by linear interpolation between the CASSCF optimized geometries. The positions of the minima and CoIns are indicated by vertical lines. The minimum structures are shown as well along the path.

between the S_1 and the triplet states (Fig. 7). In addition near and after the barrier strong SOC of the S_1 state with the triplet states occur ($\approx$20–100 cm^{-1}, Table S9 in the ESI†) due to the rising πσ* character of the S_1 state.

The results clearly elucidate why the deactivation path of 2T is dominated by ISC and the relaxation path of 1T by S_1/S_0 CoIns. First of all after excitation to the S_1 state only for 2T effective ISC possibilities exist during the initial motion (compare Fig. 2 and 3). Secondly the barrier to reach a CoIn is higher for 2T (0.40 eV) than for 1T (0.26 eV). And finally even if the barrier to the S_1/S_0 CoIn is overcome, the ISC to several triplet states is probable in 2T and depopulates the S_1 state.

The calculations along the ring-opening path RC_{S2} (Fig. 7) also reveal the existence of a low lying intersection between the T_1 and the S_0 state. The optimized T_1/S_0 intersection is a planar structure with a broken C–S bond of 3.04 Å (Fig. 5) where the T_1 state has πσ* character and accordingly large SOC values with the S_0 state ($\approx$100 cm^{-1}). This intersection found along the ring-opening path could also be responsible for the overall relaxation from the triplets back to the ground state. We therefore estimated the barrier from the endpoint of the triplet cascade, T_1-Min, to the T_1/S_0 intersection by linear interpolation at the CASPT2 level of theory (Fig. S12 in the ESI†). The calculated barrier height of 1.39 eV should account for the long triplet lifetime of 100 μs of 2T.[25] The reaction coordinate of this path is mainly characterized by an elongation of the C–S distance. As the gradient difference vector at the T_1/S_0 intersection is nearly orthogonal to this reaction coordinate (Fig. S10, ESI†), the probability for intersystem crossing is quite high after the system has crossed the barrier (for details, see ESI†). All in all the T_1/S_0 intersection completes the deactivation pathway of 2T.

3.2.3 Terthiophene (3T). In 3T for both nearly isoenergetic ground state minima (Section 3.1) the T_4 state is now above and the T_3 state is slightly below the bright S_1 state (see Table 4). Relaxation of the S_1 state again leads to a planar minimum (S_1-Min-a) with C_{2v} symmetry. The energy profiles are calculated at the CCSD/6-31G* level along the linear interpolated reaction coordinate RC_S between the isoenergetic ground state minima and S_1-Min-a. As in 2T the S_1 state intersects with the T_3 state (Fig. 8a and Fig. S19a, ESI†) and the SOC between the S_1 and the triplet states decrease along the RC_S and vanishes at the planar S_1-Min-a (Fig. 8b and Fig. S19b, ESI†). Analogous to 2T this can be understood by symmetry selection rules and varying πσ* contribution in the S_1 state. In the planar C_{2v} geometry the spin–orbit coupling between the $S_1(B_1)$ and the $T_1/T_3(B_1)$ is again symmetry forbidden. Overall the πσ* contribution in the S_1 state is smaller for 3T than for 2T resulting in generally lower SOC values. The intermediate degeneracy of the S_1 state and the T_3 state should again compensate their moderate spin–orbit interaction making T_3 the most probable candidate for an efficient ISC along the initial relaxation (ISC1, see Fig. 9). Like in 2T the T_2 and the S_1 state come closer during geometry relaxation to S_1-Min-a.[59] At the CCSD/6-31G* level the S_1–T_2 energy gap is still 0.64 eV (see Table S12 in the ESI†). But the gap reduces to 0.46 eV using the larger basis set 6-311+G** and approaches

Table 4 Calculated CASPT2 vertical singlet and triplet excitation energies (eV) for the low-lying valence excited states of 3T at the ground-state (S_0-Min) and the S_1 state (S_1-Min-a) minima. Oscillator strengths are shown in parentheses

		S_0-Min (C_s)		S_1-Min-a (C_{2v})		
State	Character	Sym.	CASPT2	Sym.	CASPT2	Exp.
S_1	$\pi_1 \rightarrow \pi_1^*$	A''	4.03 (0.55)	B_1	3.08 (0.68)	2.91[a]
S_2	$\pi_2 \rightarrow \pi_1^*$	A''	4.42 (0.06)	A_1[b]	3.56 (0.00)	—
T_1	$\pi_1 \rightarrow \pi_1^*$	A''	2.40	B_1	1.75	1.90[c]
T_2	$\pi_1 \rightarrow \pi_2^*$	A'	3.19	A_1	2.87	2.99[c]
T_3	$\pi_1 \rightarrow \pi_3^*$	A''	3.85	B_1	3.81	—
T_4	$\pi_3 \rightarrow \pi_1^*$	A'	4.30	A_1	4.19	—

[a] Maximum of the fluorescence spectrum in dioxane at room temperature.[25] [b] At S_1-Min-a the S_2 state is described by an double excitation ($\pi_1 \rightrightarrows \pi_1^*$). [c] Photodetachment photoelectron spectrum in the gas phase.[47]

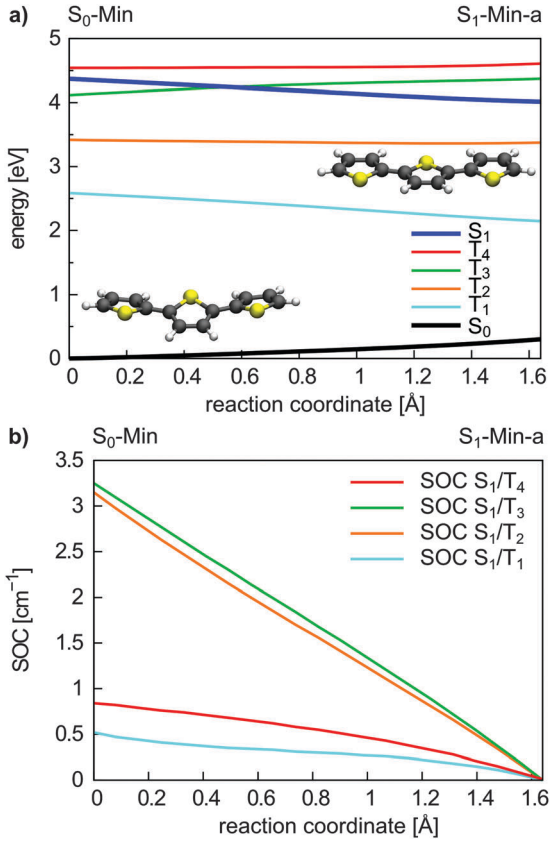

Fig. 8 Energy profile of the S_0, the S_1 and the four lowest lying triplet states (a) and SOC between the S_1 and triplet states (b) along the S_1 relaxation coordinate of 3T. The energy calculations were performed at the CCSD/6-31G* level of theory and the SOCs were calculated with the CASSCF method. The reaction coordinate was generated by linear interpolation between the optimized S_0-Min (C_s symmetry) and S_1-Min-a (C_{2v} symmetry) geometries.

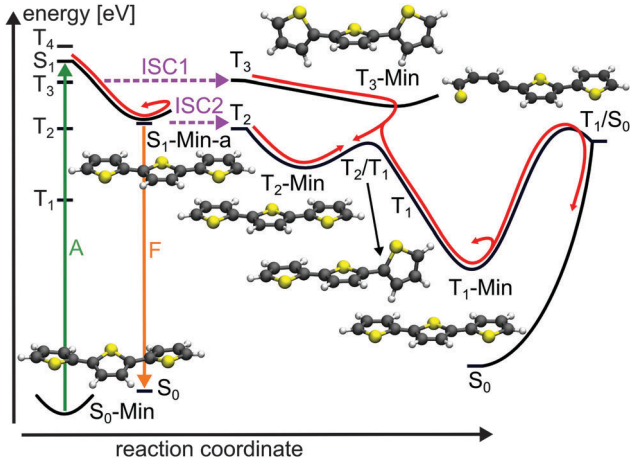

Fig. 9 Schematic illustration of the proposed deactivation mechanism of 3T after optical excitation to the S_1 state (A: absorption; F: fluorescence; ISC: intersystem crossing). The deactivation pathway is represented by red arrows. The relevant optimized geometries are shown as well.

the value of 0.21 eV obtained at the CASPT2/6-31G* level (Table 4). Analogous to 2T for the second ISC process (ISC2, see Fig. 9) out of the S_1-Min-a some torsional vibrational activity is needed.

Also for 3T both ISC channels are confirmed by experimental results. Beyond that the experimental observations can now be understood more deeply. Rentsch and co-workers carried out femtosecond time-resolved spectroscopy with dependence on the excitation wavelength.[28,33,34] They observed a biexponential decay for the S_1 state with a fast and slow component occurring in parallel with the triplet formation. Both processes and the triplet quantum yield were found to depend on the excitation energy. At a wavelength of 400 nm (low-energy side of the $S_0 \rightarrow S_1$ absorption band) the S_1 decay and the rise of the TTA are determined by the fluorescence lifetime of the S_1 state (165 ps).[34] With increasing excitation energies an additional fast channel for triplet formation with a time constant of about 2 ps occurs. The triplet quantum yield reaches a maximum value at 381 nm and remains constant up to 370 nm. Rentsch and co-workers suggested that the fast ISC channel is populated by excitation of non-planar molecules and opens while the planar S_1-Min-a is approached. With the low energy pulse mainly planar molecules are excited among the ensemble as the planar conformation has the lowest excitation energy.[74] The fast ISC channel is considered to be responsible for the highly effective triplet formation and has been quantified by temperature dependent measurements of the fluorescence quantum yield by Rossi *et al.*[75] They estimated that more than half of the T_1 population of 3T arises from this channel. The details of the two ISC channels are clearly elucidated by the results of the present work. Only if non-planar conformations are excited the fast ISC from the S_1 state to the T_3 state can happen. If planar conformations are excited thermal torsional vibrational activity can induce the second ISC from the S_1 to the T_2 state.

Like in 2T a remaining question is the possible role of S_1/S_0 CoIns as deactivation path. Based on the results of 2T we focused on the most promising one and optimized a planar S_1/S_0 conical intersection with a singly broken C–S bond. We also located the corresponding S_1 minimum (S_1-Min-b), which was found again in the vicinity of the CoIn. The barrier between S_1-Min-a and S_1-Min-b was estimated by linear interpolation at the CCSD/6-31G* level of theory (see Fig. S20 in the ESI†). The optimized CoIn geometry (Fig. 10) is similar to the ones of the

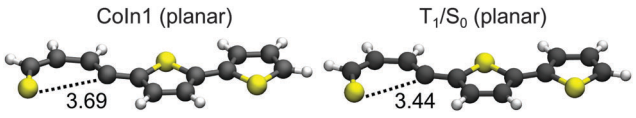

Fig. 10 Optimized geometries of the conical intersection (CoIn) and the T_1/S_0 intersection of 3T obtained at the CASSCF/6-31G* level of theory. The distance of the broken C–S bonds are given in Angstrom (Å).

smaller systems, only the C–S distance (3.69 Å) is slightly larger than in 2T (3.42 Å) and 1T (3.41 Å).

In Table 5 the relevant points of the pathway to the CoIns are compared for 1T–3T. The adiabatic energy difference in the CoIns stays in the same range while the S_1 ($\pi\pi^*$) state is significantly stabilized at the FC point and at S_1-Min-a due to the increased π system. At the CoIns the S_1 state has $\pi\sigma^*$ character and is thus more localized and does not profit to the same extent from the elongation of the π-system. The significant lowering of the $\pi\pi^*$ relative to the $\pi\sigma^*$ character in the S_1 state is also reflected by the increased barrier between S_1-Min-a and S_1-Min-b from 1T to 3T inhibiting the passage to the S_1/S_0 CoIn for the oligothiophenes. The higher barrier for 3T relative to 2T is confirmed by the even smaller rate constant for internal conversion.[25] The low barrier for 1T can be further understood comparing the structures of the S_1-Min-a minima. Only in 1T it is non-planar (Fig. 2) and the C–S bond is already slightly elongated in comparison to S_0-Min. Thus in 1T the initial relaxation is directed towards the ring-opening while the initial relaxation of 2T and 3T is characterized by inter-ring rotation leading to planar geometries.

From the planar S_1-Min-a the ring-opening path is thus highly unlikely for 3T. Even if the high barrier is overcome, several intersections of the S_1 state with the triplet states (see Fig. S20 in the ESI†) with strong SOC ($\approx$20–100 cm^{-1}, Table S15 in the ESI†) exist and would again induce ISC. Another deactivation possibility out of S_1-Min-a is fluorescence. The S_1 state has a reasonable oscillator strength and the calculated vertical energy compares well with the maximum of the fluorescence spectrum (see Table 4). The higher fluorescence quantum yield of 3T (ϕ_F = 0.054) in comparison to 2T (ϕ_F = 0.024)[25] can be explained by the lower SOC values along the initial relaxation towards S_1-Min-a and the higher barrier for the ring-opening path. Still the major part of the S_1 population decays *via* ISC.

The depopulation pathways of the triplet states proceeds again *via* a cascade. Relaxation of the T_3 state leads to its minimum.

Table 5 Adiabatic excitation energies (eV) of the S_1 state at the FC point, S_1 minima (S_1-Min-a and S_1-Min-b) and at the CoIn of 1T, 2T (CoIn1) and 3T at the CASPT2/6-31G* level of theory. The barriers between S_1-Min-a and S_1-Min-b were obtained by linear interpolation between the optimized geometries and calculated using the CCSD method. The value for the barrier of 1T is taken from ref. 17

	1T	2T	3T
FC point	5.58	4.51	4.03
S_1-Min-a	5.07	4.01	3.27
S_1-Min-b	4.00	3.75	4.16
Conical intersection	4.08	3.85	4.32
Barrier	0.26	0.40	0.81

Like the T_2 state of 2T the T_3 state of 3T is described by an excitation to an antibonding π-orbital (π_3^*, Table 4) with nodal planes between the thiophene rings (see Fig. S14 in the ESI†). Accordingly, the T_3 minimum is a twisted structure with orthogonal thiophene rings (T_3-Min, Fig. 9). At this minimum the first three triplet states are close in energy (see Table S14 in the ESI†) and a fast internal conversion from T_3 to T_2 or T_1 can happen. The T_2 minimum is planar (T_2-Min, Fig. 9) and in contrast to the non-planar T_2-Min of 2T now an energy gap of 0.76 exists between T_2 and T_1 and a barrier of 0.32 eV has to be overcome to reach the T_2/T_1 conical intersection. The T_2/T_1 conical intersection is characterized by one terminal thiophene ring being orthogonal to two planar thiophene rings (Fig. 9). In T_1 the global excited state minimum is reached, which is again planar (Fig. 9). As no phosphorescence was detected,[25] a possible relaxation back to the ground state is again *via* the T_1/S_0 intersection with one broken C–S bond (Fig. 10). We estimated again the barrier between T_1-Min and T_1/S_0 by interpolation at the CCSD level of theory. The high value of 2.17 eV to reach this intersection could account for the long triplet lifetime of 3T.[25] But after crossing this barrier, the probability for intersystem crossing is quite high like in 2T (for details, see ESI†).

3.2.4 Quaterthiophene (4T). For 3T we showed that only the inclusion of all π-orbitals in the active space of the CASPT2 calculations results in the correct electronic state order of the S_1 and the triplet states. This order, especially T_3 below S_1 at the FC point, proved to be crucial to understand and explain the ISC processes resulting in high triplet quantum yields of 2T and 3T. For 4T such an active space means 24 electrons in 20 orbitals. In spite of symmetry restrictions, this active space is too large to be handled within a reasonable computation time. Due to the good agreement of the CCSD and TDDFT results with the CASPT2 results for 1T–3T (see Tables S1–S4 in the ESI†), we studied 4T using the faster CCSD and TDDFT methods. The choice of these methods allows no calculation of the SOC and we can only extrapolate from our knowledge of 2T and 3T. The depopulation of the S_1 state occurs *via* ISC as in the smaller oligothiophenes. The initial relaxation leads to the planar S_1-Min-a, the T_3 state intersects with the S_1 state (see Table 6 and Table S16 (ESI†) and Fig. 11) and should allow for the fast ISC channel (ISC1, Fig. 12). For the second ISC channel (ISC2) out of S_1-Min-a to the T_2 state torsional vibrational activity is again necessary to induce SOC between T_2 and S_1. For symmetry reasons the SOC between the $S_1(B_u)$ and the $T_3(B_u)$ is allowed at both the twisted S_0-Min and the planar S_1-Min-a geometries, while the SOC between the $S_1(B_u)$ and the $T_2(A_g)$ is allowed only for the twisted S_0-Min.

Our conclusions are supported by the slow (390 ps) and fast (36 ps) time constants measured for the decay of the fluorescence of 4T.[27] For comparison the fast time constant for this signal is found to be 16 ps for 3T while for the fast ESA decay and TTA rise it was 2 ps. The 390 ps time constant coincides well with the recently determined time constant for the TTA rise of 398 ps of 4T.[40] In addition a biexponential triplet formation was mentioned for 4T.[31] We assume that the fast ISC channel of 4T has not been observed until now as no femtosecond

Table 6 Calculated CCSD vertical singlet and triplet excitation energies (eV) for the low-lying valence excited states of 4T at the ground-state (S_0-Min) and the S_1 state (S_1-Min-a) minima. Oscillator strengths are shown in parentheses

		S_0-Min (C_2)		S_1-Min-a (C_{2h})		
State	Character	Sym.	CCSD	Sym.	CCSD	Exp.
S_1	$\pi_1 \rightarrow \pi_1^*$	B	4.00 (1.30)	B_u	3.30 (1.40)	2.59[a]
S_2	$\pi_1 \rightarrow \pi_2^*$	A	4.89 (0.00)	A_g	4.40 (0.00)	—
T_1	$\pi_1 \rightarrow \pi_1^*$	B	2.36	B_u	1.59	1.75[b]
T_2	$\pi_1 \rightarrow \pi_2^*$	A	3.00	A_g	2.58	2.56[b]
T_3	$\pi_1 \rightarrow \pi_3^*$	B	3.64	B_u	3.44	—
T_4	$\pi_2 \rightarrow \pi_1^*$	A	4.16	A_g	4.14	—

[a] Maximum of the fluorescence spectrum in dioxane at room temperature.[25] [b] Photodetachment photoelectron spectrum in the gas phase.[47]

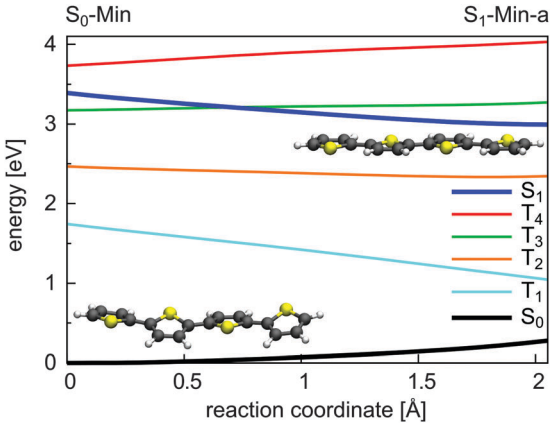

Fig. 11 Energy profile of the S_0, the S_1 and the four lowest lying triplet states along the S_1 relaxation coordinate of 4T. The energy calculations were performed at the TDDFT/6-31G* level of theory. The reaction coordinate was generated by linear interpolation between the optimized S_0-Min (C_2 symmetry) and S_1-Min-a (C_{2h} symmetry) geometries.

time-resolved measurements with dependence on the excitation wavelength were performed similar to 3T. Based on the presented results we suggest that also in 4T the fast ISC to the T_3 state accounts for the high triplet quantum yield of 0.73.[25] Reasons for the decreasing triplet quantum yield from 2T to 4T are the diminishing SOC values along the initial relaxation (ISC1) and the increasing S_1–T_2 energy gap at S_1-Min-a (ISC2) (see Table S18 in the ESI†), also shown by photodetachment photoelectron spectroscopy.[47]

The return from the triplets back to the ground state involves similar steps as in 2T. T_3 relaxation leads to its minimum where the outer thiophene rings are twisted *versus* the two planar inner rings (Fig. 12) due to the π_3^*-orbital (Table 6) characterizing nonbonding and bonding interactions between the thiophene rings (see Fig. S23 in the ESI†). The moderate T_3–T_2 energy gap of 0.41 eV at T_3-Min suggests the possibility of an internal conversion to T_2. From there the T_2 minimum can be reached characterized by an orthogonal arrangement of the thiophene rings with respect to the central bond (Fig. 12) due to the π_2^* orbital (see Fig. S23 in the ESI†). At T_2-Min the T_2 and T_1 states are degenerated like in 2T (see Table S17 in ESI†), leading to fast

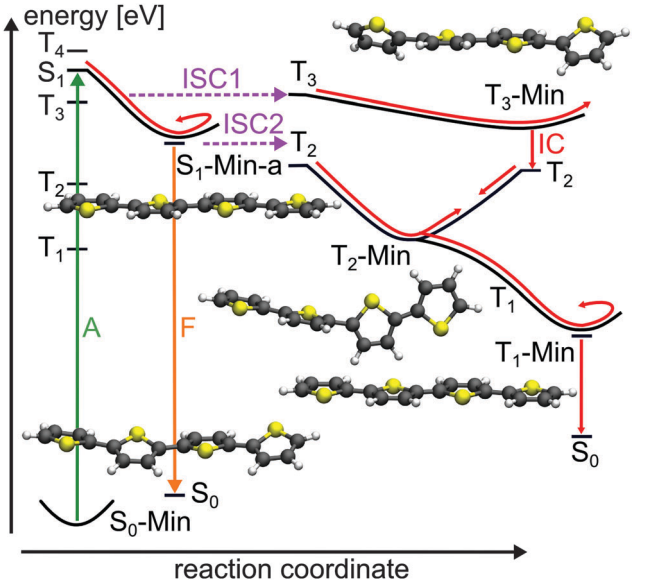

Fig. 12 Schematic illustration of the proposed deactivation mechanism of 4T after excitation to the S_1 state (A: absorption; F: fluorescence; ISC: intersystem crossing; IC: internal conversion). The deactivation pathway is represented by red arrows. The relevant optimized geometries are shown as well.

internal conversion to T_1. In T_1 the global excited state minimum is reached, which is again planar (see Fig. 12). As no phosphorescence was detected,[25] an ISC like in 2T and 3T should lead the molecule back to the ground state. The smaller T_1–S_0 energy gap of 1.0 eV (CCSD/6-31G* level) at the T_1-Min in comparison to 3T (1.42 eV) and 2T (1.77) could account for the decreasing triplet lifetime from 2T to 4T.[25] Although the fluorescence from S_1 is increased compared to 2T and 3T,[25] the major part of the 4T population still relaxes to the ground state *via* ISC and triplet states.

4 Conclusions

For thiophene 1T and the oligothiophenes 2T–4T the relaxation processes from the first excited singlet state were investigated using quantum chemical calculations. We demonstrated that 1T decays primarily *via* its singlet states. Due to large singlet–triplet energy gaps intersystem crossing (ISC) is ineffective, while internal conversion *via* a low lying S_1/S_0 conical intersection (CoIn) seam is associated with a very small barrier and thus highly efficient. In contrast the deactivation paths of the oligothiophenes are dominated by ISC. The S_1/S_0 CoIns are inactive although their energetic position with respect to the ground state minimum is similar for all systems. However, the excited S_1 state is significantly stabilized with increasing chain length due to its $\pi\pi^*$ character in the Franck–Condon (FC) region and at the S_1 minimum (S_1-Min-a). At the S_1/S_0 CoIns the S_1 state character has changed to $\pi\sigma^*$ which is more localized and does not profit to the same extent from the elongation of the π-system. Thus in the oligothiophenes the barriers towards the CoIns are increased and inhibit the passage through them.

Furthermore the extension of the π-system induces more ππ* states and shifts the triplet state T_3 below and close to the S_1 state at the FC point for all investigated oligothiophenes. During the initial relaxation from the non-planar conformation to the planar S_1-Min-a the T_3 state intersects with the S_1 state opening the first ISC path. Around S_1-Min-a thermal torsional fluctuations can induce the second, less effective ISC channel with the T_2 state. In view of the experimental findings and our results, we conclude that the first ISC channel is responsible for the high triplet quantum yields. Hereby we can say that the correlation between the planarization and the ISC is the key property. The overall diminishing SOC from 2T to 4T and the increasing S_1–T_2 energy gaps at S_1-Min-a should account for the slightly decreasing triplet and increasing fluorescence quantum yields.[25] A quantitative determination of the rate constants and branching ratios of the two ISC channels would require dynamical studies but these are clearly beyond the scope of the present work. The return from the triplets back to the ground state is made possible by inter-ring torsions and T_1/S_0 intersections, the latter are characterized by open-ring structures similar to the S_1/S_0 CoIns of 1T. We found two different kinds of triplet relaxation. For the even-numbered oligothiophenes we found a $T_3 \rightarrow T_2 \rightarrow T_1$ cascade, while for the odd oligothiophene an additional direct $T_3 \rightarrow T_1$ path exists.

The present results in combination with previous theoretical and experimental observations offer a quite complete picture of the photophysics of 1T–4T and allow making predictions for the longer oligothiophenes. Also for the longer oligothiophenes and polythiophenes triplet formation has been observed.[25,76–79] From our results for 2T–4T we extrapolate that the first ISC path should be present as well and non-planarity should enhance its efficiency. Preliminary calculations for 5T–10T show, with the exception of 6T, an intersection of the S_1 state with a triplet state along the planarization to S_1-Min-a (see Tables S19 and S20 in the ESI†). The special behavior of 6T is consistent with its highest fluorescence quantum yield (ϕ_F) in the row from 2T to 7T.[25] Furthermore for polythiophenes in solution and films it was shown that ϕ_F decreases due to more efficient nonradiative decay channels when the non-planarity of the thiophene backbone is increased by substitution.[80] The higher degree of non-planarity should enhance the SOC and prolong the interaction time for the ISC. As triplet states are also present in polythiophene-based solar cells[81,82] a deeper understanding of the relaxation processes and the factors influencing the efficiency of these processes should be a first step in improving the performance of the thiophene-based devices.

Acknowledgements

Financial support of this work from the Deutsche Forschungsgemeinschaft through the SFB749 and the excellence cluster 'Munich-Centre for Advanced Photonics' (MAP) is gratefully acknowledged. We thank Alexander André and Moritz Hönig for their contribution to the initial calculations of 1T and 2T.

References

1 *Handbook of Conducting Polymers*, ed. T. A. Skotheim and J. R. Reynolds, CRC Press, Boca Raton, FL, 3rd edn, 2007.
2 *Handbook of Thiophene-Based Materials: Applications in Organic Electronics and Photonics*, ed. I. F. Perepichka and D. F. Perepichka, John Wiley & Sons Ltd, Chichester, UK, 2007.
3 B. L. Rupert, W. J. Mitchell, A. J. Ferguson, M. E. Köse, W. L. Rance, G. Rumbles, D. S. Ginley, S. E. Shaheen and N. Kopidakis, *J. Mater. Chem.*, 2009, **19**, 5311–5324.
4 F. Zhang, D. Wu, Y. Xu and X. Feng, *J. Mater. Chem.*, 2011, **21**, 17590–17600.
5 G. Gigli, O. InganKäs, M. Anni, M. De Vittorio, R. Cingolani, G. Barbarella and L. Favaretto, *Appl. Phys. Lett.*, 2001, **78**, 1493–1495.
6 M. Mazzeo, D. Pisignano, L. Favaretto, G. Barbarella, R. Cingolani and G. Gigli, *Synth. Met.*, 2003, **139**, 671–673.
7 M. Irie, T. Fukaminato, K. Matsuda and S. Kobatake, *Chem. Rev.*, 2014, **114**, 12174–12277.
8 G. Barbarella, M. Zambianchi, A. Ventola, E. Fabiano, F. Della Sala, G. Gigli, M. Anni, A. Bolognesi, L. Polito, M. Naldi and M. Capobianco, *Bioconjugate Chem.*, 2006, **17**, 58–67.
9 H.-A. Ho, A. Najari and M. Leclerc, *Acc. Chem. Res.*, 2008, **41**, 168–178.
10 M. Zambianchi, F. D. Maria, A. Cazzato, G. Gigli, M. Piacenza, F. D. Sala and G. Barbarella, *J. Am. Chem. Soc.*, 2009, **131**, 10892–10900.
11 R. Håkansson, B. Nordén and E. W. Thulstrup, *Chem. Phys. Lett.*, 1977, **50**, 306–308.
12 D. Birnbaum and B. E. Kohler, *J. Chem. Phys.*, 1989, **90**, 3506–3510.
13 H. Chosrovian, S. Rentsch, D. Grebner, D. Dahm, E. Birckner and H. Naarmann, *Synth. Met.*, 1993, **60**, 23–26.
14 D. Lap, D. Grebner, S. Rentsch and H. Naarmann, *Chem. Phys. Lett.*, 1993, **211**, 135–139.
15 R. Rossi, M. Ciofalo and P. Glauco, *J. Photochem. Photobiol., A*, 1993, **70**, 59–67.
16 S. Yamaguchi and H.-o. Hamaguchi, *Chem. Phys. Lett.*, 1994, **227**, 255–260.
17 J. E. Chadwick and B. E. Kohler, *J. Phys. Chem.*, 1994, **98**, 3631–3637.
18 W. J. Buma, B. E. Kohler and T. A. Shaler, *J. Phys. Chem.*, 1994, **98**, 4990–4992.
19 M. Belletête, M. Leclerc and G. Durocher, *J. Phys. Chem.*, 1994, **98**, 9450–9456.
20 R. Colditz, D. Grebner, M. Helbig and S. Rentsch, *Chem. Phys.*, 1995, **201**, 309–320.
21 R. S. Becker, J. Seixas de Melo, A. L. Maçanita and F. Elisei, *Pure Appl. Chem.*, 1995, **67**, 9–16.
22 D. Grebner, M. Helbig and S. Rentsch, *J. Phys. Chem.*, 1995, **99**, 16991–16998.
23 G. Lanzani, M. Nisoli, S. De Silvestri and R. Tubino, *Chem. Phys. Lett.*, 1996, **251**, 339–345.
24 P. Landwehr, H. Port and H. Wolf, *Chem. Phys. Lett.*, 1996, **260**, 125–129.

25 R. S. Becker, J. Seixas de Melo, A. L. Maçanita and F. Elisei, *J. Phys. Chem.*, 1996, **100**, 18683–18695.
26 D. V. Lap, D. Grebner and S. Rentsch, *J. Phys. Chem. A*, 1997, **101**, 107–112.
27 A. Yang, M. Kuroda, Y. Shiraishi and T. Kobayashi, *J. Phys. Chem. B*, 1998, **102**, 3706–3711.
28 W. Paa, J.-P. Yang, M. Helbig, J. Hein and S. Rentsch, *Chem. Phys. Lett.*, 1998, **292**, 607–614.
29 N. DiCésare, M. Belletête, M. Leclerc and G. Durocher, *Chem. Phys. Lett.*, 1998, **291**, 487–495.
30 N. DiCésare, M. Belletête, C. Marrano, M. Leclerc and G. Durocher, *J. Phys. Chem. A*, 1999, **103**, 795–802.
31 J. Yang, W. Paa and S. Rentsch, *Synth. Met.*, 1999, **101**, 624–625.
32 S. Rentsch, J. P. Yang, W. Paa, E. Birckner, J. Schiedt and R. Weinkauf, *Phys. Chem. Chem. Phys.*, 1999, **1**, 1707–1714.
33 J.-P. Yang, W. Paa and S. Rentsch, *Chem. Phys. Lett.*, 2000, **320**, 665–672.
34 W. Paa, J.-P. Yang and S. Rentsch, *Appl. Phys. B: Lasers Opt.*, 2000, **71**, 443–449.
35 W. Paa, J.-P. Yang and S. Rentsch, *Synth. Met.*, 2001, **119**, 525–526.
36 H. Haberkern, K. R. Asmis, M. Allan and P. Swiderek, *Phys. Chem. Chem. Phys.*, 2003, **5**, 827–833.
37 R. Weinkauf, L. Lehr, E. W. Schlag, S. Salzmann and C. M. Marian, *Phys. Chem. Chem. Phys.*, 2008, **10**, 393–404.
38 D. M. P. Holland, A. B. Trofimov, E. A. Seddon, E. V. Gromov, T. Korona, N. de Oliveira, L. E. Archer, D. Joyeux and L. Nahon, *Phys. Chem. Chem. Phys.*, 2014, **16**, 21629–21644.
39 J. Zhou, W. Yu and A. E. Bragg, *J. Phys. Chem. Lett.*, 2015, **6**, 3496–3502.
40 S.-m. Sun, S. Zhang, K. Liu, Y.-p. Wang and B. Zhang, *Photochem. Photobiol. Sci.*, 2015, **14**, 853–858.
41 S. Salzmann, M. Kleinschmidt, J. Tatchen, R. Weinkauf and C. M. Marian, *Phys. Chem. Chem. Phys.*, 2008, **10**, 380–392.
42 X.-F. Wu, X. Zheng, H.-G. Wang, Y.-Y. Zhao, X. Guan, D. L. Phillips, X. Chen and W. Fang, *J. Chem. Phys.*, 2010, **133**, 134507.
43 M. Stenrup, *Chem. Phys.*, 2012, **397**, 18–25.
44 G. Cui and W. Fang, *J. Phys. Chem. A*, 2011, **115**, 11544–11550.
45 D. Fazzi, M. Barbatti and W. Thiel, *Phys. Chem. Chem. Phys.*, 2015, **17**, 7787–7799.
46 A. Prlj, B. F. E. Curchod and C. Corminboeuf, *Phys. Chem. Chem. Phys.*, 2015, **17**, 14719–14730.
47 S. Siegert, F. Vogeler, C. M. Marian and R. Weinkauf, *Phys. Chem. Chem. Phys.*, 2011, **13**, 10350–10363.
48 M. Rubio, M. Merchán, R. Pou-Amérigo and E. Ortí, *ChemPhysChem*, 2003, **4**, 1308–1315.
49 S. H. Vosko, L. Wilk and M. Nusair, *Can. J. Phys.*, 1980, **58**, 1200–1211.
50 C. Lee, W. Yang and R. G. Parr, *Phys. Rev. B: Condens. Matter Mater. Phys.*, 1988, **37**, 785–789.
51 P. J. Stephens, F. J. Devlin, C. F. Chabalowski and M. J. Frisch, *J. Phys. Chem.*, 1994, **98**, 11623–11627.
52 A. D. Becke, *J. Chem. Phys.*, 1993, **98**, 5648–5652.
53 R. Krishnan, J. S. Binkley, R. Seeger and J. A. Pople, *J. Chem. Phys.*, 1980, **72**, 650–654.
54 H. A. Duarte, H. F. Dos Santos, W. R. Rocha and W. B. De Almeida, *J. Chem. Phys.*, 2000, **113**, 4206–4215.
55 P. Celani and H.-J. Werner, *J. Chem. Phys.*, 2000, **112**, 5546–5557.
56 J. F. Stanton and R. J. Bartlett, *J. Chem. Phys.*, 1993, **98**, 7029–7039.
57 T. Yanai, D. P. Tew and N. C. Handy, *Chem. Phys. Lett.*, 2004, **393**, 51–57.
58 M. M. Francl, W. J. Pietro, W. J. Hehre, J. S. Binkley, M. S. Gordon, D. J. DeFrees and J. A. Pople, *J. Chem. Phys.*, 1982, **77**, 3654–3665.
59 M. Rubio, M. Merchán and E. Ortí, *ChemPhysChem*, 2005, **6**, 1357–1368.
60 M. Merchán, L. Serrano-Andrés, M. A. Robb and L. Blancafort, *J. Am. Chem. Soc.*, 2005, **127**, 1820–1825.
61 A. Berning, M. Schweizer, H.-J. Werner, P. J. Knowles and P. Palmieri, *Mol. Phys.*, 2000, **98**, 1823–1833.
62 H.-J. Werner, P. J. Knowles, G. Knizia, F. R. Manby and M. Schütz, *Wiley Interdiscip. Rev.: Comput. Mol. Sci.*, 2012, **2**, 242–253.
63 H.-J. Werner, P. J. Knowles, G. Knizia, F. R. Manby, M. Schütz, P. Celani, T. Korona, R. Lindh, A. Mitrushenkov, G. Rauhut, K. R. Shamasundar, T. B. Adler, R. D. Amos, A. Bernhardsson, A. Berning, D. L. Cooper, M. J. O. Deegan, A. J. Dobbyn, F. Eckert, E. Goll, C. Hampel, A. Hesselmann, G. Hetzer, T. Hrenar, G. Jansen, C. Köppl, Y. Liu, A. W. Lloyd, R. A. Mata, A. J. May, S. J. McNicholas, W. Meyer, M. E. Mura, A. Nicklass, D. P. O'Neill, P. Palmieri, D. Peng, K. Pflüger, R. Pitzer, M. Reiher, T. Shiozaki, H. Stoll, A. J. Stone, R. Tarroni, T. Thorsteinsson and M. Wang, *MOLPRO, version 2012.1, a package of ab initio programs*, 2012, see http://www.molpro.net/.
64 M. J. Frisch, G. W. Trucks, H. B. Schlegel, G. E. Scuseria, M. A. Robb, J. R. Cheeseman, G. Scalmani, V. Barone, B. Mennucci, G. A. Petersson, H. Nakatsuji, M. Caricato, X. Li, H. P. Hratchian, A. F. Izmaylov, J. Bloino, G. Zheng, J. L. Sonnenberg, M. Hada, M. Ehara, K. Toyota, R. Fukuda, J. Hasegawa, M. Ishida, T. Nakajima, Y. Honda, O. Kitao, H. Nakai, T. Vreven, J. A. Montgomery, Jr., J. E. Peralta, F. Ogliaro, M. Bearpark, J. J. Heyd, E. Brothers, K. N. Kudin, V. N. Staroverov, R. Kobayashi, J. Normand, K. Raghavachari, A. Rendell, J. C. Burant, S. S. Iyengar, J. Tomasi, M. Cossi, N. Rega, J. M. Millam, M. Klene, J. E. Knox, J. B. Cross, V. Bakken, C. Adamo, J. Jaramillo, R. Gomperts, R. E. Stratmann, O. Yazyev, A. J. Austin, R. Cammi, C. Pomelli, J. W. Ochterski, R. L. Martin, K. Morokuma, V. G. Zakrzewski, G. A. Voth, P. Salvador, J. J. Dannenberg, S. Dapprich, A. D. Daniels, Ö. Farkas, J. B. Foresman, J. V. Ortiz, J. Cioslowski and D. J. Fox, *Gaussian 09, Revision D.01*, Gaussian Inc., Wallingford, CT, 2009.
65 M. Ciofalo and G. L. Manna, *Chem. Phys. Lett.*, 1996, **263**, 73–78.
66 S. Millefiori, A. Alparone and A. Millefiori, *J. Heterocycl. Chem.*, 2000, **37**, 847–853.
67 F. Liu, P. Zuo, L. Meng and S. J. Zheng, *THEOCHEM*, 2005, **726**, 161–169.

68 G. Zerbi, B. Chierichetti and O. Ingänas, *J. Chem. Phys.*, 1991, **94**, 4637–4645.
69 D. Beljonne, Z. Shuai, G. Pourtois and J. L. Bredas, *J. Phys. Chem. A*, 2001, **105**, 3899–3907.
70 M. Richter, P. Marquetand, J. González-Vázquez, I. Sola and L. González, *J. Phys. Chem. Lett.*, 2012, **3**, 3090–3095.
71 D. Parker, R. Minns, T. Penfold, G. Worth and H. Fielding, *Chem. Phys. Lett.*, 2009, **469**, 43–47.
72 T. Penfold and G. Worth, *Chem. Phys.*, 2010, **375**, 58–66.
73 M. Stenrup and A. Larson, *Chem. Phys.*, 2011, **379**, 6–12.
74 M. Breza, V. Lukeš and I. Vrábel, *THEOCHEM*, 2001, **572**, 151–160.
75 W. Porzio, S. Destri, M. Mascherpa, S. Rossini and S. Brückner, *Synth. Met.*, 1993, **55**, 408–413.
76 B. Kraabel, D. Moses and A. J. Heeger, *J. Chem. Phys.*, 1995, **103**, 5102.
77 H. Burrows, J. Seixas de Melo, C. Serpa, L. Arnaut, M. G. Miguel, A. Monkman, I. Hamblett and S. Navaratnam, *Chem. Phys.*, 2002, **285**, 3–11.
78 S. Cook, A. Furube and R. Katoh, *Energy Environ. Sci.*, 2008, **1**, 294.
79 D. Sahoo, Y. Tian, G. Sforazzini, H. L. Anderson and I. G. Scheblykin, *J. Mater. Chem. C*, 2014, **2**, 6601.
80 M. Theander, O. Inganäs, W. Mammo, T. Olinga, M. Svensson and M. R. Andersson, *J. Phys. Chem. B*, 1999, **103**, 7771–7780.
81 Z. Xu and B. Hu, *Adv. Funct. Mater.*, 2008, **18**, 2611–2617.
82 M. Liedtke, A. Sperlich, H. Kraus, A. Baumann, C. Deibel, M. J. M. Wirix, J. Loos, C. M. Cardona and V. Dyakonov, *J. Am. Chem. Soc.*, 2011, **133**, 9088–9094.

3. Energy transfer in perylene diimide dyads

Another class of molecules commonly used in organic electronics are perylene diimides (PDI). Because of their outstanding high chemical and photochemical stability they find wide range of applications [111–116]. In contrast to the thiophenes molecules of chapter 2, they exhibit fluorescence quantum yields close to unity due to vanishing internal conversion and intersystem crossing rates [117, 118]. In addition, perylene diimides are characterized by strong electron accepting and charge transport properties and therefore are used as acceptor materials in organic solar cells [18]. As their absorption and emission properties can be controlled by chemical substitution [18,119,120], they have also attracted great interest for the design of intramolecular energy and charge transfer systems. In particular, they are used as model systems to study the electron and energy transfer processes in organic photovoltaics.

3.1. Hole-transfer induced energy transfer

In the article "Hole-transfer induced energy transfer in perylene diimide dyads with a donor-spacer-acceptor motif" published in *Physical Chemistry Chemical Physics* [121] the photoinduced dynamics of perylene diimide dyads based on a donor-spacer-acceptor motif are investigated by pump-probe spectroscopy, time resolved fluorescence, chemical variation and quantum chemical calculations in order to elucidate the energy transfer mechanism. All studied compounds were synthesized in the group of Heinz Langhals while the experimental measurements have been performed in the group of Eberhard Riedle. The structures of the studied dyads and associated abbreviations used are shown in chart 1 on page 27. The central statements of the article are:

- Time-resolved fluorescence and transient absorption measurements clearly demonstrate that the energy transfer efficiency and mechanism varies with the spacer present in the dyads. In the dyads with pyridine spacers, after optical excitation of the donor a direct energy transfer to the acceptor moiety occurs with near-unity quantum efficiency. Thereby the energy transfer is made possible by the noise-induced Förster Resonant Energy Transfer (FRET) mechanism which is based on an extended Förster model [122]. The observed direct energy transfer is described by one time constant and the pyridine spacer is not involved in the transfer process.

- When the nitrogen atoms in the electron-poor pyridine spacers (Py) are replaced by carbon atoms to form phenyl spacers (Ph), the energy transfer efficiency drops below 50%. The electron-rich phenyl spacer enables an electron transfer from the spacer to the donor which quenches the donor fluorescence and is in competition to the direct energy transfer from the donor to the acceptor. However, the transient absorption spectra, reveal that the electron transfer itself is involved in a second energy transfer process which is mediated by an intermediate state.

- Transient absorption measurements on a dyad containing a Dexter blocker in the spacer (D-(Ph-BCO-Ph)-A, see chart 1, page 27), also indicate a sequential electron and energy transfer process mediated by a FRET mechanism. The Dexter blocker breaks any π conjugation between the donor, spacer and acceptor and therewith a through bond Dexter-type energy transfer can be excluded.

- Measurements on two representative donor-spacer subsystems of the dyads with phenyl spacers, D-(Me4-Ph) and D-(Ph) (see chart 1, page 27), verify that the intermediate state is a photoinduced charge transfer from the spacer to the donor. Furthermore, while for D-(Me4-Ph) a notable fluorescence can be detected, a fluorescence quenching electron transfer is observed for D-(Ph).

- Quantum chemical calculations of the two donor-spacer systems D-(Me4-Ph) and D-(Ph) lead to similar local minima with $\pi\pi^*$ character (denoted as π-Min) after vertical excitation of the donor. The minima exhibit minor structural changes in comparison to the FC point and the long lived fluorescence of D-(Me4-Ph) is ascribed to the emission from this π-Min.

- In the case of D-(Ph) two additional excited state minima with charge transfer (CT) character are accessible from π-Min. Both minima are associated with a rotation of the spacer towards the plane of the donor moiety. The first CT minimum represents the global excited state minimum and the corresponding charge transfer state is characterized by a low oscillator strength and is denoted as dark charge transfer state, d-CT. The d-CT minimum results from an electron transfer from the spacer to the donor and is responsible for the fast fluorescence quenching in D-(Ph). From the d-CT minimum a conical intersection with the ground state can be easily reached, explaining the fast backward electron transfer dynamics. At the second CT minimum the electronic state has a significant oscillator strength and is denoted as bright charge transfer state, b-CT. A conical intersection in the vicinity of the b-CT minimum leads to a fast population transfer from the b-CT to the d-CT state. Therewith the b-CT state plays no significant role in the excited state dynamics of D-(Ph).

- In D-(Me4-Ph) the rotation of the spacer is sterically inhibited by bulky methyl groups and therefore no fluorescence quenching electron transfer can happen.

- For the dyad with the Dexter blocker (D-(Ph-BCO-Ph)-A), the quantum chemical calculations show that the electronic excitation of the donor also lead to the initial relaxation into the π-Min of the donor. Here, the locally excited (LE) state of the donor is isoenergetic to the LE state of the acceptor and allow for the direct energy transfer from the donor to the acceptor *via* noise-induced FRET. But the major part of the molecules accesses from the π-Min by rotation of the whole spacer-acceptor moiety and by an electron transfer from the donor to the acceptor the d-CT and b-CT minimum. The population of the d-CT minimum leads like in the donor-spacer system D-(Ph) to a backward electron transfer without transferring energy to the acceptor. In the dyad the b-CT minimum is more stable than in D-(Ph) and no fast depopulation of the b-CT state can happen. Furthermore in the dyad the b-CT state and the LE state of the acceptor are nearly isoenergetic at the b-CT minimum. Since the transition dipole moments of the states are parallel to each other, an energy transfer from the donor to acceptor *via* multipole-multipole interactions can occur. This new energy transfer mechanism is denoted as coupled hole-transfer FRET and is enabled by a bright charge transfer state. The different processes taking place in the dyad after excitation of the donor are summarized in figure 6 on page 33.

- The *ab initio* calculations reveal that the hole-transfer induced FRET mechanism is also present in all others dyads with phenyl spacer and that it is the main contributor to the overall energy transfer.

The joint experimental and theoretical work demonstrate for the first time that a bright charge transfer state can indeed act as an energy donor. In the resulting hole-transfer FRET mechanism an electron transfer induces an energy transfer and allow to invert the usual order of these processes present in artificial photosynthetic systems and solar cells. Systems with engineered bright charge transfer states could find applications in novel photovoltaic devices. In

addition, the work reveal that the energy transfer dynamics, efficiencies and mechanisms can be controlled by the choice of the substituents. Quantum chemical calculations can be used as an essential tool for obtaining a deeper understanding of the molecular processes and to predict optimal substitution to achieve the desired properties [123].

On the next pages the article "Hole-transfer induced energy transfer in perylene diimide dyads with a donor-spacer-acceptor motif" published in *Physical Chemistry Chemical Physics* is reprinted with permission from *Phys. Chem. Chem. Phys* **17**, 25061-25072. (2015). The supporting information of this article is available under http://dx.doi.org/10.1039/C5CP02981C.

PCCP

PAPER

Cite this: *Phys. Chem. Chem. Phys.*, 2015, **17**, 25061

Hole-transfer induced energy transfer in perylene diimide dyads with a donor–spacer–acceptor motif†

Patrick Kölle,‡[a] Igor Pugliesi,‡[b] Heinz Langhals,[a] Roland Wilcken,[b] Andreas J. Esterbauer,[a] Regina de Vivie-Riedle*[a] and Eberhard Riedle*[b]

Received 23rd May 2015,
Accepted 23rd August 2015

DOI: 10.1039/c5cp02981c

www.rsc.org/pccp

We investigate the photoinduced dynamics of perylene diimide dyads based on a donor–spacer–acceptor motif with polyyne spacers of varying length by pump–probe spectroscopy, time resolved fluorescence, chemical variation and quantum chemistry. While the dyads with pyridine based polyyne spacers undergo energy transfer with near-unity quantum efficiency, in the dyads with phenyl based polyyne spacers the energy transfer efficiency drops below 50%. This suggests the presence of a competing electron transfer process from the spacer to the energy donor as the excitation sink. Transient absorption spectra, however, reveal that the spacer actually mediates the energy transfer dynamics. The ground state bleach features of the polyyne spacers appear due to the electron transfer decay with the same time constant present in the rise of the ground state bleach and stimulated emission of the perylene energy acceptor. Although the electron transfer process initially quenches the fluorescence of the donor it does not inhibit energy transfer to the perylene energy acceptor. The transient signatures reveal that electron and energy transfer processes are sequential and indicate that the donor–spacer electron transfer state itself is responsible for the energy transfer. Through the introduction of a Dexter blocker unit into the spacer we can clearly exclude any through bond Dexter-type energy transfer. *Ab initio* calculations on the donor–spacer and the donor–spacer–acceptor systems reveal the existence of a bright charge transfer state that is close in energy to the locally excited state of the acceptor. Multipole–multipole interactions between the bright charge transfer state and the acceptor state enable the energy transfer. We term this mechanism coupled hole-transfer FRET. These dyads represent a first example that shows how electron transfer can be connected to energy transfer for use in novel photovoltaic and optoelectronic devices.

1 Introduction

Förster resonant energy transfer (FRET)[1] is a fundamental photophysical process, where electronic energy is transferred from an optically excited donor to a neighbouring acceptor. The process is mediated by multipole–multipole coupling in contrast to Dexter energy transfer, where orbital overlap between the donor and the acceptor is required.[2–6] The probability for Dexter energy transfer decreases exponentially with the distance of the components.[7,8] In contrast, the probability for FRET decreases with the sixth power of the donor–acceptor distance and thus has a much larger range of action. The Förster radii (the donor–acceptor distance at which the rate of energy transfer equals that of fluorescence of the excited donor) lie in the order of 30 Å.

In a recent Feature article Silbey[9] showed that the habitual formulation of Förster theory for the resonant energy transfer has been successfully applied in many instances. However, due to the approximations done to get to this multipole–multipole description, there are many instances where the theory breaks down and mechanisms that go beyond Förster theory are required to explain the resonant energy transfer.[10–16] Here the light harvesting complex has to be mentioned, where the observation of coherences in the dynamics of the energy transfer cannot be described *via* the Förster approach.[17,18]

Also in simpler systems a breakdown of the standard Förster approach can occur. We have recently shown that in a perylene diimide dyad based on a donor–spacer–acceptor motif (D–(Me4-Ph)–A in Chart 1) rapid FRET from the donor to the

[a] *Department of Chemistry, Ludwig-Maximilians-Universität München, Butenandstrasse 5-13, 81377 München, Germany. E-mail: Regina.de_Vivie@cup.uni-muenchen.de*

[b] *Lehrstuhl für BioMolekulare Optik, Ludwig-Maximilians-Universität München, Oettingenstrasse 67, 80538 München, Germany. E-mail: riedle@physik.uni-muenchen.de*

† Electronic supplementary information (ESI) available: Experimental details, Chart S1, Table S1 and Fig. S1–S19. Computational details, Tables S2–S6 and Fig. S20–S24. See DOI: 10.1039/c5cp02981c

‡ These authors contributed equally.

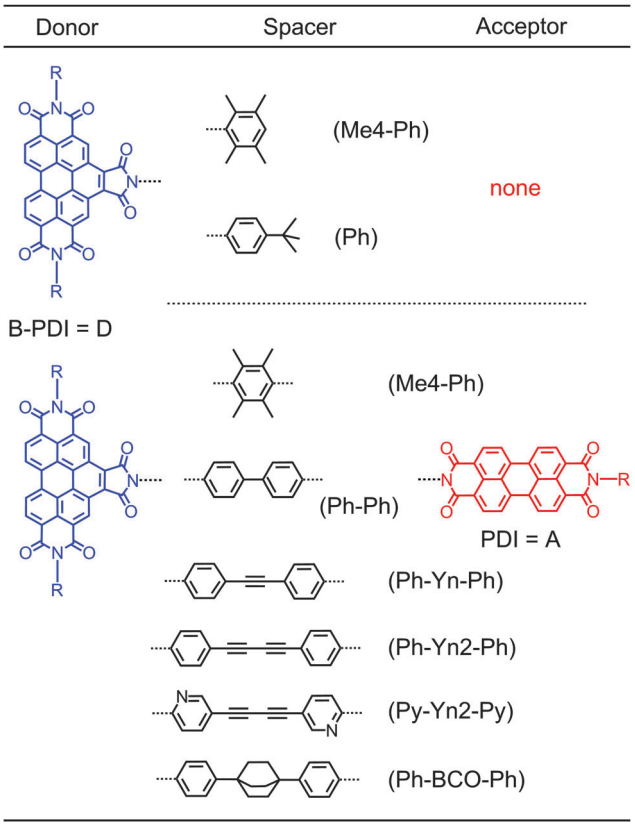

Chart 1 Perylene diimide dyads investigated in this work together with the associated abbreviation used in the paper. B-PDI = benzoperylene diimide; PDI = perylene diimide; Ph = phenyl; Me = methyl; Py = pyridine; Yn = alkyne; BCO = bicyclooctane, R = 1-hexyl-heptyl.

acceptor moiety is occurring although the transition dipole moments are orthogonal to each other.[19] According to the point dipole approximation used in Förster theory no energy transfer should occur in an orthogonal arrangement. Experimentally we do, however, observe an ultrafast transfer time of 9.4 ps. The determination of the Coulombic coupling *via* the transition density cube approach furthermore reveals that in the orthogonal arrangement the higher multipole moments are not responsible for the energy transfer. Pump–probe experiments revealed that the energy transfer rate increases upon increasing the sample temperature.[19] This temperature dependence can only be reproduced within an extended Förster model that includes low wavenumber ground state vibrations and structural and electronic deformations induced by solvent fluctuations.[20] These deformations break the orthogonal arrangement of the dipoles and enable the ultrafast and near-unity efficient energy transfer. We termed this energy transfer mechanism noise-induced FRET.

Time-resolved measurements on perylene diimide dyads with orthogonal transition dipole moments and pyridine polyyne spacers of varying length (Chart S1 and Table S1 in the ESI†) show that these dyads also undergo the noise-induced FRET with near-unity quantum efficiency. If the N centres in these spacers are replaced with carbons to form phenyl polyyne spacers the fluorescence quantum yield out of the energy acceptor decreases from the near 100% to below 50%. In ref. 19 it was envisioned that an electron transfer (ET) from the spacer to the energy donor acts as a parasitic process. However, for the corresponding donor–spacer–acceptor system we observe donor fluorescence quantum yields below 1%. The electron transfer times between perylene diimides and electron rich phenyl spacers are in the order of up to 10 ps at most.[21] With energy transfer times ranging from 10 to 50 ps this would lead to FRET efficiencies below 10%, thus far less than observed.

Here we investigate the photoinduced dynamics of these dyads by pump–probe spectroscopy, time resolved fluorescence and quantum chemical calculations in order to elucidate the steps comprising the full energy transfer mechanism.

2 Experimental determination of energy transfer rates

The theory in ref. 20 predicts that the noise-induced FRET rate has a donor–acceptor distance R dependence that scales with $(1/R^3)$. This is in contrast to the standard FRET $(1/R^6)$ dependence. Time-resolved measurements on perylene diimide dyads with orthogonal transition dipole moments and pyridine polyyne spacers of varying length (Chart S1 and Table S1 in the ESI†) show that the noise-induced FRET indeed deviates from the $(1/R^6)$ behaviour and points towards a contribution from the predicted $(1/R^3)$ distance dependence (Fig. S3 in the ESI†).

We now investigate the difference in behaviour in the related perylene diimide dyads with phenyl polyyne spacers shown in Chart 1. All newly determined transfer rates are collected in Table 1. Selected measurements are discussed in detail to decipher the underlying processes. All other measurements are shown in the ESI.† We start by recording the time resolved fluorescence for the two dyads D–(Py-Yn2-Py)–A and D–(Ph-Yn2-Ph)–A.

2.1 Time resolved fluorescence: two transfer mechanisms

The time resolved fluorescence data of D–(Py-Yn2-Py)–A and D–(Ph-Yn2-Ph)–A were measured using a streak camera setup described in detail in ref. 22 and femtosecond excitation by the frequency doubled output of a CPA-system (CPA-2001; Clark MXR). At the 389 nm wavelength the donor is selectively excited in the S_2 absorption band (Fig. S1 and S2 in the ESI†) as the extinction coefficients of the donor and acceptor are 22 400 L mol^{-1} cm^{-1} and 4250 L mol^{-1} cm^{-1}. For experimental details, see ESI.†

False colour plots of the time-resolved fluorescence data for the 0.5 ns window are shown in Fig. 1a and b. Immediately after excitation of D–(Py-Yn2-Py)–A we observe fluorescence bands which spectrally coincide with the steady state fluorescence bands of the donor and acceptor moieties. With the increasing pump-detection delay we observe a concerted decay of the donor fluorescence and a rise of the acceptor fluorescence which then lasts for several nanoseconds. This behaviour is a clear indication of energy transfer. A global fit analysis as well as single line fits on the five distinct band maxima yields a time constant of 53 ps for the energy transfer from the benzoperylene diimide (B-PDI) to the perylene diimide (PDI) moiety

Table 1 Global fit results from the transient absorption data in chloroform for all the compounds presented in Chart 1 together with fluorescence quantum yields Φ_{Fluo}. The global fit results obtained from the time resolved (TR) fluorescence measurements on D–(Ph-Yn2-Ph)–A and D–(Py-Yn2-Py)–A are in italics. The association of the time constants with processes is explained in the footnotes

Compound	τ_1[a]/ps	τ_2[b]/ps	τ_3[c]/ps	τ_{Fluo}[f]/ns	Φ_{Fluo}[g] (%)
D–(Me4-Ph)	0.2	—	—	1.3	30
D–(Ph)	0.6	5.9	61[d]	—	n.d.
D–(Ph-Ph)–A	0.6	4.7	22	2.0	58
D–(Ph-Yn-Ph)–A	0.3	2.6	30	1.5	33
D–(Ph-Yn2-Ph)–A	0.7	4.0	35	2.1	53
In benzonitrile	0.8	8.5	40	2.5	—
TR fluorescence		*5.6*	*35*	*3.0*	
D–(Me4-Ph)–A	0.3	—	9.4[e]	4.0	100
D–(Py-Yn2-Py)–A	1.5	—	54[e]	2.4	100
TR fluorescence		—	*53*[e]	*3.3*	
D–(Ph-BCO-Ph)–A	0.4	5.0	45	3.3	44

[a] τ_1 corresponds to the vibrational relaxation from the FC point to the π-minimum of the excited B-PDI donor. [b] For the dyads $\tau_2 = (1/\tau_{FRET} + 1/\tau_{d\text{-}CT} + 1/\tau_{b\text{-}CT})^{-1}$. See Fig. 6. [c] For the dyads $\tau_3 = (1/\tau_{HT\text{-}FRET} + 1/\tau_{d\text{-}CT\rightarrow S0})^{-1}$. See Fig. 6. [d] For the donor–spacer system D–(Ph), this time constant is for the backward electron transfer from the B-PDI donor to the spacer $\tau_{d\text{-}CT\rightarrow S0}$. See Fig. 5. [e] For D–(Me4-Ph)–A and D–(Py-Yn2-Py)–A $\tau_3 = \tau_{FRET}$. [f] For the donor–spacer systems D–(Me4-Ph) and D–(Ph) τ_{Fluo} is the lifetime of the bright LE state of the B-PDI donor; for the dyads it is the lifetime of the bright LE state of the PDI acceptor moiety. [g] The fluorescence quantum yield was determined by excitation at 437 nm with reference to 2,10-bis(1-hexylheptyl)-6-[2-[3,8,9,10-tetrahydro-9-(1-octylnonyl)-1,3,8,10-tetraoxoanthra[2,1,9-*d*,*e*,*f*:6,5,10-*d*′,*e*′,*f*′]diisoquinolin-2(1*H*)-yl]ethyl]-1*H*-pyrrolo[3′,4′:4,5]pyreno[2,1,10-*d*,*e*,*f*:7,8,9-*d*′,*e*′,*f*′]diisoquinoline-1,3,5,7,9,11(2*H*,6*H*,10*H*)-hexone RN335458-21-4 with Φ = 1.00.[23] For the donor–spacer systems it is the fluorescence quantum yield of the B-PDI chromophore. For the dyads it is the fluorescence quantum yield of the PDI energy acceptor obtained by excitation of the B-PDI energy donor.

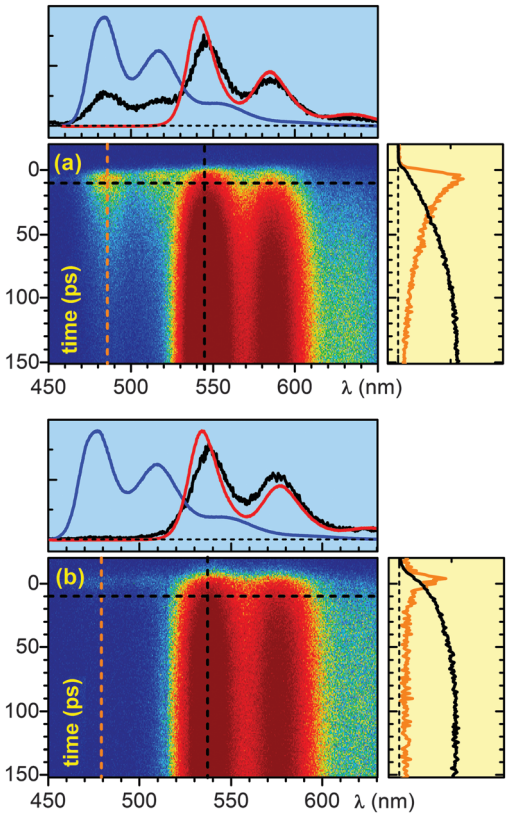

Fig. 1 False colour plots of the time resolved fluorescence of the perylene diimide dyad (a) D–(Py-Yn2-Py)–A and (b) D–(Ph-Yn2-Ph)–A in chloroform. Blue indicates low fluorescence and red indicates high fluorescence. The top profile graphs (blue background) show the fluorescence at a delay of 10 ps (black line) together with the time integrated fluorescence of the free B-PDI donor (blue line) and the free PDI acceptor (red line) for reference. The lineouts on the right side (light yellow background) show the temporal evolution of the fluorescence for the donor (orange line multiplied by 5) at 486 nm and for the acceptor (black line) at 546 nm.

and an acceptor excited state lifetime of 3.3 ns. This compares well with the 3.8 ns time constant reported in ref. 23.

The temporal evolution of the fluorescence for the dyad D–(Ph-Yn2-Ph)–A is substantially different. The shortest time window of 0.2 ns reveals that the donor fluorescence decays within the first 10 ps, while the fluorescence of the acceptor rises on the 30 ps timescale. Global analysis and single line fits yield a time constant of 5.6 ps for the quenching of the donor fluorescence, while the time constant for the acceptor rise is 35 ps. A concerted fluorescence rise and fall characteristic for direct energy transfer is missing.

A change of the spacer from a pyridine to a phenyl unit results in efficient quenching of the fluorescence of the donor. One would expect that this prevents energy transfer from the B-PDI to the PDI moiety. Still a substantial rise of the acceptor fluorescence occurs. This is a clear indication that the mechanisms for energy transfer in D–(Ph-Yn2-Ph)–A and D–(Py-Yn2-Py)–A are different.

2.2 Transient absorption of D–(Ph-Yn2-Ph)–A: the role of the spacer

To investigate the dynamics of D–(Ph-Yn2-Ph)–A further, we carried out time-resolved transient absorption measurements using a broadband setup described in detail in ref. 24. The B-PDI donor moiety of D–(Ph-Yn2-Ph)–A was excited at 465 nm with the output of NOPA. The transient absorption spectra in chloroform at various delay times are shown in Fig. 2a and the corresponding transient absorption kinetics at selected wavelengths is shown in Fig. 2b. Immediately after optical excitation we observe the ground state bleach (GSB; between 350 nm to 500 nm). The GSB is partially shifted to positive transient absorption by the overlapping broad excited state absorption (ESA; from 500 to 700 nm) of the blue absorbing B-PDI donor moiety. As the spectra evolve in time, the transient signatures of the donor give way to a GSB signature below 350 nm within the first 10 ps. The usual negative transient absorption of a GSB is shifted into the positive regime by overlapping ESA. However, the GSB spectral structure is matched by the very characteristic triple peaked absorption structure of the isolated diphenyl butadiyne (Ph-Yn2-Ph) spacer with a slightly red shift. Within 50 ps the spacer GSB decays and the GSB, SE and ESA of the green absorbing acceptor rises. These features last for several nanoseconds, the characteristic excited state lifetime of perylene diimides.

To quantify the temporal evolution of the absorption changes a maximum entropy analysis[25] followed by a global fit analysis[26] has been carried out. The results are shown in

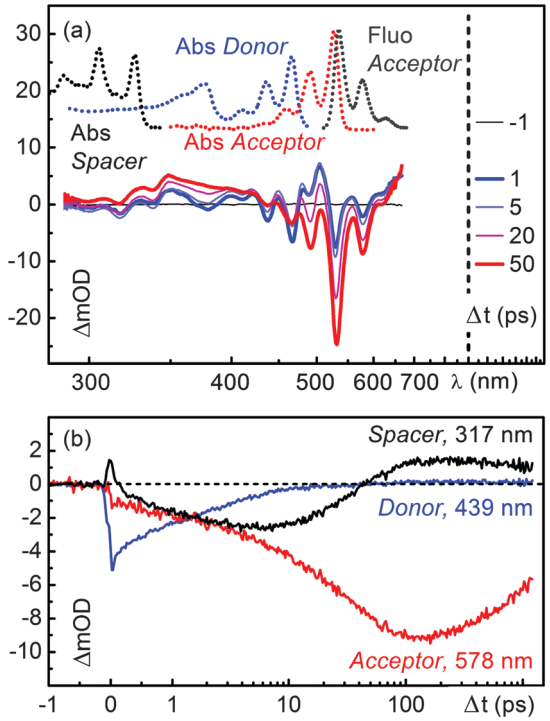

Fig. 2 (a) Transient absorption spectra of the perylene bisimide dyad D–(Ph-Yn2-Ph)–A in chloroform. For reference the stationary absorption of the B-PDI donor moiety, the spacer and the PDI acceptor are shown together with the fluorescence spectrum of the PDI in chloroform. (b) Temporal evolution of the ground state bleach (GSB) of the spacer (black line), the GSB of the donor (blue line) and the stimulated emission (SE) of the acceptor (red line).

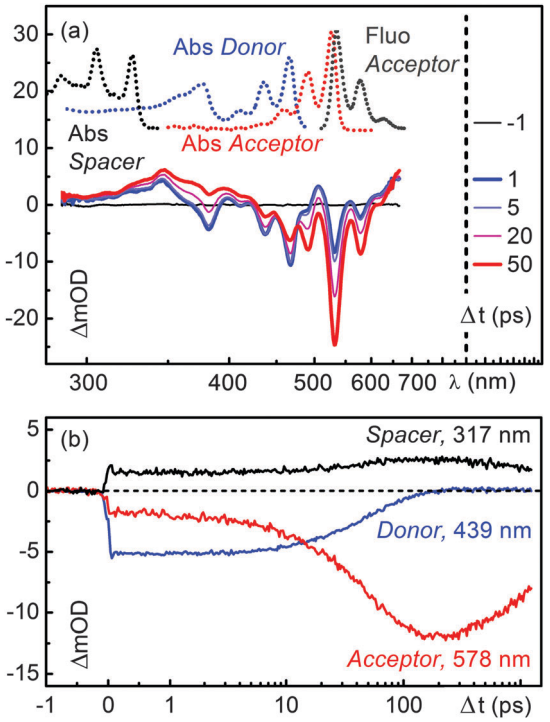

Fig. 3 (a) Transient absorption spectra of the perylene bisimide dyad D–(Py-Yn2-Py)–A in chloroform. For reference the stationary absorption of the B-PDI donor moiety, the spacer and the PDI acceptor are shown together with the fluorescence spectrum of the PDI in chloroform. (b) Temporal evolution of the GSB of the spacer (black line), the GSB of the donor (blue line) and the stimulated emission (SE) of the acceptor (red line).

Fig. S16 (ESI†) and Table 1. The GSB of the B-PDI energy donor moiety decays with two time constants of 4 and 35 ps while the GSB of the spacer rises with the 4 ps time constant and decays with the 35 ps time constant. The GSB, SE and ESA of the PDI energy acceptor rise with the two time constants of 4 and 35 ps. The 4 ps time constant coincides with the fluorescence decay of the donor observed in the time resolved fluorescence measurements suggesting that an electron transfer between the spacer and the energy donor occurs.

Furthermore the presence of this time constant in the initial rise of the spectral signatures of the PDI acceptor indicates that during the quenching process direct energy transfer occurs. The 35 ps time constant associated with the decay of the spacer GSB and the major rise of the spectral signatures of the PDI acceptor coincides with the rise of its fluorescence observed in the time resolved fluorescence measurements. These spectral changes are a clear indication that a substantial part of the excitation energy is transferred from the B-PDI to the PDI moiety with the involvement of the spacer.

Compared to D–(Ph-Yn2-Ph)–A (Fig. 2), the transient absorption spectra of D–(Py-Yn2-Py)–A in Fig. 3a show a less complex dynamics. The GSB signatures of the initially excited B-PDI donor moiety decay giving directly rise to the GSB, SE and ESA features of the PDI, in analogy to the D–(Me4-Ph)–A dyad published in ref. 19. The time constant for this direct energy transfer is 54 ps.[20] The spacer is not electronically involved in the energy transfer process. The transient absorption kinetics in the region of the spacer at 317 nm in fact shows no significant dynamics (Fig. 3b, black line).

2.3 Transient absorption of a dyad with a Dexter blocker

The two main mechanisms responsible for energy transfer in molecules are FRET[1] and Dexter.[7] While the former is a through space multipole–multipole interaction, the latter occurs in a through bond fashion *via* orbital overlap between the donor, spacer and acceptor. To verify which energy transfer mechanism is playing a role in the dyad D–(Ph-Yn2-Ph)–A we carried out transient absorption measurements on D–(Ph-BCO-Ph)–A which contains a chemically engineered Dexter blocker in the spacer moiety. Just like D–(Ph-Yn2-Ph)–A this dyad has electron rich phenyl rings comprising the spacer and thus affords charge transfer from the spacer to the energy donor moiety. Excitation of the donor moiety however leads to fluorescence from the energy acceptor with a quantum yield of 44%.[19] In contrast to D–(Ph-Yn2-Ph)–A the spacer of this dyad also contains the aliphatic, stiff, linear spacer bicyclo[2.2.2]octane. Due to its aliphatic character, this group breaks any π conjugation between the donor, spacer and acceptor and thus acts as a Dexter-type blocker inhibiting any Dexter type energy transfer.

For the time-resolved measurements, D–(Ph-BCO-Ph)–A was selectively excited at 435 nm with the frequency doubled

output of NOPA. The 435 nm wavelength ensures the highest contrast between the donor and the residual acceptor excitation at the cost of some vibrational excitation. Supplementary experiments (ESI†) showed, however, that excitation at 465 nm leads to no noticeable differences in the dynamics. As it is technically much less demanding it was used for some of the investigated molecules.

The transient absorption spectra in chloroform of D–(Ph-BCO-Ph)–A at various delay times are shown in Fig. 4c. The optical excitation leads to the GSB between 350 nm to 500 nm and a broad ESA from 500 to 700 nm of the blue absorbing B-PDI moiety. The ESA again shifts the highly structured GSB and SE of the donor and the partially excited acceptor from the expected negative transient optical density into the positive regime. As the spectra evolve in time, the transient signatures of the donor give way to two distinct ESA bands located at 340 nm and 490 nm within the first 10 ps. Within 50 ps these ESA bands decay and the familiar nanosecond long lived GSB, SE and ESA of the green absorbing acceptor rise.

To quantify the temporal evolution of the absorption changes again a maximum entropy analysis followed by a global fit analysis has been carried out. The results are shown in the ESI† (Fig. S19). The GSB of the B-PDI donor moiety decays with two time constants of 5 ps and 45 ps. The ESA bands at 340 nm and 490 nm rise with the 5 ps time constant. The decay of the ESA bands and the rise of the GSB, SE and ESA of the PDI energy acceptor occur with a time constant of 45 ps. The observed spectral changes clearly indicate that energy is transferred from the B-PDI to the PDI moiety through an intermediate state which is populated after the excitation of the B-PDI moiety and shows distinct absorption bands at 340 nm and 490 nm. The presence of the bicyclo[2.2.2]octane excludes that a Dexter through bond energy transfer is responsible for the energy transfer in D–(Ph-BCO-Ph)–A and possibly also in D–(Ph-Yn2-Ph)–A.

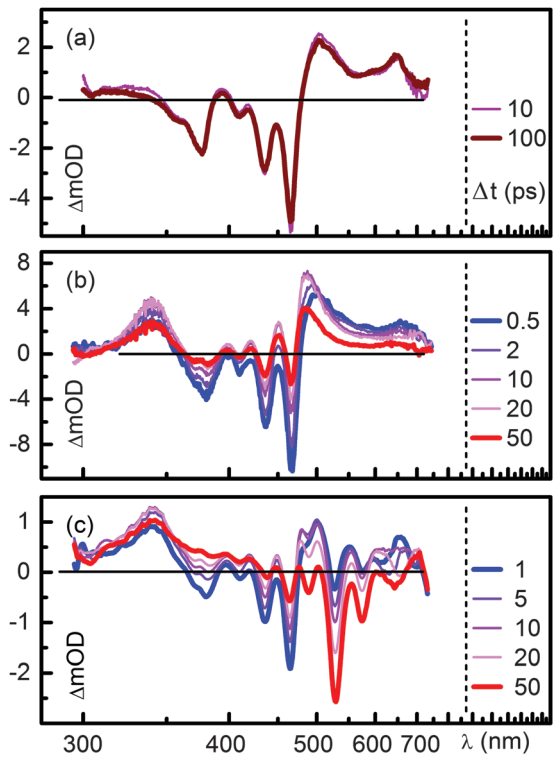

Fig. 4 Transient absorption spectra of (a) the donor–spacer system D–(Me4-Ph) and (b) D–(Ph) together with (c) the perylene diimide dyad D–(Ph-BCO-Ph)–A in chloroform.

2.4 Evidence for a charge transfer state

The results obtained from the time resolved fluorescence measurements in Section 2.2 and the transient absorption measurements on D–(Ph-Yn2-Ph)–A in Section 2.3 suggest that after excitation of the B-PDI moiety electron transfer from the spacer to the B-PDI moiety occurs. In order to verify if the intermediate state with the characteristic absorption bands at 340 nm and 490 nm is a charge transfer state we carried out transient absorption measurements on the two systems D–(Me4-Ph) and D–(Ph). These compounds are representative donor–spacer subsystems of the dyads investigated. Furthermore the fluorescence quantum yield of D–(Me4-Ph) is 30%, while for D–(Ph) no noticeable fluorescence could be detected[19] indicating that these are the right candidates for the identification of the charge transfer signatures. The transient absorption spectra of D–(Me4-Ph) and D–(Ph) in chloroform at various delay times Δt are shown in Fig. 4a and b.

The 465 nm optical excitation of D–(Me4-Ph) leads to the GSB features between 350 nm and 500 nm and the broad ESA from 500 to 700 nm of the blue absorbing B-PDI moiety as already observed in D–(Ph-BCO-Ph)–A and D–(Ph-Yn2-Ph)–A. These features show no significant temporal change (Fig. S9 in the ESI†) and the global fit yields a single lifetime of 1.3 ns. In conjunction with the 30% fluorescence quantum yield this compares well to the 6.8 ns fluorescence lifetime in ref. 23. Despite the sizeable fluorescence quantum yield no SE can be observed in the transient spectra. We believe that the spectral signatures of the SE are cancelled out by ESA that matches the spectral features of the SE.

For D–(Ph) the 465 nm optical excitation yields the same GSB and ESA features as for D–(Me4-Ph). However, these features decay within the first 10 ps and give rise to two distinct new ESA bands which coincide spectrally with the intermediate ESA features at 340 nm and 490 nm observed in D–(Ph-BCO-Ph)–A. The whole system returns back to the ground state within 300 ps. The maximum entropy and global fit yield two time constants of 5.9 ps and 61 ps, which we ascribe to electron transfer from the phenyl spacer to the B-PDI chromophore and backward electron transfer to reach the ground state of D–(Ph).

This assignment to a forward and backward electron transfer is further supported by spectroelectrochemical measurements on the unreactive D–(Me4-Ph) in dichloromethane. The results are shown in the ESI† (Fig. S13). With a reducing voltage of 1.4 V two strong absorption bands appear to the red and the blue of the neutral B-PDI absorption bands at 622 nm and below 300 nm. The energy difference between the 622 nm absorption

band and the neutral absorption band at 466 nm is 0.7 eV. This compares well to the energy difference between the strongest absorption bands of neutral (518 nm) and monoionic (705 nm) perylene diimides of 0.6 eV reported in ref. 27. We therefore assign the spectral bands to the monoionic B-PDI moiety. This assignment is further supported by *ab initio* calculations of the D–(Me4-Ph) anion (Table S4 in the ESI†). No signatures that can be ascribed to the anion of the Me4 spacer can be observed.[28] The appearance of monoionic absorption bands to the red and the blue of the neutral absorption of D–(Me4-Ph) can be compared to the transient spectra of D–(Ph) that feature distinct ESA signatures on both sides of the GSB signatures (Fig. 4b) albeit the spectral positions do not coincide. We believe that this discrepancy can be ascribed to the absence of the positively charged spacer moiety in the spectroelectrochemical measurements. We therefore assign the ESA signatures at 340 nm and 490 nm observed after excitation of D–(Ph) and D–(Ph-BCO-Ph)–A to the absorption of the B-PDI anion generated by photoinduced charge transfer from the spacer to the donor. The reason why electron transfer occurs in D–(Ph) and not in D–(Me4-Ph) is explained in Section 3, where the results of the *ab initio* calculations are presented.

The postulated ultrafast electron transfer leads to the population of a charge transfer (CT) state. Due to its high dipole moment it should be strongly influenced by the polarity of the solvent. To test the impact on the energy transfer we performed additional transient absorption measurements of D–(Ph-Yn2-Ph)–A in benzonitrile. The dielectric constant ε is 25.2 for benzonitrile as compared to 4.8 for chloroform. The recording is shown in Fig. S15 of the ESI.† The general appearance is quite similar to the chloroform recording. A closer look reveals that the decay of the donor GSB monitored at 441/439 nm is slowed down in benzonitrile. The spacer GSB at 319/317 nm appears somewhat slower and is weakened in strength as seen from the less negative transient optical density. Finally, the maximum of the GSB of the acceptor at 583/580 nm is decreased roughly by a factor of two as compared to the donor GSB signal at very early times. This suggests a strongly decreased overall energy transfer. The slowing of the processes can also be seen from a comparison of the maximum entropy analyses (Fig. S16 and S17 in the ESI†). The global fit shows that the vibrational relaxation is not much changed between the two solvents (compare τ_1 in Table 1). The first transfer time τ_2 is slowed down from 4.0 to 8.5 ps in benzonitrile. Also the second transfer time τ_3 is increased from 35 to 40 ps.

The results in benzonitrile clearly show that the dynamics are much more severely changed as it would be expected for only locally excited states in basic FRET. The high polarity of benzonitrile might be expected to lower the charge transfer state sufficiently that the energy is trapped there and cannot subsequently be transferred to the acceptor. However, besides the polarity we have to consider the solvation times of the two solvents. The characteristic time $\langle\tau\rangle$ increases from 2.8 to 5.1 ps from chloroform to benzonitrile.[29] As the intrinsic rates of D–(Ph-Yn2-Ph)–A are quite comparable to the solvation times, a full modelling of the increased polarity is well beyond the scope of this work. The intricate interplay between solvent polarity and solvation times on the dynamics of CT states has been documented in detail.[30] Furthermore, we find that the weak donor LE dipole moment vector points opposite to the strong CT dipole moment vector. The solvation could well be slowed down even further by this situation and this underscores the importance of the solvation time besides the polarity. Last but not least, the $1/n^4$ scaling of the FRET rate with the refractive index n and possible screening should slow the direct transfer in benzonitrile considerably. The observed behaviour therefore is a highly complex dynamical interplay between the various solvent properties.

Overall we suggest that the observed changes due to the increase in polarity are not compatible with LE state dynamics. Rather they support the suggestion of an intermediate CT state responsible for the complex behaviour in the perylene diimide dyads with phenyl polyyne spacers.

2.5 Towards a detailed model for the complete dynamics

For the dyads D–(Ph-BCO-Ph)–A and D–(Ph-Yn2-Ph)–A the experimental evidence obtained from time resolved fluorescence and time resolved absorption suggests that after excitation of the B-PDI donor, a few ps electron transfer occurs from the spacer to the B-PDI moiety. The tens of ps backward electron transfer from the B-PDI moiety to the spacer excite the green absorbing PDI acceptor. The analysis of the additional systems D–(Ph-Ph)–A and D–(Ph-Yn-Ph)–A fully confirms this interpretation. The presence of the BCO Dexter blocker suggests that this process occurs *via* a through space interaction. The required multipole–multipole interactions between the charge transfer state of the donor–spacer moiety and the excited state of the acceptor can only exist, if the charge transfer state has some oscillator strength. The existence of partial charge transfer states with oscillator strength has been recently observed in related core-substituted naphthalene diimides[31,32] and postulated to act as energy donors in pyrene-borondipyrromethene dyads[33] albeit in the latter case no spectral or theoretical identification of such a state could be obtained.

3 *Ab initio* calculations identify a bright charge transfer state

To gain further understanding about the mechanism behind the energy transfer in the dyads D–(Ph-BCO-Ph)–A and D–(Ph-Yn2-Ph)–A, we have carried out an extensive set of quantum chemical calculations. We first investigated the smaller donor spacer systems D–(Me4-Ph) and D–(Ph) at the MP2, CC2 and CASSCF level of theory and then moved onto the larger D–(Ph-BCO-Ph)–A dyad. A detailed description of the calculations can be found in the ESI.†

The excited states involved in the investigation processes of the perylene diimide dyads in this work are all described by π orbitals. Orbitals located on the B-PDI donor are denoted as π_D respectively as π_{1D}^* (LUMO) and π_{2D}^* (LUMO+1, Fig. S20 in the ESI†). The orbitals of the spacer and the acceptor are termed as π_S respectively as π_A and π_A^* (Fig. S21 in the ESI†).

MP2 ground state geometry optimizations for both D–(Me4-Ph) and D–(Ph) result in a planar structure of the B-PDI donor and the spacer rotated about an angle α with respect to the plane of B-PDI. The different spacers lead to a larger torsional angle ($\alpha = 67.4^\circ$) for D–(Me4-Ph) than for D–(Ph) ($\alpha = 48.0^\circ$, Fig. 5, FC-point).

Vertical excitations at the MP2 ground state minima obtained with the CC2 method are shown in Table 2. The first two vertical transitions in both molecules are localized on the B-PDI chromophore. The S_1 state is a dark $\pi\pi^*$ transition and is characterized by an excitation from the HOMO (π_D) to an orbital (LUMO+1, π_{2D}^*) with significant contributions on the maleimide ring (Fig. S20 in the ESI†). The S_2 state has a large oscillator strength and corresponds to a transition from the HOMO to the LUMO (π_{1D}^*) which is mainly localized on the perylene diimide framework of the B-PDI moiety (Table 1 and Fig. S20 in the ESI†). The excitation energy of 3.07 eV obtained at the RI-CC2/def2-SV(P) level of theory compares well with the experimental absorption maxima of D–(Me4-Ph) and D–(Ph) at 2.66 eV (465 nm) in $CHCl_3$ when the 0.2 eV blue-shift intrinsic to the RI-CC2 method and the smaller basis set compared to the benchmark reference are considered.[34] We therefore regard this as the locally excited (LE) state that is accessed by the 465 nm excitation in the transient absorption measurements. The S_3 and the S_4 state in both systems are characterized by an excitation from an orbital (HOMO-1, π_S, Fig. S20 in the ESI†) which is mostly localized on the phenyl spacer. The S_3 state has a charge transfer character exhibiting a low oscillator strength and is described by a transition to the LUMO+1 (π_{2D}^*). We denote this state as the dark charge transfer state, d-CT. In contrast the S_4 state has a charge transfer character with sizeable oscillator strength characterized by a transition to the LUMO (π_{1D}^*). This state is denoted as the bright charge transfer state, b-CT.

Table 2 CC2 vertical excitation energies (ΔE) and oscillator strengths (f) of the donor–spacer systems D–(Me4-Ph) and D–(Ph) at the MP2-optimized ground-state equilibrium geometries (LE, locally excited state; d-CT, dark charge transfer state; and b-CT, bright charge transfer state). The calculated energies are compared with the experimental absorption maxima of D–(Me4-Ph) and D–(Ph) in $CHCl_3$

		D–(Me4-Ph)		D–(Ph)	
Transition	Character	ΔE (eV)	f	ΔE (eV)	f
$S_0 \rightarrow S_1$	$\pi_D \rightarrow \pi_{2D}^*$	2.99	0.001	2.99	0.004
$S_0 \rightarrow S_2$	$\pi_D \rightarrow \pi_{1D}^*$ (LE)	3.07	0.545	3.07	0.542
$S_0 \rightarrow S_3$	$\pi_S \rightarrow \pi_{2D}^*$ (d-CT)	3.56	0.006	3.48	0.024
$S_0 \rightarrow S_4$	$\pi_S \rightarrow \pi_{1D}^*$ (b-CT)	3.70	0.548	3.64	0.574
Exp.	—	**2.66**	—	**2.66**	—

Geometry optimizations for the LE, d-CT and b-CT states were carried out using the CC2 method. During the optimizations the electronic character of the adiabatic states changes. Therefore both, the state number and the current electronic character are given *e.g.* S_1(LE). For both donor spacer systems optimization of the LE state (S_2 state at the FC-point) lowers its energy below the S_1 state and leads to similar local minima with $\pi\pi^*$ character (S_1(LE), Fig. 5, denoted as π-Min), exhibiting minor structural changes, mainly bond length rearrangements in the B-PDI chromophore and a small change in the torsional angle α from 67.4° to 66.3°, respectively from 48° to 45.7°. Consequently, the calculated oscillator strengths for the transition to the ground state are almost unchanged from the FC points ($f = 0.571/0.570$, Table S2 in the ESI†). We ascribe the long lived 1.3 ns fluorescence observed for D–(Me4-Ph) to the emission from this π-Min.

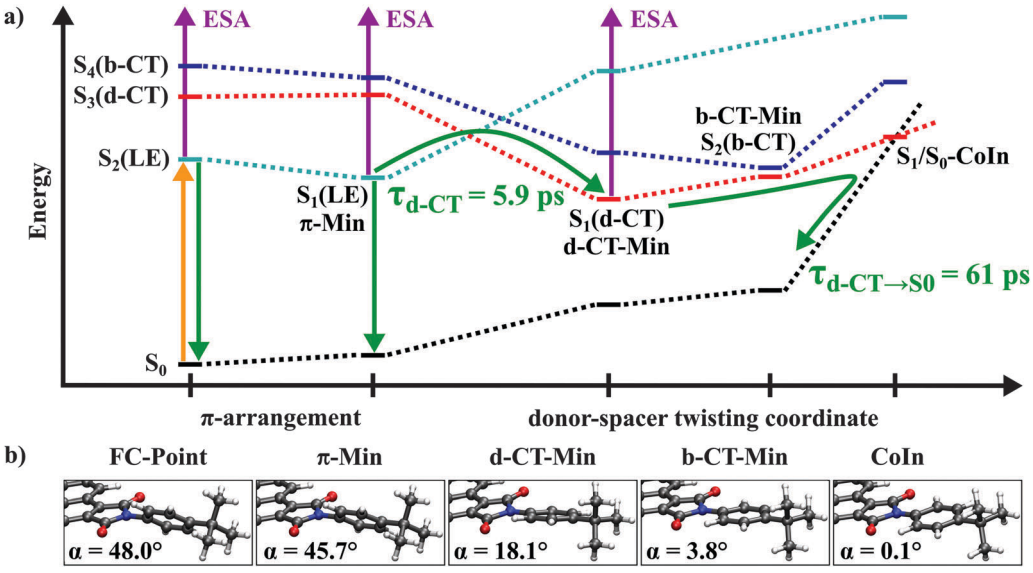

Fig. 5 (a) Scheme of the state energies involved in the CT process of the donor–spacer system D–(Ph). Solid arrows indicate optical transitions and dotted lines visualize the different diabatic courses conserving the electronic character (black: ground state; cyan: LE, locally excited state; red: d-CT, dark charge transfer state; and blue: b-CT, bright charge transfer state). The adiabatic states are indicated by the state number with the current electronic character given in parenthesis. (b) Minimum energy geometries for the relevant states (FC, Franck–Condon; CoIn, Conical Intersection). The shown angle α is the torsion angle between the B-PDI donor and the phenyl spacer.

For D–(Me4-Ph) the optimization of the d-CT and b-CT states leads to excited state minima that are much higher in energy than the FC point accessed by the optical excitation. In the case of D–(Ph) optimization of the d-CT state (S_3 state at the FC-point) leads to the global minimum (d-CT-Min) on the S_1 potential energy surface (Fig. 5). This minimum lies 0.4 eV lower than the π-Min and is associated with a large decrease of the angle α to 18.1°. This rotation energetically shifts the spacer orbital π_S above the donor orbital π_D. Thus the global minimum is of CT character with an oscillator strength of 0.003. It results from an electron transfer from the spacer to the maleimide ring of the donor. Therewith it confirms the assumption about the origin of the experimental time constants of D–(Ph) made in Section 2.4.

The large stabilization of the excited d-CT state is accompanied by a considerable destabilization of the ground state. Both states are separated by only 1.56 eV at the d-CT Min. Further rotation of the phenyl ring to a torsional angle α of 0.1° leads to a conical intersection between the d-CT state and the ground state. As the single reference CC2 method breaks down when two electronic states get energetically close to each other, the conical intersection was optimized using the CASSCF method and found to be accessible from the FC point. This explains the fast picosecond backward electron transfer dynamics to the ground state (see Table S3 in the ESI† for details).

CC2 optimization of the b-CT state (S_4 state at the FC-point) in D–(Ph) yields a minimum on the S_2 potential energy surface (b-CT-Min, Fig. 5). The associated structural change is a rotation of the spacer decreasing the angle α to 3.8° (Fig. 5). The electronic structure is characterized by a charge transfer from the spacer to the donor and has a significant oscillator strength of 0.192. At this point the energy difference between the S_2(b-CT) and S_1(d-CT) states is only 0.1 eV. A conical intersection between the two states can be located in the vicinity of the b-CT-Min (Table S3 in the ESI†). Consequently even if the b-CT state in D–(Ph) is populated by relaxation from the π-Min it is quickly depopulated due to this conical intersection.

The theoretical results on the donor spacer systems reveal the existence of a bright charge transfer state which, however, does not seem to play a significant role in their excited state dynamics. This state however may become important for the observed energy transfer in the complete D–(Ph-BCO-Ph)–A dyad. With the focus on this bright charge transfer state we have carried out quantum chemical calculations on the donor–spacer–acceptor dyad D–(Ph-BCO-Ph)–A. Due to the large size of the D–(Ph-BCO-Ph)–A dyad geometry optimizations were carried out using the DFT and TDDFT method with the B3LYP[35] and the CAM-B3LYP functional,[36] respectively. Excitation energies and oscillator strengths at these geometries were then determined using the more robust and qualitatively correct CC2 method. This strategy of combining TDDFT optimized geometries with CC2 single-point calculations was successfully employed for other large molecules.[37–40]

The ground state geometry optimization results in a structure where the spacer (Ph-BCO-Ph) as well as the acceptor is rotated with respect to the B-PDI donor (Fig. 6). The torsional angle α between the phenyl ring of the spacer and the donor is 43.3° and 31.9° between the acceptor and donor. The first excited state is a bright ππ* transition and is localized on the acceptor (Table 3). The CC2 excitation energy of 2.80 eV compares well with the experimental absorption maximum of

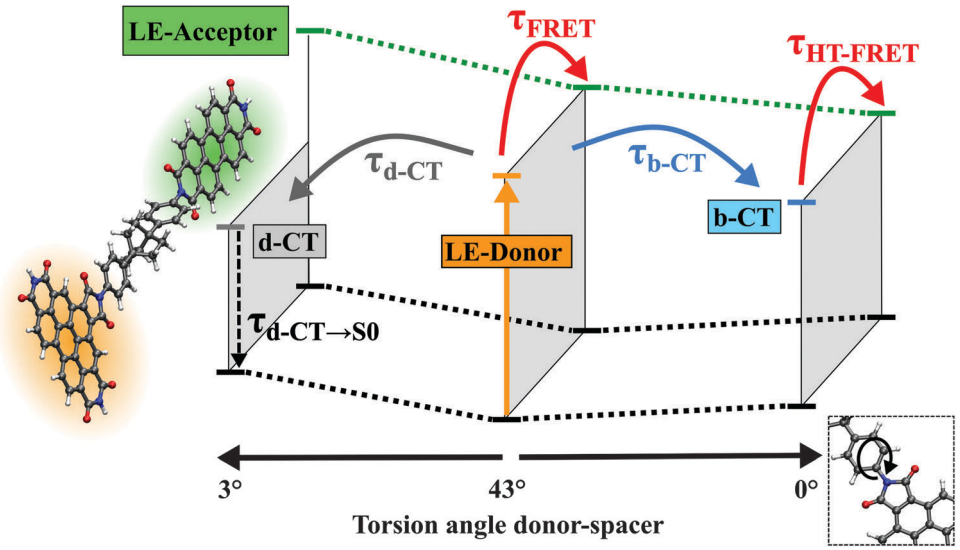

Fig. 6 Scheme of the coupled hole-transfer FRET mechanism of the donor–spacer–acceptor dyad D–(Ph-BCO-Ph)–A. Arrows indicate the different processes with the corresponding time constants occurring after optical excitation of the B-PDI donor. Horizontal and dotted lines visualize the different electronic states and potential energy surfaces (black: ground state; orange: LE-donor, locally excited donor state; gray: d-CT, dark charge transfer state; blue: b-CT, bright charge transfer state; and green: LE-acceptor, locally excited acceptor state). The d-CT and b-CT excited state minimum geometries are associated with a rotation of the spacer and a decrease of the torsional angle between the B-PDI donor and the first phenyl ring of the spacer to 3° respectively 0°.

Table 3 CC2 vertical excitation energies (ΔE) and oscillator strengths (f) of the donor spacer acceptor dyad D–(Ph-BCO-Ph)–A at the B3LYP-optimized ground-state equilibrium geometry (LE_A, locally excited acceptor state; LE_D, locally excited donor state; d-CT, dark charge transfer state; and b-CT, bright charge transfer state). The calculated energies are compared with the experimental absorption maximum of the donor chromophore (B-PDI) within D–(Ph-BCO-Ph)–A dissolved in $CHCl_3$

		D–(Ph-BCO-Ph)–A	
Transition	Character	ΔE (eV)	f
$S_0 \rightarrow S_1$	$\pi_A \rightarrow \pi_A^*$ (LE_A)	2.80	1.024
$S_0 \rightarrow S_2$	$\pi_D \rightarrow \pi_{2D}^*$	3.03	0.008
$S_0 \rightarrow S_3$	$\pi_D \rightarrow \pi_{1D}^*$ (LE_D)	3.13	0.586
$S_0 \rightarrow S_4$	$\pi_S \rightarrow \pi_{2D}^*$ (d-CT)	3.46	0.036
$S_0 \rightarrow S_5$	$\pi_S \rightarrow \pi_{1D}^*$ (b-CT)	3.54	0.715
Exp.	—	**2.66**	—

(Ph)–A at 2.35 eV (527 nm) in $CHCl_3$ taking the blue-shift corrections into account.[34] We therefore regard this as the locally excited (LE_A) state of the acceptor which is populated by the energy transfer. The next four vertical transitions are localized on the donor–spacer moiety and are identical in character and comparable in energy and oscillator strength to those found in the donor–spacer systems D–(Me4-Ph) and D–(Ph). The dark $\pi\pi^*$ transition in the dyad is now the S_2 state while the S_3 state is the locally excited (LE_D) donor state with bright $\pi\pi^*$ character and accessed by optical excitation. The S_4 and the S_5 states are the d-CT and the b-CT states. The spacer orbital π_S that contributes to the d-CT and b-CT states is mainly located on the phenyl ring attached to the donor (Fig. S21 in the ESI†) and is thus similar to the spacer orbital π_S of the donor–spacer systems D–(Me4-Ph) and D–(Ph).

Geometry optimization of the LE_D state (S_3 state at the FC-point) leads likely for the small subsystems to a local S_1 state minimum with $\pi\pi^*$ character requiring minor structural changes (denoted as π-Min). Here the LE_D state is almost isoenergetic to the bright LE_A state of the acceptor (S_2 state). Consequently at this π-Min direct energy transfer from the donor to the acceptor can occur *via* noise induced FRET. This theoretical result confirms the initial rise of the spectral signatures of the PDI energy acceptor observed in the transient measurements.

Optimization of the d-CT state (S_4 state at the FC-point) leads likely in D–(Ph) to the global minimum on the S_1 potential energy surface associated with a decrease of the torsional angle α to 3.0° (Fig. 6). Optimization of the b-CT state (S_5 state at the FC-point) leads to a third minimum on the S_1 potential energy surface with a torsional angle α of 0.5°. The b-CT state in the dyad is more stabilized than in the donor–spacer system D–(Ph) and becomes the S_1 state. Now the d-CT state is 0.3 eV higher in energy at the b-CT-Min and consequently no fast depopulation from the b-CT to the d-CT state can occur unlike in D–(Ph). Furthermore in the dyad the S_1(b-CT) state at the b-CT-Min is nearly isoenergetic to the $S_2(LE_A)$ acceptor state. Since the transition dipole moments of the b-CT and LE_A states are parallel to each other, an energy transfer from the donor to the acceptor should be possible *via* multipole–multipole interactions. This energy transfer denoted coupled hole-transfer FRET and enabled by a bright charge transfer state will be discussed in detail in the next section.

4 Discussion and conclusion: the transfer mechanism is a coupled hole-transfer-FRET

The experimental results of Section 2 indicate that for suitable spacers ultrafast electron transfer (ET) is found. The spacer is located between an optically excited B-PDI chromophore that energetically can act as an energy donor and PDI as a potential acceptor. According to established thinking this ET would compete with the through space energy transfer and lower its efficiency dramatically. The quantum chemical calculations of Section 3 and the very good agreement between the experimental and calculated transition energies are now used to derive a detailed picture of the mechanism behind the efficient energy transfer process observed in D–(Ph-BCO-Ph)–A. We will argue that the electron transfer between the spacer and the B-PDI donor does actually not lead to a loss of the energy stored in the bright LE_D donor state as confirmed by the overall energy transfer efficiency. The involvement of the spacer as an intermediate energy storage unit in energy transfer in a donor–spacer–acceptor system has already been postulated.[41]

Starting with the donor–spacer subsystems D–(Ph) and D–(Me4-Ph) the following excited state mechanism arises (see Fig. 5): after electronic excitation into the S_2(LE) state both molecules relax into the S_1(LE) state π-Min within a few 100 fs (time constant τ_1 in Table 1). While D–(Me4-Ph) relaxes back into the ground state from the π-Min *via* fluorescence with τ_{fluo} = 1.3 ns and moderate internal conversion, D–(Ph) undergoes fluorescence quenching by accessing the d-CT-Min on the S_1 potential energy surface with τ_{CT} = 5.9 ps. This process is associated with a rotation of the phenyl spacer into the plane of the B-PDI chromophore. A quite similar fluorescence quenching mechanism has already been observed for PDI-based donor–spacer systems.[42] In D–(Me4-Ph) the rotation is sterically inhibited by the bulky methyl groups on the spacer. This also explains why for the dyad D–(Me4-Ph)–A with the same spacer near-unity fluorescence quantum yield and no fluorescence quenching electron transfer is observed. Furthermore this illustrates the crucial role of the spacer on the energy and electron transfer as also investigated for other donor–spacer–acceptor systems.[12,15,43–55] From the d-CT-Min, D–(Ph) reaches a S_1/S_0 conical intersection and relaxes back into the ground state with $\tau_{d\text{-}CT \rightarrow S0}$ = 61 ps.

In the case of D–(Ph-BCO-Ph)–A electronic excitation into the S_3(LE) donor state also leads to a relaxation into the donor $S_1(LE_D)$ state π-Min within a few 100 fs. From this minimum a small part of the molecules undergoes direct noise-induced FRET to the nearly isoenergetic $S_2(LE_A)$ acceptor state with τ_{FRET}. A second part accesses the d-CT-Min on the S_1 potential energy surface *via* rotation of the whole spacer–acceptor moiety with $\tau_{d\text{-}CT}$. This motion aligns the planes of the B-PDI chromophore, the phenyl ring attached to the B-PDI chromophore and

the PDI acceptor to each other. The remaining third part of the molecules accesses the b-CT-Min with $\tau_{b\text{-}CT}$, which is also located on the S_1 potential energy surface and associated with a rotation of the whole spacer–acceptor moiety into the plane of the B-PDI chromophore. These three processes occur with an overall time constant of $\tau_2 = (1/\tau_{FRET} + 1/\tau_{d\text{-}CT} + 1/\tau_{b\text{-}CT})^{-1} = 5$ ps. In the donor–spacer system D–(Ph) the b-CT-Min is located on the S_2 potential energy surface and isoenergetic to the π-Min of the S_1(LE) state. Thus the population of this state does not lead to any energy stabilization of the system, in contrast to D–(Ph-BCO-Ph)–A, where the b-CT-Min is on the S_1 potential energy surface and lies 0.15 eV below the $S_1(LE_D)$ state π-Min. Furthermore in D–(Ph) the conical intersection in the vicinity of the b-CT-Min leads to a fast population transfer from the b-CT to the d-CT state. For these reasons the b-CT state does not get populated in D–(Ph), while in D–(Ph-BCO-Ph)–A it does. In the D–(Ph-BCO-Ph)–A dyad, the b-CT-Min is nearly isoenergetic to the $S_2(LE_A)$ state of the acceptor. Since the transition dipole moments of the b-CT and LE_A acceptor states are parallel to each other, an efficient energy transfer from the donor to the acceptor occurs *via* multipole–multipole interactions with $\tau_{HT\text{-}FRET}$. The part of the molecules that have populated the d-CT state undergo backward electron transfer without transferring energy to the acceptor with $\tau_{d\text{-}CT \rightarrow S0}$, as here the LE_A state of the acceptor is 0.78 eV higher in energy and the d-CT state has negligible oscillator strength. These two processes occur with an overall time constant $\tau_3 = (1/\tau_{HT\text{-}FRET} + 1/\tau_{d\text{-}CT \rightarrow S0})^{-1} =$ 45 ps. The excited PDI acceptor finally relaxes back into the ground state *via* fluorescence with a time constant $\tau_{Fluo} = 3.3$ ns.

The *ab initio* calculations show that the hole-transfer induced FRET mechanism is also present in the molecules D–(Ph-Yn2-Ph)–A, D–(Ph-Yn-Ph)–A and D–(Ph-Ph)–A, even though the spacer is an aromatic π system without an aliphatic Dexter blocker. Geometry optimizations show that in the ground state equilibrium structures the π-planes of the donor, spacer and acceptor have significant torsional angles to each other, which breaks any donor–spacer–acceptor π-conjugation. At the ground state equilibrium structures we find the same states (LE_A, LE_D, d-CT and b-CT) and energetic ordering of them (Tables S5 and S6 in the ESI†) as in D–(Ph-BCO-Ph)–A. Furthermore excited state geometry optimizations locate the same three excited state minima on the S_1 potential energy surface (LE_D donor π-Min, the d-CT and b-CT minima) responsible for the HT-FRET. As the b-CT state has a significant oscillator strength at its minimum, one could expect to observe this state in the time resolved fluorescence measurements on D–(Ph-Yn2-Ph)–A (Fig. 1b). The calculated fluorescence energy at the b-CT minimum is 2.58 eV (Table S6 in the ESI†). Taking into account the blue-shift of *ca.* 0.4 eV (between theory and experiment, see also Tables 2 and 3) leads to a fluorescence energy of 2.18 eV (569 nm) overlapping with the strong fluorescence of the acceptor (Fig. 1b). Thus it cannot be discriminated in the time-resolved fluorescence measurements. Also one could expect to see the b-CT state in the stationary absorption spectrum. But again, the calculations show that the absorption band of the b-CT state is overlaid by the strong donor absorption bands. For example in D–(Ph-Yn2-Ph)–A the calculated excitation energy into the b-CT (S_5) state including the blue-shift amounts to 3.44 eV, *i.e.* 360 nm. Comparison with the measured absorption spectrum shown in Fig. S2c (ESI†) reveals the existence of donor absorption bands in this region.

For the through-bond Dexter energy transfer to be active in the dyads with the polyyne spacers significant orbital overlap either directly between the donor and acceptor or indirectly *via* the spacer would be required.[56,57] No states delocalized over the whole donor–spacer–acceptor π-system, required for the direct donor–acceptor orbital overlap, could be found in the calculations. For the indirect overlap the required donor–spacer and spacer–acceptor charge transfer states are too far apart in energy for an effective coupling. The energetically lowest spacer–acceptor charge transfer states are at least 1 eV above the d-CT or b-CT states in all dyads with the polyyne spacers, *i.e.* D–(Ph-Yn2-Ph)–A, D–(Ph-Yn-Ph)–A and D–(Ph-Ph)–A.

From the theoretical results we conclude that the experimentally observed τ_2 and τ_3 time constants (see Table 1) are composed of several branching processes. That τ_2 originating from three processes ($\tau_2 = (1/\tau_{FRET} + 1/\tau_{d\text{-}CT} + 1/\tau_{b\text{-}CT})^{-1}$) can also be observed experimentally. The existence of the direct noise induced energy transfer pathway τ_{FRET} is seen in an initial rise of the fluorescence or the GSB, SE and ESA of the PDI energy acceptor. The pathways for $\tau_{d\text{-}CT}$ and $\tau_{b\text{-}CT}$ are observed in the rise of the GSB of the spacer and the rise of the CT ESA bands characterised by the thus formed B-PDI anion. For the dyads D–(Ph-Yn2-Ph)–A, D–(Ph-Yn-Ph)–A and D–(Ph-Ph)–A we know the direct energy transfer time constants τ_{FRET} from the analogous systems D–(Py-Yn2-Py)–A, D–(Py-Yn-Py)–A and D–(Py-Ph)–A, where the donor–acceptor distance is the same but no electron transfer from the spacer to the B-PDI energy donor occurs (see Chart S1 and Table S1 in the ESI†). The near-unity fluorescence quantum yield of the PDI energy acceptor obtained by excitation of the energy donor shows that in these dyads no non-radiative process effectively competes with the noise-induced FRET. The quantum yield for the direct noise induced FRET ($\phi_{FRET} = k_{FRET}/k_2$) is thus 21%, 7% and 9% for D–(Ph-Ph)–A, D–(Ph-Yn-Ph)–A and D–(Ph-Yn2-Ph)–A. Comparing these values with the measured fluorescence quantum yields in Table 1 shows that the direct noise induced FRET has only a minor contribution to the overall energy transfer and that the major part comes from the coupled HT-FRET mechanism. Using $\phi_{HT\text{-}FRET} = \phi_{Fluo} - \phi_{FRET}$ we obtain 37% for D–(Ph-Ph)–A, 26% for D–(Ph-Yn2-Ph)–A and 44% for D–(Ph-Yn-Ph)–A. For the dyad D–(Ph-BCO-Ph)–A we do not know the time constant for the direct noise induced FRET as the synthesis of an analogous system where the phenyl rings are replaced by pyridine rings is challenging and still in progress. As the donor–acceptor distance for D–(Ph-BCO-Ph)–A of 26 Å is comparable to that of D–(Py-Yn2-Py)–A, we envision that the coupled HT-FRET contributes to a similar extent to the overall energy transfer and is the major contributor just like in the dyads with the polyyne spacers.

One can determine the quantum yield for the coupled HT-FRET process over a second route. We know that the near-unity quantum yield cannot be achieved using the HT-FRET process as it competes with the relaxation of the d-CT state to the

ground state. For D–(Ph-BCO-Ph)–A we can determine the components of $\tau_{\text{HT-FRET}} = (1/\tau_3 - 1/\tau_{\text{d-CT}\rightarrow\text{S0}})^{-1}$ as we know $\tau_{\text{d-CT}\rightarrow\text{S0}}$ from D–(Ph), which is chemically most comparable to the donor–spacer moiety of the D–(Ph-BCO-Ph)–A dyad. We obtain that $\tau_{\text{TH-FRET}}$ = 172 ps. The quantum yield for the pure coupled HT-FRET process thus would amount to $\phi_{\text{HT-FRET}} = k_{\text{HT-FRET}}/k_3$ = 26%.

The coupled HT-FRET process is the major contributor to the energy transfer process that takes place in the perylene diimide dyads investigated in this work. Since this process is mediated by the bright charge transfer state on the donor–spacer moiety, one would expect solvent effects. The measurements on D–(Ph-Yn2-Ph)–A in benzonitrile confirms this expectation. We do find significant changes compared to the chloroform solution. In the ultrafast dynamics investigated solvent effects on the charge transfer dynamics and the resulting energy transfer are highly complex as they depend on the interplay of refractive index, polarity, viscosity and solvation dynamics of the solvent.[21,30,31] A systematic investigation of this issue is thus beyond the scope of this paper taking also into account the complex synthetic routes and the resulting limited availability of the substances.

Energy transfer from states with high charge transfer character has recently been invoked in order to explain the inverse Förster behaviour observed in pyrene-borondipyrromethene dyads[33] or anthracenyl-borondipyrromethene dyads.[58] The perylene diimide model systems investigated here have shown for the first time by direct experimental observation that a bright charge transfer state can indeed act as an energy donor. We envision that the resulting HT-FRET mechanism mediated by these bright charge transfer states can find applications in artificial photosynthetic systems as well as solar cells. So far in these systems the conversion of light into chemical or electric energy is based on the coupling between energy and electron transfer.[59–61] In these chromophoric systems the energy transfer induces an electron transfer, which then causes the desired charge separation. Chromophoric systems with engineered bright charge transfer states allow one to invert the order of these processes.

Acknowledgements

Financial support of this work by Deutsche Forschungsgemeinschaft through the SFB 749 and the excellence cluster 'Munich Center for Advanced Photonics' (MAP) is gratefully acknowledged. We thank F. Graupner for valuable help with the streak camera recordings and A. Walter for the B-PDI-(Null)-PDI synthesis. We also thank P. Schneider for his contribution in the recording of the transient absorption spectra and P. Hummel for his contribution in the analysis of the data.

References

1 T. Förster, *Ann. Phys.*, 1948, **437**, 55–75.
2 G.-S. Jiao, L. H. Thoresen and K. Burgess, *J. Am. Chem. Soc.*, 2003, **125**, 14668–14669.
3 R. Bandichhor, A. D. Petrescu, A. Vespa, A. B. Kier, F. Schroeder and K. Burgess, *J. Am. Chem. Soc.*, 2006, **128**, 10688–10689.
4 W. Lin, L. Yuan, Z. Cao, Y. Feng and J. Song, *Angew. Chem.*, 2010, **122**, 385–389.
5 T. G. Kim, J. C. Castro, A. Loudet, J. G.-S. Jiao, R. M. Hochstrasser, K. Burgess and M. R. Topp, *J. Phys. Chem. A*, 2006, **110**, 20–27.
6 Y.-J. Gong, X.-B. Zhang, C.-C. Zhang, A.-L. Luo, T. Fu, W. Tan, G.-L. Shen and R.-Q. Yu, *Anal. Chem.*, 2012, **84**, 10777–10784.
7 D. L. Dexter, *J. Chem. Phys.*, 1953, **21**, 836–850.
8 A. Osuka, N. Tanabe, S. Kawabata, I. Yamazaki and Y. Nishimura, *J. Org. Chem.*, 1995, **60**, 7177–7185.
9 D. Beljonne, C. Curutchet, G. D. Scholes and R. J. Silbey, *J. Phys. Chem. B*, 2009, **113**, 6583–6599.
10 D. Beljonne, G. Pourtois, C. Silva, E. Hennebicq, L. M. Herz, R. H. Friend, G. D. Scholes, S. Setayesh, K. Müllen and J. L. Brédas, *Proc. Natl. Acad. Sci. U. S. A.*, 2002, **99**, 10982–10987.
11 R. Métivier, F. Nolde, K. Müllen and T. Basché, *Phys. Rev. Lett.*, 2007, **98**, 047802.
12 B. Fückel, A. Köhn, M. E. Harding, G. Diezemann, G. Hinze, T. Basché and J. Gauss, *J. Chem. Phys.*, 2008, **128**, 074505.
13 A. Harriman, L. Mallon and R. Ziessel, *Chem. – Eur. J.*, 2008, **14**, 11461–11473.
14 C. Y. Wong, C. Curutchet, S. Tretiak and G. D. Scholes, *J. Chem. Phys.*, 2009, **130**, 081104.
15 B. Albinsson and J. Mårtensson, *Phys. Chem. Chem. Phys.*, 2010, **12**, 7338–7351.
16 J. Megow, B. Röder, A. Kulesza, V. Bonačić-Koutecký and V. May, *ChemPhysChem*, 2011, **12**, 645–656.
17 J. M. Anna, G. D. Scholes and R. van Grondelle, *BioScience*, 2014, **64**, 14–25.
18 G. D. Scholes, G. R. Fleming, A. Olaya-Castro and R. van Grondelle, *Nat. Chem.*, 2011, **3**, 763–774.
19 H. Langhals, A. J. Esterbauer, A. Walter, E. Riedle and I. Pugliesi, *J. Am. Chem. Soc.*, 2010, **132**, 16777–16782.
20 P. Nalbach, I. Pugliesi, H. Langhals and M. Thorwart, *Phys. Rev. Lett.*, 2012, **108**, 218302.
21 L. Flamigni, B. Ventura, A. Barbieri, H. Langhals, F. Wetzel, K. Fuchs and A. Walter, *Chem. – Eur. J.*, 2010, **16**, 13406–13416.
22 G. Ryseck, T. Schmierer, K. Haiser, W. Schreier, W. Zinth and P. Gilch, *ChemPhysChem*, 2011, **12**, 1880–1888.
23 S. Kalinin, M. Speckbacher, H. Langhals and L. B.-Å. Johansson, *Phys. Chem. Chem. Phys.*, 2001, **3**, 172–174.
24 U. Megerle, I. Pugliesi, C. Schriever, C. F. Sailer and E. Riedle, *Appl. Phys. B: Lasers Opt.*, 2009, **96**, 215–231.
25 R.-J. Kutta, T. Langenbacher, U. Kensy and B. Dick, *Appl. Phys. B: Lasers Opt.*, 2013, **111**, 203–217.
26 P. Fita, E. Luzina, T. Dziembowska, Cz. Radzewicz and A. Grabowska, *J. Chem. Phys.*, 2006, **125**, 184508.
27 J. Salbeck, H. Kunkely, H. Langhals, R. W. Saalfrank and J. Daub, *Chimia*, 1989, **43**, 6–9.
28 A. Ishitani and S. Nagakura, *Mol. Phys.*, 1967, **12**, 1–12.

29 M. L. Horng, J. A. Gardecki, A. Papazyan and M. Maroncelli, *J. Phys. Chem.*, 1995, **99**, 17311–17337.
30 U. Schmidhammer, U. Megerle, S. Lochbrunner, E. Riedle and J. Karpiuk, *J. Phys. Chem. A*, 2008, **112**, 8487–8496.
31 I. Pugliesi, P. Krok, S. Lochbrunner, A. Błaszczyk, C. von Hänisch, M. Mayor and E. Riedle, *J. Phys. Chem. A*, 2010, **114**, 12555–12560.
32 I. Pugliesi, U. Megerle, S.-L. Suraru, F. Würthner, E. Riedle and S. Lochbrunner, *Chem. Phys. Lett.*, 2011, **504**, 24–28.
33 D. Bai, A. C. Benniston, J. Hagon, H. Lemmetyinen, N. V. Tkachenko and R. W. Harrington, *Phys. Chem. Chem. Phys.*, 2013, **15**, 9854–9861.
34 N. O. C. Winter, N. K. Graf, S. Leutwyler and C. Hättig, *Phys. Chem. Chem. Phys.*, 2013, **15**, 6623–6630.
35 A. D. Becke, *J. Chem. Phys.*, 1993, **98**, 5648–5652.
36 T. Yanai, D. P. Tew and N. C. Handy, *Chem. Phys. Lett.*, 2004, **393**, 51–57.
37 K. Sadeghian, M. Bocola and M. Schütz, *J. Am. Chem. Soc.*, 2008, **130**, 12501–12513.
38 K. Sadeghian, M. Bocola and M. Schütz, *Phys. Chem. Chem. Phys.*, 2010, **12**, 8840–8846.
39 T. Merz, K. Sadeghian and M. Schütz, *Phys. Chem. Chem. Phys.*, 2011, **13**, 14775–14783.
40 T. Merz and M. Schütz, in *Chemical Photocatalysis*, ed. B. König, De Gruyter, Berlin, 2013, vol. 1, ch. 14, p. 263.
41 G. Duvanel, J. Grilj and E. Vauthey, *J. Phys. Chem. A*, 2013, **117**, 918–928.
42 M. W. Holman, P. Yan, K.-C. Ching, R. Liu, F. I. Ishak and D. M. Adams, *Chem. Phys. Lett.*, 2005, **413**, 501–505.
43 J.-S. Hsiao, B. P. Krueger, R. W. Wagner, T. E. Johnson, J. K. Delaney, D. C. Mauzerall, G. R. Fleming, J. S. Lindsey, D. F. Bocian and R. J. Donohoe, *J. Am. Chem. Soc.*, 1996, **118**, 11181–11193.
44 W. B. Davis, M. A. Ratner and M. R. Wasielewski, *J. Am. Chem. Soc.*, 2001, **123**, 7877–7886.
45 W. B. Davis, M. A. Ratner and M. R. Wasielewski, *Chem. Phys.*, 2002, **281**, 333–346.
46 T. K. Ahn, Z. S. Yoon, I.-W. Hwang, J. K. Lim, H. Rhee, T. Joo, E. Sim, S. K. Kim, N. Aratani, A. Osuka and D. Kim, *J. Phys. Chem. B*, 2005, **109**, 11223–11230.
47 S. Wallin, L. Hammarström, E. Blart and F. Odobel, *Photochem. Photobiol. Sci.*, 2006, **5**, 828–834.
48 A. C. Benniston and A. Harriman, *Chem. Soc. Rev.*, 2006, **35**, 169–179.
49 B. Albinsson, M. P. Eng, K. Pettersson and M. U. Winters, *Phys. Chem. Chem. Phys.*, 2007, **9**, 5847–5864.
50 O. S. Wenger, *Chem. Soc. Rev.*, 2011, **40**, 3538–3550.
51 M. A. H. Alamiry, J. P. Hagon, A. Harriman, T. Bura and R. Ziessel, *Chem. Sci.*, 2012, **3**, 1041–1048.
52 C. Schubert, M. Wielopolski, L.-H. Mewes, G. de Miguel Rojas, C. van der Pol, K. C. Moss, M. R. Bryce, J. E. Moser, T. Clark and D. M. Guldi, *Chem. – Eur. J.*, 2013, **19**, 7575–7586.
53 M. Natali, S. Campagna and F. Scandola, *Chem. Soc. Rev.*, 2014, **43**, 4005–4018.
54 L. G. Heinz, O. Yushchenko, M. Neuburger, E. Vauthey and O. S. Wenger, *J. Phys. Chem. A*, 2015, **119**, 5676–5684.
55 M. Gilbert and B. Albinsson, *Chem. Soc. Rev.*, 2015, **44**, 845–862.
56 G. D. Scholes, *Annu. Rev. Phys. Chem.*, 2003, **54**, 57–87.
57 J. Otsuki, Y. Kanazawa, A. Kaito, D.-M. S. Islam, Y. Araki and O. Ito, *Chem. – Eur. J.*, 2008, **14**, 3776–3784.
58 D. Bai, A. C. Benniston, J. Hagon, H. Lemmetyinen, N. V. Tkachenko, W. Clegg and R. W. Harrington, *Phys. Chem. Chem. Phys.*, 2012, **14**, 4447–4456.
59 G. Kodis, P. A. Liddell, L. de la Garza, P. C. Clausen, J. S. Lindsey, A. L. Moore, T. A. Moore and D. Gust, *J. Phys. Chem. A*, 2002, **106**, 2036–2048.
60 M. H. Stewart, A. L. Huston, A. M. Scott, E. Oh, W. Russ Algar, J. R. Deschamps, K. Susumu, V. Jain, D. E. Prasuhn, J. Blanco-Canosa, P. E. Dawson and I. L. Medintz, *ACS Nano*, 2013, **7**, 9489–9505.
61 H.-W. Wang, M.-Y. Yeh, C.-H. Chen, T.-S. Lim, W. Fann and T.-Y. Luh, *Macromolecules*, 2008, **41**, 2762–2770.

3.2. Solvent effects on the electron and energy transfer

In the previous section a new energy transfer mechanism, termed as hole-transfer induced FRET, was elucidated for the perylene diimide dyads. Since this process is mediated by a bright charge transfer state, it should be strongly influenced by the used solvent. All presented experimental results up to here were derived from measurements in the solvent chloroform. To investigate the solvent effects, additional experiments for one representative dyad with a phenyl spacer (D-(Ph-Yn2-Ph)-A) were performed in benzonitrile [121]. Benzonitrile was chosen because the dyads are soluble in this solvent and the dielectric constant ϵ is 25.2 for benzonitrile as compared to 4.8 for chloroform.

Generally, the measurements in benzonitrile leads to similar energy transfer dynamics. The higher polarity of benzonitrile could be expected to stabilize the charge transfer state in a way that the energy is trapped and no subsequently energy transfer to the acceptor occurs. This is just partly valid as the overall energy transfer is only decreased. In addition, the energy transfer dynamics are slowed down in benzonitrile. This can be explained by the increased solvation time of 5.1 ps for benzonitrile in comparison to 2.8 ps for chloroform. The increased solvation time could also be an explanation for the still occurring energy transfer as perhaps the energy just cannot be trapped fast enough.

To have a closer look at the effects of the solvent polarity and solvation time on the charge transfer dynamics, two additional modified perylene diimides were investigated. The molecules were synthesized in the group of Heinz Langhals and have been studied by transient spectroscopy in the group of Eberhard Riedle. These compounds are analog to the donor-spacer systems of section 3.1 subsystems of the investigated dyads. The first one is the pure perylene diimide chromophore with alkyl chains at the N-termini to increase the solubility and is denoted as PDI-19 (see fig. 1, page 45). In the second molecule, termed as PDI-13-N, one alkyl chain is substituted by an electron donating amino group. While the fluorescence quantum yield of PDI-19 is close to unity, for PDI-13-N only a very weak fluorescence is observed which is proposed to be quenched by a charge transfer state [117, 124]. This indicates that these compounds are the right candidates to investigate the solvent effects on the charge transfer states. Moreover, as these systems are of moderate size and significantly smaller than the molecules of section 3.1, they could be studied with the highly correlated CASPT2 method. Additionally, the solvent effects were incorporated by the state-specific approach in combination with non-equilibrium calculations allowing the discrimination between the fast and slow response of the solvent [52]. As this model combination is presently not within the scope of the CASPT2 level of theory, the TDDFT method was used for the PCM calculations describing the solvent in an implicit way (for details see section 1.1). The TDDFT/PCM approach has been shown to provide quite reliable results [125–127] and for the studied systems the TDDFT results of the gas phase are in good agreement with the CASPT2 calculations.

The experimental and theoretical results of the two systems PDI-19 and PDI-13-N are presented in the manuscript "Ultrafast emission quenching in a perylene diimide by structure rearrangement induced electron transfer from its substituent". The major conclusions are as follows:

- The relaxation of both photoexcited molecules leads to a local minimum with $\pi\pi^*$ character (π-Min). The 4 ns fluorescence of the PDI-19 system happens from this stable π-Min and consequently no dynamics in the sub-nanosecond time region are observed.

- In contrast, PDI-13-N exhibits ultrafast dynamics on a sub-picosecond timescale, caused by a fluorescence quenching electron transfer from the amino substituent to the PDI chromophore. The transfer is made possible by geometrical deformations in the substituent which facilitate the dynamic population of a charge transfer state. In the proximity of the corresponding charge transfer minimum (CT-Min) a conical intersection with the ground state enables the

fast back electron transfer. The electron transfer dynamics of PDI-13-N are therewith similar to the ones observed in the dyads with phenyl spacers of section 3.1.

- Experiments in different solvents show that the quenching dynamics in PDI-13-N accelerate from chloroform over DMSO to THF. Consequently, the quenching dynamics are in contrast to the polarity of the solvent but in line with the solvation times.

- Quantum chemical calculations in the different solvents explicate this behavior. Crucial for the fluorescence quenching dynamics is the crossover from the π-Min to the CT-Min and the associated barrier. If only the fast response of the solvent is taking into account, the calculated barrier is for the most polar solvent DMSO the highest one. First, by considering also the slow response of the solvent, DMSO causes the largest stabilization of the CT state. This can be understood as from the π-Min to the CT-Min not only the absolute value of the dipole moment vector changes but also its orientation. The weak dipole moment vector at π-Min points opposite to the strong one of the CT state (see fig. 3.1). When for the energy calculation of the CT state only the fast component of the solvent response is regarded, the solvent molecules are still in the orientation adjusted to the locally excited state at π-Min. The most polar solvent DMSO leads then to the lowest stabilization of the CT state. Overall, the polarity of the solvent does not seem to influence the CT energetics in a significant way. No relevant barriers exist in all investigated solvents and the charge transfer is expected for each environment in accord with the measurements. The only influence of the specific solvent on the CT dynamics is its speed to readjust to changes in the charge distribution or in other words the solvation time of the solvent.

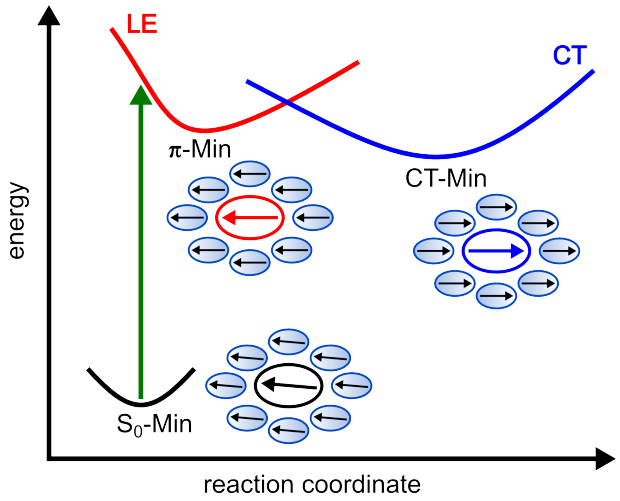

Figure 3.1.: Scheme of the different states and solvations involved in the charge transfer process occurring in PDI-13-N after optical excitation (LE, locally excited state; CT, charge transfer state). At the three minima (S_0-min, π-Min, CT-Min) the surrounding solvent molecules are equilibrated to the solute in its corresponding electronic state. The arrows represent the dipole moment vectors of the solute and of the solvent molecules.

The work elucidates that the dynamics of the CT process of the two perylene diimide molecules are only significantly influenced by the solvation time and not by the polarity of the specific solvent. The situation of opposite dipole moment vectors is also found for the π-Min and the two CT minima of the dyad D-(Ph-Yn2-Ph)-A. This indicates that also for the energy transfer dynamics the solvation time of the solvent could play the crucial role. The lower energy transfer efficiency and slower dynamics of the dyad observed in benzonitrile in comparison to chloroform

confirm this hypothesis. Further investigations of the solvent effects may clearly unveil the complex interplay of the solvent properties on the energy transfer and allow to influence it in the desired way.

The results also demonstrate again that chemical substitution can be used to control the dynamics in the perylene diimides. By the introduction of an amino group the fluorescence is quenched in the PDI-13-N system by a charge transfer from the substituent to the PDI chromophore as in the donor-spacer system D-(Ph). But in the case of D-(Ph) the functionalization of the benzoperylene diimide with a phenyl group leads to an increase of the lifetime of the charge separation by more than a factor of ten in comparison to PDI-13-N. The investigated systems therewith reveal how the energy dissipation *via* fluorescence can be avoided and the persistence of the charge separation can be increased which is of high importance for perylene diimides used in photovoltaic applications.

Hereafter, the manuscript "Ultrafast emission quenching in a perylene diimide by structure rearrangement induced electron transfer from its substituent" is printed. The supporting information is printed in appendix A.

Ultrafast Emission Quenching in a Perylene diimide by Structure Rearrangement Induced Electron Transfer from its Substituent

Patrick Kölle[a], Artur Nenov[a], Uwe Megerle[b], Patrizia Krok[b], Heinz Langhals[a], Regina de Vivie-Riedle[a], and Eberhard Riedle[b]*

[a] Department Chemie, Ludwig-Maximilians-Universität (LMU), Butenandtstraße 5-13, 81377 München, Germany

[b] Lehrstuhl für BioMolekulare Optik, Ludwig-Maximilians-Universität (LMU), Oettingenstraße 67, 80538 München, Germany

* Corresponding author. Fax: +49-89-2180-9202
E-mail address: riedle@physik.uni-muenchen.de

ABSTRACT

The ultrafast excited-state dynamics of the fluorescent perylene diimide chromophore and its non-fluorescent amino-functionalized derivative are investigated by transient spectroscopy and quantum chemical calculations. The fluorescent system shows no dynamics in the sub-nanosecond time region. For the functionalized molecule the stimulated emission signal decays rapidly on a sub-picosecond timescale, while the excited state absorption decreases with a time constant of several picoseconds. The theoretical analysis assigns the fast decay to a charge transfer from the amino substitutient to the perylene diimide chromophore. The transfer is made possible by a decrease of the N-N distance and a planarization of the substituent as the system moves away from the Franck-Condon point. Experiments in different solvents demonstrate that the dynamics of this fluorescence quenching correlate with the solvation time. The rapid relaxation from the charge transfer state into the ground state is observed on a picosecond timescale and is attributed to a passage through a conical intersection.

Kewords:

femtosecond, hole transfer, conical intersection, CASPT2, charge separation

I. Introduction

Due to practically vanishing internal conversion and intersystem crossing perylene dyes [1,2] can exhibit a fluorescence quantum yield very close to unity [3,4]. Because of their unusually high chemical and photochemical stability they find application as pigments [5,6], laser dyes [7,8] and as fluorescence standards [3]. Appropriate substitution at the terminal nitrogen atoms leads to a high solubility in organic solvents and even in water without changing the spectroscopic properties [9,10]. The assembly of two or three chromophores provides intense dyes through chromophore – chromophore interaction [11]. Promising applications of perylene dyes as building blocks for supramolecular architectures are given by Würthner [12].

Recently perylene dyes attracted great interest for the design of intramolecular energy and charge transfer systems [13-16]. Chemical substitution of the perylene chromophore can be used as a tool to control its absorption and in particular its emission properties [17]. By choosing an appropriate substituent, the intrinsic high fluorescence yield of the perylene chromophore is effectively turned off [18]. The quenching process can be suppressed by addition of aldehydes in the vicinity of the substituted perylene and an optical sensor for on-line monitoring of the aldehyde concentration results [19]. The chemical equilibrium of the reversible protonation reaction responsible for the degree of quenching can be shifted towards the fluorescence quenched state with a suitable base. In recent publications [20,21] we could show that the fluorescence quenching in the case of naphthalene diimides can be influenced through core-substitution. The fluorescence quenching was shown to be due to a photoinduced charge transfer from the substituent to the naphthalene diimides chromophore.

In this present work we investigate the influence of substitution at the N-termini of perylene diimide with an electron donating amino group on the ultrafast intramolecular dynamics leading to efficient fluorescence quenching. We performed femtosecond pump-probe experiments and state of the art multi-configuration quantum chemical calculations on the highly fluorescent species *N,N′*-bis(1-nonyldecyl)-3,4:9,10-perylenebis(dicarboximide) (PDI-19; see Figure 1a) and the non-fluorescent species *N*-amino-*N′*-(1-hexylheptyl)perylene-3,4:9,10-tetracarboxyldiimide (PDI-13-N; see Figure 1b). In this way we hope to establish a sound microscopic picture that explains the observed dependence of the fluorescence yield on the substituent.

The strongly decreased fluorescence quantum yield should correspond to a significant decrease of the fluorescence lifetime of 4 ns [22] down to a few picoseconds.

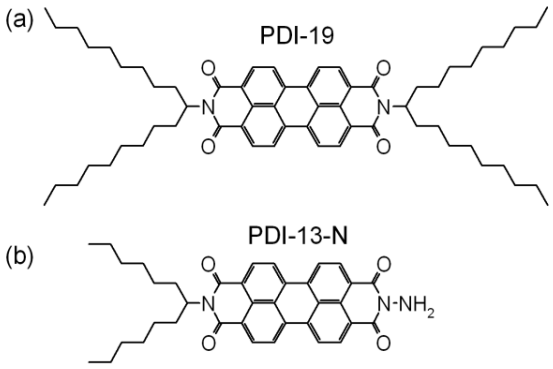

Figure 1. Structural formulae of the investigated perylene derivatives:

(a) *N,N′*-bis(1-nonyldecyl)-3,4:9,10-perylenebis(dicarboximide) (PDI-19),

(b) *N*-amino-*N′*-(1-hexylheptyl)perylene-3,4:9,10-tetracarboxylbisimide (PDI-13-N).

II. Experimental and Theoretical Methods

The synthesis and the optical properties of PDI-19 and PDI-13-N have been described in detail [10,11,18]. The solvents chloroform, THF and DMSO used for the transient absorption measurements were of spectroscopic quality. The solutions were pumped through a flow cell of 120 µm thickness and had an optical density of ~0.2 at the excitation wavelength. The broadband femtosecond spectrometer has been described in detail [23]. A Ti:sapphire amplifier system (CPA 2001; Clark MXR) was used to pump a noncollinear optical parametric amplifier tuned to 490 or 530 nm, corresponding to the maxima of the first two vibronic bands (see Figure 2). The pulses were compressed to ~ 40 fs and focused down to a diameter of 220 µm FWHM inside the sample. The pulse energy was attenuated to about 110 nJ. A CaF_2 continuum spanning from below 300 nm to 720 nm and polarized at the magic angle was used as the probe light. Throughout the probe range, the spectral resolution was better than 100 cm^{-1} and the temporal resolution was better than 150 fs, well below all observed decay rates.

For the ab-initio calculations the energetically irrelevant alkyl chains at the N-termini of both molecules were replaced by hydrogen atoms to reduce the computational time. The ground

state (S_0) geometries of PDI-19 and PDI-13-N were optimized with the second-order Møller-Plesset (MP2) method. The vertical excitation energies at the S_0 equilibrium geometry and the excited-state potential energy surfaces in the vicinity of the Franck-Condon region have been determined with the coupled cluster (CC2) method [24]. The Karlsruhe triple-ζ basis set augmented with one set of polarization functions (def2-TZVP) [25] and the resolution-of-the-identity (RI) approximation were used for the MP2 and CC2 calculations [26, 27].

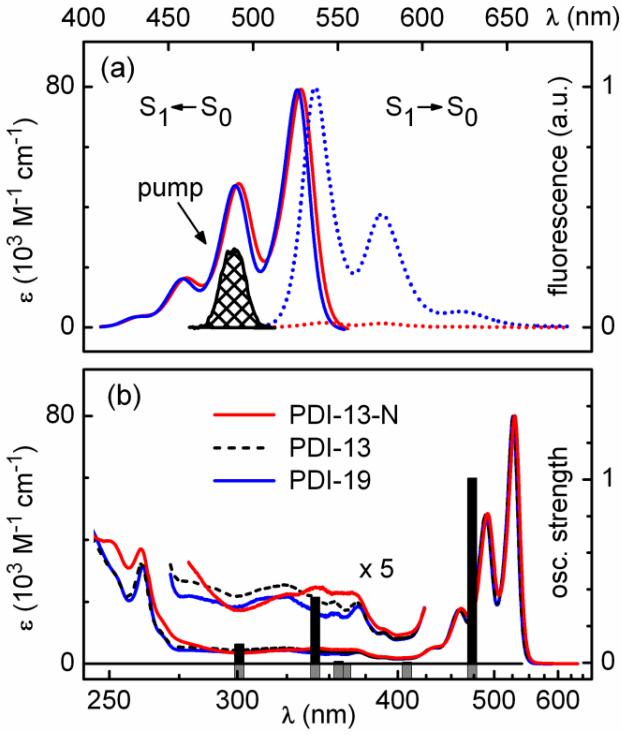

Figure 2. (a) Absorption and emission spectra of PDI-19 (blue lines) and PDI-13-N (red lines) measured in chloroform. The hashed area corresponds to a typical spectrum of the 490-nm pump pulse. (b) Comparison of the absorption spectra with calculated transitions from the electronic ground state of PDI-13-N (bars). The spectra in the region from 270 to 420 nm are magnified by a factor of 5, the spectrum of the symmetric PDI-13 is shown for comparison.

The CC2 method is not applicable when two electronic states get energetically close (as in the case of conical intersections) because the single reference approach breaks down [28]. As a

conical intersection was expected to play a role in the ultrafast relaxation process of PDI-13-N, its excited state potential energy surface was explored with the single state (SS) perturbation theory (CASPT2) [29] using state-averaged complete active space self consistent field (CASSCF) wavefunctions (5 roots for PDI-19, 7 roots for PDI-13-N) and a standard Pople basis set 6-31G* [30]. The active space was benchmarked against the results of the CC2 calculations. It consisted of 8 π-electrons and 5 π-orbitals for PDI-19, for PDI-13-N two additional occupied orbitals exhibiting significant contributions from the amino substituent were included (see Figure S1). To validate our proposed mechanism we also performed CASPT2 calculations of the excited state absorption spectrum and on the single charged PDI-13-N anion. Here, a state-averaged CASSCF wavefunction over 4 roots and an active space containing 2 respectively 3 π-electrons and 4 π-orbitals were used (see Figures S2 and S3). The active space was adapted to describe sufficent higher excitations by including more virtual orbitals. A level shift parameter of 0.2 was employed in all CASPT2 calculations [31]. A conical intersection between the S_1 and S_0 energy surfaces of PDI-13-N at the CASPT2 level of theory was obtained by extrapolation from the global minimum using the CASSCF optimized conical intersection geometry. The program package MOLPRO [32] was used for the CASSCF and CASPT2 calculations, while the package TURBOMOLE [33] was used for the MP2 and CC2 calculations.

The influence of the solvents on the photochemical reaction was determined with the Polarizable Continuum Model (PCM) [34] and the TDDFT [35] method. The Karlsruhe split valence basis set with a polarization function (def2-SV(P)) [36] and the CAM-B3LYP functional [37] were used in all calculations, which have been performed with the program package Gaussian09 [38].

IV. Results and Discussion

Figure 2 presents the absorption and fluorescence spectra of PDI-19 and PDI-13-N in chloroform, the absorption spectrum of the symmetric PDI-13 (N,N′-bis(1-hexylheptyl)-3,4:9,10-perylenebis(dicarboximide)) is shown in (b) for comparison. The shape of the absorption spectrum is very similar for a wide variety of perylene dyes [13, 39, 40]. In the visible, it is dominated by a strong absorption around 500 nm with four distinct vibronic bands. Both the CASPT2 and the CC2 calculations attribute this band to an intense $\pi\pi^*$ transition from the HOMO to the LUMO found at ~500 nm (corresponding to ~ 2.6 eV and large oscillator strength; see Table 1

and Table S1). The good agreement between both methods justifies the choice of the active space for the SS-CASPT2 calculations. The much weaker and broader absorption in the range from 275 to 420 nm is due to additional $\pi\pi^*$ transitions localized on the chromophore (see Table 1).

Table 1: CASPT2 vertical excitations energies and oscillator strengths of PDI-19 (CAS(8,5) and PDI-13-N (CAS(12,7)) at the MP2-optimized ground-state equilibrium geometries (LE, locally exited state; CT, charge transfer state). The calculated energies are compared with the experimental absorption maxima of PDI-19 and PDI-13-N in $CHCl_3$.

		PDI-19		**PDI-13-N**	
transition	character	ΔE (eV)	f	ΔE (eV)	f
$S_0 \rightarrow S_1$	$\pi_1 \rightarrow \pi^*$ (LE)	2.70	1.078	2.62	1.077
$S_0 \rightarrow S_2$	$\pi_1^2 \rightarrow \pi^{*2}$	3.10	0.000	3.04	0.002
$S_0 \rightarrow S_3$	$\pi_2 \rightarrow \pi^*$	3.50	0.000	3.43	0.000
$S_0 \rightarrow S_4$	$(\pi/n)_1 \rightarrow \pi*$ (CT)	-	-	3.48	0.008
$S_0 \rightarrow S_5$	$\pi_3 \rightarrow \pi^*$	3.68	0.408	3.63	0.358
$S_0 \rightarrow S_8$	$(\pi/n)_2 \rightarrow \pi*$	-	-	4.12	0.102
Exp.	-	-	2.34	-	

The fluorescence spectrum is highly symmetric to the absorption spectrum with only a small Stokes shift (e.g. 370 cm^{-1} for PDI-19 in chloroform; see Figure 2a). This indicates minor geometric distortions upon excitation and consequently only a slight displacement of the excited state energy surface. Whereas PDI-19 is strongly fluorescent, a pure PDI-13-N solution shows only weak fluorescence. The remaining fluorescence of PDI-13-N is mostly due to the presence of molecules with a protonated amino moiety. To shift the chemical equilibrium towards the non-protonated form we added small amounts of the base triethyl amine to the solution. Thereby, the residual fluorescence is further reduced.

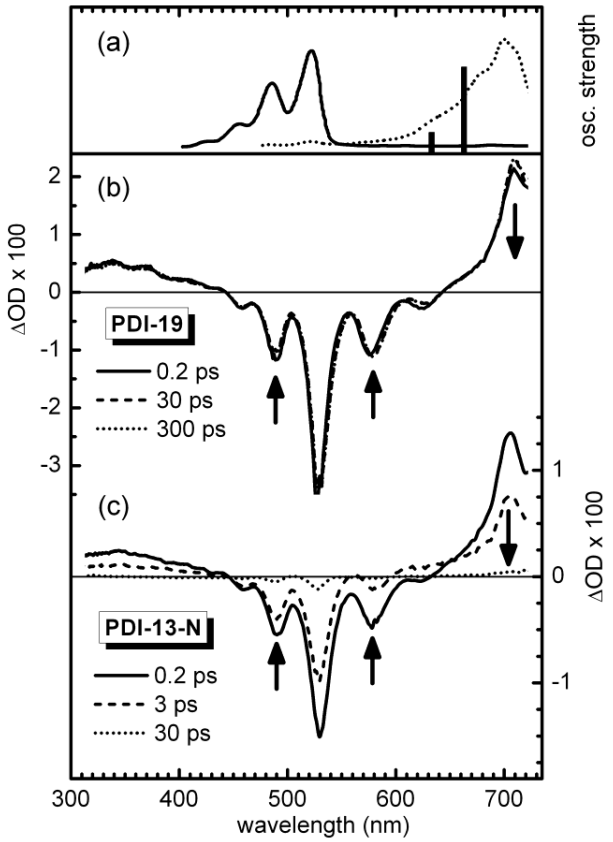

Figure 3. (a) Absorption spectrum of the neutral species (solid line) of *N,N'*-bis(2,5-di-*tert*-butylphenyl)-3,4:9,10-perylenebis(dicarboximide) and its electrochemically prepared radical anion (dotted line) in acetonitrile (taken from ref. 45). For comparison the calculated transitions from the radical anion of PDI-13-N (CAS(3,4)/CASPT2) are shown (bars). Transient absorption spectra of PDI-19 (b) and PDI-13-N (c) in chloroform at different delay times after excitation at 490 nm.

Figure 3 shows the evolution of the transient absorption spectra of PDI-19 (b) and PDI-13-N (c) in chloroform after excitation at 490 nm. At early delay times of a few 100 fs, the spectra of both molecules are nearly identical. We find a broad excited state absorption (ESA) in the spectral region below 440 nm and a sharp ESA band around 710 nm. The negative absorption changes observed between 440 and 640 nm arise from the ground state bleach (GSB) and the

stimulated emission (SE): the former is attributed to the peaks at 440 and 490 nm, the latter to the peaks at 580 and 625 nm. The strong peak at 530 nm originates from the overlap of the first absorption and emission band.

The temporal evolution of the spectra of the two species shows significant differences. For the fluorescent dye PDI-19, both the signatures and the amplitudes hardly change on a timescale of a few 100 ps. In contrast, the signal of the non-fluorescent PDI-13-N vanishes almost completely within 30 ps. The ultrafast decay of the GSB, the SE and the ESA of PDI-13-N is suggested to be due to the same microscopic processes that also quench the time integrated fluorescence. The analysis of the time resolved measurements and the results from the quantum chemical calculations therefore allow the unambiguous determination of these processes.

Since spectral shifts play only a minor role in the evolution of the signals, the reaction dynamics can best be monitored in the band maxima of the GSB, SE and ESA indicated by arrows in Figure 3. The corresponding kinetics are shown in Figure 4a-c for PDI-19 and in Figure 4d-f for PDI-13-N. All three signatures of PDI-19 remain nearly constant after the excitation. This agrees nicely with the reported fluorescence decay time of about 4 ns and is in line with the high fluorescence quantum yield [22]. There is no indication for any additional deactivation channel.

Global data analysis

To quantify the relaxation dynamics we applied multiexponential global fits [41] shown as solid lines in Figure 4. The fit of the PDI-19 data consisted of a dominant nanosecond component and an almost negligible picosecond contribution reflecting minor relaxations in the excited state (see Figure S4).

In contrast, for PDI-13-N we find ultrafast dynamics in the picosecond regime. For the GSB and the ESA we observe a synchronous decay (see Figure 4e-f), while the SE decays significantly faster (Figure 4d). Now, a set of three time constants was necessary and sufficient to obtain a good agreement between model function and experimental data (see bold values in Table 2). A small constant offset was added to account for the residual protonated species, which was accordingly observed in the stationary fluorescence spectrum. The fastest contribution of 0.79 ps is predominantly found in the spectral region of the SE and dominates the emission quenching dynamics (see Figure S5). The decay of the GSB and ESA is mostly characterized by the second time constant of 4.6 ps which reflects the internal conversion of the system to the ground state. In the same spectral region the third time constant of 14 ps contributes to the overall amplitude and

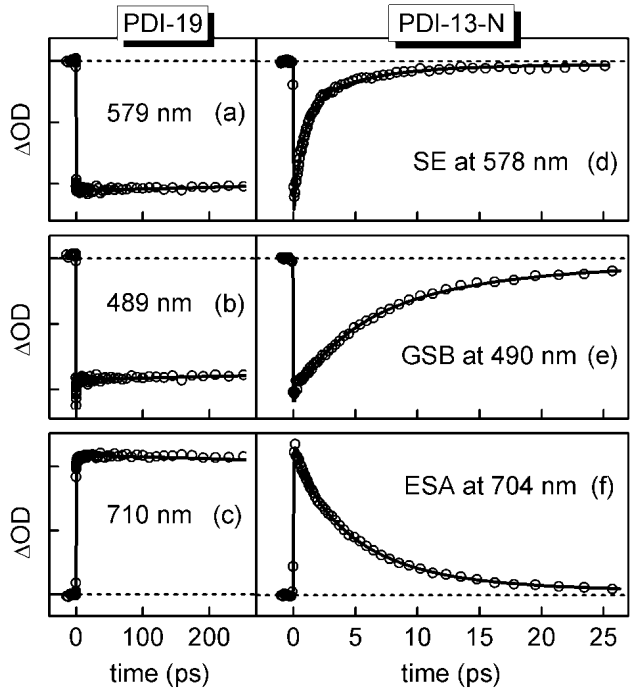

Figure 4. Kinetic profiles in the band maxima of the stimulated emission (SE), ground state bleach (GSB) and excited state absorption (ESA) of PDI-19 (a-c) and PDI-13-N (d-f), see arrows in Figure 3. While the PDI-19 signatures essentially remain constant up to several 100 ps, the PDI-13-N signals decay on the few ps timescale: The SE dynamics are governed by a 0.8 ps component, the GSB and ESA show a slower decay characterized by a time constant of 4.6 ps.

indicates a vibrational cooling process on this timescale after the relaxation to the electronic ground state (See Figure S5).

Quantum chemical computations

To gain further insight into the quenching mechanism, we explored the first excited-state energy surface (S_1) at the SS-CASPT2 level of theory. Ground state geometry optimizations for both the amino substituted PDI-13-N and the unsubstituted PDI-19 result in a planar structure of the PDI chromophore. In addition, in PDI-13-N the amino group exhibits a pyramidal conformation as the nitrogen is sp^3-hybridized (Figure 5c, FC-Point). The first three vertical transitions

in both molecules are localized on the chromophore. The S_1 and S_2 states are characterized by single and double excitations from the HOMO (π) to the LUMO (π^*) (see Table 1 and Figure 5a), the S_3 state by an excitation from the HOMO-1 to the LUMO. The S_4 state of PDI-13-N is characterized by a single electron excitation to the LUMO from an orbital with significant contribution from the nitrogen lone pair of the amino group (π/n). Naturally, this π/n$\rightarrow\pi^*$-excitation has no analog in the PDI-19 system. In contrast to the S_1 state, the transitions to the higher lying states $S_{2\text{-}4}$ have negligible oscillator strength (see Table 1).

Table 2: Time constants obtained from the multiexponential global fit of PDI-13-N in different solvents. The discussion in the paper concentrates on the data in $CHCl_3$ at 490 nm excitation (bold values).

[a] The 1/e solvation times for coumarin 153 from ref. [43] are given for comparison.

	τ_{1e} (ps) [a]	τ_1 (ps)	τ_2 (ps)	τ_3 (ps)	$\lambda_{exc.}$ (nm)
THF	0.70	0.3	1.4	9.2	490
DMSO	0.90	0.67	3.1	28	490
$CHCl_3$	2.3	**0.79**	**4.6**	**14**	**490**
		0.88	5.3	14	530

Geometry optimization from the Franck-Condon (FC) points of PDI-13-N and PDI-19 on the bright S_1 state leads to similar local minima with $\pi\pi^*$ character (Figure 5c, denoted as π-Minimum) for both molecules, exhibiting minor structural changes, mainly bond length rearrangement in the PDI-framework. Consequently, the calculated oscillator strengths for the transition to the ground state are alike and almost unchanged from the FC points (f=1.036/1.077, see Table S2).

Optimization on the above mentioned S_4 state in PDI-13-N reveals that the π/n$\rightarrow\pi^*$-configuration stabilizes along a combined N-N shortening / NH_2 planarization coordinate (see Figure 5b, red line). Following this coordinate, a second minimum on the S_1 potential energy surface which is almost isoenergetic to the π-Minimum is found (see Table S2). Here, the N-N distance is reduced from 1.39 to 1.27 Å and the amino group is completely planarized (sp^2-

hybridization of the nitrogen, see Figure 5c). The geometrical distortion of the amino group localizes the formerly delocalized π/n-orbital on the amino substituted dicarboxyimid moiety and shifts its energy above the energy of the π-orbital (see Figure 5a). Thus, in PDI-13-N the S_1 state in the vicinity of the second minimum is described by a charge transfer from the amino group to the PDI chromophore. Hence, we denote this minimum as CT-Minimum. The CT character is reflected by the strongly reduced oscillator strength of 0.008 for the transition to the ground state and a high dipole moment (~ 14 D).

The stabilization of the excited CT state is accompanied by a considerable destabilization of the closed shell ground state, so that both states are separated by only 1.22 eV at the CT- minimum. Further shortening of the N-N distance to 1.24 Å locates a conical intersection 0.48 eV above the CT-minimum (Figure 5c). Presently, optimization of conical intersections is not within the scope of the CASPT2 method. Hence, to retrieve the location of the conical intersection the geometrical changes between the SA-2-CASSCF(2,2) optimized conical intersection and CT-minimum structure were transferred to the CASPT2 optimized CT-minimum geometry. We expect that a full optimization on the CASPT2 level would lower the energy further and make the conical intersection accessible from the CT-minimum. The vibrational excess energy acquired by the relaxation from the FC point to the CT-Minimum and the optical excitation into an excited vibronic band will further enhance this relaxation probability.

Immediately after the optical excitation, the initial relaxation towards the π-Minimum on a femtosecond timescale occurs in both PDI-13-N and PDI-19. The absence of significant changes in the transient spectra of PDI-19 indicates that the observed 4 ns fluorescence occurs from the π-Minimum. Furthermore, it proves that the appreciable spectral evolutions of PDI-13-N cannot be assigned to this initial relaxation process. Hence, we consider the π-Minimum as starting point for the observed dynamics of PDI-13-N.

The presumably low barrier between the originally isoenergetic π- and CT-Minimum allows the partial population of the CT state. Due to the high static dipole moment this initiates the dynamic lowering of the CT state in polar solvents by reorientation of the solvent molecules and an accumulative charge transfer [42]. Consequently, a dynamic emission quenching is observed in the transient spectra. There are three contributions to the emission quenching. First, the rise of the ground state energy and the approximate conservation of the energy of the excited electron would shift a potential emission to beyond 1000 nm, well outside of our observation region.

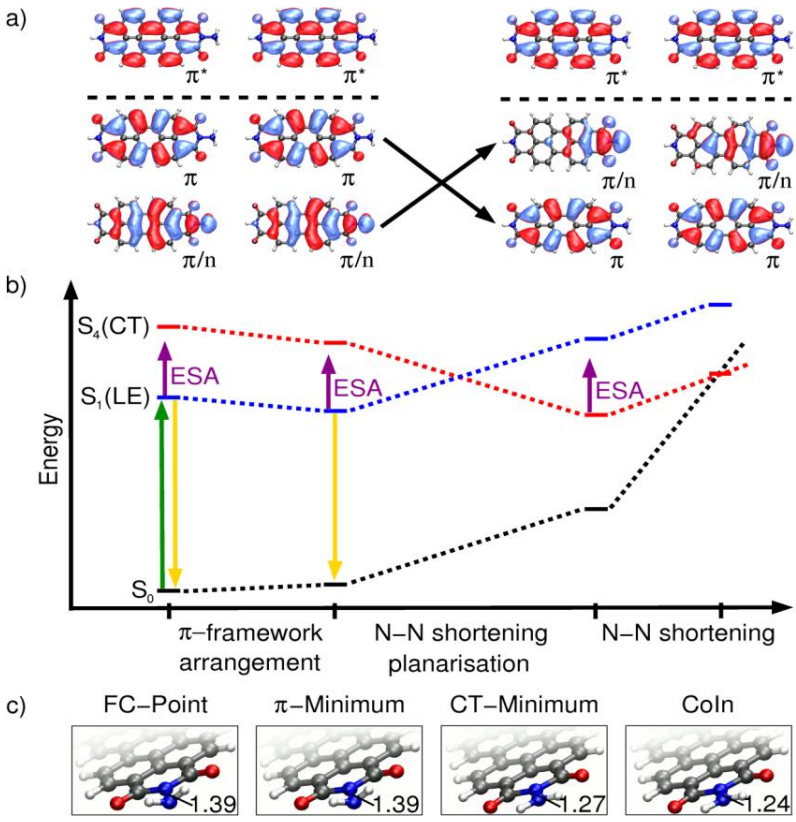

Figure 5. (a) Molecular orbitals describing the relevant points of the photoreaction of PDI-13-N (CAS(12,7)/CASPT2). The black arrows indicate the evolution of the energetic order of the orbitals during the relaxation process. (b) Scheme of the state energies involved in the CT process. Solid arrows indicate optical transitions and dotted lines visualize the different potential energy surfaces (black: ground state; blue: LE, locally excited state; red: CT, charge transfer state). (c) Minimum energy geometries for the relevant states (FC, Franck-Condon; CoIn, Conical Intersection). The calculated N-N bond length is given in Å.

Secondly, the oscillator strength between the CT state and the ground state is vanishingly small (see Table S2). Thirdly, the CT from the amino group fills up the hole in the former HOMO. A radiative decay into this state would therefore violate the Pauli rule. To corroborate the proposed mechanism we performed experiments in the two additional solvents DMSO and THF

which show faster solvation dynamics than chloroform [43] and should therefore affect the CT dynamics. Indeed the quenching dynamics of PDI-13-N are found to accelerate from chloroform over DMSO to THF, in line with the known solvation timescales (see Table 2 and Figures S6 and S7). Further support for the suggested mechanism is obtained from the dependence of the CT dynamics on the pump wavelength: A lower excess energy leads to a somewhat lower initial population of the CT state and, therefore, a slower quenching (see Table 2 and Figure S8).

A rather small coupling matrix element of only 6 meV has been derived for the CT in related perylene derivatives [44]. This would typically not allow a sub-picosecond transfer due to a lack of energy resonance between the locally excited (LE) and the CT state. The dynamics along the reaction coordinate does, however, bring the states into exact resonance for a short period and the transfer can proceed efficiently. The excited state ordering at the FC-Point is mainly given by the reduced nitrogen-nitrogen interaction in the out-of-plane ground state geometry. The sp^3 hybridization of the amino substituent allows for a spatial separation of the lone pair nitrogen electrons and therefore lowers the energy of the LE state. As the planarization proceeds, the lone pairs interact more strongly and the energy of the LE state is increased while the energy of the CT state is simultaneously lowered. The two states become isoenergetic (see Figure 5b) and c)) and eventually reverse order.

Due to the shallow potential energy surface along the reaction coordinate in the excited state, the population dynamics is not very well described by a simple rate model. This explains the need for multiexponential fits and the difficulty to assign individual time constants directly to specific molecular processes. However, to a good approximation the transition from the π-Minimum to the CT state can be related to the fastest observed time constant τ_1. The synchronous decay of the ESA and GSB signatures of PDI-13-N with a dominant time constant τ_2 of 4.6 ps (see Figure 4e-f) indicates the subsequent fast return to the ground state. From our theoretical treatment we can attribute this process to the relaxation to the ground state through the conical intersection in the vicinity of the CT-Minimum. We expect this relaxation to be very efficient, as the conical intersection is reached along the N-N shortening coordinate that already promotes the transition from the π- to the CT-Minimum. The quenching process most likely converts a major part of the electronic excitation into vibrational energy in the N-N stretching mode. The internal vibrational redistribution and cooling by the solvent is reflected in the third time constant τ_3. The

associated difference spectrum is dominated by the differential line shapes expected for vibrational cooling (see Figures S5 to S7).

The rapid return to the electronic ground state is well monitored by the recovery of the GSB (see Figure 4e)). What remains to be discussed is the decay of the transient absorption around 700 nm with the same time behavior as the GSB, yet much slower than the decay of the stimulated emission. The latter is often a good indication of the depopulation of the excited state. For an understanding we resort to the previously reported absorption spectrum of *N,N'*-bis(2,5-di-*tert*-butylphenyl)-3,4:9,10-perylenebis(dicarboximide) (PDI-tBP) and its electrochemically generated radical anion [45] (see Figure 3a). The absorption spectrum of the neutral PDI-tBP (solid line) is nearly identical to the absorption spectra of PDI-19 and PDI-13-N and we can expect the anion spectra also to be very similar. CASPT2 calculations on the PDI-13-N anion yield a strong transition at 1.87 eV (see Table S3), in good agreement with the experimental absorption peak of the PDI-tBP anion around 700 nm (dotted line in Figure 3a). The LE state of all investigated PDIs shows a strong transient absorption at 700 nm which matches the weak but significant absorption in the ground state spectrum around 300 nm (see Figure 2b)). A higher excited state with good oscillator strength from the S_1 state is found by the calculation at 1.47 eV above the S_1 state (see Table S4). The CT process therefore does not change the position of the red transient absorption and only slightly decreases its strength (see Figure 3c). Vice versa, the persistence of the red absorption while the stimulated emission vanishes is additional proof that the PDI^{-}-N^{+} biradical is the intermediate state of the reaction. We have previously made quite similar observations for fluorescence quenching due to a charge transfer from an electron donor (NH_2, benzol, etc.) to the chromophore [20, 21, 46, 47]. The present CASPT2 calculations of PDI-13-N at the relevant structures (FC, π-Minimum, CT-Minimum) confirm this interpretation. At all points one can find intensive low energy transitions from the first excited state (S_1) state involving the promotion of the electron from the highest SOMO (corresponding to the π^*-LUMO of the ground state molecule) to a higher unoccupied π^*-orbital (see Figure S3). These transitions are characterized by the same orbitals as the calculated bright transition of the PDI-13-N anion (see Figure S2).

Strictly speaking, the calculations presented so far are only valid for isolated molecules, i.e. in the hypothetical gas phase. To check for the influence of the solvents on the charge transfer dynamics, we performed additional calculations that describe the quasi-static influence of the

used solvents (for details see Table S5). Explicit solvent calculations of such a complex photophysical reaction are still out of range. The CASPT2 method used so far cannot be augmented by a dielectric surrounding and we therefore resorted to the TD-DFT level of theory. The energy of the ground, LE and CT state at all relevant points were determined (for the optimized geometries in each environment) and the important ones are summarized in Table 3. We report the energy relaxation due to the fast and slow response of the solvent. The electronic response of the PDI-13-N and the surrounding solvent molecules occurs instantaneously with the excitation pulse and is already included in the shift of the absorption energy from gas phase to the solution. The calculation uses the optical dielectric constant $\varepsilon_\infty = n^2$ (with n being the refraction index of the solvent) and the resulting energy is the one denoted as "fast". We find that the dipole moment of PDI-13-N (about 1.3 D) only changes very slightly upon optical excitation and as the molecule propagates to the π-Minimum. Accordingly the orientational relaxation of the solvent will not give any significant contribution and the E(fast) is appropriate in this regime. As the system changes into the CT state, the dipole moment jumps to 13 D and on the long time scale the full solvent relaxation will minimize the system energy to E(slow). For the determination of E(slow) the static dielectric constant εof the solvent molecules is used in the calculation.

The calculated values shown in Table 3 are referenced to the energy at the FC point for each solvent. The stabilisation of the π-Minimum is reduced by the same amount for all solvents in good agreement with the nearly identical refractive indices. The CT state is nearly half an eV above and can certainly not be reached in the π-Minimum geometry. In the CT-Minimum the LE state is already raised by about half an eV above the FC point and the CT state is significantly lowered below the LE energy in the π-Minimum already for the electronic response (fast) in all solvents. The slow relaxation of the solvents further stabilizes the CT state. From an interpolation between the two structures we obtain an estimate of the barrier and find values around 0.1 eV. This is significantly lower than available kinetic energy from the relaxation through the π-Minimum in all solvents and the electron transfer can proceed unhindered.

Somewhat surprisingly we find that the details of the solvent polarity, i.e. the quasi-static properties, do not seem to influence the energetics in a significant way. The charge transfer is expected for all investigated solvents in accord with the measurements and it would even proceed in the gas phase. Since there is no relevant barrier and need for thermal activation, the only influence of the specific solvent will be due to its speed of geometric rearrangement (inertial and

librational) or in other terms the solvation times. The additional calculations clearly corroborate the conjectures made above about the reaction mechanism.

Table 3: Relative energies of PDI-13-N for the gas phase and different solvents for all relevant points discussed in the paper (LE, locally excited state; CT, charge transfer state). Vertical excitation energies of the Franck-Condon points in each environment were chosen as reference points. The barriers between the π- and CT-Minimum were obtained by interpolation using the two minimum structures. The geometries were optimized in each environment.

ΔE (eV)	state	gas phase	THF	DMSO	$CHCl_3$
π-Minimum	LE(fast)	-0.20	-0.18	-0.18	-0.19
	LE(slow)		-0.19	-0.18	-0.19
	CT(fast)	+0.37	+0.23	+0.33	+0.11
CT-Minimum	LE(fast)	+0.39	+0.44	+0.45	+0.43
	CT(fast)	-0.35	-0.46	-0.37	-0.55
	CT(slow)		-1.08	-1.25	-0.98
barrier (π-/CT-Minimum)	-	0.12	0.08	0.11	0.03

V. Conclusions and Outlook

A time-resolved spectroscopic study together with high level quantum chemical calculations establishes the molecular process behind the low fluorescence quantum yield of PDI-13-N in contrast to PDI-19. The measured lifetime of 4 ns of PDI-19 is assigned to a stable $\pi\pi^*$-minimum in the first excited state. Consequently, no significant changes on a picosecond timescale are observed in the transient spectra. In contrast, PDI-13-N exhibits ultrafast dynamics in the picosecond regime. The sub-picosecond quenching of the SE signal is attributed to a charge transfer from the amino substituent to the PDI-chromophore. Our theoretical calculations reveal that geometrical deformations in the substituent (combined N-N shortening / NH_2 planarization) stabilize the CT-state and facilitate its dynamic population. To confirm this mechanism, we could

demonstrate that the quenching dynamics in three solvents with largely varied polarity correlate with the solvation times. Furthermore, the synchronous decay of the ESA and GSB signatures which occurs on a longer timescale of several picoseconds can be attributed to the relaxation to the ground state through a conical intersection. We showed that such a conical intersection exists in the proximity of the CT minimum.

The presented modeling of the electron transfer process goes far beyond the typical quasi-static level picture of a ground state, a LE and a CT state successfully used in many investigations. The quantum chemical results clearly demonstrate that the state ordering at the FC-Point would not allow the charge transfer. It is only through the initial wavepacket motion toward and beyond the LE state potential minimum geometry that the LE and CT state come into resonance and eventually the CT state is the lowest excited state. The energetics are largely determined by the interaction of the nitrogen lone pairs. The polar solvent adds to the stabilization by dynamic solvation. The energetic resonance makes the charge transfer possible even for a small coupling matrix element. Strictly speaking, a hole transfer from the photoexcited chromophore to the substituent is induced.

The comparison between PDI-19 and PDI-13-N reveals that the ultrafast dynamics in perylene dyes can be controlled by the choice of substituents. The additional degrees of freedom by the substituents and new intramolecular interactions provided in particular by heteroatoms allow a very effective mechanism for efficient electron transfer from the substituent to the chromophore. We recently reported a comparable influence of the substituents on naphthalene diimides [20, 21]. The fundamental understanding of the molecular processes after optical excitation in organic dyes is a promising first step in deciphering the much more complex electron and energy transfer processes of new organic compounds: highly intense and light-fast fluorescent dyes like bichromophoric perylene dicarboxylic imides [4], artificial light harvesting systems such as ring-type oriented multichromophores [48] or molecular squares [49], and photofunctional nanoparticles [50]. In photovoltaic applications the main thrive will be to maximize the persistence of the charge separation. Theoretical calculations can be used to predict optimal substituents to achieve these desired properties [51].

ACKNOWLEDGEMENT

We thank I. Kozma, R.-B. Singh and S. Mahanta for valuable experimental help and discussions on the interpretation of the dynamics. S. Lochbrunner made important contributions in the early stages of the project. We gratefully acknowledge funding by the Austrian FWF through the grant F016 (SFB Advanced Light Sources) and the German Science Foundation through the SFB 749 and the GRK 1626.

Supporting Information Available: The orbitals of the various active spaces for the CASPT2 calculations; tables of excitation energies, assignments and oscillator strength; Cartesian coordinates of relevant geometries; color maps of the transient absorption spectra. This material is available free of charge via the Internet at http://pubs.acs.org.

Table of Contents Image

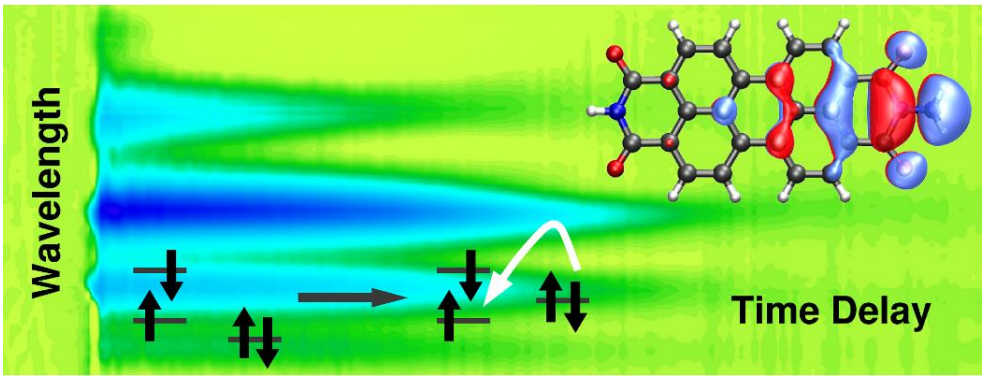

REFERENCES

1. Langhals, H. *Heterocycles* **1995**, *40*, 477-500.
2. Langhals, H. *Helv. Chim. Acta.* **2005**, *88*, 1309-1343.
3. Langhals, H.; Karolin, J.; Johansson, L. B.-Å. *J. Chem. Soc., Faraday Trans.* **1998**, *94*, 2919-2922.
4. Kalinin, S.; Speckbacher, M.; Langhals, H.; Johansson, L. B.-Å. *Phys. Chem. Chem. Phys.* **2001**, *3*, 172-174.
5. Zollinger, H. *Color Chemistry, Synthesis, Properties, and Applications of Organic Dyes and Pigments*, 3rd ed.; Wiley-VCH: Zürich, 2003.
6. Herbst, W.; Hunger, K. *Industrielle Organische Pigmente. Herstellung, Eigenschaften, Anwendung*, 2nd ed.; VCH Verlagsges.: Weinheim, 1995.
7. Sadrai, M.; Bird, G. R. *Opt. Commun.* **1984**, *51*, 62-64.
8. Sheridan, A. K.; Buckley, A. R.; Fox, A. M.; Bacher, A.; Bradley, D. D. C.; Samuel, I. D. W. *J. Appl. Phys.* **2002**, *92*, 6367-6371.
9. Demmig, S.; Langhals, H. *Chem. Ber.* **1988**, *121*, 225-230.
10. Langhals, H.; Demmig, S.; Potrawa, T. *J. f. prakt. Chemie* **1991**, *333*, 733-748.
11. Langhals, H.; Jona, W. *Angew. Chem. Int. Ed.* **1998**, *37*, 952-955.
12. Würthner, F. *Chem. Commun.* **2004**, *14*, 1564-1579.
13. Langhals, H.; Saulich, S. *Chem. Eur. J.* **2002**, *8*, 5630-5643.
14. Langhals, H.; Saulich, S. *Z. Naturforsch.* **2003**, *58b*, 695-697.
15. Sautter, A.; Kaletaş, B. K.; Schmid, D. G.; Dobrawa, R.; Zimine, M.; Jung, G.; van Stokkum, I. H. M.; De Cola, L.; Williams, R. M.; Würthner, F. *J. Am. Chem. Soc.* **2005**, *127*, 6719-6729.

16. Xiao, S.; El-Khouly, M. E.; Li, Y; Gan, Z.; Liu, H.; Jiang, L.; Araki, Y.; Ito, O.; Zhu, D. *J. Phys. Chem. B* **2005**, *109*, 3658-3667.

17. Rademacher, A.; Märkle, S.; Langhals, H. *Chem. Ber.* **1982**, *115*, 2927-2934.

18. Langhals, H.; Jona, W. *Chem. Eur. J.* **1998**, *4*, 2110-2116.

19. Mohr, G. J.; Spichiger, U. E.; Jona, W.; Langhals, H. *Anal. Chem.* **2000**, *72*, 1084-1087.

20. Pugliesi, I.; Krok, P.; Lochbrunner, S.; Blaszczyk, A.; von Hänisch, C.; Mayor, M.; Riedle, E. *J. Phys. Chem. A* **2010,** *114,* 12555-12560.

21. Pugliesi, I.; Megerle, U.; Suraru, S.-B.; Würthner, F.; Riedle, E.; Lochbrunner, S. *Chem. Phys. Lett.* **2011,** *504*, 24-28.

22. Johansson, L. B.-Å.; Langhals, H. *Spectrochim. Acta A* **1991**, *47*, 857-861.

23. Megerle, U.; Pugliesi, I.; Schriever, C.; Sailer, C.F.; Riedle, E. *Appl. Phys. B.* **2009,** *96*, 215-231.

24. Christiansen, O.; Koch, H.; Jørgensen, P. *Chem. Phys. Lett.* **1995,** *243*, 409-418.

25. Schäfer, A.; Huber, C.; Ahlrichs, R. *J. Chem. Phys.* **1994**, *100*, 5829-5835.

26. Weigend, F.; Köhn, A.; Hättig, C. *J. Chem. Phys.* **2002**, *116*, 3175-3183.

27. Hättig, C; Köhn, A. *J. Chem. Phys.* **2002**, *117*, 6939-6951.

28. Adelia, J.; Lischka, H. *J. Chem. Phys. A* **2005**, *109*, 3201-3208.

29. Celani, P.; Werner, H.-J. *J. Chem. Phys.* **2000**, *112*, 5546-5558.

30. Binkley, J. S.; Pople, J. A.; Hehre, W. J. *J. Am. Chem. Soc.* **1980**, *102*, 939-947.

31. Ross, B. O.; Anderson K. *Chem. Phys. Lett.* **1995**, *245*, 215-223.

32. Werner, H.-J.; *et al.*, MOLPRO, *version 2006.1, a package of ab initio programs,* 2006, see http: //www.molpro.net and supplementary material for a complete reference.

33. Ahlrichs, R.; Bär, M.; Häser, M.; Horn H.; Kölmel C. *Chem. Phys. Lett.* **1989**, *162*, 165-169.

34. Improta, R.; Scalmani G.; Frisch M. J.; Barone V, *J. Chem. Phys.* **2007**, *127*, 074504.

35. Scalmani, G,; Frisch M.J.; Mennucci, B.; Tomasi, J.; Cammi, R,; Barone V, *J. Chem. Phys.* **2006**, *124*, 094607.

36. Weigend, F.; Ahlrichs, R. *Phys. Chem. Chem. Phys.* **2005**, *7*, 3297-3305.

37. Yanai, T.; Tew, D.; Handy, N. *Chem. Phys. Lett.* **2004**, *393*, 51-57.

38. Gaussian 09, Revision A.02, Frisch, M. J.; *et al.*, Gaussian, Inc., Wallingford CT, 2009, see supplementary material for a complete reference.

39. Würthner F.; Thalacker, C.; Diele, S.; Tschierske, C. *Chem. Eur. J.* **2001**, *7*, 2245-2253.

40. Fron, E., Schweitzer, G.; Osswald, P.; Würthner, F.; Marsal, P.; Beljonne, D.; Müllen, K; De Schryver, F. C.; Van der Auweraer, M. *Photochem. Photobiol. Sci.* **2008**, *7*, 1509-1521.

41. Fita, P.; Luzina, E.; Dziembowska, T.; Radzewicz, Cz.; Grabowska, A. *J. Chem. Phys.* **2006**, *125*, 184508.

42. Schmidhammer, U.; Megerle, U.; Lochbrunner, S.; Riedle, E.; Karpiuk, J. *J. Phys. Chem.* A **2008,** *112*, 8487-8496.

43. Horng, M. L.; Gardecki, J.; Papazyan, A.; Maroncelli, M. *J. Phys. Chem.* **1995,** *99*, 17311-17337.

44. Beckers, E. H. A. ; Meskers, S. C. J.; Schenning, A. P. H. J.; Chen, Z.; Wuerthner, F.; Janssen, R. A. J. *J. Phys. Chem. A* **2004**, *108*, 6933-6937.

45. Salbeck, J.; Kunkely, H.; Langals, H.; Saalfrank, R. W.; Daub, J. *Chimia* **1989**, *43*, 6-9.

46. Megerle, U.; Wenninger, M.; Kutta, R.-J.; Lechner, R.; König, B.; Dick, B.; Riedle, E. *Phys. Chem. Chem. Phys.* **2011,** *13*, 8869-8880.

47. Wenninger, M.; Fazio, D.; Megerle, U.; Trindler, C.; Schiesser, S.; Riedle, E.; Carell, T. *ChemBioChem.* **2011,** *12*, 703706.

48. Langhals, H.; Speckbacher, M. *Eur. J. Org. Chem.* **2001**, *2001*, 2481-2485.

49. Sautter, A.; Kaletas, B. K.; Schmid, D. G.; Dobrawa, R.; Zimine, M.; Jung, G.; van Stokkum, I. H. M.; De Cola, L.; Williams, R. M.; Würthner, F. *J. Am. Chem. Soc.* **2005**, *127*, 6719-6729.

50. van der Boom, T.; Hayes, R. T.; Zhao, Y.; Bushard, P. J.; Weiss, E. A.; Wasielewski, M. R. *J. Am. Chem. Soc.* **2002**, *124*, 9582-6590.

51. Nenov, A.; de Vivie-Riedle, R. *J. Chem. Phys.* **2011**, *135*, 034304.

4. Photochemical synthesis of natural products

Through the ages, nature has been a continuous source of medicinal products for humans, providing many useful drugs developed from plant, animal and later from microbial sources. Additionally, nature is a major source of new structural leads to bioactive molecules, and effective drug development depends on interdisciplinary collaborations [23]. The improvement of diving techniques over the last decades has opened the sea as natural product source and the number of discovered marine products has increased drastically [128, 129]. But as still supply problems exist for these materials, advances in organic synthesis play an important role to investigate natural products from marine organisms.

4.1. Biomimetic synthesis of intricarene

Gorgonian octocorals are marine organisms being rich in bioactive metabolites like acetogenins, sesquiterpenoids, prostanoids, steroids and furanocembranoids [130]. Furanocembranoids belong to the large family of diterpenoids, which have been isolated exclusivly from marine source. They have gained the interest of natural products chemists due to their attractive molecular architectures and considerable bioactivities. Their investigation has lead to novel biosynthetic speculations, new pharmacological discoveries and advances in synthetic methods [22].

Intricarene is a novel furanocembranoid isolated from the Caribbean gorgonian octocoral *Pseudopterogorgia kallos* [25]. For the furanocembranoid bielschowskysin which was previously isolated from this species of sea plume, antimalarial activity and a significant level of cytotoxicity against two human cancer cell lines were detected [131]. The pharmacological properties of intricarene itself could not yet been investigated, because the substance was only available in minimal amounts. As the gorgonian octocoral live at moderate depths (1 - 45 m) in the Caribbean Sea and are exposed to relatively intense sun light [132], the biosynthesis of intricarene is proposed to proceed photochemically.

In the present interdisciplinary project the compound was indeed synthesized photochemically in the laboratory of the group of Dirk Trauner. Photophysical measurements by the group of Eberhard Riedle revealed that the conditions used in the experiments mimic those in the corals natural habitat. Furthermore, the complicated and surprising mechanism that underlies the light-induced reaction cascade was elucidated by quantum chemical calculations. These findings are reported in the article "Photochemical formation of intricarene" published in *Nature Communications* [133]. The key state statements drawn in the article are:

- Irradiation of a derivative of the compound bipinnatin J, which has been isolated from the coral *P. kallos* as well, resulted in the formation of intricarene and a previously unknown byproduct. The results suggest that the structurally intriguing byproduct may be in the corals too. In the photochemical synthesis the precursor was exposed for eight hours to light from a reptile lamp, whose emission spectrum resembles that of sunlight.

- The comparison of the emission spectrum of the reptile lamp with the measured and calculated absorption spectra of the precursor, deduced that an excitation of a weak absorption is essential for the formation of intricarene. The long exposure time used in the experiments corresponds to the conditions found in the coral's natural habitat, and provides for the photochemical initiation of the reaction.

- On the basis of quantum chemical calculations the mechanism responsible for the cascade of reactions leading to the final product was revealed. The complex reaction mechanism is summarized in figure 6 on page 71. Through the photoexcitation of the bipinnatin J derivative an oxidopyrylium intermediate is reached by a bond cleavage, ring closure and hydrogen transfer reaction. Intricarene is then be formed by a stepwise 1,3-dipolar cycloaddition. Alternatively, from the oxidopyrylium species a disrotatory electrocyclization can lead to the byproduct. The various reaction steps proceed thereby *via* triplet states. Their long lifetimes enable that the reactants can undergo the extensive reaction cascade in the excited state. In this way, the steep energy barriers present in the ground state are avoided. Indeed, even if the molecule decays to the ground state, the intermediate oxidopyrylium can reenter the reaction cascade by additional light absorption of the reptile lamp. By the reexcitation of the oxidopyrylium a low lying conical intersection seam connecting the three lowest singlet states can be reached which leads either to intricarene or to the byproduct.

- Additional photochemical experiments with a different derivative of bipinnatin J confirmed the theoretically derived reaction mechanism.

The interdisciplinary work provides a rationale for the formation of intricarene, which includes all facets of photochemistry, from light absorption to the redistribution of radiant energy. It could be shown how a complex and challenging reaction cascade can be accomplished by only using light. The excitation through the weak absorption band, characterized by a $n\pi^*$ transition, provides the optimal conditions to initiate the photochemical reaction. In contrast, the population of the intense absorption band of the precursor, attributed to a $\pi\pi^*$ excitation, leads directly back to the ground state through a conical intersection seam.

The present results demonstrate the importance of the initial population of long-lived triplet states as already observed for the photophysics of the thiophenes in chapter 2. The clear understanding of the reaction mechanism should allow future synthesis of intricarene in quantities large enough to properly investigate its potential pharmacological and biological properties.

On the following pages the article "Photochemical formation of intricarene" published in *Nature Communications* is reprinted with permission from *Nat. Commun.* **5**, 5597 (2014). The supporting information of this article is available under http://dx.doi.org/10.1038/ncomms6597.

nature COMMUNICATIONS

ARTICLE

Received 12 Aug 2014 | Accepted 17 Oct 2014 | Published 3 Dec 2014

DOI: 10.1038/ncomms6597

Photochemical formation of intricarene

Desiree Stichnoth[1,2,*], Patrick Kölle[1,*], Thomas J. Kimbrough[1,2], Eberhard Riedle[3], Regina de Vivie-Riedle[1] & Dirk Trauner[1,2]

Sunlight is the ultimate driver of biosynthesis but photochemical steps late in biosynthetic pathways are very rare. They appear to play a role in the formation of certain furanocembranoids isolated from Caribbean corals. One of these compounds, intricarene, has been suspected to arise from an intramolecular 1,3-dipolar cycloaddition involving an oxidopyrylium. Here we show, by a combination of experiments and theory, that the oxidopyrylium forms under photochemical conditions and that its cycloaddition occurs via a triplet state. The formation of a complex by-product can be rationalized by another photochemical step that involves a conical intersection. Our work raises the question whether intricarene is biosynthesized in the natural habitat of the corals or is an artefact formed during workup. It also demonstrates that the determination of exact irradiation spectra, in combination with quantum chemical calculations, enables the rationalization of complex reaction pathways that involve multiple excited states.

[1] Department of Chemistry, Ludwig-Maximilians-Universität, 81377 Munich, Germany. [2] Center for Integrated Protein Science, 81377 Munich, Germany. [3] Faculty of Physics, Lehrstuhl für BioMolekulare Optik, Ludwig-Maximilians-Universität, 80538 Munich, Germany. * These authors contributed equally to this work. Correspondence and requests for materials should be addressed to R.de.V.-R. (email: Regina.de_Vivie@cup.uni-muenchen.de) or to D.T. (email: dirk.trauner@lmu.de).

Photosynthesis involves the interconversion of light energy into chemical energy, which then drives the complex pathways of secondary metabolism. Photochemical reactions that occur late in a biosynthesis, however, are very rare. In addition, it is often debatable whether they are genuine biosynthetic steps or they take place when biological materials get processed and stored in light. The former seems to apply to the photochemical formation of cholecalciferol (vitamin D_3) from 7-dehydrocholesterol. Although the majority of cholecalciferol is taken up from dietary sources, it has been suggested that a lack of sunlight is responsible for the development of rickets and other diseases associated with low levels of vitamin D_3 (ref. 1).

As with the aetiology of rickets, the geographical latitude and solar irradiance have to be taken into account when the biological significance of photochemical reactions is considered. Situated at the Tropic of Cancer, the Caribbean belongs to the most intensely irradiated regions of the earth. Therefore, it is not surprising that several natural products have been isolated from the Caribbean whose formation seems to require light. The photochemical isomerization of bipinnatin J (**1**) to kallolide A (**2**) is a case in point (Fig. 1)[2]. Both furanocembranoids have been isolated from gorgonian octocorals, which live at various depths (1–45 m) in the Caribbean Sea and can get exposed to relatively intense sunlight[2,3]. It is therefore conceivable that this photochemical reaction, which can be reproduced in high yield in the laboratory[2,4], also occurs in the native environment of the animals.

Bielschowskysin (**3**) (ref. 5) and intricarene (**4**) (ref. 6), both isolated from the octocoral *Pseudopterogorgia* kallos, are two other natural products that have attracted much interest by the synthetic community[7–15]. According to a biosynthetic hypothesis that has been explored by biomimetic total synthesis, intricarene appears to stem from bipinnatin J (**1**) as well (Fig. 2 (refs 7,8)). Oxidation of **1** with photochemically generated singlet oxygen, followed by hydrolysis and rearrangement would yield hydroxy pyrenone **5**. A formal 1,3-elimination of water would then produce an oxidopyrylium **6**, whose diastereoselective transannular 1,3-dipolar cycloaddition would afford intricarene (**4**) in a final, concerted step. As such, intricarene could be one of the few natural products whose biosynthesis involves a 1,3-dipolar cycloaddition.

Tantillo *et al.*[16] have provided computational evidence that the key cycloaddition step is thermally feasible. According to their report, however, the calculated activation barrier of $\sim$20 kcal mol^{-1} (both in nonpolar and polar environments) appears to be relatively high, albeit still within the bounds of a reasonably fast thermal process. Reflecting this value, the published syntheses of intricarene require temperatures and conditions that certainly cannot be deemed 'biomimetic' (refluxing DMSO or DMF) and the yields obtained were generally poor[7,8]. In addition to this, the exact biosynthetic pathway that would lead from the Achmatowicz oxidation product **5** to the high-energy oxidopyrylium **6** remained unclear.

We now show that intricarene can be formed photochemically from a derivative of bipinnatin J (**1**) under conditions that resemble those found in the Caribbean. In the course of our studies, we have identified a structurally intriguing by-product that may well be found in extracts from *P. bipinnata* too. To interpret our results, we have carried out *ab initio* calculations on the photochemical formation of the oxidopyrylium species and their reactions in the excited state that provide new insights into the chemistry of these useful intermediates.

Results

Photochemical synthesis of intricarene. Our experimental results were obtained serendipitously during a model study directed at bielschowskysin, the formation of which could also involve photochemistry (Fig. 3 and Supplementary Discussion). Treatment of racemic bipinnatin J (**1**), obtained by total synthesis[17], with methanol under slightly acidic conditions gave *O*-Methyl bipinnatin J (**7**). The latter has been isolated before, in enantiomerically pure form, from a methanolic extract of *Pseudopterogorgia bipinnata*[18]. Oxidation of **7** with singlet oxygen yielded the sensitive diene dione **8**, which, being an ether, cannot undergo acetal formation. Structurally, it resembles the known diene-dione natural products coralloidolide E and isoepilophodione B[19,20]. We reasoned that conjugate attack of a molecule of water at C8 of **8** could give rise to enol acetal **9**, which bears the requisite functional groups for a photochemical [2 + 2] cycloaddition. If successful, this reaction would yield cyclobutane derivative **10**, a close congener of bielschowskysin.

To mimic Caribbean sunlight, we decided to use a reptile lamp, a type of light source that is known for its significant UV content. Irradiation of **8** in a 1:1 mixture of deuterated acetone and water with a commercially available reptile lamp (nominal power consumption of 275 W) yielded two isolable products. To our considerable surprise, one of them was intricarene (**4**), isolated with a yield of 25%, whereas the other one was hydroxy cyclopentenone **11**, which was isolated with a yield of 15%. The X-ray structures of racemic compounds **4** and **11** are shown in Fig. 4. Structural data of racemic **4** and **11** have been deposited

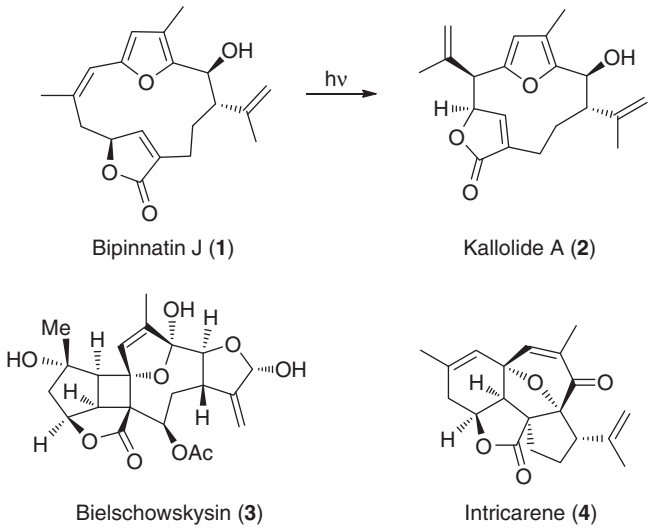

Figure 1 | Photochemically formed natural products. The natural products relevant to the present work are shown.

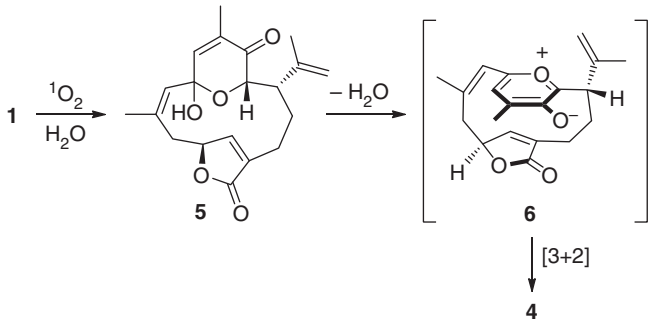

Figure 2 | Biosynthetic relationship of bipinnatin J and intricarene. Achmatowizc-type oxidation of bipinnatin J, followed by dehydration and 1,3-dipolar cycloaddition was proposed to account for the formation of intricarene.

NATURE COMMUNICATIONS | DOI: 10.1038/ncomms6597 ARTICLE

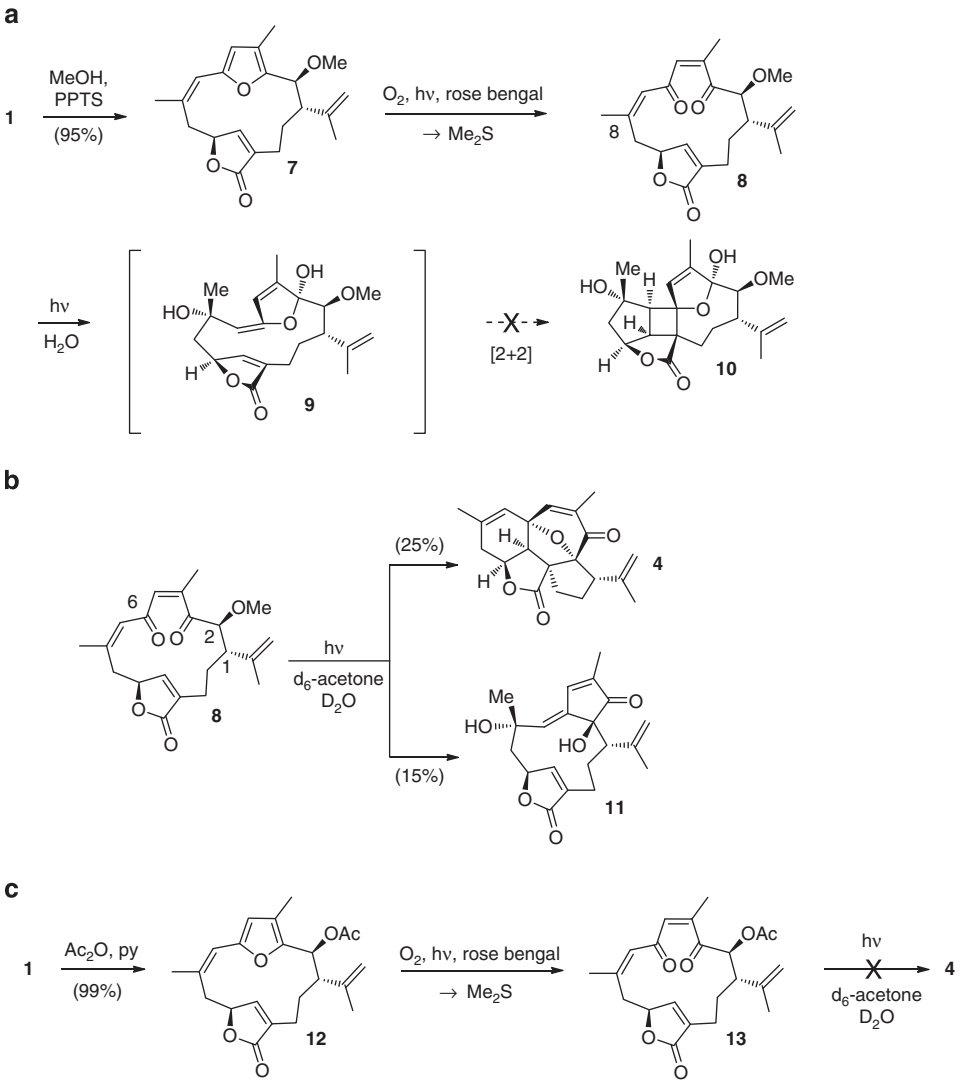

Figure 3 | Overview of the synthetic route from bipinnatin J (1) to intricarene (4) and hydroxy cyclopentenone 11. (**a**) Attempted synthesis of the bielschowskysin skeleton via conjugate addition of water and photochemical interception of the presumed intermediate. Conversion of bipinnatin J (**1**) to its methyl ether **8** via S_N1 reaction was followed by oxidative cleavage of the furan ring to yield diene dione **8**. Conjugate addition of water was supposed to yield **9** and enable a photochemical [2 + 2] cycloaddition to form the central four-membered ring of bielschowskysin. (**b**) Unexpected formation of intricarene (**4**) and hydroxy cyclopentenone **11** under photochemical conditions. (**c**) Synthesis of acetate **12** and diene-dione **13** and failure to yield intricarene under identical photochemical conditions.

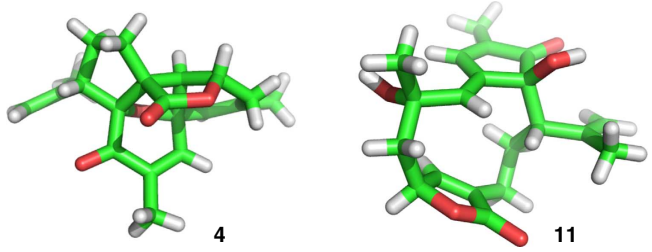

Figure 4 | X-ray structures of the final products. X-ray structure of racemic intricarene (**4**) and hydroxy cyclopentenone **11**.

with the Cambridge Crystallographic Data Centre (CCDC accession numbers 1026998 and 1026997, respectively). The photochemical procedure was highly reproducible provided the reptile lamp was used. Notably, it failed when other substrates, such as acetal **5** and acetate **13**, were employed.

Identification of the photo-induced reaction path. Our experimental results raise interesting mechanistic and biosynthetic questions, which we decided to address with photophysical considerations and quantum chemical calculations at the CASSCF/CASPT2 and DFT/TDDFT level of theory[21]. Solvation effects (water) were incorporated implicitly by single-point calculations of the optimized gas phase geometries using the state-specific polarizable continuum model (PCM, see Supplementary Table 4). As intersystem crossing plays a key role in photochemistry[22,23] and intermediate triplet states can be involved in light-induced cycloadditions[24,25], we investigated the singlet as well as the triplet states of the initially excited **8**. As a first step, we measured the emission spectrum of the reptile lamp to compare it with the calculated and experimentally determined absorption spectrum of our starting materials and postulated key intermediates. As can be seen in Fig. 5, the lamp spectrum has sharp lines in the visible and UV-A region of the electromagnetic spectrum and only negligible contributions below 360 or above 700 nm. The peak emissions at $\lambda_{max} = 366$, 405, 436, 492, 546, 578 and 679 nm can all be

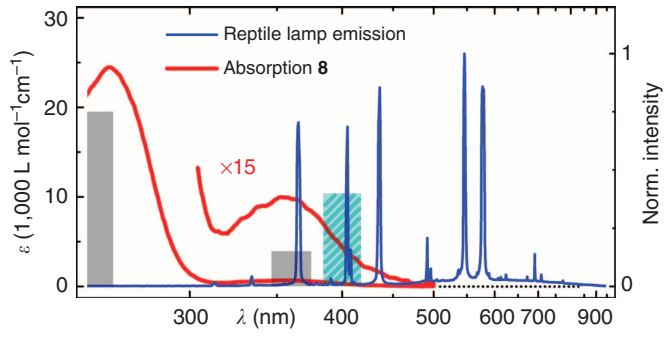

Figure 5 | Comparison of the precursor absorption spectrum with the illumination spectrum and the calculated transitions. Emission spectrum of the reptile lamp (blue). Absorption of **8** (red) and calculated transitions for **8** (grey bars) and **6** (cyan bar).

assigned to Hg emissions. This means that UV-B light is virtually absent in this type of lamp, presumably due to the type of glass used for the outer bulb. To determine the irradiance applied in the photochemical synthesis, we determined the light intensity at a distance of 15 cm in front of the lamp (see Supplementary Discussion). This geometry corresponds to the synthetic conditions. Standard chemical actinometry proved applicable only to a limited extent due to the high intensity of the lamp and the constrained geometry of the NMR tube used as vessel. It therefore provides only a lower boundary. For comparison photometry was also employed that provides an upper boundary for the irradiance.

The experimentally determined absorption spectrum of diene dione **8** shows a weak absorption band in the deep blue and UV-A region around $\lambda_{max} = 360$ nm and strong absorption around $\lambda_{max} = 265$ nm (Fig. 5). Only the weak absorption band (360 nm) matches with the emission of our reptile lamp. The photo-initiation of the conversion of **8** therefore has to proceed through the 360 nm transition.

In good agreement with the experiment, calculations reveal two absorption bands in the spectral region of interest (grey bars in Fig. 5; see Supplementary Methods (quantum chemical calculations) and Supplementary Table 1 and Fig. 3 for details). The most intense band is attributed to an intense $\pi\pi^*$ transition from the S_0 to the S_4 state at 260 nm with partial charge transfer character. As the reptile lamp used does not emit in the UV-B region, however, it is irrelevant and we focus on the 360-nm band.

For the synthesis the solution of **8** was contained in a standard NMR tube with 4.2 mm inner diameter. We determined the maximum of the molar absorption coefficient of **8** to $\varepsilon_{265\,nm} = 24{,}500\,l\,mol^{-1}\,cm^{-1}$. This renders a value of $670\,l\,mol^{-1}\,cm^{-1}$ for $\varepsilon_{360\,nm}$ and a penetration depth of the UV-A light on the order of 1 mm (see Supplementary Fig. 1). As a consequence, certainly all of the light that spectrally overlaps with the 360 nm band (the strong lines at 366, 405 and 436 nm) and penetrates the reaction vessel is absorbed by the bulk sample. The total number of absorbed photons during the 8 h irradiation time is $>2 \times 10^{21}$ according to the actinometry and $<1.2 \times 10^{22}$ according to the photometry. This photon number has to be compared with the total of 1.7×10^{19} molecules of **8** in the 1 ml sample with a concentration of $28\,mmol\,l^{-1}$. Nominally, this means that each molecule would be excited on average >120 times and <700 times. Even if the photochemical quantum yield is as low as 0.01 due to an efficient photophysical return path to the ground state of **8**, practically all molecules will undergo the photochemical conversion in accord with the experimental observation. The long irradiation time ensures that the molecules are sufficiently exchanged by diffusion or most likely convection.

Quantum chemical analysis of the reaction path. Our rationalization of the photochemical formation of intricarene (**4**) and its by-product **11** from diene dione **8** is shown in Fig. 6. Irradiation of **8** with UV-A light initially populates the excited singlet state **8**(S_1). From the quantum chemical calculations, we find that at the Franck-Condon region the S_1 and the T_4 state of **8** are degenerate (Fig. 6a). Their spin-orbit coupling has a reasonable size of about $30\,cm^{-1}$, consequently effective sub-ps intersystem crossing (ISC) can occur[26]. The resulting excited triplet state **8**(T_4) then crosses the transition state TS1(T_1), which describes the homolytic bond cleavage of the methoxy group, to yield a triplet diradical **14**(T_1). This step corresponds to a photochemical cleavage of an α-carbon-heteroatom bond, a well-known process in carbonyl photochemistry[27]. In case the barrier is not passed and the system relaxes back to the ground state, it can be re-excited and has again the possibility to cross the barrier with a finite probability. The large number of excitation probabilities for each molecule (see above) should allow the system to effectively overcome this barrier. In case no ISC takes place, the system will relax to the S_1 state minimum as high-energy barriers hinder the bond cleavage reaction in the singlet state. In the vicinity of the S_1 minimum a S_1/S_0 conical intersection seam is reached leading the system again back to the ground state (see Supplementary Table 28).

Once formed, the triplet diradical **14**(T_1) undergoes hydrogen transfer via the transition state TS2(T_1) to yield triplet oxidopyrylium **6**(T_1) and methanol. According to our calculations, the oxidopyrylium **6**(T_1) in its triplet state has two possible fates: initial bond formation between C6 and C11, via transition state TS3(T_1), yields triplet diradical **15**(T_1), which undergoes intersystem crossing and a second bond formation to furnish intricarene (**4**) (pathway ①). Overall, this amounts to a stepwise cycloaddition.

Alternatively, relaxation of **6**(T_1) to the oxidopyrylium ground state **6**(S_0) can occur (pathway ②). The calculated absorption spectrum of **6**(S_0) at $\lambda_{max} = 405$ nm is well-matched with the emission spectrum of the reptile lamp (see Fig. 5, cyan bar; see Supplementary Table 5 and Fig. 4 for details), allowing it to undergo another photochemical reaction. After excitation to **6**(S_2) a low lying conical intersection seam connecting all three singlet states S_2, S_1 and S_0 can be reached. The geometry leading to the formation of epoxy cyclopentenone **16** is marked as S_1/S_0-CoIn in Fig. 6b (see Supplementary Tables 6 and 33). From a more synthetic point of view, this process can be classified as a disrotatory electrocyclization in the excited state. From **6**(S_2), the formation of intricarene (**4**) can also occur via the T_1 state and via conical intersections among the singlet states.

In the presence of water, the vinyl epoxy cyclopentenone **16** is presumably highly unstable. We propose that it undergoes vinylogous nucleophilic substitution to afford the experimentally observed hydroxy cyclopentenone **11**.

Our mechanism for the formation of the oxidopyrylium via homolytic bond cleavage in the excited state explains why the reaction can take place in the presence of water and why the acetate **13** failed to yield intricarene. The bond dissociation energy (BDE) of methanol ($DH_{298} = 104.6 \pm 0.7$ kcal mol^{-1}) is significantly lower than that of water ($DH_{298} = 118.82 \pm 0.07$ kcal mol^{-1}). In contrast, homolytic cleavage of the acetate **13** would yield a highly unstable acetoxy radical (the BDE of acetic acid is $DH_{298} = 112 \pm 3$ kcal mol^{-1}) and is therefore less favourable than the homolytic cleavage of methyl ether **8** (ref. 28).

Discussion

Our work raises interesting questions regarding the classification of intricarene as a natural product. We define a natural product as

NATURE COMMUNICATIONS | DOI: 10.1038/ncomms6597 ARTICLE

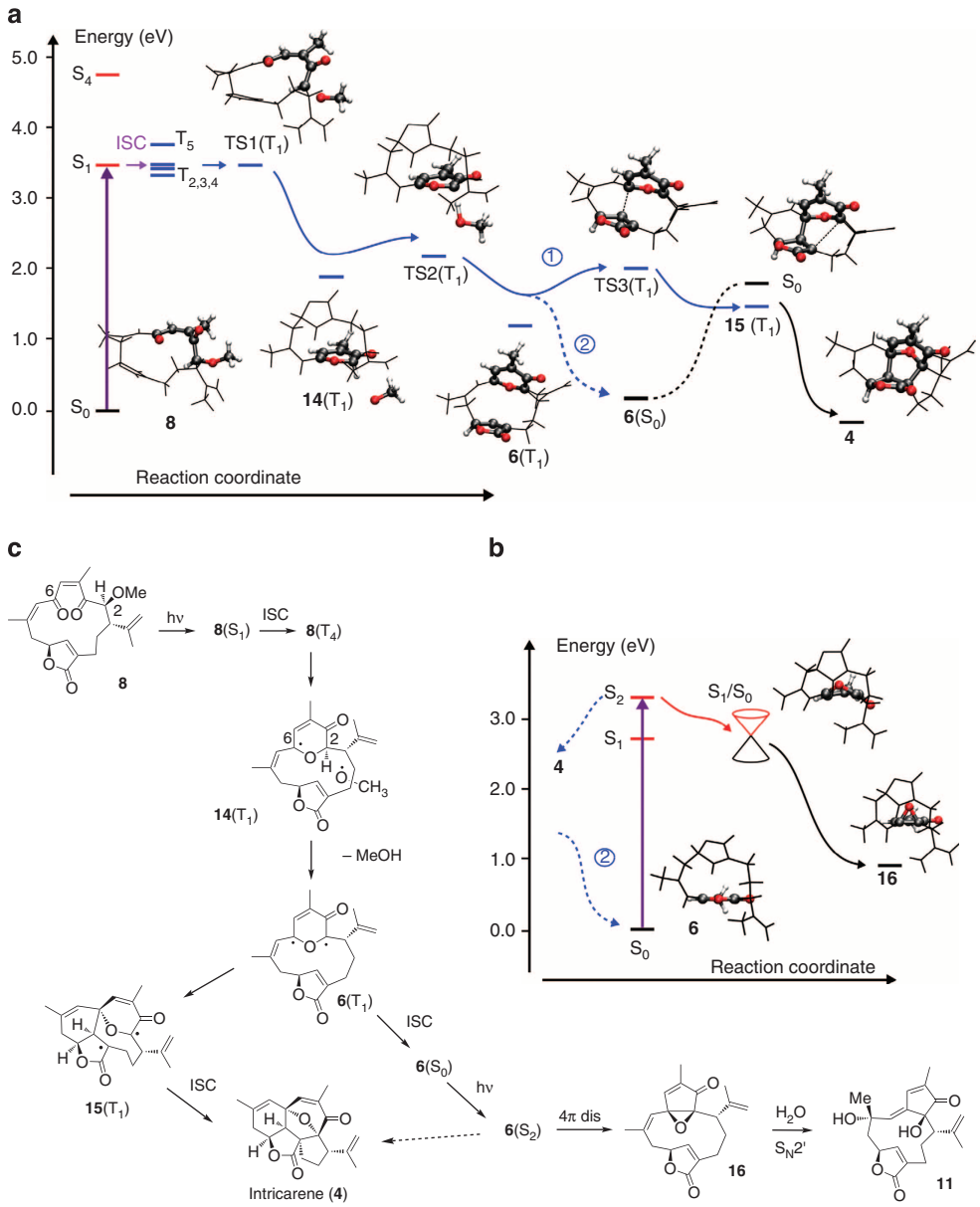

Figure 6 | Overview of all reactions steps for the proposed mechanism. (**a**) Calculated reaction path for photo-excited **8**. Shown are the ΔG values (in eV) for the isolated molecules. Excitation of **8** with UV-A light and sub-ps ISC to the degenerate T4 state and IC to the T1 state allows the formation of the intermediate diradical **14**(T_1). Next, a hydrogen atom is transferred to afford the triplet diradical **6**(T_1). This intermediate either undergoes a stepwise 1,3 dipolar cycloaddition, including an ISC, to afford **4** (pathway ①), or relaxes to the ground state oxidopyrylium **6**(S_0) (via pathway ②). (**b**) Oxidopyrylium **6**(S_0) can undergo further photochemical reactions. After excitation with blue light to the S2 state, a S1/S0 conical intersection seam can lead to epoxy cyclopentenone **16** in a reaction that could be interpreted as a conrotatory 4π-electrocyclization. (**c**) Graphical representation of the reaction path. Vinylogous nucleophilic substitution with water affords **11** from **16**.

a compound that is present within or in the immediate vicinity of the producing organism. As such, many compounds that are spontaneously formed from reactive intermediates, for instance *via* cascade reactions[29–34], can indeed be classified as natural products. Our hypothetical starting material *O*-Methyl bipinnatin J (**7**), however, has been suspected to be an isolation artefact as methanolysis of bipinnatin J (**1**) and of kallolide (**2**) is a very facile process[18]. In addition, while **4** could biosynthetically formed from **1** and *S*-adenosyl methionine by an *O*-methyl transferase, it is conspicuous that **4** is the only C2 methyl ether known in the entire furanocembranoid series[35].

In the course of the isolation of intricarene, *P. kallos* was partially sun-dried (with indirect sunlight), frozen and lyophilized before extraction[6]. The dry organism was blended using a 1:1 mixture of dichloromethane and methanol. This suggests that the photochemical oxidation and cycloaddition could have taken place during workup. In contrast, clear sea water is known to only weakly attenuate UV-A/blue light[36,37]. Thus, at a depth of 25–28 m, where the octocoral was collected, the intensity of incident UV-A and blue light is still well within the range of indirect sunlight at sea level and high enough to promote the proposed photochemistry over time (see Supplementary Fig. 2 and Supplementary Discussion (Irradiance in the natural habitat of the coral)). All things considered, we cannot decide whether intricarene is a genuine natural product according to the definition given above or an isolation artefact that was formed in the course of the isolation/purification procedure. This question could be settled by isolating intricarene under

conditions that rigorously exclude air, intense light and methanol during workup.

In sum, our work provides a rationale for the formation of intricarene, which is based on photochemistry and overcomes the need to invoke a thermally challenging 1,3-dipolar cycloaddition. Our quantum chemical calculations provide detailed insights into the largely unexplored excited state chemistry of oxidopyrylium species. Finally, our results demonstrate that photochemical reactions, especially reaction cascades that proceed through a series of intermediates, need to be properly matched to the emission spectrum of the lamp used. As absorption spectra of putative intermediates can nowadays be calculated with relative ease, detailed information on the light source will greatly facilitate the planning and execution of photochemical reactions.

References

1. Dewick, P. M. *Medicinal Natural Products* (John Wiley & Sons, 2009).
2. Rodríguez, A. D. & Shi, J.-G. The first cembrane – pseudopterane cycloisomerization. *J. Org. Chem.* **63,** 420–421 (1998).
3. Look, S. A., Burch, M. T., Fenical, W., Zheng, Q. & Clardy, J. Kallolide A, a new antiinflammatory diterpenoid, and related lactones from the Caribbean octocoral *Pseudopterogorgia kallos* (Bielschowsky). *J. Org.Chem.* **50,** 5741–5746 (1985).
4. Weinstabl, H., Gaich, T. & Mulzer, J. Application of the Rodriguez–Pattenden photo-ring contraction: total synthesis and configurational reassignment of 11-Gorgiacerol and 11-Epigorgiacerol. *Org. Lett.* **14,** 2834–2837 (2012).
5. Marrero, J. *et al.* Bielschowskysin, a Gorgonian-derived biologically active diterpene with an unprecedented carbon skeleton. *Org. Lett.* **6,** 1661–1664 (2004).
6. Marrero, J., Rodríguez, A. D. & Barnes, C. L. Intricarene, an unprecedented trispiropentacyclic diterpene from the caribbean sea plume *Pseudopterogorgia kallos*. *Org. Lett.* **7,** 1877–1880 (2005).
7. Roethle, P. A., Hernandez, P. T. & Trauner, D. Exploring biosynthetic relationships among furanocembranoids: synthesis of (−)-bipinnatin J, (+)-intricarene, (+)-rubifolide, and (+)-isoepilophodione B. *Org. Lett.* **8,** 5901–5904 (2006).
8. Tang, B., Bray, C. D. & Pattenden, G. A biomimetic total synthesis of (+)-intricarene. *Tetrahedron Lett.* **47,** 6401–6404 (2006).
9. Doroh, B. & Sulikowski, G. A. Progress toward the total synthesis of bielschowskysin: a stereoselective [2 + 2] photocycloaddition. *Org. Lett.* **8,** 903–906 (2006).
10. Miao, R., Gramani, S. & Lear, M. Stereocontrolled entry to the tricyclo[3.3.0]oxoheptane Core of bielschowskysin by a [2 + 2] cycloaddition of an allene-butenolide. *Tetrahedron Lett.* **50,** 1731–1733 (2009).
11. Nicolaou, K. C., Adsool, V. & Hale, C. An expedient synthesis of a functionalized core structure of bielschowskysin. *Angew. Chem. Int. Ed.* **50,** 5149–5152 (2011).
12. Farcet, J.-B., Himmelbauer, M. & Mulzer, J. A non-photochemical approach to the bicyclo[3.2.0]heptane core of bielschowskysin. *Org. Lett.* **14,** 2195–2197 (2012).
13. Himmelbauer, M., Farcet, J.-B., Gagnepain, J. & Mulzer, J. A palladium-catalyzed carbo-oxygenation: the bielschowskysin case. *Org. Lett.* **15,** 3098–3101 (2013).
14. Townsend, S. D. & Sulikowski, G. A. Progress toward the total synthesis of bielschowskysin. *Org. Lett.* **15,** 5096–5098 (2013).
15. Yang, E. G., Sekar, K. & Lear, M. J. A macrolactonisation approach to the cembrane carbocycle of bielschowskysin. *Tetrahedron Lett.* **54,** 4406–4408 (2013).
16. Wang, S. C. & Tantillo, D. J. Theoretical studies on synthetic and biosynthetic oxidopyrylium – alkene cycloadditions: pericyclic pathways to intricarene. *J. Org. Chem.* **73,** 1516–1523 (2008).
17. Roethle, P. A. & Trauner, D. Expedient synthesis of (±)-bipinnatin j. *Org. Lett.* **8,** 345–347 (2006).
18. Rodríguez, A. D., Shi, J.-G. & Shi, Y.-P. Isolation, structural characterization, and synthesis of a naturally occurring bisfuranopseudopterane ether: biskallolide A. Evidence for a carbocation intermediate during the facile conversion of kallolide A and isokallolide A into various solvolysis products. *J. Org. Chem.* **65,** 3192–3199 (2000).
19. Ambrosio, M. D., Guerriero, A. & Pietra, F. Novel cembranolides (coralloidolide D and E) and a 3,7-cyclized cembranolide (coralloidolide C) from the mediterranean coral *Alcyonium coralloides*. *Helv. Chim. Acta* **72,** 1590–1596 (1989).
20. Williams, D., Andersen, R. J., Van Duyne, G. D. & Clardy, J. Cembrane and pseudopterane diterpenes from the soft coral *Gersemia rubiformis*. *J. Org. Chem.* **52,** 332–335 (1987).
21. Olivucci, M. *Computational Photochemistry* (Elsevier B.V., 2005).
22. Klessinger, M. & Michl, J. *Excited States and Photochemistry of Organic Molecules* (VHC Publisher Inc, 1995).
23. Marian, C. M. Spin-orbit coupling and intersystem crossing in molecules. *WIREs Comput. Mol. Sci.* **2,** 187–203 (2012).
24. Griesbeck, A. G., Abe, M. & Bondock, S. Selectivity control in electron spin inversion processes: regio- and stereochemistry of paternò-büchi photocycloadditions as a powerful tool for mapping intersystem crossing processes. *Acc. Chem. Res.* **37,** 919–928 (2004).
25. Serrano-Pérez, J. J., Merchán, M. & Serrano-Andrés, L. Photoreactivity of furocoumarins and DNA in PUVA therapy: formation of psoralen-thymine adducts. *J. Phys. Chem. B* **112,** 14002–14010 (2008).
26. Richter, M., Marquetand, P., González-Vázquez, J., Sola, I. & González, L. Femtosecond intersystem crossing in the DNA nucleobase cytosine. *J. Phys. Chem. Lett.* **3,** 3090–3095 (2012).
27. Albini, A. & Fagnoni, M. *Photochemically-Generated Intermediates in Synthesis* 74–75 and 145–147 (John Wiley & Sons, 2013).
28. Blanksby, S. J. & Ellison, G. B. Bond dissociation energies of organic molecules. *Acc. Chem. Res.* **36,** 255–263 (2003).
29. Grondal, C., Jeanty, M. & Enders, D. Organocatalytic cascade reactions as a new tool in total synthesis. *Nat. Chem.* **2,** 167–178 (2010).
30. Nicolaou, K. C. & Chen, J. S. The art of total synthesis through cascade reactions. *Chem. Soc. Rev.* **38,** 2993–3009 (2009).
31. Volgraf, M. *et al.* Biomimetic Synthesis of the IDO inhibitors exiguamine A and B. *Nat. Chem. Bio.* **4,** 535–537 (2008).
32. Strych, S. & Trauner, D. Biomimetic synthesis of santalin A, B and santarubin A, B, the major colorants of red sandalwood. *Angew. Chem. Int. Ed.* **52,** 9509–9512 (2013).
33. Sofiyev, V., Navarro, G. & Trauner, D. Biomimetic Synthesis of the Shimalactones. *Org. Lett.* **10,** 149–152 (2008).
34. Beaudry, C. M. & Trauner, D. Total Synthesis of (−)-SNF4435 C and (+)-SNF4435 D. *Org. Lett.* **7,** 4475–4477 (2005).
35. Roethle, P. A. & Trauner, D. The chemistry of marine furanocembranoids, pseudopteranes, gersolanes, and related natural products. *Nat. Prod. Rep.* **25,** 298–317 (2008).
36. Armstrong, F. A. J. & Boalch, G. T. The ultra-violet absorption of sea water. *J. Mar. Biol. Ass. UK* **41,** 591–597 (1961).
37. Hargreaves, B. R. Helbling, E. W. & Zagarese, H. E. (eds) *Comprehensive Series in Photochemical and Photobiological Sciences* (Royal Society of Chemistry, 2003).

Acknowledgements

We thank the Deutsche Forschungsgemeinschaft (SFB749) for financial support.

Author contributions

D.S. and T.J.K. performed the synthetic work and analysed the obtained products. D.T. devised the study. P.K. performed the quantum chemical calculations. E.R. devised and accompanied the photophysical aspects of the study. D.T., P.K., E.R. and R.dV.-R. wrote the manuscript.

Additional information

Accession codes: The X-ray crystallographic coordinates for structures reported in this article have been deposited at the Cambridge Crystallographic Data Centre (CCDC), under deposition numbers CCDC 1026998 and 1026997. These data can be obtained free of charge from The Cambridge Crystallographic Data Centre via http://www.ccdc.cam.ac.uk/data_request/cif.

Supplementary Information accompanies this paper at http://www.nature.com/naturecommunications

Competing financial interests: The authors declare no competing financial interests.

Reprints and permission information is available online at http://npg.nature.com/reprintsandpermissions/

How to cite this article: Stichnoth, D. *et al.* Photochemical formation of intricarene. *Nat. Commun.* 5:5597 doi: 10.1038/ncomms6597 (2014).

4.2. Photocycloaddition of dactylone to aplydactone

Other marine organisms exhibiting various bioactive molecules are sea mollusks [128, 129, 134–136]. Mollusks of the genus *Aplysia* feed on red algae who are the main producer of halogenated sesquiterpenoids. In this way the mollusks accumulate large amounts of halogenated sesquiterpenoids and protect themselves from predators [137]. For a variety of the sesquiterpenoids interesting properties like bactericidal [135], antifouling [138], insecticidal [139] and antitumor activity [140] were detected.

The two sesquiterpenoids dactylone (**1**) and aplydactone (**2**) were isolated from the sea hare *Aplysia dactylomela* [29,30]. While dactylone displays cancer inhibiting activity [141], the pharmacological properties of aplydactone were not yet investigated. Both compounds are still available only in small amounts as for both no total synthesis has been achieved until now. The biosynthesis of aplydactone **2** is proposed to proceed by a photochemical [2+2] cycloaddition out of dactylone **1** [30].

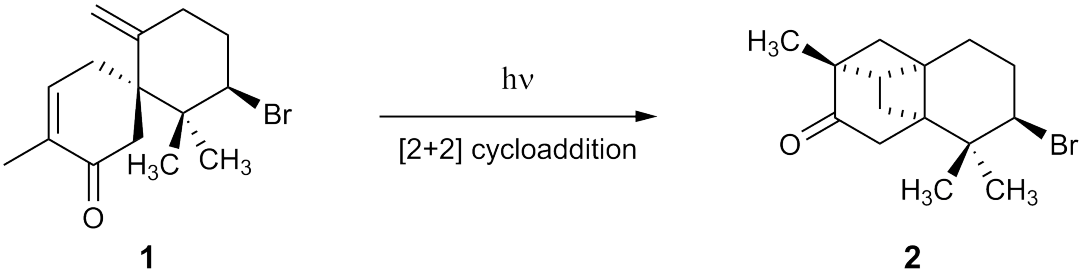

1 **2**

Figure 4.1.: Proposed biosynthesis of aplydactone **2** from dactylone **1**.

However, attempts to synthesize **2** through long-term UV irradiation of **1** failed [30]. A possible explanation for this was proposed by Dirk Trauner. The UV irradiation might have excited the strong absorption bands of the precursor **1**. As shown for intricarene in chapter 4.1 this could have led to the population of the wrong excited states to enable the photochemical reaction and the formation of the product. In addition, for intricarene it was demonstrated that for a biomimetic synthesis the absorption spectrum of the precursor needs to be properly matched to the solar spectral irradiation.

Inspired by the results of intricarene and the suggestion of Dirk Trauner, in this chapter the photochemical [2+2] cycloaddition of dactylone to aplydactone is studied by quantum chemical calculations. The major aim is to elucidate the conditions to allow for the photochemical synthesis of aplydactone. For this purpose in the first section a brief outline of the established reaction mechanism of [2+2] photocycloaddition of enones is given as the precursor **1** contains the characteristic enone moiety. In the next section the absorption spectrum and the crucial excited states of the precursor are analyzed. Subsequently, the photophysical relaxation pathway to the starting point of the cycloaddition is elucidated. The following section covers the photochemical reaction leading to the formation of **2**. In the last section the conclusion and the connection to the biomimetic formation of intricarene is given. The following results are based on the bachelor thesis of Jerome Ring [142].

4.2.1. Intramolecular [2+2] photocycloadditions of enones

The [2+2] photocycloaddition is probably the most important and most frequently used photochemical reaction [143]. In synthetic organic chemistry the photochemical cycloaddition of cyclic and acyclic α,β-unsaturated ketones (enones) is widely applied for the assembly of cyclobutane derivatives [144, 145]. Moreover, intramolecular photocycloadditions are in contrast to intermolecular ones, usually highly regio- and stereoselective [146]. The underlying reaction

mechanism of intramolecular photocycloadditions of enones is illustrated in figure 4.2. Typically,

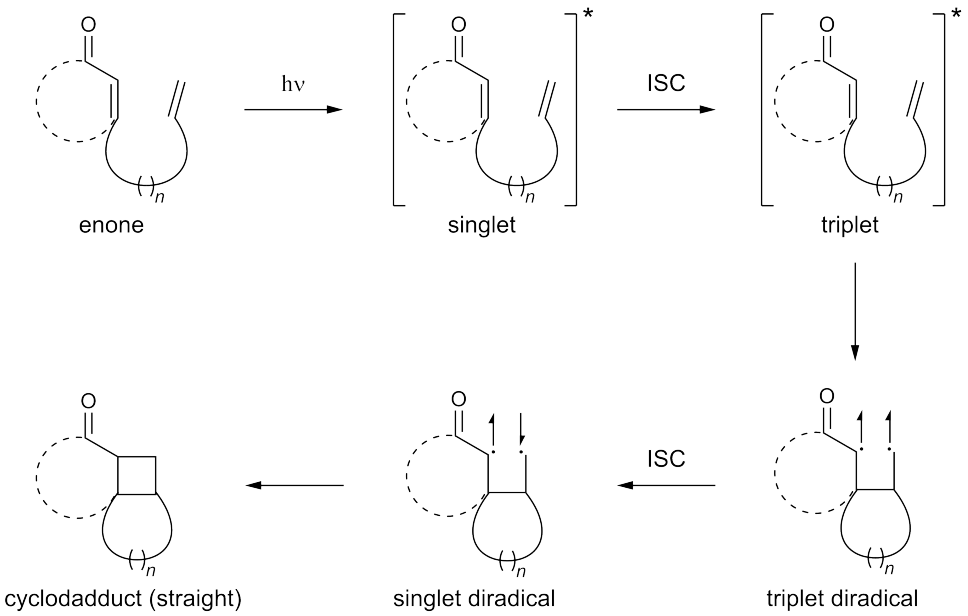

Figure 4.2.: Reaction mechanism of intramolecular [2+2] photocycloadditions of enones.

enones can be directly excited to the their first excited singlet state from which a rapid ISC to the respective triplet state can occur. The long lifetime of triplet states allow an intramolecular attack of the ethylene moiety to generate a triplet 1,4-diradical intermediate. Subsequent ISC to the singlet hypersurface leads to a singlet diradical (^{1}DR) which finally can furnish the cycloadduct [143]. Thereby two different regioisomers are possible depending on whether a straight or crossed attack of the ethylene moiety on the enone moiety occurs (see fig. 4.3). The regioselectivity outcome of [2+2] photocycloaddition is often rationalized by the "rule of five" which states that the formation of diradical intermediates exhibiting a five-membered ring is favored [147–149]. Therefore if the tether length between the ethylenic bonds is only two atoms ($n = 2$), the generation of the crossed cycloadduct is preferred. In the case the tether link is $n = 3$ or $n = 4$, the formation of the straight cycloadduct prevails [143]. For the precursor **1** the tether length is $n = 2$ and therewith the formation of the crossed cycloadduct should be favored according to the "rule of five". But only the straight attack of the ethylene moiety leads to the natural product aplydactone **2**. However, exceptions to the rule are known and instead the regioselectivity is explained by "diradical conformation control" [150, 151].

While computational studies of intermolecular [2+2] photocycloadditions are abundant in the literature [152–154], no corresponding one for an intramolecular photocycloaddition has been reported. In the following the intramolecular [2+2] photocycloaddition of dactylone to aplydactone, including the regioselectivity outcome of the reaction, is investigated by quantum chemical calculations.

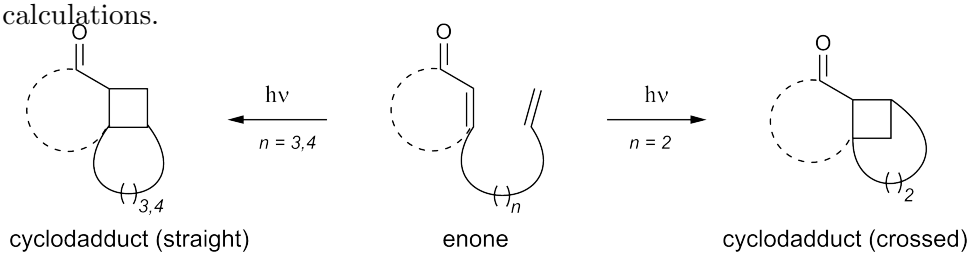

Figure 4.3.: Regioselectivity preferences in intramolecular [2+2] photocycloadditions of enones in dependency of the tether length between the ethylenic bonds [143].

4.2.2. Vertical excited states of the precursor dactylone

First, based on their crystal structures the ground states geometries of **1** and **2** were optimized at the B3LYP/6-31G* level of theory (fig. 4.4). In figure 4.5 it can be seen that the distances between the carbon atoms for both, the straight and the crossed attack of the ethylene moiety on the enone moiety, are already relatively small in the precursor.

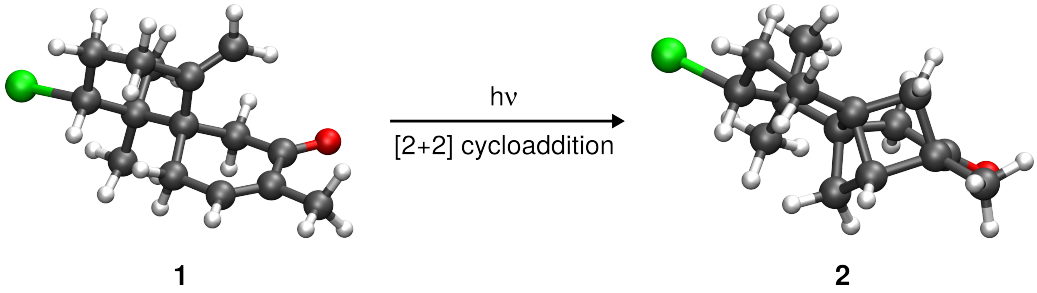

Figure 4.4.: Optimized B3LYP/6-31G* ground state structures of the precursor **1** and aplydactone **2**.

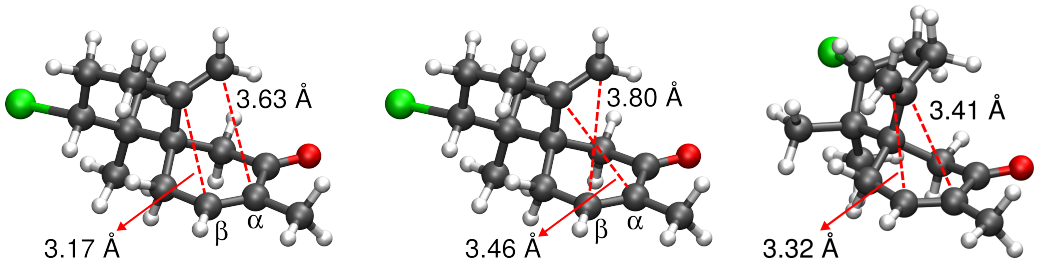

Figure 4.5.: Inter-carbon distances for the straight (left) and the crossed attack (middle) of the ethylene moiety on the enone moiety present in the precursor **1**. On the right the inter-carbon distances for the crossed attack from a conformer of **1** are shown.

However, the distances for the straight attack are somewhat smaller than for the crossed attack indicating a preference for the formation of the desired natural product **1**. Only a rotation about the carbon-carbon bond connecting the cyclohexenone and the ethylene moiety leads to a conformation where the crossed attack should be favored (fig. 4.5, right). But the optimized geometry of this conformer is 0.26 eV higher in energy in terms of ΔG than the optimized conformation present in the crystal structure of **1**. The corresponding calculated equilibrium constant[1] of $3.8{\cdot}10^3$ clearly reveal that the conformer preferring the straight attack, is present in an excess in the ground state and therefore the other conformer is neglected in the following.

The vertical excited states at the ground state minimum of **1** were computed with the CASPT2, the CCSD and the TDDFT method. The comparison of the results is given in table 4.1. The orbitals describing the important excited states are shown in figure B.1 in appendix B. The first excited singlet state S_1 has $n\pi^*$ character and a very low oscillator strength and is similar in energy across all methods. Moreover, for all methods a higher lying excited singlet state (S_4) with $\pi\pi^*$ character and a considerable oscillator strength exist. With the computationally cheap TDDFT method it was in addition possible to calculate higher lying excited singlet states. The resulting absorption spectrum is visualized in figure 4.6 by plotting Gaussian functions around the electronic transitions.

Three important peaks are visible in the spectrum. The first, very weak peak around 320 nm corresponds to the S_1 state with $n\pi^*$ character while the second and stronger absorption band

[1]The equilibrium constant K was determined according to the equation $K{=}e^{-\frac{\Delta G}{RT}}$; T=298.15 K, R=gas constant.

Table 4.1.: Calculated vertical singlet and triplet excitation energies (eV) and oscillator strengths for the low-lying valence excited states of the precursor **1** at the ground state minimum. The first given state order corresponds to the CASPT2 and CCSD methods. The state order in parenthesis applies to the TDDFT method. CASPT2 and CCSD calculations were performed using the 6-31G* basis set and the TDDFT calculations using the CAM-B3LYP functional and the 6-311+G** basis set. As reference the measured absorption maximum of the precursor **1** is given [29].

		CASPT2		CCSD		TDDFT		
State	Character	ΔE	f	ΔE	f	ΔE	f	Exp.
S_1 (S_1)	$n_o \rightarrow \pi_4^*$	3.95	10^{-4}	4.01	10^{-4}	3.89	10^{-4}	—
S_2 (S_4)	$n_{Br1} \rightarrow \sigma_{Br}^*$	6.37	0.011	6.29	0.001	5.82	0.007	—
S_3 (S_5)	$n_{Br2} \rightarrow \sigma_{Br}^*$	6.43	0.019	6.34	0.002	5.88	0.001	—
S_4 (S_2)	$\pi_3 \rightarrow \pi_4^*$	6.77	0.469	6.47	0.168	5.47	0.094	5.25
S_5 (S_3)	$\pi_2 \rightarrow \pi_4^*$	—	—	6.92	0.032	5.75	0.077	—
S_7 (S_7)	$n_o \rightarrow \sigma_{Br}^*$	—	—	—	—	6.71	0.244	—
T_1	$n_o \rightarrow \pi_4^*$	3.70	—	3.58	—	3.10 (3.26[a])	—	—
T_2	$\pi_3 \rightarrow \pi_4^*$	3.96	—	3.83	—	3.35	—	—
T_3	$\pi_2 \rightarrow \pi_5^*$	4.68	—	4.55	—	3.86	—	—

[a] Calculated with the UB3LYP functional.

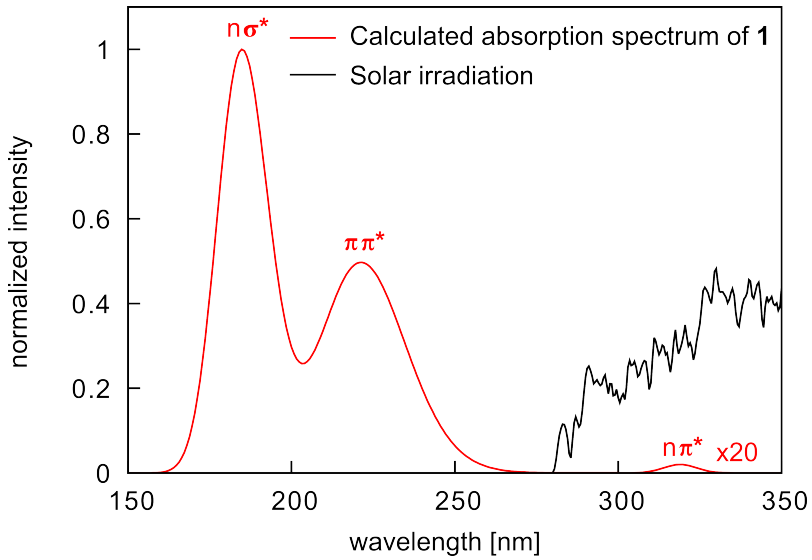

Figure 4.6.: Calculated TDDFT/6-311+G** normalized absorption spectrum of the precursor **1** and solar spectral irradiance AM 1.5 [155]. The spectrum was obtained by plotting Gaussian functions around the electronic transitions. The corresponding characters of the excited states are given and the interval from 300 to 340 is enhanced by a factor of 20.

around 220 nm is composed of two $\pi\pi^*$ excitations ($\pi_3\pi_4^*$ and $\pi_2\pi_4^*$, see tab. 4.1). The second absorption band is relatively close to the experimental absorption maximum of 236 nm [29]. The third, very intense peak around 190 nm is related to the S_7 state which is characterized by a charge transfer from the lone-pair of the oxygen atom to the antibonding σ^*-orbital of the carbon-bromine bond. Population of this state leads to an unwanted homolytic cleavage of the

bromine. Irradiation at the corresponding wavelength might have been the cause for the failed photochemical [2+2] cycloaddition approach of Fedorov *et al.* [30]. In figure 4.6 also the solar spectral irradation is plotted showing that only the weak absorption band is reachable by solar light. Therefore, the excitation into this band will initiate the photochemical reaction under biomimetic conditions and will be the starting point of the relaxation pathway of the precursor considered in the next section.

As shown in the section 4.2, intersystem crossing and triplet states play an important role in the mechanism of [2+2] photocycloadditions. Both, the CASPT2 and the CSSD method place the triplets state T_3 substantially above the S_1 state at the FC point, while the T_2 and T_1 lie only slightly below the S_1 (see tab. 4.1). The TDDFT method using the CAM-B3LYP functional underestimates the excited triplet energies and places also the T_3 state below the S_1 state. The somewhat to low excited triplet energies are a known problem for the TDDFT method caused by triplet instabilities [156, 157]. However, for the triplet "ground" state T_1 the unrestricted DFT method (UDFT) using the UB3LYP functional leads to qualitatively correct values [46]. Also for the precursor **1** a higher T_1 excitation energy is obtained with the UB3LYP functional, which is closer to the CASPT2 and the CSSD method (Tab. 4.1). Therefore, in the following for the investigation of the reaction pathway of the cycloaddition the CASSCF/CASPT2 and the UDFT method are used as the CCSD method is too expensive to describe the complete reaction path in a reasonable computational time.

4.2.3. Photophysical relaxation pathway of dactylone

Our rationalization of the photophysical relaxation pathway of the excited precursor **1** to the starting point of the cycloaddition is shown in figure 4.7. Alternative pathways leading back to ground state of the precursor and therewith interfering with the cycloaddition are show in figure 4.9.

After excitation to the S_1 ($n\pi^*$) state, its relaxation leads to a minimum (S_1-Min) exhibiting minor structural changes, mainly a slight elongation of the carbonyl bond. As a result, the state order remains the same as at the FC point and the triplet states T_1 and T_2 are still close in energy to the S_1 state (see tab. B.1 in appendix B). We further investigated the energy progression of the S_1 and three lowest lying triplet states by constructing a simplified reaction path RC_S by linear interpolation between the optimized S_0-Min and S_1-Min geometries. The calculated energies along RC_S reveal that the S_1, T_1 and T_2 states stay close in energy while the energy gap of the S_1 and the T_3 state even increases towards the S_1-Min (4.8a). To evaluate the ISC probability not only the energy gaps of the states involved have to be considered, but also the spin-orbit coupling (SOC) between them. We therefore calculated the SOC between the S_1 the three lowest lying triplet states along the reaction coordinate RC_S (4.8b).

The SOC value between the S_1 and the T_2 state is already strong at the FC point (25 cm^{-1}) and even increases towards the S_1-Min to a maximum value of 41 cm^{-1}. In contrast, for the T_1 and the T_3 state the SOC values are negligible along the complete relaxation coordinate. In view of the calculated SOC and the S_1-triplet energy gaps, a large ISC probability along the reaction coordinate RC_S exists for the S_1 with the T_2 state. As the transition from the S_1 ($n_o\pi_4^*$) to the T_2 ($\pi_3\pi_4^*$) state involves exactly one change of orbital type, this is in accordance with the selection rules for intersystem crossing known as *El Sayed's rules* [158].

In the case no ISC to the T_2 state occurs during the relaxation, the ISC can also be accomplished by a low lying S_1/T_2 intersection located in vicinity of the S_1-Min (S_1/T_2 IS in fig. 4.7). This intersection is characterized by rotation of the methyl group attached to the α-carbon atom and is only slightly higher in energy (0.05 eV) than S_1-Min. The S_1/T_2 crossing is therewith easily reachable from S_1-Min as already observed for other α,β-enones [159, 160].

Alternative processes to ISC occurring after excitation to the S_1 state of **1** are fluorescence or internal conversion. Fluorescence is highly unlikely as the oscillator strength of the S_1 state

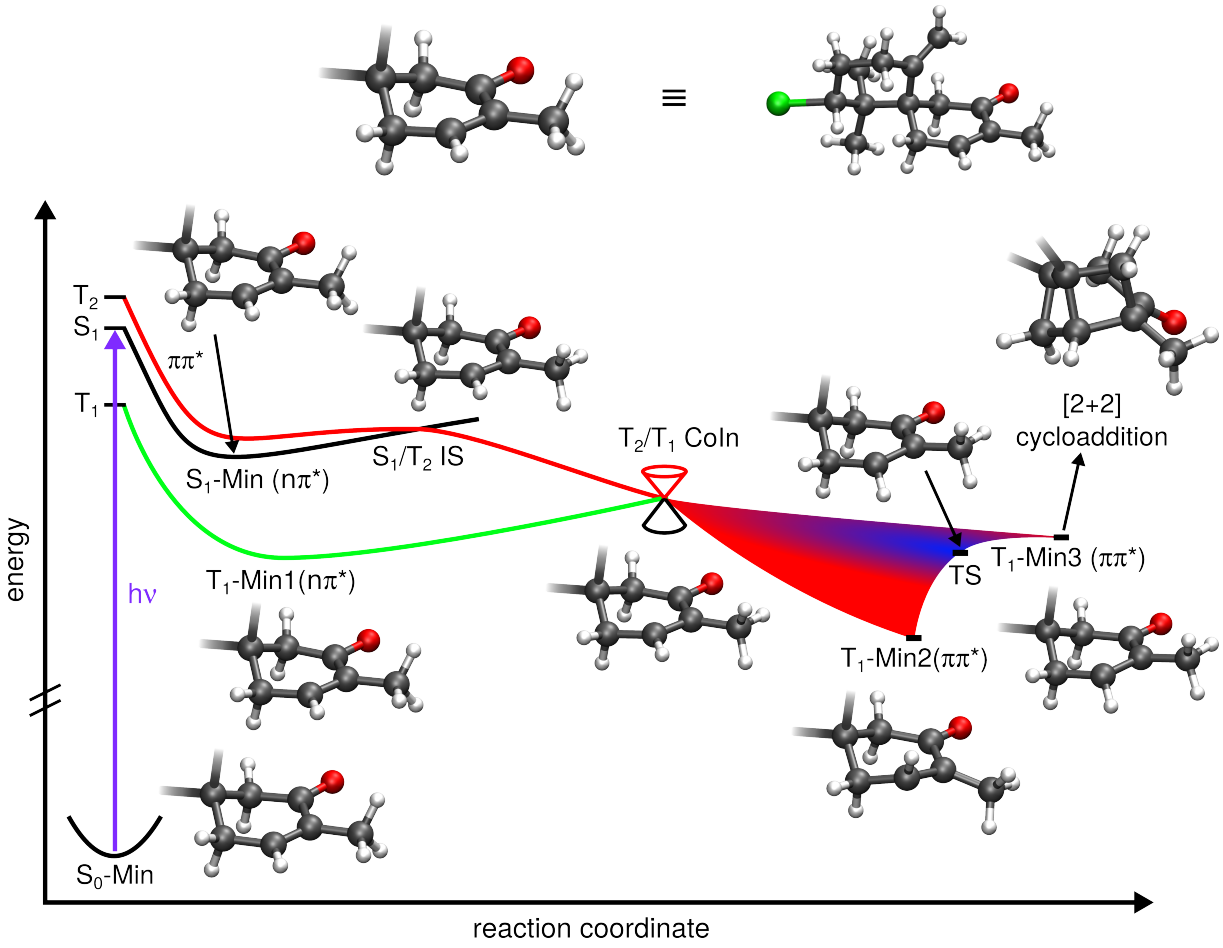

Figure 4.7.: Schematic illustration of the proposed relaxation pathway from the excited S_1 state of the precursor **1** to the starting point of the [2+2] cycloaddition (T_1-Min3). The electronic characters and relevant optimized geometries are given. The abbreviation of the molecular structure of **1** used for the schematic is shown at the top.

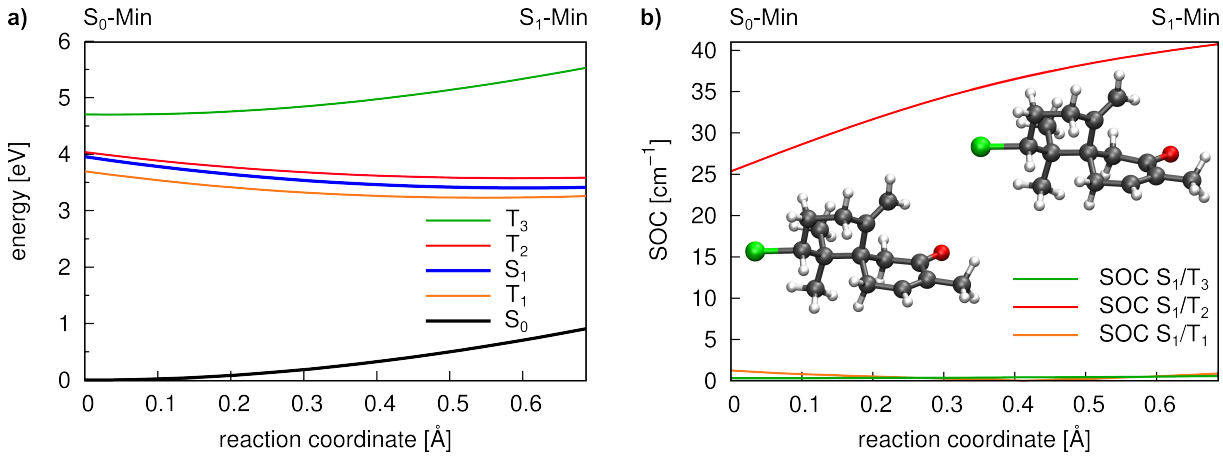

Figure 4.8.: Energy profile of the S_0, the S_1 and the three lowest lying triplet states (a) and SOC between the S_1 and the triplet states (b) along the S_1 relaxation coordinate of **1**. The energy calculations were performed at the CASPT2/6-31G* level of theory and the SOCs were calculated with the CASSCF method. The reaction coordinate was generated by linear interpolation between the optimized S_0-Min and S_1-Min geometries.

remains low (10^{-4}) during the relaxation. For an effective internal conversion from the S_1 state, a S_1/S_0 conical intersection has to be accessible. But the optimized S_1/S_0 CoIn is located 1.38 eV above the S_1-Min and is characterized by a strong bending of the hydrogen atom attached to the β-carbon atom and by a twisting of the cyclohexenone framework (fig. 4.9a). High barriers to access the relevant S_1/S_0 CoIns are a general feature observed in α,β-enones [159–161]. Consequently, upon direct excitation to the S_1 state, ISC is the major relaxation pathway of α,β-enones [162]. Also for the precursor **1** the main part of the S_1 population should undergo ISC to the triplet T_2 state.

Once crossed over into the T_2 ($\pi\pi^*$) state, an energetically close lying conical intersection with the T_1 state can be reached (T_2/T_1 CoIn in fig. 4.7). Here, the relaxation path splits into three branches. A relaxation into the T_1 minimum T_1-Min1 can happen which is accompanied by a change in character from the T_2 ($\pi\pi^*$) to the T_1 ($n\pi^*$) state and a rotation of the methyl group. Secondly, the system can preserve the $\pi\pi^*$ character and relax diabatically into T_1-Min2. The T_1-Min2 structure is described by a bending of the hydrogen atom attached to the β-carbon towards the ethylene moiety (see fig. 4.7). Finally, the molecule can relax diabatically into the second T_1 minimum with $\pi\pi^*$ character (T_1-Min3) by bending the same hydrogen atom under the cyclohexenone plane. The two $\pi\pi^*$ minima (T_1-Min2 and T_1-Min3) are slightly lower in energy than T_1-Min1 with $n\pi^*$ character (see tab. B.1 in appendix B). This should lead to a preferred population of them confirmed by dynamic simulations of small α,β-enones [160]. The two $\pi\pi^*$ minima on the T_1 potential energy surface are close in energy to each other and are connected *via* a transition state (TS in fig. 4.7) characterized by wagging of the hydrogen atom attached to the β-carbon. As the barrier to the transition state (TS) is small from both minima, the interchange between the structures should be strong.

For the cycloaddition to proceed the ethylene moiety has to attack from above the cyclohexenone ring and therewith the position of the hydrogen atom at T_1-Min3 under the ring plane

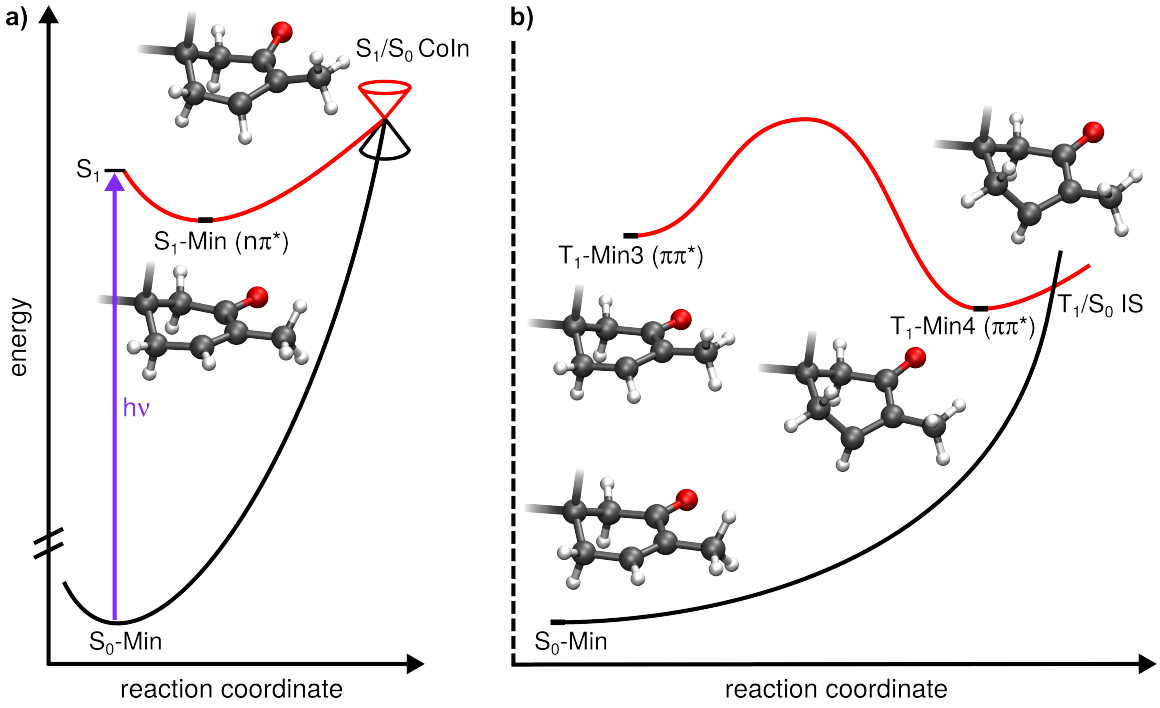

Figure 4.9.: Schematic illustration of the internal conversion *via* the S_1/S_0 conical intersection after excitation to the S_1 state of **1** (a). Alternative pathway to the cycloaddition from T_1-Min3 leading back to ground state of **1** (b). The relevant optimized geometries are shown.

allow the direct attack of the ethylene moiety. On the contrary, the hydrogen atom being above the ring present at T_1-Min2, prevent the direct attack and therefore starting from T_1-Min2 the system has first to cross the small barrier to T_1-Min3 to allow for the cycloaddition.

Alternative to the cycloaddition from T_1-Min3 also the possibility of an ISC back to ground state exists. An intersection of the T_1 and the S_0 state (T_1/S_0 IS) which can mediate this ISC, is located near a third $\pi\pi^*$ minimum on the T_1 potential surface (T_1-Min4, see fig. 4.9). The structures of both, T_1-Min4 and T_1/S_0 IS, are characterized by a further bending of the hydrogen atom below the ring plane and by a twisting of cyclohexenone framework into a twist-boat like geometry. This different conformation also leads to a twisting of the cyclohexane framework attached to the cyclohexenone ring (fig. 4.10). In contrast to all other geometries reported until now, T_1-Min4 is the first one where the geometrical changes are not completely localized on the cyclohexenone ring. T_1-Min4 is slightly lower in energy than T_1-Min3, but the structural distortions necessary to reach it are large from T_1-Min3. The corresponding barrier was estimated again by using a simplified reaction path constructed by linear interpolation between T_1-Min3 and T_1-Min4 (see fig. B.2 in appendix B). The estimated value of about 4 eV indicate a immense reaction barrier but is only an upper limit for the real one. Optimization of the corresponding transition state would lower this barrier [97]. However, in the next section it will be shown that the barriers for the cycloaddition are substantially lower. T_1-Min4 is no plausible starting point for cycloaddition as the twisting of the cyclohexenone and cyclohexane frameworks results in a large displacement of the ethylene and enone moiety to each other (see fig. 4.10).

In contrast to the precursor **1**, for the intermolecular reference system of cyclohexenone and ethylene only one $\pi\pi^*$ minimum on the T_1 potential energy surface was reported [153] which is equivalent to the twisted T_1-Min4. For the intermolecular system the twisted T_1 minimum can serve as starting point of the cycloaddition [153] due to the higher degree of freedom present in the system. But also in cyclohexenone and other enones, a T_1/S_0 intersection in the vicinity of the twisted T_1 minimum exists and is associated with a small barrier [153, 154, 160]. Therefore, in these compounds an ISC *via* the T_1/S_0 intersections leading back to the ground state is a highly competitive process to the cycloaddition. In the precursor **1** the ethylene and enone moiety are connected by a rigid cyclohexane ring, and the barrier to access this deactivation path is hence much larger.

In summary, after excitation to the S_1 ($n\pi^*$) state by a weak absorption band, a high ISC probability to the T_2 ($\pi\pi^*$) state exist in the precursor **1**. The relaxation then leads to two $\pi\pi^*$ minima on the T_1 potential energy surface which can act as starting point for the cycloaddition. Alternative processes leading back to the ground state *via* internal conversion or ISC are highly unlikely due to high barriers present in the natural product.

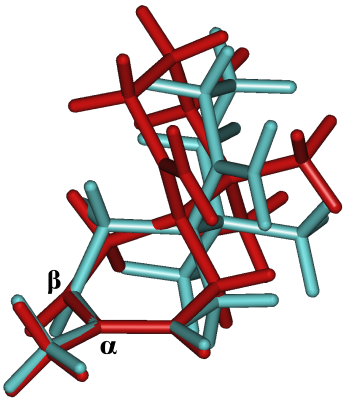

Figure 4.10.: Comparison of the optimized geometries of T_1-Min3 (red) and T_1-Min4 (cyan). The positions of the α- and β-carbon atoms are shown.

4.2.4. Photochemical cycloaddition to aplydactone

So far, the calculated reaction pathway followed the reaction mechanism shown in figure 4.2 to the triplet state in a quite effective way. The next important step is the formation of a triplet diradical (^{3}DR) intermediate. In general, for the precursor **1** from the triplet minimum T_1-Min3 four different triplet diradicals are possible (fig. 4.11). The first diradical ^{3}DR1 results from a straight attack of the ethylene on the β-carbon of the enone moiety, while ^{3}DR2 from a straight attack on the α-carbon. The crossed attack on the β-carbon leads to ^{3}DR3 and the crossed attack on the α-carbon to ^{3}DR4. From the diradicals ^{3}DR1 and ^{3}DR2 the straight cycloadduct aplydactone **2** can be formed, while the diradical ^{3}DR3 could lead to the crossed regioisomer **3**. For the diradical ^{3}DR4 the second σ-bond formation is sterically inhibited by the first formed σ-bond.

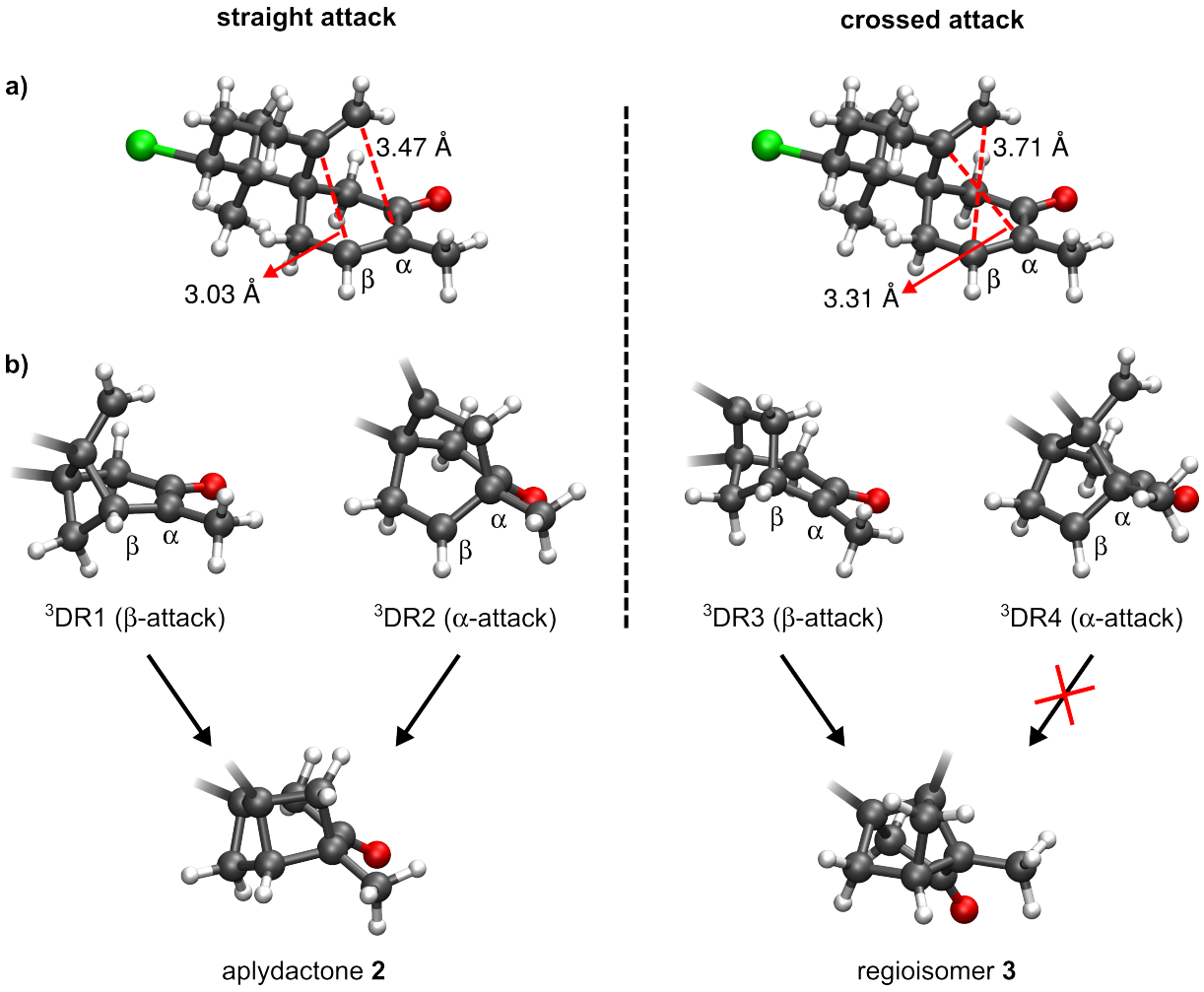

Figure 4.11.: Inter-carbon distances for the straight (left) and the crossed attack (right) of the ethylene on the enone moiety at the triplet minimum T_1-Min3 of **1** (a). Optimized geometries of the four triplet diradicals (^{3}DR) possible from T_1-Min3 (b). The shown structures were optimized at the CASSCF/6-31G* level of theory.

To investigate the formation of the two possible regioisomers, all relevant geometries of the four diradical pathways were optimized with the CASSCF and UB3LYP method and we found a good agreement of the optimized structures. For the optimized geometries the energy differences (ΔE) were calculated relative to the T_1-Min3 with the CASPT2 and the UB3LYP method. With

Table 4.2.: Calculated CASPT2 energy differences ΔE (eV) of the optimized structures of the four diradical pathways DR1 - DR4. The triplet state minimum T_1-Min3 was chosen as reference point. ^{3}TS are the transition states in the T_1 state describing the formation of the first σ-bond and leading to the corresponding triplet diradical minima ^{3}DR. ^{1}DR are the singlet diradical minima from which either the cycloadducts can be formed through the transition states ^1TS_P or a relaxation back to the initial reagent **1** can occur *via* the transition states ^1TS_R. Only for the singlet diradical ^{1}DR4 the second σ-bond formation is sterically inhibited and no corresponding transition state ^1TS_P exist. For the transition states ^1TS_P and ^1TS_R the energy barriers relative to the singlet diradicals ^{1}DR are given in parentheses.

	DR1	DR2	DR3	DR4
T_1-Min3	0.00	0.00	0.00	0.00
^{3}TS	0.16	0.36	0.42	0.31
^{3}DR	-0.48	-1.08	-1.32	-0.65
^{1}DR	-0.50	-1.08	-1.33	-0.69
^1TS_P	-0.49 (0.01)	-0.97 (0.11)	-1.29 (0.04)	—
^1TS_R	-0.48 (0.02)	-0.90 (0.18)	-0.82 (0.51)	-0.54 (0.15)

the UB3LYP method also the free energy differences (ΔG) were determined. For all calculations the standard Pople basis set 6-31G* was used. In the table B.2 in appendix B it can be seen that both methods leads qualitatively to the same ΔE values which are only shifted to each other. Moreover, as the ΔE and ΔG values of the UB3LYP method are very similar for all structures, the inclusion of thermal corrections leads to no significant changes. However, the results of the DFT method for radical reaction pathways often depend significantly on the used functional [154, 163–166]. For these reasons, in the following the discussion will focus on the optimized CASSCF structures and the corresponding ΔE values of the CASPT2 method.

At the structure of T_1-Min3 (fig. 4.11) the inter-carbon distances for both attacks are decreased in comparison to the ground state minimum (fig. 4.5) and the distances for the straight attack are smaller than for the crossed attack. The formation of all triplet diradicals ^{3}DR is strongly exothermic (see tab. 4.2) and exergonic (see tab. B.2) relative to T_1-Min3. Moreover, the triplet diradicals can undergo a rapid ISC to the degenerated singlet diradicals ^{1}DR (see tab. 4.2) [154, 167] which then can further react. This is illustrated exemplarily for the reaction path of the straight β-attack in figure 4.12. Therewith in the excited state no equilibrium between T_1-Min3 and the triplet diradicals ^{3}DR is present and the reaction to the diradicals should be kinetically controlled. The crucial point for the formation of the diradicals is the barrier to reach them. For all four triplet diradicals ^{3}DR a corresponding transition state ^{3}TS could be located. The values in table 4.2 show that the transition state ^{3}TS of the straight β-attack (DR1) is associated with the smallest barrier while the crossed β-attack (DR3) with the highest barrier. This can be understood as the geometrical distortions to reach the ^{3}TS of DR1 from T_1-Min3 are the smallest (root-mean-square deviation (RMSD) from T_1-Min3 is 0.55 Å), whereas the ^{3}TS of DR3 is connected with the largest distortions (RMSD from to T1-Min3 is 0.78 Å). This is already indicated in the inter-carbon distances at T_1-Min3 (see fig. 4.11, 3.03 Å versus 3.71 Å).

Once formed, the triplet diradicals ^{3}DR lead to the singlet diradicals ^{1}DR from which either the cycloadduct can be formed through the transition states ^1TS_P or a relaxation back the reagent can occur *via* the transition states ^1TS_R. Only the singlet diradical DR4 can evolve solely back to the reagent. According to the calculated barriers of the transition states ^1TS_P and

^1TS_R relative to the singlet diradicals ^1DR (see values in parentheses in tab. 4.2), the reaction channel leading to the cycloadduct is always favored over the reversion to the reagent.

Overall, the results of the last section demonstrate that four triplet diradicals DR1 - DR4 are possible from T_1-Min3 which then can lead by ISC to the cycloadduct or back to the reagent. However, both diradical pathways leading to aplydactone **2**, DR2 and especially DR1, are associated with smaller barriers than the one pathway DR3 leading to the regioisomer **3**. Thus, the formation of the natural product **2** is strongly favored over the formation of **3**.

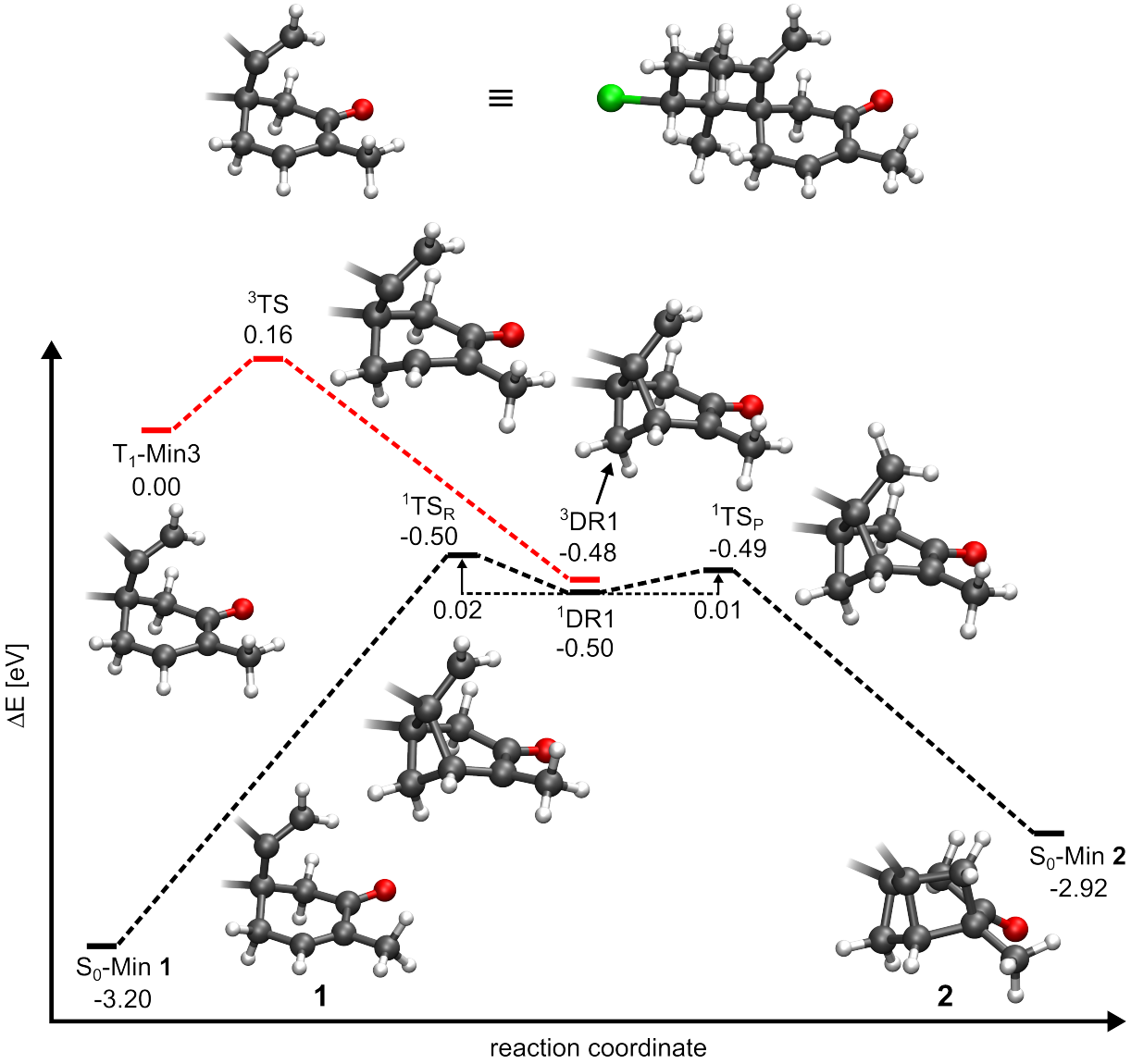

Figure 4.12.: Schematic illustration of the reaction pathway starting from the triplet minimum T_1-Min3 to either the cycloadduct **2** or back to the initial reagent **1**. Shown is the straight β-attack of the ethylene on the enone moiety leading to the diradical DR1 with the relevant optimized geometries. The reaction path in the triplet T_1 state is colored red, whereas the path in the singlet ground state is colored black. The given values are the CASPT2 energy differences ΔE (eV) of the optimized structures relative to T_1-Min3. The abbreviation of the molecular structure of **1** used for the schematic is shown at the top.

4.2.5. Conclusions

The quantum chemical study of the [2+2] photocycloaddition of dactylone **1** to aplydactone **2** demonstrates that an excitation to the singlet S_1 ($n\pi^*$) state of dactylone by a weak absorption band can initiate the photochemical reaction. The excitation into the S_7 state, which leads to an unwanted homolytic cleavage of the bromine, is assumed as possible explanation for the failure to produce **2** *via* long-term UV irradation of **1**.

The excited S_1 state is located on the enone moiety of **1** and subsequently efficient ISC leads to a triplet minimum which serves as starting point of the cycloaddition. Alternative photophysical relaxation pathways leading back to the ground state of the initial reagent, shown to be quite active in other enones, are highly unlikely due to high barriers present in the natural product **1**. Furthermore, in case the system relaxes back to the ground state, it can be reexcited and has another chance to follow the cycloaddition. From the triplet minimum four diradical pathways are possible. The calculated barriers show that the two pathways leading to the formation of aplydactone **2** are strongly favored over the one leading to the regioisomer **3**. Overall, the theoretical results predict that an optical excitation of dactylone **1** to the S_1 state leads to the photochemical and biomimetic formation of aplydactone **2**.

In summary, this chapter clearly demonstrates the importance of weak absorption bands for the initiation of the photochemical syntheses of the two natural products intricarene and aplydactone. In the both syntheses the crucial reaction steps are made possible by long-lived triplet states. Even if the reactants decay to the ground state during both reaction pathways, the excited states can be readily replenished by additional light absorption.

The initiation of photochemical reactions by weak absorption bands could be quite general for the biosynthesis of natural products. The intense absorption bands of natural products without extended conjugated π-systems, are too high in energy to be excited by solar light. But the most biomolecules exhibit low lying excited states characterized by weak transition probabilities such as the presented $n\pi^*$ states. The long exposure times present in nature can enable the population of these excited states and allow for the photochemical biosynthesis of natural products.

5. Summary and outlook

Processes initiated by the absorption of solar light play a of fundamental role in photovoltaic devices as well as in biosyntheses. In the first and second part of the present work, the photoinduced processes in two classes of molecules commonly used in organic-based optoelectronic devices were investigated and potential factors influencing the performance of the optical devices were revealed. In the third part, the photochemical and biomimetic syntheses of two natural products were studied and the details of the reaction mechanisms and the optimal conditions to initiate the reactions were elucidated.

In the first part of the present work, the deactivation processes from the first excited singlet state S_1 of thiophene and of small oligothiophenes up to four rings were investigated by quantum chemical calculations. It was demonstrated that the monomer thiophene decays primarily *via* its singlet states. A low-lying S_1/S_0 conical intersection seam is easily accessible and drives the fast internal conversion which is associated with an opening of the thiophene ring. Intersystem crossing (ISC) and triplet states are ineffective in the relaxation pathway of thiophene due to small spin-orbit couplings and large singlet-triplet energy gaps. In contrast the deactivation paths of the oligothiophenes are dominated by ISC. The extension of the π-system in the oligothiophenes increases the barriers towards the conical intersections and inhibits the passage through them. Moreover, the elongation of the π-system induces low-lying triplet states which intersect with the S_1 state during the initial relaxation and enable a fast ISC channel. Therewith in the oligothiophenes high barriers together with an efficient ISC prevent the rapid loss of the absorbed energy and the related bond breaking which would be detrimental for the thiophene-based devices. The present work demonstrate the importance of intersystem crossing and triplet states for the excited lifetime and for the stability of the oligothiophenes. Preliminary calculations for longer oligothiophenes indicate that triplet states are significant for the photophysics of the longer oligothiophenes as well. Further investigation of the relaxation processes of longer oligothiophenes and polythiophenes should allow a deeper understanding of the factors tuning these processes which is of potential interest for the performance of thiophene-based devices.

In the second part of this thesis, the photoinduced dynamics of perylene diimide dyads based on a donor-spacer-acceptor motif were investigated in collaboration with the groups of Heinz Langhals and Eberhard Riedle. The work revealed that the energy transfer efficiency and mechanism varies with the spacer present in the dyads. In the dyads with pyridine spacers a direct energy transfer of the excited donor to the acceptor moiety occurs with near-unity quantum efficiency without the involvement of the spacer. The replacement of the electron-poor pyridine spacers by electron-rich phenyl spacers leads to a competing electron transfer from the spacer to the donor. According to the established thinking this electron transfer should lower the energy transfer efficiency dramatically, but in the studied dyads still a significant energy transfer is observed. *Ab initio* calculations in combination with the investigation of donor-spacer subsystems elucidate that in the dyads with phenyl spacers two different kinds of charge transfer states are responsible for the observed dynamics. The dark charge transfer states are characterized by low transition dipole moments and lead to a backward electron transfer without transferring energy to the acceptor. In contrast the bright charge transfer states exhibit considerable transition dipole moments and are isoenergetic to the locally excited acceptor states allowing an energy transfer from the donor to the acceptor *via* multipole-multipole interactions. This new energy transfer mechanism is the main contributor to the overall energy transfer in the dyads with phenyl spacers and demonstrate for the first time that bright charge transfer states can indeed

act as energy donors. Chromophoric systems with engineered bright charge transfer states could find applications in novel photovoltaic devices. The investigated solvent effects on two modified perylene diimide systems reveal that the crucial property of the solvent for the charge transfer dynamics is the solvation time and not the polarity of the solvent. Overall, the studied dyads represent a first example that shows how an electron transfer can induce an energy transfer and allow to invert the usual order of these processes present in artificial photosynthetic systems and solar cells. The work elucidate how the charge and energy transfer dynamics and efficiencies as well as the lifetime of the charge separation can be controlled by the choice of the substituents. These properties are of high importance for organic-based solar cells (OSCs), especially for the novel ternary OSCs, and quantum chemical calculations can be used as a tool to predict the optimal substituents to achieve the desired properties.

In the last part of the present work, the photochemical syntheses of the two natural products intricarene and aplydactone were studied in collaboration with the group of Dirk Trauner. In the case of intricarene the first biomimetic synthesis of it was accomplished by using light alone at moderate temperatures and in the absence of highly reactive chemicals. The irradation of the derivative of the natural product bipinnatin J for eight hours to light from a reptile lamp yielded intricarene and revealed the biosynthetic relationship between bipinnatin J and intricarene. The photochemical reaction also resulted in the formation of a structurally intriguing by-product that may well be found in the Caribbean corals too. The emission spectrum of the reptile lamp and the long exposure time used in the experiments mimic the conditions found in the coral's natural habitat. The long irradiation enables the excitation by a weak absorption band which provides the optimal conditions for the initiation of the photochemical reaction. The quantum chemical calculations revealed that the complex and surprising mechanism involves a cascade of reactions and all facets of photochemistry, from light absorption to the redistribution of radiant energy. Intricarene is derived from an oxidopyrylium intermediate via a photochemically driven cycloaddition. The different reaction steps require the formation of triplet states as their long lifetimes ensure that the reactants can undergo the various steps of the reaction cascade in the excited state. In this way, the steep energy barriers present in the ground state are avoided and even if the molecule decay to the ground state, the intermediate oxidopyrylium can reenter the reaction cascade by additional light absorption. Finally, the interdisciplinary work provides new insights into the largely unexplored excited state chemistry of the useful oxidopyrylium species and elucidates the details of the reaction mechanism and the optimal conditions to initiate the photochemical reaction which should allow to produce intricarene in quantities large enough to properly investigate its potential pharmacological properties.

In the second part of the last chapter the quantum chemical study of the [2+2] photocycloaddition of dactylone to aplydactone is presented. Similar to the synthesis of intricarene the excitation to the first excited singlet state S_1 by a weak absorption band provides for the initiation of the photochemical reaction. Also analogous to intricarene the calculations suggest that the population of the most intense absorption band would not lead to formation of the product and in the case of dactylone even to the decomposition of the reagent. From the S_1 state an efficient ISC leads to the starting point of the cycloaddition, a minimum in the lowest triplet state, which is strongly favored over the alternative photophysical relaxation pathways. From this starting point four diradical pathways are possible and according to the calculated barriers the two pathways leading to the natural product aplydactone are preferred. The theoretical results therewith indicate that an optical excitation of dactylone to the S_1 state should allow the total and biomimetic synthesis of aplydactone. Overall, the last part of the present work clearly demonstrates the importance of weak absorption bands and long-lived triplet states for the photochemical syntheses of the natural products. For natural products without extended conjugated π-systems, the initiation of photochemical reactions by weak absorption bands could be quite general as these bands are the only ones accessible by solar light. The long exposure

times present in nature can enable the population of these excited states and allow for the photochemical biosynthesis of natural products.

A. Supporting information for chapter 3.2

In the following, the supporting information of the manuscript "Ultrafast emission quenching in a perylene diimide by structure rearrangement induced electron transfer from its substituent" is printed.

Supplementary Information to

Ultrafast Emission Quenching in a Perylene diimide by Structure Rearrangement Induced Electron Transfer from its Substituent

Patrick Kölle[a], Artur Nenov[a], Uwe Megerle[b], Patrizia Krok[b], Heinz Langhals[a], Regina de Vivie-Riedle[a], and Eberhard Riedle[b*]

[a] Department Chemie, Ludwig-Maximilians-Universität (LMU), Butenandtstraße 5-13, 81377 München, Germany

[b] Lehrstuhl für BioMolekulare Optik, Ludwig-Maximilians-Universität (LMU), Oettingenstraße 67, 80538 München, Germany

[*] Corresponding author. Fax: +49-89-2180-9202
E-mail address: riedle@physik.uni-muenchen.de

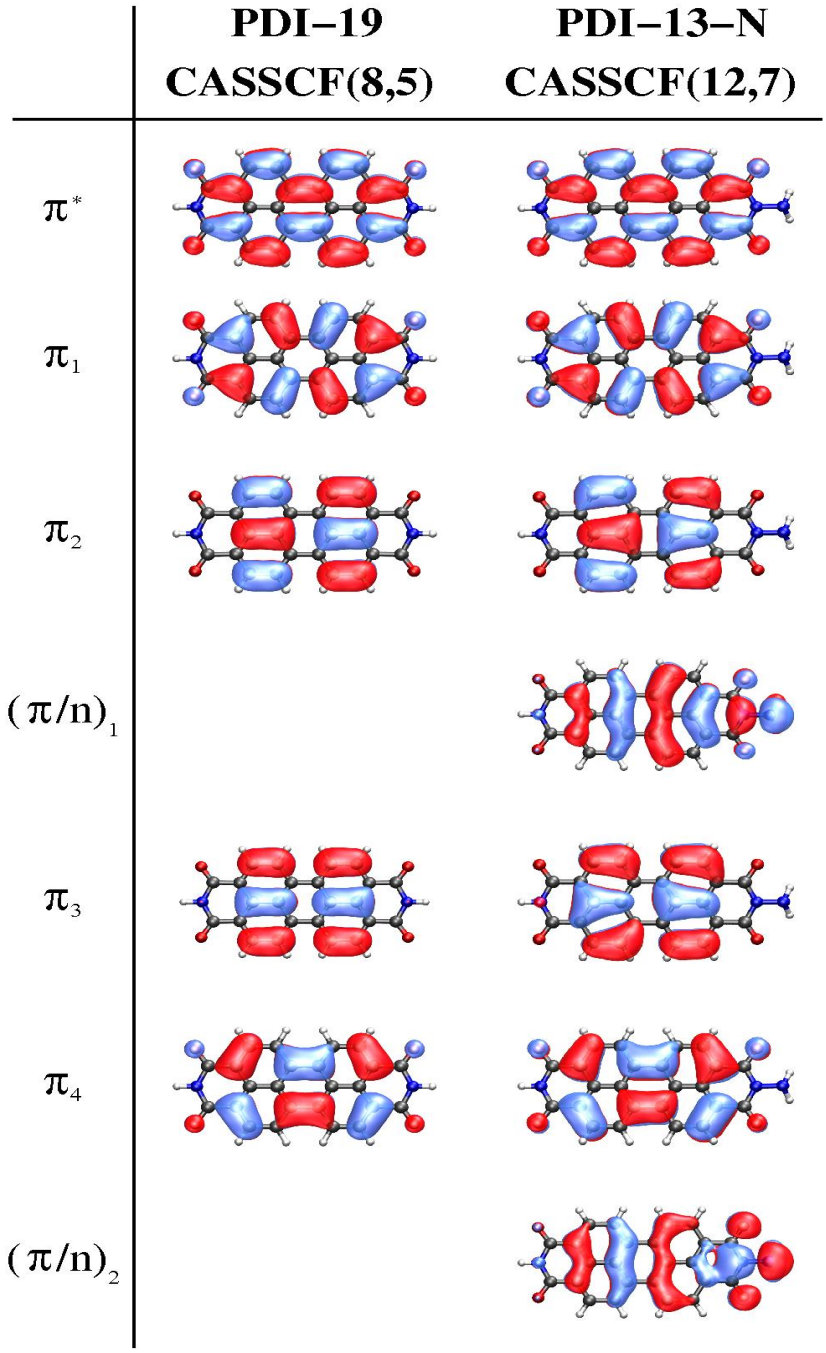

Fig. S1: State-averaged CASSCF molecular orbitals included in the active space of PDI-19 (left) and PDI-13-N (right), obtained with the 6-31G* basis set at the MP2-optimized ground-state equilibrium geometries.

			PDI-19		**PDI-13-N**	
method	transition	character	ΔE (eV)	f	ΔE (eV)	f
CC2	$S_0 \rightarrow S_1$	$\pi_1 \rightarrow \pi^*$ (LE)	2.59	0.719	2.57	0.731
	$S_0 \rightarrow S_2$	$\pi_1^2 \rightarrow \pi^{*2}$	-	-	-	-
	$S_0 \rightarrow S_3$	$(\pi/n)_1 \rightarrow \pi^*$ (CT)	-	-	3.01	0.016
	$S_0 \rightarrow S_4$	$\pi_2 \rightarrow \pi^*$	3.45	0.000	3.44	0.000
	$S_0 \rightarrow S_5$	$\pi_3 \rightarrow \pi^*$	3.70	0.000	-	-
CASPT2	$S_0 \rightarrow S_1$	$\pi_1 \rightarrow \pi^*$ (LE)	2.70	1.078	2.62	1.077
	$S_0 \rightarrow S_2$	$\pi_1^2 \rightarrow \pi^{*2}$	3.10	0.000	3.04	0.002
	$S_0 \rightarrow S_3$	$\pi_2 \rightarrow \pi^*$	3.50	0.000	3.43	0.000
	$S_0 \rightarrow S_4$	$(\pi/n)_1 \rightarrow \pi^*$ (CT)	-	-	3.48	0.008
	$S_0 \rightarrow S_5$	$\pi_3 \rightarrow \pi^*$	3.68	0.408	3.63	0.358
Exp.		-	2.36	-	2.34	-

Tab. S1: CC2 and SS-CASPT2 vertical excitation energies and oscillator strengths of PDI-19 (active space CAS(8,5)) and PDI-13-N (CAS(12,7)) at the MP2-optimized ground-state equilibrium geometries (LE, locally exited state; CT, charge transfer state). The calculated energies are compared with the experimental absorption maxima of PDI-19 and PDI-13-N in $CHCl_3$.

Tab. S2 (next page): Relative energies (SS-CASPT2 calculation) and main configurations for eight electronic states (states 6 and 7 see Tab. S4) of PDI-19 (CAS(8,5)) and PDI-13-N (CAS(12,7)) for all relevant points discussed in the paper. Oscillator strengths for the corresponding excitations are also given. For PDI-19 the excited state geometry was optimized at the CC2 level of theory, for PDI-13-N at the SS-CASPT2 level. Ground state minima energies were chosen as reference points.

			PDI-19		PDI-13-N	
Point	State	Main configuration	ΔE (eV)	f	ΔE (eV)	f
Franck-Condon	**S_0**	**closed shell (π_1^2)**	**0.00**	-	**0.00**	-
	S_1	$\pi_1^1\pi^{*1}$ (LE)	2.70	1.078	2.62	1.077
	S_2	$\pi_1^0\pi^{*2}$	3.10	0.000	3.04	0.002
	S_3	$\pi_2^1\pi^{*1}$	3.50	0.000	3.43	0.000
	S_4	$(\pi/n)_1^1\pi^{*1}$ (CT)	-	-	3.48	0.008
	S_5	$\pi_3^1\pi^{*1}$	3.68	0.408	3.63	0.358
	S_8	$(\pi/n)_2^1\pi^{*1}$	-	-	4.12	0.102
π-Minimum	S_0	closed shell (π_1^2)	0.09	-	0.12	-
	S_1	$\pi_1^1\pi^{*1}$ (LE)	2.51	1.064	2.46	1.036
	S_2	$\pi_1^0\pi^{*2}$	2.72	0.000	2.68	0.004
	S_3	$(\pi/n)_1^1\pi^{*1}$ (CT)	-	-	3.36	0.001
	S_4	$\pi_2^1\pi^{*1}$	3.42	0.000	3.40	0.001
	S_5	$\pi_3^1\pi^{*1}$	3.57	0.371	3.58	0.323
	S_8	$(\pi/n)_2^1\pi^{*1}$	-	-	3.97	0.100
CT-Minimum	S_0	closed shell (π_1^2)	-	-	1.21	-
	S_1	$(\pi/n)_1^1\pi^{*1}$ (CT)	-	-	2.43	0.008
	S_2	$\pi_1^1\pi^{*1}$ (LE)	-	-	3.40	0.994
	S_3	$\pi_1^0\pi^{*2}$	-	-	3.70	0.036
	S_4	$\pi_2^1\pi^{*1}$	-	-	4.35	0.019
	S_5	$\pi_3^1\pi^{*1}$	-	-	4.36	0.381
	S_8	$\pi_4^1\pi^{*1}$	-	-	4.65	0.003
Conical Intersec-tion	S_0	closed shell (π_1^2)	-	-	2.91	-
	S_1	$(\pi/n)_1^1\pi^{*1}$ (CT)	-	-	2.91	0.000
	S_2	$\pi_1^1(\pi/n)_1^1\pi^{*2}$	-	-	4.78	0.001
	S_3	$\pi_1^1\pi^{*1}$ (LE)	-	-	4.91	0.800
	S_4	$\pi_1^0\pi^{*2}$	-	-	5.31	0.184
	S_5	$\pi_2^1\pi^{*1}$	-	-	5.85	0.004
	S_8	$(\pi/n)_1^0\pi^{*2}$	-	-	6.03	0.010

Cartesian coordinates for the ground state minimum (FC, MP2/def2-TZVP) and first excited state minimum (π-Minimum, CC2/def2-TZVP) of PDI-19

FC

	x	y	z
C	-3.577991	-1.228966	-0.016027
C	-5.065180	-1.252574	-0.002480
N	-5.671075	-0.000005	-0.018235
C	-5.065153	1.252551	-0.003005
C	-3.577967	1.228947	-0.016482
O	-5.727006	-2.275816	0.011086
O	-5.726961	2.275810	0.010103
C	-2.883062	-2.431396	0.010904
C	-2.883026	2.431392	0.010031
C	-2.868940	-0.000008	0.010883
C	-1.434300	0.000014	-0.030910
C	-1.481616	-2.435157	0.006039
C	-0.733311	-1.247607	0.019421
C	-1.481572	2.435196	0.005295
C	-0.733307	1.247636	0.019212
C	0.733312	-1.247586	-0.019476
C	0.733319	1.247607	-0.019276
C	1.434339	0.000007	0.031213
C	1.481553	-2.435168	-0.005931
C	2.882991	-2.431392	-0.010346
C	3.578003	-1.229016	0.016304
C	2.868993	-0.000016	-0.010357
C	1.481523	2.435195	-0.005172
C	2.882968	2.431386	-0.009489
C	3.577978	1.228999	0.016736
C	5.065201	-1.252716	0.002271
C	5.065168	1.252695	0.002758
N	5.671201	-0.000003	0.015272
O	5.726986	-2.275975	-0.010503
O	5.726939	2.275963	-0.009501
H	6.693374	0.000014	0.003838
H	3.451653	-3.368459	-0.010436
H	0.975316	-3.404718	-0.032070
H	-0.975407	-3.404731	0.031812
H	-3.451714	-3.368472	0.010776
H	-3.451680	3.368464	0.009515
H	-0.975382	3.404794	0.030744
H	0.975309	3.404775	-0.030916
H	3.451649	3.368441	-0.009151
H	-6.693256	0.000013	-0.006949

π-Minimum

	x	y	z
C	-3.5479671	-1.2259515	-0.0012089
C	-5.0159193	-1.2507784	-0.0013864
N	-5.6241889	-0.0000070	-0.0040108
C	-5.0159217	1.2507696	-0.0023700
C	-3.5479744	1.2259579	-0.0020947
O	-5.6892420	-2.2852437	-0.0000519
O	-5.6892583	2.2852284	-0.0020798
C	-2.8465599	-2.4441322	0.0081104
C	-2.8465715	2.4441440	0.0063075
C	-2.8468914	0.0000075	0.0032172
C	-1.4144170	-0.0000016	-0.0052737
C	-1.4682261	-2.4549941	0.0057897
C	-0.7147710	-1.2410991	0.0073395
C	-1.4682368	2.4550002	0.0042679
C	-0.7147734	1.2411052	0.0069558
C	0.7147690	-1.2410991	-0.0074334
C	0.7147746	1.2411039	-0.0070655
C	1.4144177	-0.0000027	0.0051817
C	1.4682254	-2.4549922	-0.0058340
C	2.8465586	-2.4441311	-0.0082254
C	3.5479673	-1.2259505	0.0012071
C	2.8468932	0.0000069	-0.0032798
C	1.4682375	2.4549984	-0.0043531
C	2.8465709	2.4441434	-0.0064667
C	3.5479744	1.2259574	0.0020659
C	5.0159191	-1.2507781	0.0014725
C	5.0159221	1.2507692	0.0024603
N	5.6241895	-0.0000076	0.0042665
O	5.6892421	-2.2852441	0.0001225
O	5.6892580	2.2852284	0.0022483
H	6.6424595	-0.0000108	0.0041820
H	3.4202398	-3.3656317	-0.0102562
H	0.9556696	-3.4087715	-0.0253770
H	-0.9556714	-3.4087719	0.0254031
H	-3.4202490	-3.3656274	0.0101389
H	-3.4202640	3.3656389	0.0074251
H	-0.9556994	3.4088061	0.0228847
H	0.9556991	3.4088041	-0.0229366
H	3.4202644	3.3656384	-0.0076120
H	-6.6424591	-0.0000090	-0.0038586

Cartesian coordinates for the ground state minimum (FC, SS-CASPT2/6-31G*), first excited state minima (π-/CT-Minimum, SS-CASPT2/6-31G*) and conical intersection of PDI-13-N

FC

	x	y	z
C	-3.278797	-0.024993	-1.217608
C	-4.762110	-0.012824	-1.229365
N	-5.370366	-0.019377	-0.001020
C	-4.742493	0.002255	1.197525
C	-3.277758	-0.023614	1.209798
O	-5.397227	-0.025568	-2.247542
N	-6.756494	0.131068	0.017485
O	-5.400877	0.014783	2.268340
C	-2.595838	-0.008596	-2.426447
C	-2.600090	-0.009199	2.420755
H	-7.096937	-0.296535	-0.810621
H	-7.099894	-0.302319	0.836786
C	-2.560932	0.004350	-0.001855
C	-1.157072	-0.028046	-0.005574
C	-1.190565	-0.006627	-2.437004
C	-0.463991	0.009830	-1.247254
C	-1.194101	-0.009849	2.425380
C	-0.461461	0.008216	1.234706
C	1.001226	-0.011758	-1.249025
C	0.997934	-0.014008	1.245021
C	1.685342	0.022723	-0.004492
C	1.728495	0.004508	-2.443252
C	3.128666	0.004844	-2.432285
C	3.805795	0.015609	-1.219285
C	3.093950	-0.005092	-0.000964
C	1.723663	-0.000136	2.439203
C	3.125631	-0.000248	2.431942
C	3.803148	0.011787	1.219398
C	5.261829	0.003609	-1.215872
C	5.260666	0.002198	1.222267
N	5.870171	0.000112	0.005577
O	5.953914	-0.000322	-2.245179
O	5.943821	0.000133	2.256843
H	6.863123	-0.006479	0.004976
H	3.675491	0.010431	-3.334892
H	1.235448	-0.005520	-3.373755
H	-0.700452	0.006392	-3.370601
H	-3.151674	-0.010863	-3.323294
H	-3.134489	-0.011337	3.327718
H	-0.703391	0.003110	3.363267
H	1.231834	-0.012859	3.371104
H	3.664943	0.001739	3.337840

π-Minimum

	x	y	z
C	-3.268232	-0.027488	-1.216030
C	-4.742170	-0.011177	-1.229458
N	-5.347252	-0.014818	-0.001132
C	-4.721611	0.000287	1.198689
C	-3.266339	-0.026523	1.209620
O	-5.377289	-0.023979	-2.252930
N	-6.732636	0.136572	0.016291
O	-5.380853	0.007765	2.274613
C	-2.574147	-0.011203	-2.444053
C	-2.579188	-0.012076	2.438835
H	-7.073428	-0.290589	-0.811732
H	-7.075864	-0.294710	0.836867
C	-2.554602	0.006872	-0.000943
C	-1.146793	-0.030498	-0.005817
C	-1.188355	-0.011482	-2.461117
C	-0.450572	0.010422	-1.241465
C	-1.190774	-0.013846	2.446454
C	-0.449364	0.009305	1.227874
C	0.988835	-0.015298	-1.244363
C	0.986617	-0.016682	1.238564
C	1.672955	0.022478	-0.004381
C	1.723435	0.006801	-2.467725
C	3.105185	0.006351	-2.452256
C	3.790226	0.016908	-1.219006
C	3.085166	-0.009177	-0.000169
C	1.717095	0.003260	2.462690
C	3.101071	0.001916	2.451289
C	3.786589	0.013489	1.219045
C	5.239356	0.003429	-1.216926
C	5.237443	0.002505	1.222654
N	5.843967	-0.000088	0.005524
O	5.933172	-0.000896	-2.250056
O	5.921336	0.000322	2.261487
H	6.837664	-0.007742	0.005494
H	3.663681	0.014932	-3.346163
H	1.218965	-0.005255	-3.390697
H	-0.685777	0.004779	-3.387322
H	-3.143278	-0.015822	-3.333056
H	-3.120305	-0.017204	3.341285
H	-0.689081	0.003721	3.379771
H	1.213286	-0.011147	3.387714
H	3.649944	0.007113	3.350782

CT-Minimum

	x	y	z
C	-3.273144	0.010183	-1.228447
C	-4.658577	-0.007665	-1.276917
N	-5.301839	-0.001025	-0.003934
C	-4.662400	0.009008	1.273703
C	-3.274602	0.025779	1.231161
O	-5.450890	-0.017430	-2.269742
N	-6.571512	-0.006822	-0.001811
O	-5.452918	0.012756	2.268503
C	-2.557394	-0.015840	-2.481402
C	-2.564203	0.017448	2.489480
H	-6.992686	-0.014158	-0.897342
H	-6.992530	-0.001604	0.892900
C	-2.573962	-0.009319	-0.001753
C	-1.166946	0.020137	-0.000557
C	-1.194436	-0.012744	-2.475326
C	-0.470968	-0.019111	-1.237895
C	-1.205885	0.015531	2.482534
C	-0.473030	-0.013944	1.244255
C	0.964543	0.015036	-1.227867
C	0.970516	0.007556	1.240554
C	1.665126	-0.023228	0.001579
C	1.708044	0.007162	-2.438726
C	3.099332	0.013049	-2.438778
C	3.780620	-0.004033	-1.223541
C	3.075854	0.008017	-0.005736
C	1.706607	-0.020506	2.453629
C	3.090966	-0.019751	2.438759
C	3.782796	-0.021491	1.222697
C	5.232844	0.009992	-1.212260
C	5.254803	-0.007107	1.235241
N	5.841403	0.003658	0.000031
O	5.930724	0.022724	-2.254610
O	5.913336	-0.008036	2.241798
H	6.836486	0.014109	-0.015185
H	3.618598	0.016220	-3.351408
H	1.206649	0.027476	-3.374525
H	-0.682405	-0.034818	-3.393201
H	-3.098889	-0.019299	-3.387455
H	-3.119693	0.030430	3.382055
H	-0.681826	0.010058	3.391572
H	1.204450	-0.016991	3.379479
H	3.654511	-0.031778	3.330187

Conical Intersection

	x	y	z
C	-3.272641	0.009972	-1.244243
C	-4.628403	-0.007058	-1.340651
N	-5.302008	0.000133	-0.003952
C	-4.632241	0.009392	1.337410
C	-3.274110	0.024901	1.246957
O	-5.456792	-0.015573	-2.293524
N	-6.538822	-0.004786	-0.001839
O	-5.458838	0.013080	2.292247
C	-2.527037	-0.016988	-2.516591
C	-2.533866	0.015966	2.524684
H	-6.966242	-0.011176	-0.900916
H	-6.966092	0.000518	0.896407
C	-2.598496	-0.010167	-0.001747
C	-1.167915	0.018972	-0.000541
C	-1.189931	-0.013912	-2.506947
C	-0.465961	-0.019449	-1.232230
C	-1.201400	0.013577	2.514189
C	-0.468024	-0.015526	1.238623
C	0.947017	0.014828	-1.222413
C	0.952999	0.007209	1.235128
C	1.648283	-0.023078	0.001591
C	1.701241	0.006888	-2.449075
C	3.080212	0.013267	-2.446539
C	3.767091	-0.003551	-1.222355
C	3.067018	0.008606	-0.005734
C	1.699837	-0.020179	2.463997
C	3.071881	-0.018926	2.446523
C	3.769286	-0.020594	1.221507
C	5.214848	0.010428	-1.212483
C	5.236827	-0.006169	1.235438
N	5.823130	0.004248	0.000012
O	5.916131	0.022916	-2.255002
O	5.898780	-0.006864	2.242152
H	6.817997	0.014599	-0.015214
H	3.603440	0.016742	-3.356754
H	1.199247	0.027639	-3.383695
H	-0.662755	-0.038118	-3.414999
H	-3.069839	-0.021880	-3.422438
H	-3.090673	0.029360	3.417061
H	-0.662217	0.008440	3.413442
H	1.197104	-0.017224	3.388682
H	3.639406	-0.030827	3.335529

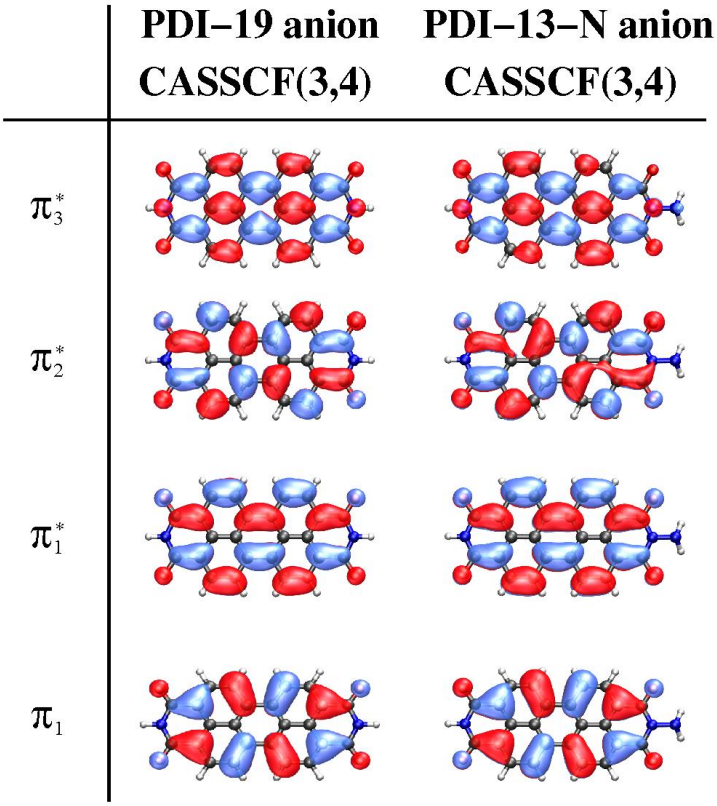

Fig. S2: State-averaged CASSCF molecular orbitals included in the active space of the PDI-19 anion (left) and the PDI-13-N anion (right).

		PDI-19 anion		**PDI-13-N anion**	
transition	character	ΔE (eV)	f	ΔE (eV)	f
$D_0 \rightarrow D_1$	$\pi_1^2\pi_1^{*1} \rightarrow \pi_1^1\pi_1^{*2}$	1.45	0.023	1.43	0.027
$D_0 \rightarrow D_2$	$\pi_1^2\pi_1^{*1} \rightarrow \pi_1^2\pi_2^{*1}$	1.90	0.821	1.87	0.808
$D_0 \rightarrow D_3$	$\pi_1^2\pi_1^{*1} \rightarrow \pi_1^2\pi_3^{*1}$	1.91	0.158	1.96	0.160
Exp.	-	1.77	-	1.77	-

Tab. S3: Calculated SS-CASPT2 (active space CAS(3,4)) vertical excitations energies and oscillator strengths of the PDI-19 and PDI-13-N radical anion at the MP2-optimized (PDI-19) and CASPT2-optimized (PDI-13-N) neutral ground-state equilibrium geometries. The calculated energies are compared with the experimental absorption maximum of the spectro-electrochemically derived radical anion PDI- tBP [S1].

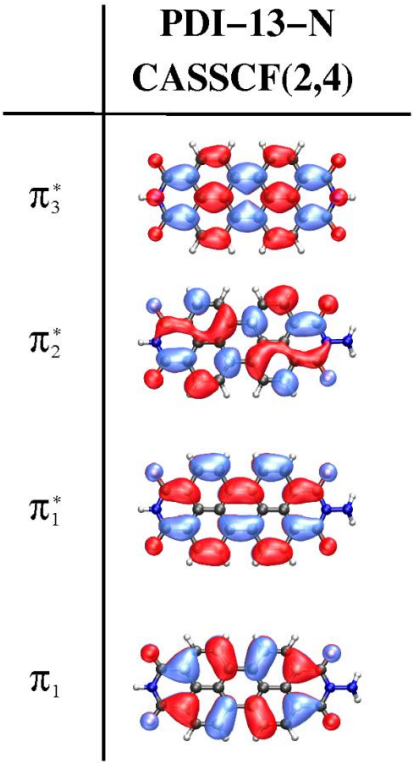

Fig. S3: State-averaged CASSCF molecular orbitals included in the active space of PDI-13-N for the determination of the excited state absorption bands (Figure 3c).

		Franck-Condon		**π-Minimum**		**CT-Minimum**	
transition	character	ΔE (eV)	f	ΔE (eV)	f	ΔE (eV)	f
$S_1 \rightarrow S_2$	$\pi_1{}^1\pi_1{}^{*1} \rightarrow \pi_1{}^{*2}$	0.50	0.002	0.34	0.031	0.46	0.026
$S_1 \rightarrow S_6$	$\pi_1{}^1\pi_1{}^{*1} \rightarrow \pi_1{}^1\pi_3{}^{*1}$	1.28	0.153	1.34	0.149	1.45	0.167
$S_1 \rightarrow S_7$	$\pi_1{}^1\pi_1{}^{*1} \rightarrow \pi_1{}^1\pi_2{}^{*1}$	1.47	0.937	1.46	0.925	1.47	0.916
Exp.	-	1.77	-	1.77	-	1.77	-

Tab. S4: Excited state transitions and oscillator strengths between the S_1 state and three higher excited states of PDI-13-N at the relevant points, calculated at the SS-CASPT2 level of theory (active space CAS(2,4)). The calculated energies are compared with the experimental absorption maximum of the spectro-electrochemically derived radical anion PDI-tBP (ref. 39).

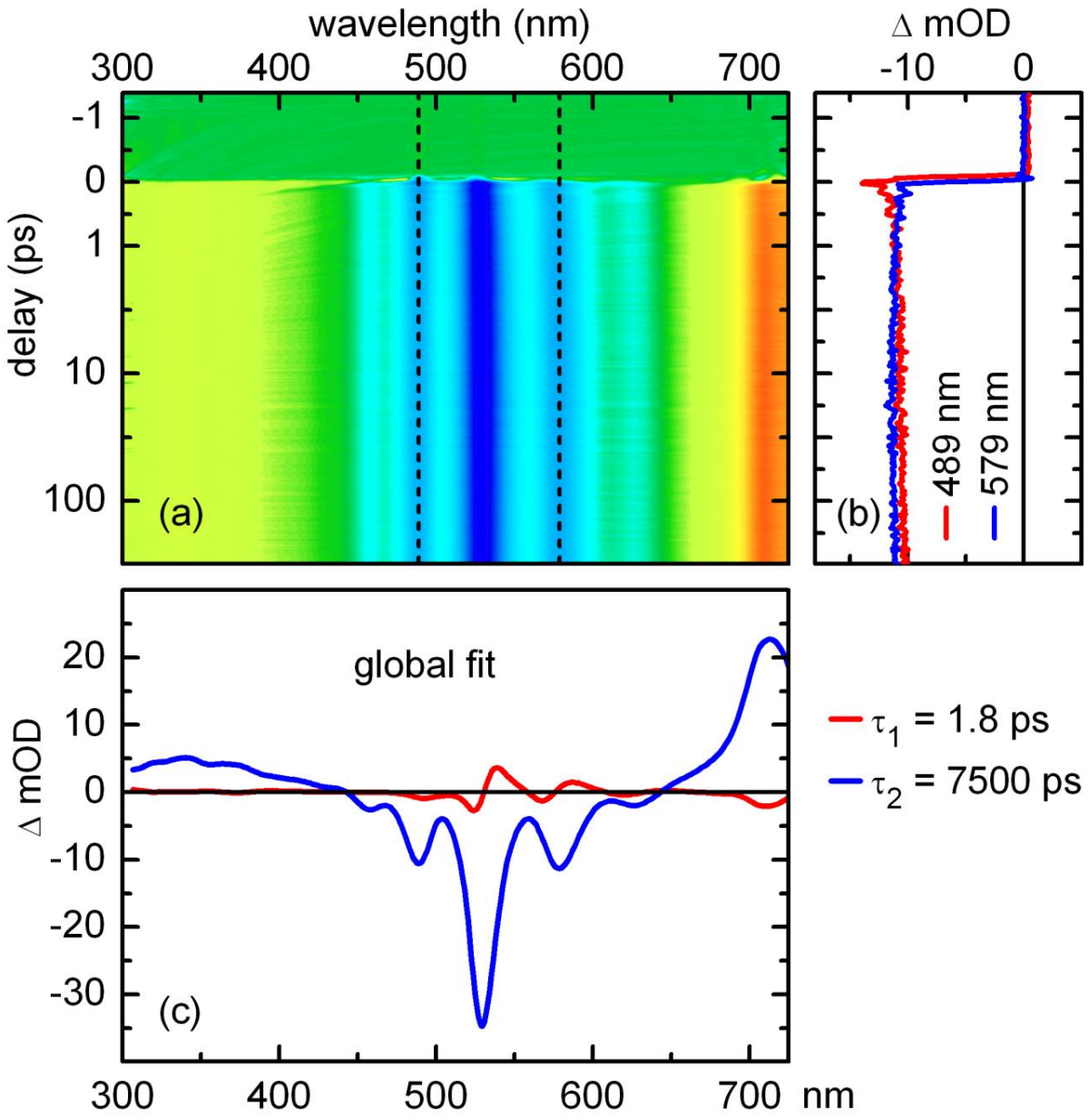

Fig. S4: (a) Color map of the transient absorption of PDI-19 in chloroform after optical excitation at 490 nm; warm colors represent positive and cold colors negative absorption changes. The time axis is linear up to 1 ps and logarithmic for longer delays. (b) Time traces at the spectral position of the GSB (489 nm) and SE (579 nm) (dotted lines in (a)). (c) Decay associated difference spectra of the biexponetial global fit.

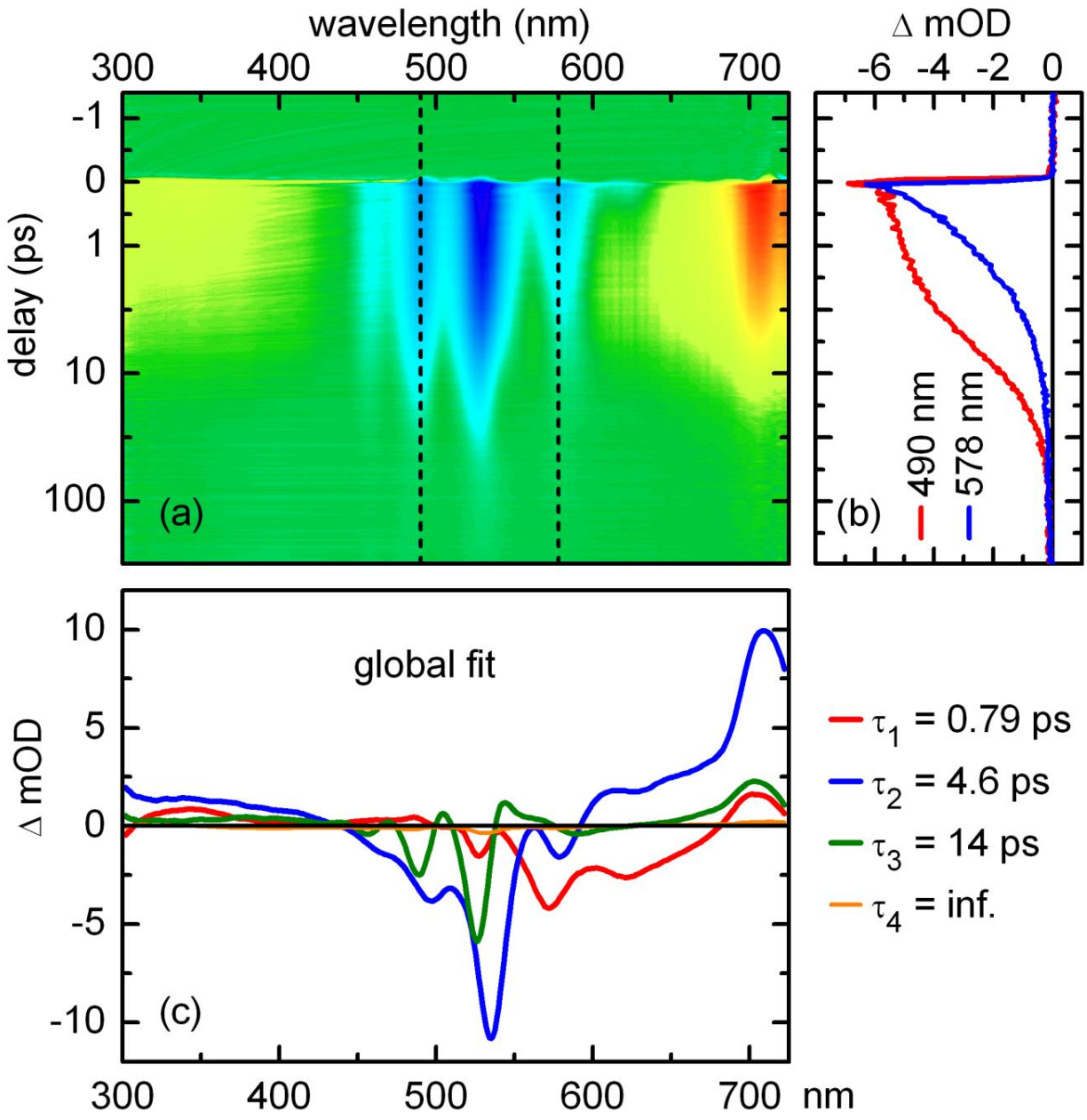

Fig. S5: (a) Color map of the transient absorption of PDI-13-N in chloroform after optical excitation at 490 nm; warm colors represent positive and cold colors negative absorption changes. The time axis is linear up to 1 ps and logarithmic for longer delays. (b) Time traces at the spectral position of the GSB (490 nm) and SE (578 nm) (dotted lines in (a)). (c) Decay associated difference spectra of the triexponetial global fit.

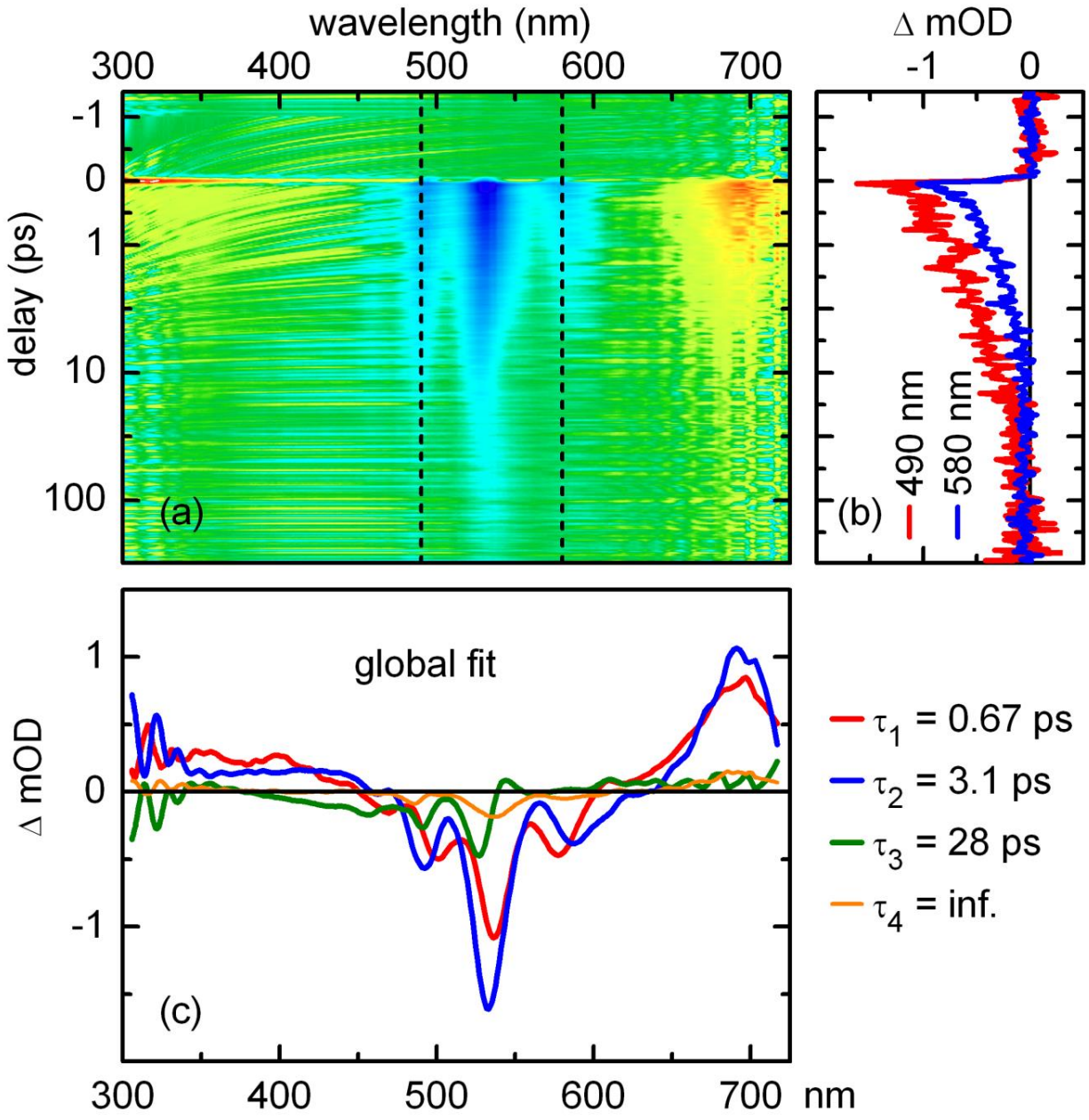

Fig. S6: (a) Color map of the transient absorption of PDI-13-N in DMSO after optical excitation at 490 nm; warm colors represent positive and cold colors negative absorption changes. The time axis is linear up to 1 ps and logarithmic for longer delays. (b) Time traces at the spectral position of the GSB (490 nm) and SE (580 nm) (dotted lines in (a)). (c) Decay associated difference spectra of the triexponetial global fit.

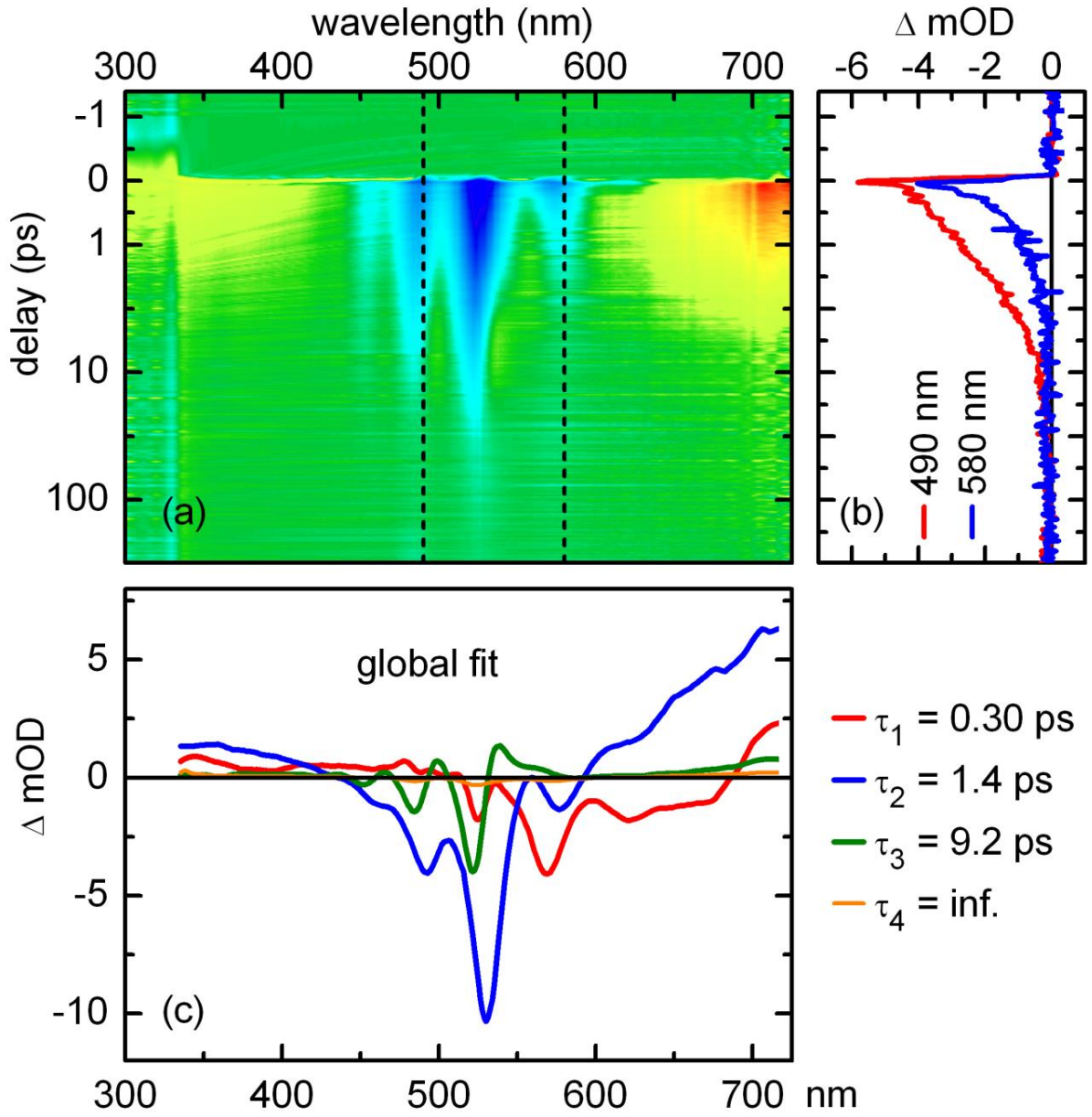

Fig. S7: (a) Color map of the transient absorption of PDI-13-N in THF after optical excitation at 490 nm; warm colors represent positive and cold colors negative absorption changes. The time axis is linear up to 1 ps and logarithmic for longer delays. (b) Time traces at the spectral position of the GSB (490 nm) and SE (580 nm) (dotted lines in (a)). (c) Decay associated difference spectra of the triexponetial global fit.

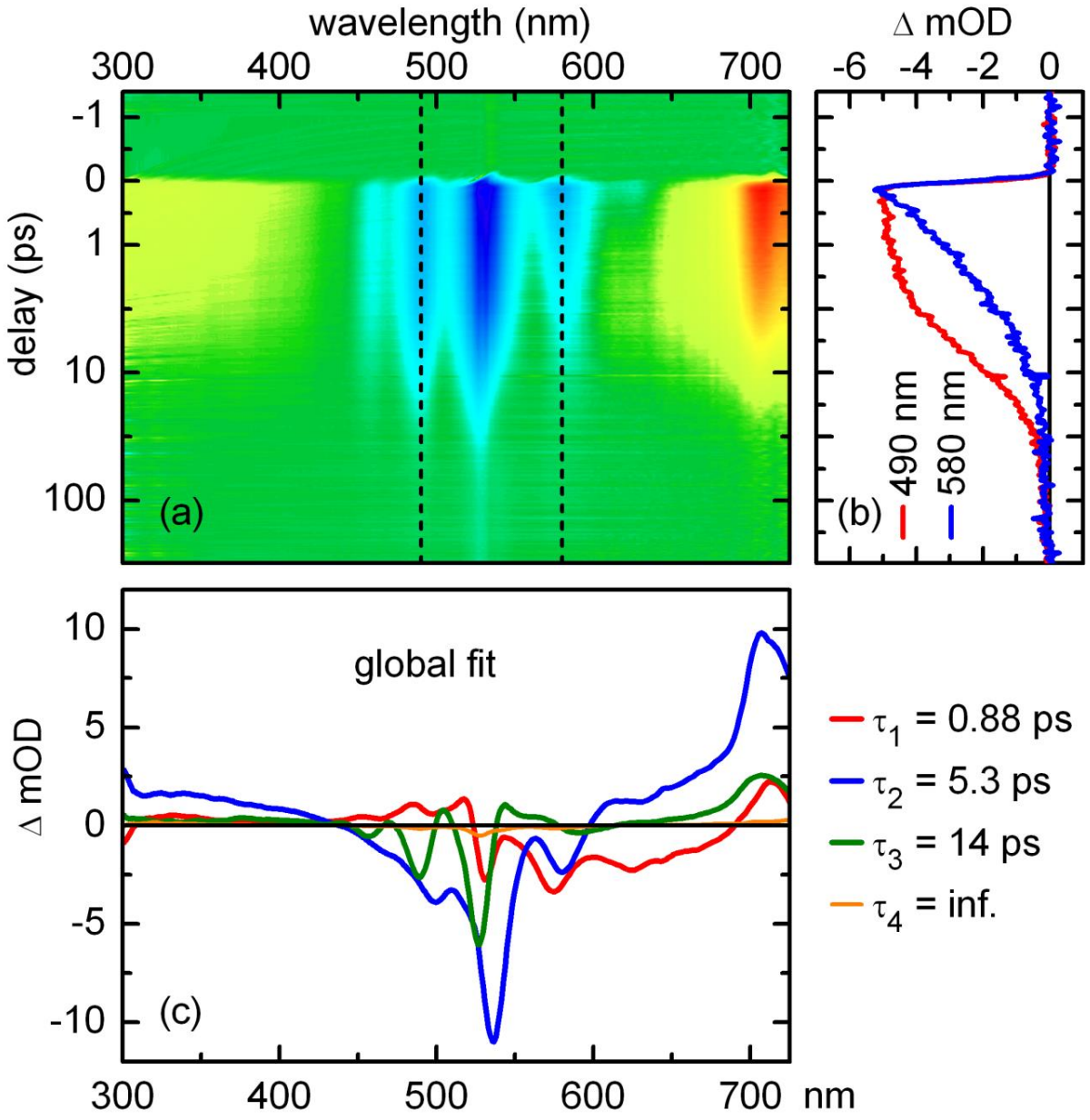

Fig. S8: (a) Color map of the transient absorption of PDI-13-N in chloroform after optical excitation at 530 nm; warm colors represent positive and cold colors negative absorption changes. The time axis is linear up to 1 ps and logarithmic for longer delays. (b) Time traces at the spectral position of the GSB (490 nm) and SE (580 nm) (dotted lines in (a)). (c) Decay associated difference spectra of the triexponetial global fit.

ΔE (eV)	state	gas phase	THF	DMSO	$CHCl_3$
Franck-Condon	LE(fast)	0.00	0.00	0.00	0.00
	CT(fast)	+0.48	+0.32	+0.42	+0.22
π-Minimum	LE(fast)	-0.20	-0.18	-0.18	-0.19
	LE(slow)		-0.19	-0.18	-0.19
	CT(fast)	+0.37	+0.23	+0.33	+0.11
CT-Minimum	LE(fast)	+0.39	+0.44	+0.45	+0.43
	CT(fast)	-0.35	-0.46	-0.37	-0.55
	CT(slow)		-1.08	-1.25	-0.98
barrier (π-/CT-Minimum)	-	0.12	0.08	0.11	0.03

Tab. S5: Relative energies of PDI-13-N for the gas phase and different solvents for all relevant points discussed in the paper (LE, locally excited state; CT, charge transfer state). Vertical excitation energies of the Franck-Condon points in each environment were chosen as reference points. The barriers between the π- and CT-Minimum were obtained by interpolation using the two minimum structures. The Karlsruhe split valence basis set with a polarization function (def2-SV(P)), the TDDFT method and the CAM-B3LYP functional were used in all calculations, which have been performed with the program package Gaussian09 [S3]. The geometry optimizations have been carried out in each environment. The "fast" energies correspond to the electronic response of the solvent molecules. Therefore the solvation effects were incorporated by non-equilibrium calculations using the Polarizable Continuum Model (PCM) e.g. only the electron distribution of the solvent was relaxed to the excited state of the solute and not the reorientation of the solvent molecule themselves. The "slow" energies correspond to the full solvent relaxation. Therefore the solvation effects were incorporated by equilibrium calculations e.g. the electron distribution of the solvent and the reorientation of the solvent molecules were relaxed to the excited state of the solute.

Cartesian coordinates for the ground state minimum (FC, CAM-B3LYP/SV(P)) and first excited state minima (π-/CT-Minimum CAM-B3LYP/SV(P)) of PDI-13-N for the gas phase

FC

	x	y	z
C	-3.288186	-1.222946	0.005160
C	-4.768655	-1.239825	0.004486
N	-5.390022	0.000000	-0.037453
C	-4.768655	1.239826	0.004458
C	-3.288186	1.222946	0.005134
O	-5.433744	-2.253976	0.043211
N	-6.781312	-0.000001	-0.178357
O	-5.433744	2.253978	0.043156
C	-2.600668	-2.415657	0.010910
C	-2.600668	2.415658	0.010856
H	-7.130506	-0.847119	0.270486
H	-7.130510	0.847111	0.270494
C	-2.576262	0.000000	0.001839
C	-1.155476	0.000000	0.002115
C	-1.199107	-2.423482	0.008727
C	-0.460107	-1.248473	0.003881
C	-1.199107	2.423483	0.008680
C	-0.460107	1.248474	0.003868
C	1.015035	-1.248409	0.001883
C	1.015035	1.248409	0.001894
C	1.711658	0.000000	0.000934
C	1.751226	-2.424809	0.000421
C	3.152497	-2.418744	-0.001535
C	3.841979	-1.227857	-0.002209
C	3.134212	0.000000	-0.001141
C	1.751227	2.424809	0.000465
C	3.152497	2.418743	-0.001481
C	3.841979	1.227857	-0.002182
C	5.327229	-1.247727	-0.004230
C	5.327230	1.247726	-0.004197
N	5.935049	0.000000	-0.005020
O	5.985001	-2.261646	-0.005097
O	5.985001	2.261646	-0.005042
H	6.952415	0.000000	-0.006490
H	3.719323	-3.351959	-0.002715
H	1.246297	-3.390117	0.000396
H	-0.696398	-3.389946	0.011259
H	-3.167833	-3.348523	0.015605
H	-3.167833	3.348523	0.015526
H	-0.696398	3.389946	0.011191
H	1.246298	3.390117	0.000462
H	3.719324	3.351958	-0.002636

π-Minimum

	x	y	z
C	-3.285424	-0.008891	-1.220619
C	-4.758663	-0.010112	-1.239537
N	-5.380207	0.028256	-0.000062
C	-4.758690	-0.010086	1.239432
C	-3.285445	-0.008873	1.220531
O	-5.423873	-0.048472	-2.257857
N	-6.771067	0.165580	-0.000056
O	-5.423913	-0.048490	2.257729
C	-2.590694	-0.014702	-2.434813
C	-2.590735	-0.014672	2.434737
H	-7.119363	-0.282150	-0.848233
H	-7.119547	-0.283169	0.847505
C	-2.578325	-0.005209	-0.000038
C	-1.150835	-0.004688	-0.000026
C	-1.210860	-0.010994	-2.447221
C	-0.454840	-0.005600	-1.242122
C	-1.210901	-0.010963	2.447168
C	-0.454861	-0.005584	1.242082
C	0.985591	-0.002508	-1.242155
C	0.985570	-0.002493	1.242139
C	1.682885	-0.000812	-0.000002
C	1.738718	-0.000988	-2.448364
C	3.118586	0.001976	-2.437214
C	3.815040	0.003450	-1.225344
C	3.112171	0.002114	0.000010
C	1.738676	-0.000959	2.448362
C	3.118544	0.002007	2.437236
C	3.815018	0.003468	1.225378
C	5.293529	0.006467	-1.247044
C	5.293508	0.006499	1.247104
N	5.901738	0.007967	0.000035
O	5.950443	0.007914	-2.265293
O	5.950403	0.007940	2.265365
H	6.919127	0.010281	0.000044
H	3.695760	0.003350	-3.363745
H	1.226600	-0.001594	-3.409448
H	-0.700655	-0.012771	-3.409340
H	-3.168200	-0.020059	-3.360954
H	-3.168259	-0.020021	3.360867
H	-0.700712	-0.012729	3.409295
H	1.226541	-0.001553	3.409437
H	3.695701	0.003397	3.363777

CT-Minimum

	x	y	z
C	-3.295293	-0.000720	-1.247862
C	-4.723646	-0.000909	-1.305889
N	-5.349614	-0.000925	0.000054
C	-4.723639	-0.001341	1.305994
C	-3.295286	-0.001194	1.247959
O	-5.473916	-0.001063	-2.259061
N	-6.661162	-0.000840	0.000057
O	-5.473905	-0.002144	2.259170
C	-2.577137	-0.000413	-2.460487
C	-2.577124	-0.001449	2.460581
H	-7.097503	-0.002913	-0.924050
H	-7.097497	-0.003210	0.924167
C	-2.609834	-0.000843	0.000047
C	-1.170080	-0.000781	0.000043
C	-1.206852	-0.000370	-2.451070
C	-0.469061	-0.000651	-1.243502
C	-1.206840	-0.001172	2.451156
C	-0.469055	-0.000712	1.243585
C	0.982956	-0.000872	-1.246422
C	0.982962	-0.000253	1.246498
C	1.682683	-0.000429	0.000036
C	1.729321	-0.001422	-2.436029
C	3.118169	-0.001363	-2.425113
C	3.816116	-0.000676	-1.228111
C	3.111929	-0.000248	0.000032
C	1.729334	0.000372	2.436100
C	3.118181	0.000637	2.425177
C	3.816123	0.000324	1.228171
C	5.291925	-0.000544	-1.249787
C	5.291931	0.000547	1.249839
N	5.897877	0.000736	0.000024
O	5.959682	-0.001338	-2.262101
O	5.959694	0.000646	2.262151
H	6.914649	0.000610	0.000022
H	3.689161	-0.001834	-3.355921
H	1.225913	-0.002015	-3.401304
H	-0.684255	-0.000012	-3.405697
H	-3.135162	-0.000194	-3.398083
H	-3.135144	-0.001825	3.398180
H	-0.684237	-0.001343	3.405781
H	1.225931	0.000677	3.401379
H	3.689179	0.001097	3.355982

Cartesian coordinates for the ground state minimum (FC, CAM-B3LYP/SV(P)) and first excited state minima (π-/CT-Minimum CAM-B3LYP/SV(P)) of PDI-13-N for the solvent THF

FC

	x	y	z
C	-3.287158	-1.223869	0.002154
C	-4.764865	-1.238914	0.000130
N	-5.387595	-0.000004	-0.023021
C	-4.764866	1.238917	-0.000495
C	-3.287158	1.223871	0.001592
O	-5.435344	-2.253455	0.023462
N	-6.784139	-0.000032	-0.143016
O	-5.435344	2.253470	0.022301
C	-2.597620	-2.416595	0.007773
C	-2.597619	2.416599	0.006663
H	-7.121166	-0.838420	0.332401
H	-7.121181	0.838521	0.332099
C	-2.576512	0.000000	-0.000579
C	-1.155815	0.000000	0.000026
C	-1.196530	-2.424792	0.007195
C	-0.460002	-1.248091	0.002092
C	-1.196529	2.424795	0.006260
C	-0.460002	1.248090	0.001841
C	1.014893	-1.248045	0.000282
C	1.014894	1.248044	0.000537
C	1.711829	-0.000001	0.000442
C	1.748769	-2.425942	-0.002433
C	3.149781	-2.419378	-0.002891
C	3.841001	-1.228499	-0.001451
C	3.134016	0.000000	-0.000470
C	1.748771	2.425942	-0.001487
C	3.149782	2.419378	-0.001771
C	3.841001	1.228498	-0.000885
C	5.323437	-1.244763	-0.001514
C	5.323437	1.244762	-0.000894
N	5.931783	-0.000001	-0.001325
O	5.986996	-2.259352	-0.001684
O	5.986997	2.259350	-0.000543
H	6.949732	-0.000001	-0.001219
H	3.708954	-3.356642	-0.004565
H	1.245080	-3.391509	-0.004848
H	-0.694873	-3.391397	0.011351
H	-3.157057	-3.353578	0.011686
H	-3.157055	3.353585	0.010050
H	-0.694870	3.391399	0.009945
H	1.245079	3.391509	-0.003427
H	3.708955	3.356643	-0.002917

π-Minimum

	x	y	z
C	-3.273177	-1.221175	0.000963
C	-4.743004	-1.238346	-0.000263
N	-5.365557	0.000007	-0.022693
C	-4.743006	1.238362	-0.000331
C	-3.273175	1.221185	0.000928
O	-5.414333	-2.257511	0.023918
N	-6.761602	0.000024	-0.139651
O	-5.414332	2.257524	0.023822
C	-2.575570	-2.436342	0.006284
C	-2.575565	2.436351	0.006230
H	-7.097580	-0.839542	0.334635
H	-7.097696	0.839059	0.335495
C	-2.567073	0.000004	-0.001284
C	-1.138428	0.000002	-0.000445
C	-1.198278	-2.448855	0.005060
C	-0.441828	-1.241193	0.000946
C	-1.198274	2.448861	0.005022
C	-0.441826	1.241197	0.000937
C	0.994828	-1.241274	-0.000353
C	0.994831	1.241275	-0.000342
C	1.692685	-0.000000	-0.000736
C	1.748629	-2.449921	-0.001536
C	3.126031	-2.438460	-0.001807
C	3.825146	-1.225612	-0.001227
C	3.122801	-0.000001	-0.001109
C	1.748634	2.449921	-0.001493
C	3.126035	2.438458	-0.001751
C	3.825148	1.225608	-0.001195
C	5.300168	-1.243962	-0.000990
C	5.300170	1.243956	-0.000933
N	5.908743	-0.000003	-0.000544
O	5.963346	-2.263389	-0.000031
O	5.963349	2.263382	0.000027
H	6.926690	-0.000004	0.000067
H	3.695725	-3.368996	-0.002664
H	1.237945	-3.411307	-0.002913
H	-0.689310	-3.411163	0.007964
H	-3.145455	-3.366600	0.009946
H	-3.145450	3.366609	0.009865
H	-0.689304	3.411167	0.007910
H	1.237951	3.411307	-0.002845
H	3.695731	3.368993	-0.002576

CT-Minimum

	x	y	z
C	3.286920	1.245363	-0.000327
C	4.716629	1.299715	-0.000018
N	5.347019	-0.000000	-0.000111
C	4.716630	-1.299716	-0.000458
C	3.286919	-1.245363	-0.000064
O	5.456118	2.264393	-0.000063
N	6.650509	0.000000	-0.000029
O	5.456118	-2.264392	0.001125
C	2.571376	2.457362	-0.000520
C	2.571376	-2.457362	0.000409
H	7.101846	0.916716	0.000905
H	7.101847	-0.916716	0.000477
C	2.594837	-0.000000	-0.000246
C	1.159903	-0.000000	-0.000193
C	1.197903	2.448158	-0.000515
C	0.459505	1.244088	-0.000261
C	1.197903	-2.448158	0.000394
C	0.459505	-1.244088	-0.000000
C	-0.992947	1.247223	-0.000001
C	-0.992948	-1.247223	-0.000176
C	-1.694446	0.000000	-0.000078
C	-1.738082	2.438041	0.000336
C	-3.125730	2.426141	0.000456
C	-3.828035	1.229164	0.000237
C	-3.124108	0.000000	-0.000030
C	-1.738082	-2.438041	-0.000419
C	-3.125730	-2.426141	-0.000450
C	-3.828035	-1.229164	-0.000231
C	-5.298139	1.247480	0.000389
C	-5.298139	-1.247480	-0.000283
N	-5.904636	0.000000	0.000031
O	-5.975209	2.259836	0.000599
O	-5.975209	-2.259836	-0.000218
H	-6.921981	0.000000	0.000134
H	-3.688919	3.361470	0.000737
H	-1.234586	3.403029	0.000560
H	0.678681	3.404988	-0.000673
H	3.126608	3.396174	-0.000625
H	3.126608	-3.396174	0.000630
H	0.678681	-3.404988	0.000694
H	-1.234586	-3.403029	-0.000645
H	-3.688919	-3.361470	-0.000661

Cartesian coordinates for the ground state minimum (FC, CAM-B3LYP/SV(P)) and first excited state minima (π-/CT-Minimum CAM-B3LYP/SV(P)) of PDI-13-N for the solvent DMSO

FC

	x	y	z
C	-3.287001	-1.223996	0.000470
C	-4.764042	-1.238644	-0.001054
N	-5.387147	-0.000001	-0.017923
C	-4.764042	1.238645	-0.001268
C	-3.287001	1.223997	0.000275
O	-5.435654	-2.253427	0.017013
N	-6.785141	-0.000008	-0.129957
O	-5.435654	2.253431	0.016625
C	-2.597072	-2.416725	0.004695
C	-2.597072	2.416727	0.004302
H	-7.118117	-0.836360	0.352261
H	-7.118130	0.836363	0.352218
C	-2.576506	0.000000	-0.001622
C	-1.155879	0.000000	-0.000846
C	-1.196031	-2.425065	0.004186
C	-0.459975	-1.248039	0.000829
C	-1.196031	2.425066	0.003849
C	-0.459975	1.248040	0.000739
C	1.014867	-1.247996	-0.000032
C	1.014868	1.247996	0.000061
C	1.711877	0.000000	-0.000038
C	1.748295	-2.426175	-0.001059
C	3.149302	-2.419447	-0.001269
C	3.840857	-1.228596	-0.000662
C	3.133944	0.000000	-0.000321
C	1.748295	2.426175	-0.000718
C	3.149302	2.419446	-0.000872
C	3.840857	1.228595	-0.000466
C	5.322633	-1.244149	-0.000636
C	5.322633	1.244148	-0.000430
N	5.931097	0.000000	-0.000955
O	5.987426	-2.258972	-0.000286
O	5.987426	2.258971	0.000096
H	6.949111	-0.000001	-0.000417
H	3.706638	-3.357698	-0.002046
H	1.245250	-3.391942	-0.001999
H	-0.694984	-3.391847	0.006945
H	-3.154660	-3.354705	0.007862
H	-3.154659	3.354708	0.007281
H	-0.694983	3.391848	0.006436
H	1.245250	3.391942	-0.001484
H	3.706639	3.357698	-0.001463

π-Minimum

	x	y	z
C	-3.272932	-1.221285	-0.000611
C	-4.741911	-1.238089	-0.001704
N	-5.364754	0.000008	-0.017816
C	-4.741912	1.238106	-0.001746
C	-3.272930	1.221295	-0.000625
O	-5.414516	-2.257561	0.017578
N	-6.762377	0.000029	-0.126476
O	-5.414513	2.257575	0.017541
C	-2.574662	-2.436741	0.003780
C	-2.574657	2.436749	0.003762
H	-7.093810	-0.837321	0.355300
H	-7.093924	0.836807	0.356214
C	-2.566955	0.000004	-0.002585
C	-1.138125	0.000002	-0.001576
C	-1.198007	-2.449340	0.002936
C	-0.441329	-1.241038	-0.000138
C	-1.198001	2.449345	0.002925
C	-0.441326	1.241042	-0.000139
C	0.994271	-1.241125	-0.000503
C	0.994273	1.241125	-0.000495
C	1.692307	-0.000000	-0.000607
C	1.748371	-2.450364	-0.000864
C	3.125161	-2.438754	-0.000710
C	3.824865	-1.225628	-0.000238
C	3.122524	-0.000001	-0.000381
C	1.748376	2.450364	-0.000842
C	3.125165	2.438751	-0.000692
C	3.824867	1.225624	-0.000233
C	5.299054	-1.243297	0.000391
C	5.299057	1.243291	0.000362
N	5.907797	-0.000003	0.000364
O	5.963628	-2.262991	-0.000095
O	5.963631	2.262984	-0.000068
H	6.925808	-0.000004	0.000368
H	3.693144	-3.370238	-0.000970
H	1.238295	-3.411936	-0.001681
H	-0.689575	-3.411796	0.005329
H	-3.142796	-3.367978	0.006915
H	-3.142790	3.367986	0.006886
H	-0.689568	3.411800	0.005313
H	1.238301	3.411936	-0.001650
H	3.693150	3.370235	-0.000949

CT-Minimum

	x	y	z
C	-3.287238	-1.244746	-0.000150
C	-4.717570	-1.298078	-0.000163
N	-5.348737	-0.000000	-0.000072
C	-4.717570	1.298078	0.000183
C	-3.287238	1.244746	0.000170
O	-5.454968	-2.265040	-0.000218
N	-6.650509	-0.000000	-0.000266
O	-5.454968	2.265040	0.000369
C	-2.572375	-2.456390	-0.000301
C	-2.572375	2.456391	0.000357
H	-7.104531	-0.915374	0.000087
H	-7.104532	0.915373	0.000335
C	-2.593669	0.000000	0.000001
C	-1.159777	0.000000	0.000007
C	-1.198004	-2.447400	-0.000254
C	-0.459507	-1.244254	-0.000056
C	-1.198004	2.447400	0.000300
C	-0.459507	1.244254	0.000075
C	0.993172	-1.247473	0.000090
C	0.993172	1.247473	-0.000077
C	1.695064	0.000000	0.000001
C	1.738054	-2.438562	0.000298
C	3.125435	-2.426375	0.000328
C	3.828714	-1.229354	0.000150
C	3.124831	-0.000000	-0.000002
C	1.738054	2.438562	-0.000292
C	3.125435	2.426375	-0.000329
C	3.828714	1.229353	-0.000159
C	5.297592	-1.247006	0.000130
C	5.297592	1.247006	-0.000141
N	5.904181	-0.000000	-0.000063
O	5.976524	-2.259439	0.000310
O	5.976524	2.259439	-0.000299
H	6.921638	-0.000000	-0.000054
H	3.686877	-3.362726	0.000483
H	1.234699	-3.403554	0.000461
H	-0.679788	-3.404835	-0.000406
H	-3.126781	-3.395575	-0.000461
H	-3.126781	3.395575	0.000542
H	-0.679788	3.404835	0.000467
H	1.234699	3.403554	-0.000455
H	3.686877	3.362726	-0.000485

Cartesian coordinates for the ground state minimum (FC, CAM-B3LYP/SV(P)) and first excited state minima (π-/CT-Minimum CAM-B3LYP/SV(P)) of PDI-13-N for the solvent chloroform

FC

	x	y	z
C	-3.287285	-1.223763	0.003099
C	-4.765382	-1.239060	0.000839
N	-5.387926	-0.000006	-0.025696
C	-4.765382	1.239063	0.000127
C	-3.287284	1.223766	0.002460
O	-5.435177	-2.253518	0.026616
N	-6.783596	-0.000039	-0.150364
O	-5.435177	2.253536	0.025294
C	-2.598008	-2.416486	0.009240
C	-2.598007	2.416492	0.007982
H	-7.123104	-0.839658	0.320847
H	-7.123118	0.839786	0.320471
C	-2.576491	0.000001	0.000165
C	-1.155773	0.000000	0.000726
C	-1.196853	-2.424610	0.008547
C	-0.460014	-1.248130	0.002875
C	-1.196852	2.424613	0.007491
C	-0.460014	1.248130	0.002591
C	1.014921	-1.248084	0.000620
C	1.014922	1.248082	0.000908
C	1.711818	-0.000001	0.000704
C	1.749087	-2.425787	-0.002601
C	3.150134	-2.419314	-0.003345
C	3.841129	-1.228430	-0.001812
C	3.134061	-0.000001	-0.000565
C	1.749088	2.425787	-0.001534
C	3.150135	2.419315	-0.002078
C	3.841129	1.228429	-0.001168
C	5.323954	-1.245154	-0.002162
C	5.323954	1.245153	-0.001453
N	5.932224	-0.000001	-0.002000
O	5.986751	-2.259655	-0.002512
O	5.986752	2.259653	-0.001207
H	6.950124	-0.000001	-0.002109
H	3.710320	-3.356030	-0.005357
H	1.245161	-3.391290	-0.005300
H	-0.694985	-3.391164	0.013060
H	-3.158467	-3.352911	0.013463
H	-3.158466	3.352920	0.011610
H	-0.694981	3.391168	0.011474
H	1.245160	3.391289	-0.003699
H	3.710322	3.356031	-0.003493

π-Minimum

	x	y	z
C	-3.273336	-1.221102	0.001859
C	-4.743671	-1.238504	0.000334
N	-5.366066	0.000006	-0.025160
C	-4.743673	1.238520	0.000272
C	-3.273334	1.221111	0.001826
O	-5.414207	-2.257513	0.026689
N	-6.761221	0.000023	-0.146946
O	-5.414206	2.257525	0.026606
C	-2.576116	-2.436106	0.007668
C	-2.576112	2.436113	0.007616
H	-7.099787	-0.840774	0.323054
H	-7.099900	0.840324	0.323858
C	-2.567124	0.000004	-0.000464
C	-1.138601	0.000002	0.000411
C	-1.198458	-2.448579	0.006347
C	-0.442107	-1.241297	0.001820
C	-1.198453	2.448585	0.006309
C	-0.442104	1.241301	0.001810
C	0.995143	-1.241375	0.000123
C	0.995146	1.241376	0.000133
C	1.692905	-0.000000	-0.000438
C	1.748805	-2.449668	-0.001406
C	3.126559	-2.438283	-0.002045
C	3.825329	-1.225591	-0.001556
C	3.122945	-0.000001	-0.001221
C	1.748809	2.449668	-0.001366
C	3.126563	2.438280	-0.001993
C	3.825331	1.225588	-0.001527
C	5.300844	-1.244371	-0.001723
C	5.300846	1.244365	-0.001669
N	5.909346	-0.000003	-0.001442
O	5.963177	-2.263641	-0.000905
O	5.963181	2.263634	-0.000849
H	6.927247	-0.000004	-0.001106
H	3.697248	-3.368273	-0.003173
H	1.237856	-3.410982	-0.002865
H	-0.689262	-3.410835	0.009469
H	-3.147021	-3.365800	0.011558
H	-3.147016	3.365808	0.011480
H	-0.689256	3.410839	0.009414
H	1.237862	3.410982	-0.002803
H	3.697254	3.368270	-0.003091

CT-Minimum

	x	y	z
C	3.286754	1.245712	-0.000299
C	4.716165	1.300631	-0.000062
N	5.346049	-0.000000	-0.000139
C	4.716165	-1.300631	-0.000295
C	3.286754	-1.245712	0.000024
O	5.457072	2.263798	-0.000152
N	6.650578	0.000000	-0.000189
O	5.457073	-2.263798	0.001042
C	2.570800	2.457874	-0.000503
C	2.570800	-2.457874	0.000471
H	7.100172	0.917589	0.000691
H	7.100172	-0.917589	0.000437
C	2.595541	-0.000000	-0.000179
C	1.159965	-0.000000	-0.000135
C	1.197826	2.448576	-0.000478
C	0.459483	1.243990	-0.000209
C	1.197826	-2.448576	0.000438
C	0.459483	-1.243990	0.000043
C	-0.992873	1.247096	0.000040
C	-0.992873	-1.247096	-0.000157
C	-1.694148	0.000000	-0.000053
C	-1.738160	2.437751	0.000380
C	-3.125968	2.426005	0.000481
C	-3.827696	1.229041	0.000239
C	-3.123753	0.000000	-0.000027
C	-1.738160	-2.437751	-0.000428
C	-3.125968	-2.426005	-0.000477
C	-3.827696	-1.229041	-0.000250
C	-5.298550	1.247778	0.000351
C	-5.298550	-1.247778	-0.000307
N	-5.904991	0.000000	-0.000015
O	-5.974447	2.260107	0.000584
O	-5.974447	-2.260107	-0.000298
H	-6.922279	0.000000	0.000068
H	-3.690164	3.360745	0.000759
H	-1.234631	3.402756	0.000618
H	0.678059	3.405068	-0.000653
H	3.126483	3.396481	-0.000641
H	3.126483	-3.396481	0.000709
H	0.678059	-3.405068	0.000733
H	-1.234631	-3.402756	-0.000661
H	-3.690164	-3.360745	-0.000705

REFERENCES

S1. Salbeck, J.; Kunkely, H.; Langals, H.; Saalfrank, R. W.; Daub, J. *Chimia* **1989**, *43*, 6.

S2. H.-J. Werner, P. J. Knowles, G. Knizia, F. R. Manby, M. Schütz, P. Celani, T. Korona, R. Lindh, A. Mitrushenkov, G. Rauhut, K. R. Shamasundar, T. B. Adler, R. D. Amos, A. Bernhardsson, A. Berning, D. L. Cooper, M. J. O. Deegan, A. J. Dobbyn, F. Eckert, E. Goll, C. Hampel, A. Hesselmann, G. Hetzer, T. Hrenar, G. Jansen, C. Köppl, Y. Liu, A. W. Lloyd, R. A. Mata, A. J. May, S. J. McNicholas, W. Meyer, M. E. Mura, A. Nicklaß, D. P. O'Neill, P. Palmieri, K. Pflüger, R. Pitzer, M. Reiher, T. Shiozaki, H. Stoll, A. J. Stone, R. Tarroni, T. Thorsteinsson, M. Wang, A. Wolf, MOLPRO, *version 2006.1*, *a package of ab initio programs*, 2006, see http: //www.molpro.net.

S3. Gaussian 09, Revision A.02, Frisch, M. J.; Trucks, G. W.; Schlegel, H. B.; Scuseria, G. E.; Robb, M. A.; Cheeseman, J. R.; Scalmani, G.; Barone, V.; Mennucci, B.; Petersson, G. A.; Nakatsuji, H.; Caricato, M.; Li, X.; Hratchian, H. P.; Izmaylov, A. F.; Bloino, J.; Zheng, G.; Sonnenberg, J. L.; Hada, M.; Ehara, M.; Toyota, K.; Fukuda, R.; Hasegawa, J.; Ishida, M.; Nakajima, T.; Honda, Y.; Kitao, O.; Nakai, H.; Vreven, T.; Montgomery, Jr., J. A.; Peralta, J. E.; Ogliaro, F.; Bearpark, M.; Heyd, J. J.; Brothers, E.; Kudin, K. N.; Staroverov, V. N.; Kobayashi, R.; Normand, J.; Raghavachari, K.; Rendell, A.; Burant, J. C.; Iyengar, S. S.; Tomasi, J.; Cossi, M.; Rega, N.; Millam, N. J.; Klene, M.; Knox, J. E.; Cross, J. B.; Bakken, V.; Adamo, C.; Jaramillo, J.; Gomperts, R.; Stratmann, R. E.; Yazyev, O.; Austin, A. J.; Cammi, R.; Pomelli, C.; Ochterski, J. W.; Martin, R. L.; Morokuma, K.; Zakrzewski, V. G.; Voth, G. A.; Salvador, P.; Dannenberg, J. J.; Dapprich, S.; Daniels, A. D.; Farkas, Ö.; Foresman, J. B.; Ortiz, J. V.; Cioslowski, J.; Fox, D. J. Gaussian, Inc., Wallingford CT, 2009.

B. Supporting information for chapter 4.2

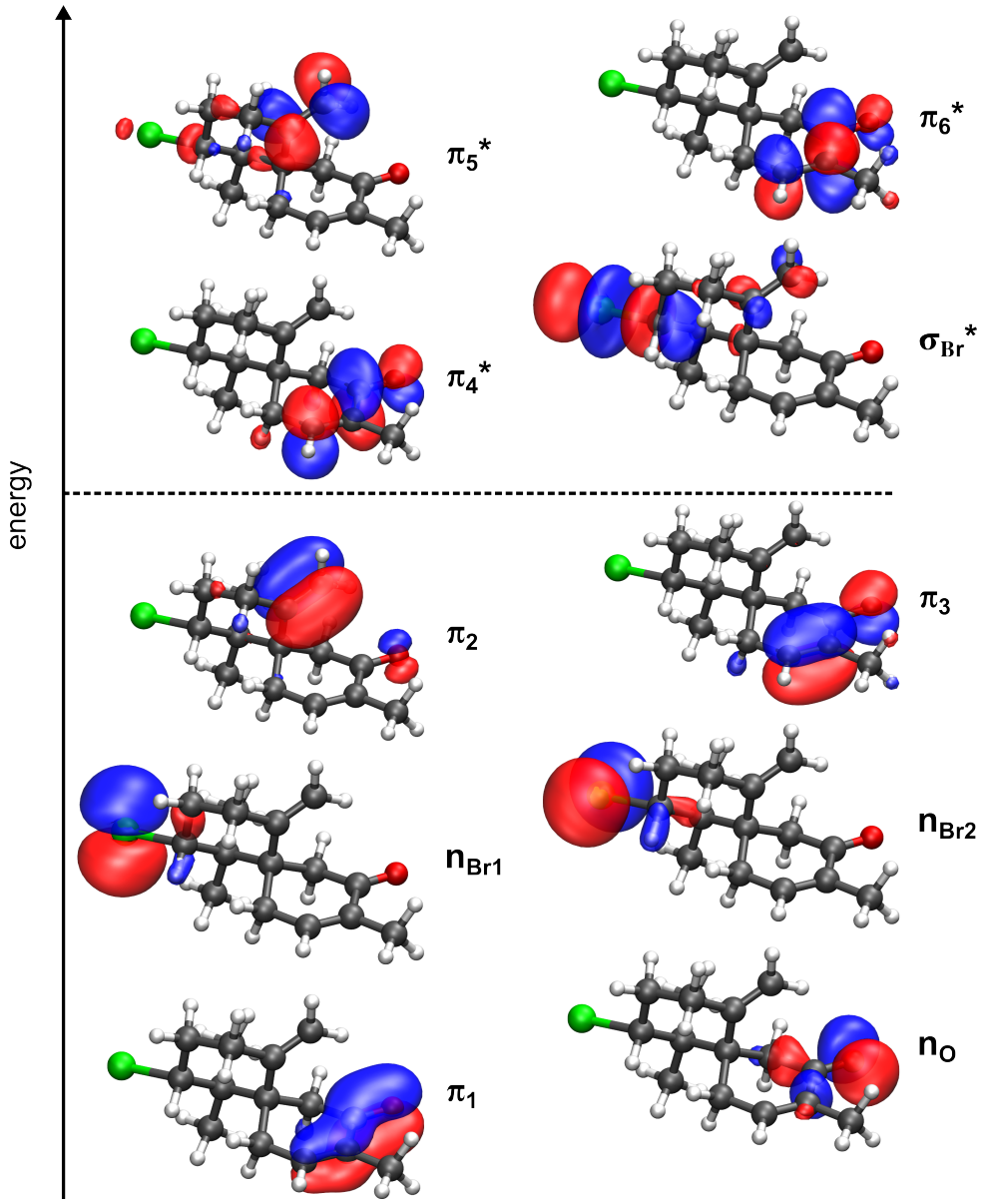

Figure B.1.: State-averaged CASSCF(12/10) molecular orbitals included in the active space of dactylone **1**, obtained with the 6-31G* basis set at the B3LYP/6-31G*-optimized ground state equilibrium geometry.

Table B.1.: Adiabatic excitation energies (eV) of the low-lying excited states at the relevant points along the relaxation pathway of dactylone **1**. The energy calculations were performed at the CASPT2 and UB3LYP level of theory in combination with the 6-31G* basis set. The values in parentheses are the calculated free energy differenes ΔG determined at the UB3LYP level of theory.

	CASPT2	UB3LYP
S_0 Minimum (Franck Condon Point)		
S_0	0.00	0.00
S_1 ($n \rightarrow \pi^*$)	3.96	3.89[a]
T_1 ($n \rightarrow \pi^*$)	3.70	3.26 / 3.10[a]
T_2 ($\pi \rightarrow \pi^*$)	4.04	3.35[a]
S_1 Minimum (S_1-Min)		
S_1 ($n \rightarrow \pi^*$)	3.41	3.32[a]
T_1 ($n \rightarrow \pi^*$)	3.25	2.50[a]
T_2 ($\pi \rightarrow \pi^*$)	3.58	2.79[a]
S_1/T_2 Intersection (S_1/T_2 IS)		
S_1 ($n \rightarrow \pi^*$)	3.46	—
T_2 ($\pi \rightarrow \pi^*$)	3.44	—
T_1/T_2 Conical Intersection (T_1/T_2 CoIn)		
T_1 ($n \rightarrow \pi^*$)	3.35	—
T_2 ($\pi \rightarrow \pi^*$)	3.36	—
T_1 Minimum (T_1-Min1)		
T_1 ($n \rightarrow \pi^*$)	3.24	—
T_1 Minimum (T_1-Min2)		
T_1 ($\pi \rightarrow \pi^*$)	3.03	2.61 (2.47)
T_1 Minimum (T_1-Min3)		
T_1 ($\pi \rightarrow \pi^*$)	3.20	2.73 (2.60)
T_1 Transition State (TS)		
T_1 ($\pi \rightarrow \pi^*$)	3.19	2.74 (2.60)
T_1 Minimum (T_1-Min4)		
T_1 ($\pi \rightarrow \pi^*$)	3.02	2.62 (2.46)
T_1/S_0 Intersection (T_1/S_0 IS)		
S_0	3.01	—
T_1 ($\pi \rightarrow \pi^*$)	3.06	—
S_0/S_1 Conical Intersection (S_0/S_1 CoIn)		
S_0	4.59	—
S_1 ($n \rightarrow \pi^*$)	4.79	—

[a] Calculated at the CAM-B3LYP/6-31+G** level of theory.

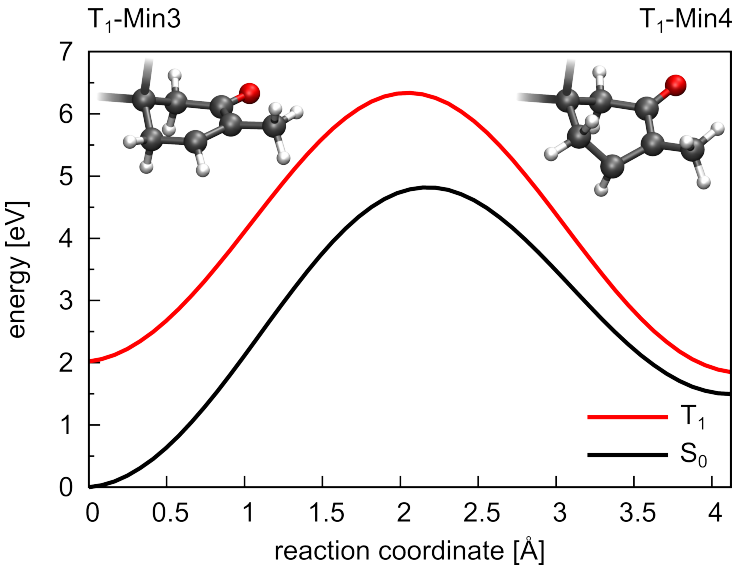

Figure B.2.: Energy profile of the S_0 and the T_1 state along the reaction path between the triplet minima T_1-Min3 and T_1-Min4 of dactylone **1**. The energy calculations were performed at the CASPT2/6-31G* level of theory. The reaction coordinate was generated by linear interpolation between the optimized T_1-Min3 and T_1-Min4 geometries.

Table B.2.: Calculated CASPT2 (PT2) and UB3LYP energy differenes ΔE (eV) of the optimized structures of the four diradical pathways DR1 - DR4. The values in parentheses are the calculated free energy differenes ΔG determined at the UB3LYP level of theory. The triplet state minimum T_1-Min3 was chosen in each case as reference point. ^{3}TS are the transition states in the T_1 state describing the formation of the first σ-bond and leading to the corresponding triplet diradical minima ^{3}DR. ^{1}DR are the singlet diradical minima from which either the cycloadducts can be formed through the transition states ^1TS_P or a relaxation back to the initial reagent **1** can occur *via* the transition states ^1TS_R. Only for the singlet diradical ^{1}DR4 the second σ-bond formation is sterically inhibited and no corresponding transition state ^1TS_P exist.

	DR1			DR2			DR3			DR4		
	PT2	B3LYP		PT2	B3LYP		PT2	B3LYP		PT2	B3LYP	
T_1-Min3	0.00	0.00	(0.00)	0.00	0.00	(0.00)	0.00	0.00	(0.00)	0.00	0.00	(0.00)
^{3}TS	0.16	0.34	(0.33)	0.36	0.57	(0.55)	0.42	0.47	(0.46)	0.31	0.77	(0.74)
^{3}DR	-0.48	-0.17	(-0.19)	-1.08	-0.71	(-0.66)	-1.32	-1.09	(-1.02)	-0.65	-0.09	(-0.13)
^{1}DR	-0.50	-0.19	(-0.18)	-1.08	-0.71	(-0.63)	-1.33	-1.09	(-1.00)	-0.69	-0.15	(-0.09)
^1TS_P	-0.49	-0.13	(-0.12)	-0.97	-0.38	(-0.30)	-1.29	-0.87	(-0.72)		—	
^1TS_R	-0.48	-0.18	(-0.17)	-0.90	-0.37	(-0.32)	-0.82	-0.50	(-0.44)	-0.54	-0.14	(-0.06)

List of abbreviations

BHJ bulk-heterojunction

DFT density functional theory

CI configuration interaction

CoIn conical intersection

CASSCF complete active space self consistent field

CASPT2 complete active space second-order perturbation theory

CC2 second-order approximate coupled cluster

CT charge transfer

^{1}**DR** singlet diradical

^{3}**DR** triplet diradical

enones α,β-unsaturated ketones

IC internal conversion

FRET Förster Resonant Energy Transfer

KS Kohn-Sham

LE locally excited

ISC intersystem crossing

OSCs organic solar cells

MO molecular orbital

MCSCF multi configuration self consistent field

PES potential energy surfaces

PCBM phenyl-C61-butyric acid methyl ester

PDI perylene diimides

PCM polarizable continuum model

P3HT poly(3-hexylthiophene)

PSCs polymer based solar cells

PV photovoltaic

RMSD root-mean-square deviation

TS transition state

SOC spin-orbit coupling

STC singlet-triplet crossing

TDDFT time-dependent density functional theory

UHF unrestricted Hartree-Fock theory

UKS unrestricted Kohn-Sham

Bibliography

[1] S. B. Darling and F. You, *RSC Adv.* **3**, 17633 (2013).

[2] L. Lu, T. Zheng, Q. Wu, A. M. Schneider, D. Zhao and L. Yu, *Chem. Rev.* **115**, 12666 (2015).

[3] G. Li, R. Zhu and Y. Yang, *Nature Photon* **6**, 153 (2012).

[4] Q. An, F. Zhang, J. Zhang, W. Tang, Z. Deng and B. Hu, *Energy Environ. Sci.* **9**, 281 (2016).

[5] G. Yu, J. Gao, J. C. Hummelen, F. Wudl and A. J. Heeger, *Science* **270**, 1789 (1995).

[6] Z. He, C. Zhong, X. Huang, W.-Y. Wong, H. Wu, L. Chen, S. Su and Y. Cao, *Advanced Materials* **23**, 4636 (2011).

[7] F. Zhang, D. Wu, Y. Xu and X. Feng, *J. Mater. Chem.* **21**, 17590 (2011).

[8] D. Chi, S. Qu, Z. Wang and J. Wang, *J. Mater. Chem. C* **2**, 4383 (2014).

[9] M. Rubio, M. Merchán, R. Pou-Amérigo and E. Ortí, *ChemPhysChem* **4**, 1308 (2003).

[10] M. Rubio, M. Merchán and E. Ortí, *ChemPhysChem* **6**, 1357 (2005).

[11] S. Salzmann, M. Kleinschmidt, J. Tatchen, R. Weinkauf and C. M. Marian, *Physical Chemistry Chemical Physics* **10**, 380 (2008).

[12] X.-F. Wu, X. Zheng, H.-G. Wang, Y.-Y. Zhao, X. Guan, D. L. Phillips, X. Chen and W. Fang, *The Journal of Chemical Physics* **133**, 134507 (2010).

[13] G. Cui and W. Fang, *The Journal of Physical Chemistry A* **115**, 11544 (2011).

[14] S. Siegert, F. Vogeler, C. M. Marian and R. Weinkauf, *Phys. Chem. Chem. Phys.* **13**, 10350 (2011).

[15] M. Stenrup, *Chemical Physics* **397**, 18 (2012).

[16] D. Fazzi, M. Barbatti and W. Thiel, *Phys. Chem. Chem. Phys.* **17**, 7787 (2015).

[17] A. Prlj, B. F. E. Curchod and C. Corminboeuf, *Phys. Chem. Chem. Phys.* **17**, 14719 (2015).

[18] E. Kozma and M. Catellani, *Dyes and Pigments* **98**, 160 (2013).

[19] L. Yang, L. Yan and W. You, *The Journal of Physical Chemistry Letters* **4**, 1802 (2013).

[20] T. Ameri, P. Khoram, J. Min and C. J. Brabec, *Advanced Materials* **25**, 4245 (2013).

[21] T. Bach and J. P. Hehn, *Angew. Chem. Int. Ed.* **50**, 1000 (2011).

[22] P. A. Roethle and D. Trauner, *Natural Product Reports* **25**, 298 (2008).

[23] G. M. Cragg and D. J. Newman, *Biochimica et Biophysica Acta (BBA) - General Subjects* **1830**, 3670 (2013).

[24] M. Oelgemöller, *Chem. Rev.* (2016).

[25] J. Marrero, A. D. Rodríguez and C. L. Barnes, *Organic Letters* **7**, 1877 (2005).

[26] P. A. Roethle, P. T. Hernandez and D. Trauner, *Organic Letters* **8**, 5901 (2006).

[27] B. Tang, C. D. Bray and G. Pattenden, *Tetrahedron Letters* **47**, 6401 (2006).

[28] A. D. Rodríguez and J.-G. Shi, *J. Org. Chem.* **63**, 420 (1998).

[29] S. N. Fedorov, M. V. Reshetnyak, A. P. Schedrin, S. G. Ilyin, Y. T. Struchkov, V. A. Stonik and G. B. Elyakov, *Dokl. Akad. Nauk SSSR* **305**, 877 (1989).

[30] S. N. Fedorov, O. S. Radchenko, L. K. Shubina, A. I. Kalinovsky, A. V. Gerasimenko, D. Y. Popov and V. A. Stonik, *Journal of the American Chemical Society* **123**, 504 (2001).

[31] S. H. Vosko, L. Wilk and M. Nusair, *Canadian Journal of Physics* **58**, 1200 (1980).

[32] C. Lee, W. Yang and R. G. Parr, *Physical Review B* **37**, 785 (1988).

[33] A. D. Becke, *J. Chem. Phys.* **98**, 5648 (1993).

[34] P. J. Stephens, F. J. Devlin, C. F. Chabalowski and M. J. Frisch, *J. Phys. Chem.* **98**, 11623 (1994).

[35] S. F. Sousa, P. A. Fernandes and M. J. Ramos, *The Journal of Physical Chemistry A* **111**, 10439 (2007).

[36] H.-J. Werner and P. J. Knowles, *J. Chem. Phys.* **82**, 5053 (1985).

[37] B. O. Roos, *Advances in Chemical Physics*, Wiley Interscience, New York, USA (1987).

[38] P. J. Knowles and H.-J. Werner, *Chemical Physics Letters* **145**, 514 (1988).

[39] P. G. Szalay, T. Müller, G. Gidofalvi, H. Lischka and R. Shepard, *Chem. Rev.* **112**, 108 (2012).

[40] O. Christiansen, H. Koch and P. Jørgensen, *Chemical Physics Letters* **243**, 409 (1995).

[41] J. F. Stanton and R. J. Bartlett, *J. Chem. Phys.* **98**, 7029 (1993).

[42] T. Yanai, D. P. Tew and N. C. Handy, *Chemical Physics Letters* **393**, 51 (2004).

[43] A. Szabo and N. S. Ostlund, *Modern Quantum Chemistry: Introduction to Advanced Electronic Structure Theory*, Macmillan Publishing Co., Inc., New York, USA (1982).

[44] J. Baker, A. Scheiner and J. Andzelm, *Chemical Physics Letters* **216**, 380 (1993).

[45] J. A. Pople, P. M. W. Gill and N. C. Handy, *International Journal of Quantum Chemistry* **56**, 303 (1995).

[46] J. M. Wittbrodt and H. B. Schlegel, *J. Chem. Phys.* **105**, 6574 (1996).

[47] P.-O. Löwdin, *Physical Review* **97**, 1509 (1955).

[48] A. T. Amos and G. G. Hall, *Proceedings of the Royal Society A: Mathematical, Physical and Engineering Sciences* **263**, 483 (1961).

[49] C. J. Cramer, F. J. Dulles, D. J. Giesen and J. Almlöf, *Chemical Physics Letters* **245**, 165 (1995).

[50] J. Tomasi, B. Mennucci and R. Cammi, *Chem. Rev.* **105**, 2999 (2005).

[51] B. Mennucci and R. Cammi, *Continuum Solvation Models in Chemical Physics: From Theory to Applications*, Wiley, Chichester, England (2008).

[52] R. Cammi, S. Corni, B. Mennucci and J. Tomasi, *J. Chem. Phys.* **122**, 104513 (2005).

[53] S. Corni, R. Cammi, B. Mennucci and J. Tomasi, *J. Chem. Phys.* **123**, 134512 (2005).

[54] R. Improta, V. Barone, G. Scalmani and M. J. Frisch, *J. Chem. Phys.* **125**, 054103 (2006).

[55] M. J. Frisch, G. W. Trucks, H. B. Schlegel, G. E. Scuseria, M. A. Robb, J. R. Cheeseman, G. Scalmani, V. Barone, B. Mennucci, G. A. Petersson, H. Nakatsuji, M. Caricato, X. Li, H. P. Hratchian, A. F. Izmaylov, J. Bloino, G. Zheng, J. L. Sonnenberg, M. Hada, M. Ehara, K. Toyota, R. Fukuda, J. Hasegawa, M. Ishida, T. Nakajima, Y. Honda, O. Kitao, H. Nakai, T. Vreven, J. A. Montgomery, Jr., J. E. Peralta, F. Ogliaro, M. Bearpark, J. J. Heyd, E. Brothers, K. N. Kudin, V. N. Staroverov, R. Kobayashi, J. Normand, K. Raghavachari, A. Rendell, J. C. Burant, S. S. Iyengar, J. Tomasi, M. Cossi, N. Rega, J. M. Millam, M. Klene, J. E. Knox, J. B. Cross, V. Bakken, C. Adamo, J. Jaramillo, R. Gomperts, R. E. Stratmann, O. Yazyev, A. J. Austin, R. Cammi, C. Pomelli, J. W. Ochterski, R. L. Martin, K. Morokuma, V. G. Zakrzewski, G. A. Voth, P. Salvador, J. J. Dannenberg, S. Dapprich, A. D. Daniels, Ö. Farkas, J. B. Foresman, J. V. Ortiz, J. Cioslowski and D. J. Fox, *Gaussian 09, Revision D.01*, Gaussian Inc. Wallingford CT 2009.

[56] H.-J. Werner, P. J. Knowles, G. Knizia, F. R. Manby and M. Schütz, *WIREs Comput Mol Sci* **2**, 242 (2012).

[57] H.-J. Werner, P. J. Knowles, G. Knizia, F. R. Manby, M. Schütz, P. Celani, T. Korona, R. Lindh, A. Mitrushenkov, G. Rauhut, K. R. Shamasundar, T. B. Adler, R. D. Amos, A. Bernhardsson, A. Berning, D. L. Cooper, M. J. O. Deegan, A. J. Dobbyn, F. Eckert, E. Goll, C. Hampel, A. Hesselmann, G. Hetzer, T. Hrenar, G. Jansen, C. Köppl, Y. Liu, A. W. Lloyd, R. A. Mata, A. J. May, S. J. McNicholas, W. Meyer, M. E. Mura, A. Nicklass, D. P. O'Neill, P. Palmieri, D. Peng, K. Pflüger, R. Pitzer, M. Reiher, T. Shiozaki, H. Stoll, A. J. Stone, R. Tarroni, T. Thorsteinsson and M. Wang, *MOLPRO, version 2012.1, a package of ab initio programs* (2012), see http://www.molpro.net/.

[58] *TURBOMOLE V6.5 2013, a development of University of Karlsruhe and Forschungszentrum Karlsruhe GmbH, 1989-2007, TURBOMOLE GmbH, since 2007; available from* `http://www.turbomole.com`.

[59] M. Klessinger and J. Michl, *Excited States and Photochemistry of Organic Molecules*, VCH Publishers, Inc., New York, USA (1995).

[60] F. Sicilia, L. Blancafort, M. J. Bearpark and M. A. Robb, *Journal of Chemical Theory and Computation* **4**, 257 (2008).

[61] A. Nenov, P. Kölle, M. A. Robb and R. de Vivie-Riedle, *J. Org. Chem.* **75**, 123 (2010).

[62] F. Bernardi, M. Olivucci and M. A. Robb, *Chem. Soc. Rev.* **25**, 321 (1996).

[63] F. Bernardi, M. Olivucci and M. A. Robb, *Journal of Photochemistry and Photobiology A: Chemistry* **105**, 365 (1997).

[64] W. Domcke, D. R. Yarkony and Köppel, *Conical Intersections: Electronic Structure, Dynamics and Spectroscopy*, World Scientific Publishing, Singapore (2004).

[65] S. Matsika and P. Krause, *Annu. Rev. Phys. Chem.* **62**, 621 (2011).

[66] A. Cannizzo, F. van Mourik, W. Gawelda, G. Zgrablic, C. Bressler and M. Chergui, *Angew. Chem. Int. Ed.* **45**, 3174 (2006).

[67] W. Gawelda, A. Cannizzo, V.-T. Pham, F. van Mourik, C. Bressler and M. Chergui, *Journal of the American Chemical Society* **129**, 8199 (2007).

[68] A. Cannizzo, A. M. Blanco-Rodríguez, A. E. Nahhas, J. Šebera, S. Záliš, J. Antonín Vlček and M. Chergui, *Journal of the American Chemical Society* **130**, 8967 (2008).

[69] C. E. Crespo-Hernández, G. Burdzinski and R. Arce, *The Journal of Physical Chemistry A* **112**, 6313 (2008).

[70] J. S. Zugazagoitia, E. Collado-Fregoso, E. F. Plaza-Medina and J. Peon, *The Journal of Physical Chemistry A* **113**, 805 (2009).

[71] D. Parker, R. Minns, T. Penfold, G. Worth and H. Fielding, *Chemical Physics Letters* **469**, 43 (2009).

[72] C. Reichardt and C. E. Crespo-Hernández, *The Journal of Physical Chemistry Letters* **1**, 2239 (2010).

[73] R. S. Minns, D. S. N. Parker, T. J. Penfold, G. A. Worth and H. H. Fielding, *Physical Chemistry Chemical Physics* **12**, 15607 (2010).

[74] C. Reichardt, C. Guo and C. E. Crespo-Hernández, *J. Phys. Chem. B* **115**, 3263 (2011).

[75] M. Chergui, *Dalton Trans.* **41**, 13022 (2012).

[76] R. Ghosh and D. K. Palit, *The Journal of Physical Chemistry A* **116**, 1993 (2012).

[77] M. Richter, P. Marquetand, J. González-Vázquez, I. Sola and L. González, *The Journal of Physical Chemistry Letters* **3**, 3090 (2012).

[78] C. Yang, H. Su, X. Sun and M. W. George, *J. Chem. Phys.* **136**, 204507 (2012).

[79] S. Mai, P. Marquetand, M. Richter, J. González-Vázquez and L. González, *ChemPhysChem* **14**, 2920 (2013).

[80] O. Bräm, F. Messina, E. Baranoff, A. Cannizzo, M. K. Nazeeruddin and M. Chergui, *The Journal of Physical Chemistry C* **117**, 15958 (2013).

[81] S. Mai, P. Marquetand and L. González, *J. Chem. Phys.* **140**, 204302 (2014).

[82] M. Richter, S. Mai, P. Marquetand and L. González, *Phys. Chem. Chem. Phys.* **16**, 24423 (2014).

[83] M. Marazzi, S. Mai, D. Roca-Sanjuán, M. G. Delcey, R. Lindh, L. González and A. Monari, *The Journal of Physical Chemistry Letters* **7**, 622 (2016).

[84] M. Olivucci, *Computational Photochemistry*, Elsevier, Amsterdam, The Netherlands (2005).

[85] A. G. Kutateladze, *Computational Methods in Photochemistry*, CRC Press, Boca Raton, USA (2005).

[86] P. A. M. Dirac, *Proceedings of the Royal Society A: Mathematical, Physical and Engineering Sciences* **114**, 243 (1927).

[87] G. Wentzel, *Z. Phys.* **43**, 524 (1927).

[88] E. Fermi, *Nuclear Physics*, University of Chicago Press, Chicago (1950).

[89] M. Bixon, *J. Chem. Phys.* **48**, 715 (1968).

[90] W. Pauli, *Z. Phys.* **43**, 601 (1927).

[91] R. Englman and J. Jortner, *Molecular Physics* **18**, 145 (1970).

[92] J. S. Wilson, N. Chawdhury, M. R. A. Al-Mandhary, M. Younus, M. S. Khan, P. R. Raithby, A. Köhler and R. H. Friend, *Journal of the American Chemical Society* **123**, 9412 (2001).

[93] T. A. Skotheim and J. R. Reynolds (eds.), *Handbook of Conducting Polymers*, CRC Press, Boca Raton, FL, third edn. (2007).

[94] I. F. Perepichka and D. F. Perepichka (eds.), *Handbook of Thiophene-Based Materials: Applications in Organic Electronics and Photonics*, John Wiley & Sons Ltd, Chichester, UK (2007).

[95] R. S. Becker, J. Seixas de Melo, A. L. Maçanita and F. Elisei, *J. Phys. Chem.* **100**, 18683 (1996).

[96] R. Weinkauf, L. Lehr, E. W. Schlag, S. Salzmann and C. M. Marian, *Physical Chemistry Chemical Physics* **10**, 393 (2008).

[97] P. Kölle, T. Schnappinger and R. de Vivie-Riedle, *Phys. Chem. Chem. Phys.* **18**, 7903 (2016).

[98] W. Paa, J.-P. Yang, M. Helbig, J. Hein and S. Rentsch, *Chemical Physics Letters* **292**, 607 (1998).

[99] A. Yang, M. Kuroda, Y. Shiraishi and T. Kobayashi, *J. Phys. Chem. B* **102**, 3706 (1998).

[100] J. Yang, W. Paa and S. Rentsch, *Synthetic Metals* **101**, 624 (1999).

[101] J.-P. Yang, W. Paa and S. Rentsch, *Chemical Physics Letters* **320**, 665 (2000).

[102] W. Paa, J.-P. Yang and S. Rentsch, *Appl Phys B* **71**, 443 (2000).

[103] E. Marcantoni and G. Renzi, *Seminars in Organic Synthesis*, Societa Chimicà Italiana, Milan, Italy (2003).

[104] M. Theander, O. Inganäs, W. Mammo, T. Olinga, M. Svensson and M. R. Andersson, *The Journal of Physical Chemistry B* **103**, 7771 (1999).

[105] Z. Xu and B. Hu, *Advanced Functional Materials* **18**, 2611 (2008).

[106] M. Liedtke, A. Sperlich, H. Kraus, A. Baumann, C. Deibel, M. J. M. Wirix, J. Loos, C. M. Cardona and V. Dyakonov, *Journal of the American Chemical Society* **133**, 9088 (2011).

[107] Y. Shao and Y. Yang, *Advanced Materials* **17**, 2841 (2005).

[108] A. Köhler and H. Bässler, *Materials Science and Engineering: R: Reports* **66**, 71 (2009).

[109] S. R. Yost, E. Hontz, S. Yeganeh and T. Van Voorhis, *The Journal of Physical Chemistry C* **116**, 17369 (2012).

[110] M. Tabachnyk, B. Ehrler, S. Gélinas, M. L. Böhm, B. J. Walker, K. P. Musselman, N. C. Greenham, R. H. Friend and A. Rao, *Nat Mater* **13**, 1033 (2014).

[111] M. Sadrai and G. R. Bird, *Optics Communications* **51**, 62 (1984).

[112] W. Herbst and K. Hunger, *Industrielle Organische Pigmente. Herstellung, Eigenschaften, Anwendung*, Wiley-VCH, Weinheim, Germany (1995).

[113] H. Langhals, J. Karolin and L. B.-A. Johansson, *Journal of the Chemical Society, Faraday Transactions* **94**, 2919 (1998).

[114] A. K. Sheridan, A. R. Buckley, A. M. Fox, A. Bacher, D. D. C. Bradley and I. D. W. Samuel, *Journal of Applied Physics* **92**, 6367 (2002).

[115] H. Zollinger, *Color Chemistry, Synthesis, Properties, and Applications of Organic Dyes and Pigments*, Wiley-VCH, Zürich, Switzerland (2003).

[116] C. Ego, D. Marsitzky, S. Becker, J. Zhang, A. C. Grimsdale, K. Müllen, J. D. MacKenzie, C. Silva and R. H. Friend, *Journal of the American Chemical Society* **125**, 437 (2003).

[117] H. Langhals, *HETEROCYCLES* **40**, 477 (1995).

[118] H. Langhals, *HCA* **88**, 1309 (2005).

[119] A. Rademacher, S. Märkle and H. Langhals, *Chem. Ber.* **115**, 2927 (1982).

[120] C. Li and H. Wonneberger, *Advanced Materials* **24**, 613 (2012).

[121] P. Kölle, I. Pugliesi, H. Langhals, R. Wilcken, A. J. Esterbauer, R. de Vivie-Riedle and E. Riedle, *Phys. Chem. Chem. Phys.* **17**, 25061 (2015).

[122] P. Nalbach, I. Pugliesi, H. Langhals and M. Thorwart, *Physical Review Letters* **108** (2012).

[123] A. Nenov and R. de Vivie-Riedle, *J. Chem. Phys.* **135**, 034304 (2011).

[124] H. Langhals and W. Jona, *Chem. Eur. J.* **4**, 2110 (1998).

[125] V. Barone and A. Polimeno, *Chem. Soc. Rev.* **36**, 1724 (2007).

[126] B. Mennucci, C. Cappelli, C. A. Guido, R. Cammi and J. Tomasi, *The Journal of Physical Chemistry A* **113**, 3009 (2009).

[127] A. V. Marenich, C. J. Cramer, D. G. Truhlar, C. A. Guido, B. Mennucci, G. Scalmani and M. J. Frisch, *Chem. Sci.* **2**, 2143 (2011).

[128] J. W. Blunt, B. R. Copp, M. H. G. Munro, P. T. Northcote and M. R. Prinsep, *Nat. Prod. Rep.* **28**, 196 (2011).

[129] J. W. Blunt, B. R. Copp, R. A. Keyzers, M. H. G. Munro and M. R. Prinsep, *Nat. Prod. Rep.* **33**, 382 (2016).

[130] G. Zanoni and M. Franzini, *ChemInform* **35** (2004).

[131] J. Marrero, A. D. Rodríguez, P. Baran, R. G. Raptis, J. A. Sánchez, E. Ortega-Barria and T. L. Capson, *Organic Letters* **6**, 1661 (2004).

[132] S. A. Look, M. T. Burch, W. Fenical, Q. Zheng and J. Clardy, *J. Org. Chem.* **50**, 5741 (1985).

[133] D. Stichnoth, P. Kölle, T. J. Kimbrough, E. Riedle, R. de Vivie-Riedle and D. Trauner, *Nat Comms* **5**, 5597 (2014).

[134] D. Faulkner, *Tetrahedron* **33**, 1421 (1977).

[135] D. J. Faulkner, *Natural Product Reports* **13**, 75 (1996).

[136] J. W. Blunt, B. R. Copp, M. H. G. Munro, P. T. Northcote and M. R. Prinsep, *Natural Product Reports* **23**, 26 (2006).

[137] E. G. Lyakhova, *Russian Chemical Bulletin, International Edition* **52**, 1022 (2003).

[138] G. M. König and A. D. Wright, *Journal of Natural Products* **60**, 967 (1997).

[139] K. A. El Sayed, D. C. Dunbar, T. L. Perry, S. P. Wilkins and M. T. Hamann, *J. Agric. Food Chem.* **45** (1997).

[140] E. G. Juagdan, R. Kalidindi and P. Scheuer, *Tetrahedron* **53**, 521 (1997).

[141] S. N. Fedorov, L. K. Shubina, A. M. Bode, V. A. Stonik and Z. Dong, *Cancer Research* **67**, 5914 (2007).

[142] J. Ring, *Quantum Chemical Study of the [2+2] Photocycloaddition of Dactylone to Aplydactone*, Bachelor thesis, Ludwig-Maximilians-Universität München (2015).

[143] S. Poplata, A. Tröster, Y.-Q. Zou and T. Bach, *Chem. Rev.* (2016).

[144] E. J. Corey, J. D. Bass, R. LeMahieu and R. B. Mitra, *J. Am. Chem. Soc.* **86**, 5570 (1964).

[145] A. Padwa, *Organic Photochemistry*, Marcel Dekker, New York, USA (1981).

[146] J.-P. Pete, *[2+2]-Photocycloaddition Reactions of Cyclopentenones with Alkenes in CRC Handbook of Photochemistry and Photobiology*, CRC Press, Boca Raton, USA (2004).

[147] R. Srinivasan and K. H. Carlough, *Journal of the American Chemical Society* **89**, 4932 (1967).

[148] R. S. H. Liu and G. S. Hammond, *Journal of the American Chemical Society* **89**, 4936 (1967).

[149] D. J. Maradyn and A. C. Weedon, *Journal of the American Chemical Society* **117**, 5359 (1995).

[150] M. Audley and N. W. Geraghty, *Tetrahedron Letters* **37**, 1641 (1996).

[151] S. A. Bradley, B. J. Bresnan, S. M. Draper, N. W. A. Geraghty, M. Jeffares, T. McCabe, T. B. H. McMurry and J. E. O'Brien, *Org. Biomol. Chem.* **9**, 2959 (2011).

[152] E. García-Expósito, M. J. Bearpark, R. M. Ortuño, V. Branchadell, M. A. Robb and S. Wilsey, *The Journal of Organic Chemistry* **66**, 8811 (2001).

[153] E. García-Expósito, M. J. Bearpark, R. M. Ortuño, M. A. Robb and V. Branchadell, *The Journal of Organic Chemistry* **67**, 6070 (2002).

[154] J. R. Cucarull-González, J. Hernando, R. Alibés, M. Figueredo, J. Font, L. Rodríguez-Santiago and M. Sodupe, *The Journal of Organic Chemistry* **75**, 4392 (2010).

[155] *Reference Solar Spectral Irradiance. http://rredc.nrel.gov/solar/spectra/am1.5/ (April 2016).*

[156] M. J. G. Peach, M. J. Williamson and D. J. Tozer, *J. Chem. Theory Comput.* **7**, 3578 (2011).

[157] M. J. G. Peach and D. J. Tozer, *J. Phys. Chem. A* **116**, 9783 (2012).

[158] M. A. El-Sayed, *J. Chem. Phys.* **38**, 2834 (1963).

[159] M. Reguero, M. Olivucci, F. Bernardi and M. A. Robb, *Journal of the American Chemical Society* **116**, 2103 (1994).

[160] J. Cao and Z.-Z. Xie, *Phys. Chem. Chem. Phys.* **18**, 6931 (2016).

[161] O. Schalk, M. S. Schuurman, G. Wu, P. Lang, M. Mucke, R. Feifel and A. Stolow, *The Journal of Physical Chemistry A* **118**, 2279 (2014).

[162] R. Bonneau, *Journal of the American Chemical Society* **102**, 3816 (1980).

[163] L. Rodríguez-Santiago, M. Sodupe, A. Oliva and J. Bertran, *Journal of the American Chemical Society* **121**, 8882 (1999).

[164] L. Rodríguez-Santiago, M. Sodupe, A. Oliva and J. Bertran, *The Journal of Physical Chemistry A* **104**, 1256 (2000).

[165] K. Hemelsoet, D. Moran, V. Van Speybroeck, M. Waroquier and L. Radom, *The Journal of Physical Chemistry A* **110**, 8942 (2006).

[166] A. Gil, S. Simon, L. Rodríguez-Santiago, J. Bertran and M. Sodupe, *Journal of Chemical Theory and Computation* **3**, 2210 (2007).

[167] S. Wilsey, L. González, M. A. Robb and K. N. Houk, *Journal of the American Chemical Society* **122**, 5866 (2000).

Danksagung

An dieser Stelle möchte ich mich bei allen bedanken, die mich in den vergangenen Jahren unterstützt haben und damit zum Gelingen dieser Doktorarbeit beigetragen haben.

Zuallererst gilt mein Dank Prof. Regina de Vivie-Riedle, die mich in ihre Arbeitsgruppe aufgenommen hat und mir die Möglichkeit und die Zeit gegeben hat, meine Doktorarbeit anfertigen zu können. Die wissenschaftliche und persönliche Freiheit, die ich in den vergangenen Jahren genießen durfte, haben für eine immer sehr angenehme Arbeitsatmosphäre gesorgt.

Des weiteren möchte ich Prof. Eberhard Riedle, Prof. Dirk Trauner und Prof. Heinz Langhals für die sehr interessanten und erfolgreichen Kooperationen danken. Auch ihren Mitarbeitern Igor, Roland, Desiree und Robin danke ich für die gute Zusammenarbeit.

Vielen Dank auch an meine momentanen und ehemaligen Arbeitskollegen – Judith, Benni, Markus, Philipp, Artur, Thali, Sven, Robert, Julius, Matthias, Daniel, Flo, Thomas, Franziska und Martin – für die entspannte und oft auch sehr lustige Arbeitsatmosphäre. Auch bedanke ich mich bei den Bacheloranden und F-Praktikanten, die ich in den letzten Jahren betreuen durfte: Alexander, Travis, Thomas, Moritz, Franziska und Jerome.

Außerdem möchte ich mich bei meinen Eltern bedanken, die mir das Studium und damit auch diese Doktorarbeit überhaupt erst ermöglicht haben. Außerdem danke ich meinem Bruder Oliver und meinen langjährigen Freunden Moe, Christian, Maxi und Tobi für den Spaß und die Unterstützung in den letzten Jahren.

Zu guter Letzt danke ich Sabrina und meiner Tochter Marie für die sehr aufregende Zeit in den letzten Jahren!